Electronic Processes in Se-Te-As-Ge Glasses

by

Nader Ali Radjy, B.Sc.(Eng.)

A thesis submitted in partial fulfilment of the requirements for the degree of Doctor of Philosophy of the University of London

Department of Electrical Engineering
Imperial College of Science and Technology

January 1978

Abstract

Electronic transport processes in Se-Te-As-Ge (SeTAG) chalcogenide semiconductors have been studied. Bulk glasses in the series $Ch_x Y_{100-x}$ ($Ch = Se_{19.7} Te_{80.3}$, $Y = As_{74.4} Ge_{25.6}$), where x = 45%, 61% and 71% were prepared.

The structure of the glasses was investigated by X-ray diffraction, scanning electron microscopy, and softening temperature measurements.

Bulk electrical transport measurements, carried out as a function of temperature and composition, were D.C. electrical resistivity, thermoelectric power, and optical absorption and reflection spectra. All glasses were found to be p-type. A model considering parallel conduction in the extended and localised valence states fitted the experimental data best. It showed an increasing width in the localised valence band tail with increasing compositional disorder, Y, in the chalcogen network, Ch. The model was, however, unsatisfactory in that the effective density of localised states was found to be about two orders of magnitude higher than that of the extended states.

Various thin film deposition techniques of the $Ch_{61}Y_{39}$ glass were investigated. Flash evaporated films were selected for electrical measurements, because of good control of film thickness, ease of film preparation, and compositional consistency.

D.C. conductivity measurements as a function of temperature and film thickness indicated that the films were similar to the bulk glasses, and that they were effectively 'flat band' at the surface. Field effect measurements were carried out at room temperature and 343 K on the thin films, which were found to be p-type. The induced surface charge was kept to about $\pm 3 \times 10^{11}$ cm^{-2}. The modulated source-drain current was found to decay monotonically with time, and no standing field effect modulation could be observed. The A.C. field-effect data were best analysed by considering a trap limited drift mobility mechanism, and estimates of the hole trap depth and density were obtained. A model has been proposed to explain the observed decay in conductivity modulation, and by considering the potential distribution in the presence of spatially fixed deep donor/acceptor centres, the final expected modulation has been shown to be very much less than present theories would account for.

Acknowledgements

I am deeply grateful to Dr. Mino Green for his continuing keen interest, guidance, and constructive criticisms, which made this thesis possible, and to Professor J.C. Anderson for providing me with the opportunity to undertake this project.

My thanks are also due to many student colleagues and academic members of staff in the Materials Section for stimulating discussions and practical assistance at various stages of this study. I especially thank Dr. W.C. Dautremont-Smith for his advice and help in carrying out the optical measurements. I also acknowledge the assistance given me by the technical staff of the Electrical Engineering Department, and that by Mr. P. Robinson in particular.

I wish to thank Miss F. Grootenhuis and Miss C.D.M. Collins for typing the text, and Mrs. J. Hill and Mr. R. Puddy for preparing the majority of the technical drawings and photographs.

Above all, however, I am indebted to my parents for their unfailing patience and encouragement throughout the duration of my studies.

CONTENTS

	Page
Title Page	1
Abstract	2
Acknowledgements	3
List of Tables	10
List of Figures	12
CHAPTER 1: INTRODUCTION	20
1.1 Switching and Other Applications of Chalcogenide Glasses	24
1.2 Localised States in Amorphous Solids	24
1.2.1 The Cohen-Fritsche-Ovshinsky (CFO) Model	25
1.2.2 The Davis and Mott Model	27
1.2.3 The Chemical Bond Approach	30
1.3 General Layout of the Thesis	38
Chapter 1 - References	40
CHAPTER 2: PREPARATION, CLASSIFICATION, AND PHYSICO-CHEMICAL PROPERTIES OF Se-Te-As-Ge (SeTAG) Glasses	43
2.1 Introduction	43
2.2 Glass Forming Regions of (Se,Te)-As-Ge Ternary Compounds	44
2.3 Method of Bulk Glass Preparation	47
2.4 Material Classification	49

		Page
2.5	Material Compositional Analysis	51
	2.5.1 Introduction	51
	2.5.2 Results of Electron Probe Micro-analysis on SeTAG	52
2.6	Physical and Chemical Properties of SeTAG	53
2.7	Softening Temperature of SeTAG Glasses	55
	2.7.1 Introduction	55
	2.7.2 Experimental Procedure	59
	2.7.3 Results	62
2.8	Discussion and Conclusions	64
Chapter 2 - References		68
CHAPTER 3:	ELECTRICAL TRANSPORT IN BULK Se-Te-As-Ge GLASSES	69
3.1	Introduction	69
3.2	Experimental Apparatus	74
	3.2.1 Thermocouple Calibration	76
3.3	Temperature Dependence of D.C. Conductivity	77
	3.3.1 Experimental Procedure	77
	3.3.2 Results	81
3.4	Ambient Effects and the Electrical Conductivity of SeTAG Glasses	88
	3.4.1 Introduction	88
	3.4.2 Experimental Procedure and Results	88

		Page
3.5	Temperature Dependence of Thermoelectric Power	90
	3.5.1 Introduction	90
	3.5.2 Experimental Procedure	93
	3.5.3 Results	103
3.6	Temperature Dependence of the Optical Gap in Ch_{61} Y_{39} SeTAG Glass	106
	3.6.1 Introduction	106
	3.6.2 Experimental Procedure	112
	3.6.3 Results	114
3.7	Analysis of Results	123
	3.7.1 The Mott and Davis (MD) Model	124
	3.7.2 The Green-Levy-Gee (GLG) Model	131
	3.7.3 The Nagels-Callaerts-Denayer (NCD) Model	135
3.8	Discussion and Conclusions	151
Appendix 3A:	The GLG Model of the Temperature Dependence of Conductivity in Amorphous Chalcogenide Semiconductors	161
Appendix 3B:	Thermocouple Calibration Procedure and Error Analysis	167
	3B.1 Method of Calibration	167
	3B.2 Calculation of Errors in Platinuum Resistance Thermometer Readings	168
	3B.3 To Calculate the Errors in the Thermocouple Readings	170

Page

Appendix 3C: The Effect of Diffuse Reflectivity Losses on the Absorption Coefficient 171

Chapter 3 - References 174

CHAPTER 4: PREPARATION OF AMORPHOUS THIN FILMS OF Se-Te-As-Ge 177

4.1 Introduction 177

4.2 The Vacuum System and the Thin Film Deposition Assembly 181

4.3 Preparation of Ch_{61} Y_{39} SeTAG Glass Thin Films 186

4.3.1 Knudsen Cell Evaporation Method 186

4.3.2 D.C. Sputtering Method 190

4.3.3 Flash Evaporation Method 193

4.4 Electron Probe Microanalysis (EPMA) of Thin Films 196

4.5 Electron Microscopy of Flash Evaporated SeTAG Films 199

4.6 Device Fabrication 202

4.7 Summary and Discussion 205

Chapter 4 - References 207

		Page
CHAPTER 5:	ELECTRICAL PROPERTIES OF THIN FILMS OF Se-Te-As-Ge	208
5.1	Introduction	208
5.2	Experimental Procedure	211
5.3	Results	217
5.3.1	Current-Voltage Characteristics	217
5.3.2	Resistance as a Function of Film Length	219
5.3.3	Resistivity as a Function of Film Thickness	219
5.3.4	Resistivity as a Function of Temperature	221
5.3.5	Measurement of Low Frequency Dielectric Constant	221
5.3.6	Field Effect Measurements	223
5.3.6.1	A.C. and Short Time Field Effect Modulations	226
5.3.6.2	A.C. and Short Time Field Effect Mobilities	231
5.3.6.3	Long Time D.C. Field Effect Data	231

Page

5.4 Analysis of Results 235

5.4.1 Resistivity Data 235

5.4.2 Field Effect Data 237

5.4.2.1 A.C. Field Effect: the Barbe Model 237

5.4.2.2 D.C. Field Effect Modulation Decay 242

5.4.2.3 The Discrete Charge Model 243

5.4.2.3.1 Prediction of an Upper Limit for $\Delta g/g_o$ at Long Times 246

5.4.2.3.2 A.C. Field Effect 259

5.5 Discussion and Conclusions 263

5.5.1 Suggestions for Future Work 269

Chapter 5 - References 270

CHAPTER 6: SUMMARY AND CONCLUDING REMARKS 272

Chapter 6 - References 275

LIST OF TABLES

		Page
Table 2.1	Electron Probe Microanalysis on Ch_xY_{100-x} SeTAG glasses.	52
Table 2.2	Densities of Ch_xY_{100-x} SeTAG glasses extrapolated from Hilton et al.'s data.	55
Table 2.3	Softening temperature in Ch_xY_{100-x} SeTAG glasses.	62
Table 3.1	Conductivity parameters for SeTAG glasses according to equation 3.1.	83
Table 3.2	The effect of skin growth on the electrical resistance of a $Ch_{61}Y_{39}$ SeTAG specimen.	89
Table 3.3	Seebeck coefficient parameters for SeTAG glasses according to equation 3.6.	104
Table 3.4	Temperature dependence of the optical gap in $Ch_{61}Y_{39}$ SeTAG glass.	122
Table 3.5	Transport parameters in bulk SeTAG calculated using the Mott and Davis model.	130
Table 3.6	Variation of conductivity parameters with conductivity curve selection in sample 8.2.	139
Table 3.7	Transport parameters in bulk Ch_xY_{100-x} SeTAG glasses computed using the NCD model.	146

		Page
Table 3.8	Room temperature effective densities of extended and localised valence states in SeTAG and Si-As-Te glasses.	150
Table 3A.1	Variation of $\Gamma(j)$ with j for $0 \leqslant j \leqslant 5$.	165
Table 4.1	Temperatures at which the constituent elements of SeTAG have vapour pressures of 0.1 mm Hg.	179
Table 4.2	EPMA on evaporated $Ch_{61}Y_{39}$ thin films.	197
Table 5.1	Room temperature resistivity as a function of film thickness	220
Table 5.2	210 Hz field effect mobility in SeTAG thin films, together with the screening length and the density of states at E_F computed from the Barbe model by neglecting surface states	241
Table 5.3	Trap limited drift mobility parameters computed from A.C. field effect data in the enhancement mode	261

LIST OF FIGURES

		Page
Fig. 1.1	Proposed band models for amorphous semiconductors.	26
Fig. 1.2	Chemical bonds; neutral and charged dangling bonds.	32
Fig. 1.3	$D^{\circ} + e \rightarrow D^{-}$.	32
Fig. 1.4	Bonding configuration and energies of a chalcogen atom (e.g. Se).	36
Fig. 2.1	Glass forming regions of Se-As-Ge and Te-As-Ge systems together with the compositions selected in this work.	45
Fig. 2.2	SEM micrograph of broken ingot of SeTAG.	50
Fig. 2.3	Variation of volume with temperature at the liquid-crystal and liquid-glass transitions.	56
Fig. 2.4	Schematic drawing of the softening temperature apparatus.	60
Fig. 2.5	Softening temperature as a function of % chalcogen in Ch_xY_{100-x} SeTAG glasses.	63
Fig. 2.6	Softening temperature in $^{\circ}C$ in Ge-As-Se system (calculated from Weber and Savage's data).	66
Fig. 3.1	Schematic drawing of the cryostat.	75

		Page
Fig. 3.2	Schematic cross-sectional drawing of the cryostat sample holder used for the conductivity measurements.	80
Fig. 3.3	Schematic drawing showing the thermocouple clamp and the position of the thermocouple with respect to the sample.	80
Fig. 3.4	Current-voltage characteristic in bulk specimen of $Ch_{45}Y_{55}$ composition.	82
Fig. 3.5	Resistivity as a function of temperature and composition for SeTAG glasses in the series Ch_xY_{100-x}.	84
Fig. 3.6	Variation of room temperature conductivity with (1) the atomic fraction of chalcogen elements present and (2) conductivity activation energy.	86
Fig. 3.7	Variation of conductivity activation energy with % chalcogen content.	87
Fig. 3.8	SEM micrograph of SeTAG thin film with no heat treatment.	91
Fig. 3.9	SEM micrograph of SeTAG thin film after heating in air for one hour at 423 K.	91
Fig. 3.10	Thermopower sample holder assembly (a) Schematic cross-section (b) Photograph	95

		Page
Fig. 3.11	Circuit diagram for thermoelectric power measurements.	97
Fig. 3.12	Seebeck coefficient of sample 7.3 as a function of heat treatment at 363 K.	97
Fig. 3.13	Resistance of sample 7.3 as a function of heat treatment at 363 K.	100
Fig. 3.14	Variation of thermoelectric power with temperature and composition.	105
Fig. 3.15	Temperature variation of Peltier coefficient with composition in Ch_xY_{100-x} glasses.	107
Fig. 3.16	Temperature variation of the Urbach edge in alkali halides.	109
Fig. 3.17	Temperature variation of the absorption edge in amorphous chalcogenides.	109
Fig. 3.18	Schematic cross-section of the presure die.	113
Fig. 3.19	Reflection spectrum of $Ch_{61}Y_{39}$ glass.	115
Fig. 3.20	Transmission of light through specimen of thickness, d, and absorption coefficient, α.	117
Fig. 3.21	Absorption spectrum of $Ch_{61}Y_{39}$ as a function of temperature with no diffuse reflectivity correction.	119

Page

Fig. 3.22 Absorption coefficient of $Ch_{61}Y_{39}$ as a function of temperature with diffuse reflectivity correction. 121

Fig. 3.23 The density of states in amorphous semiconductors as proposed by Mott and Davis. 125

Fig. 3.24 Curved fits (solid lines) to the experimental resistivity vs. temperature data of Ch_xY_{100-x} SeTAG glasses using the NCD model. 141

Fig. 3.25 Curved fits (solid lines) to the experimental thermoelectric power vs. temperature data of Ch_xY_{100-x} SeTAG glasses using the NCD model. 142

Fig. 3.26 Flow chart of method used in the NCD analysis. 143

Fig. 3.27 The ratio of localised band tail hopping conductivity to total conductivity as a function of temperature in SeTAG glasses computed using the NCD model. 145

Fig. 3.28 The energy distribution of the states dominating the conduction processes and their effective densities at 300 K as a function of composition in Ch_xY_{100-x} SeTAG glasses determined from the NCD model. 152

Fig. 3a.1 The density of states model used in GLG's derivation of the expression for conductivity. 163

		Page
Fig. 3c.1	The fractions of reflected and transmitted radiation from a scattering centre of distance $\ell(\lambda)$ into a parallel faced slab of material of thickness d.	172
Fig. 3c.2	Attenuation of transmitted radiation in specimen of Fig. 3c.1 showing the choice of $\ell(\lambda)$ so that T .d = Area under the curve $(0 \leqslant x \leqslant d)$.	172
Fig. 4.1	Vacuum apparatus and auxilliary control equipment.	182
Fig. 4.2	Top view of the carousel showing the various thin film deposition sections and the mask and substrate holders.	183
Fig. 4.3	Schematic drawing of a thin film deposition section showing the substrate and mask holders.	185
Fig. 4.4	Boat preparation and charging procedure.	188
Fig. 4.5	Knudsen cell assembly.	188
Fig. 4.6	SG8 single grain box source.	194
Fig. 4.7	Schematic drawing of the flash evaporation assembly.	194
Fig. 4.8	Electron beam damage to SeTAG film (M = 10,000).	200

		Page
Fig. 4.9	SADP of beam damaged SeTAG film.	200
Fig. 4.10	SADP of heavily beam damaged SeTAG film.	200
Fig. 4.11	Transmission electron micrograph of SeTAG film (M = 100,000).	201
Fig. 4.12	SADP of SeTAG film.	201
Fig. 4.13	Co-planar device using mica gate insulator.	204
Fig. 4.14	Co-planar device using SiO_2 gate insulator.	204
Fig. 5.1	A.C. field effect circuit.	213
Fig. 5.2	Bridge circuit for measuring long time decay of field effect modulation.	213
Fig. 5.3	A.C. field effect trace (T = 298 K).	214
Fig. 5.4	D.C. field effect trace (T = 343 K).	214
Fig. 5.5	Current-voltage characteristic in a $Ch_{61}Y_{39}$ thin film at room temperature (electrode separation = 50 μm).	218
Fig. 5.6	Resistivity vs. reciprocal temperature in a $Ch_{61}Y_{39}$ SeTAG thin film (film thickness = 1400Å).	222
Fig. 5.7	Equivalent capacitance circuit of the field effect structure.	224

		Page
Fig. 5.8	299 K field effect modulation as a function of time and charge in film 40.79 (thickness 1330Å).	227
Fig. 5.9	210 Hz and 1 kHz field effect modulation as a function of charge in film 40.79 at 343 K.	228
Fig. 5.10	Change in source-drain current at a fixed voltage as a function of frequency.	230
Fig. 5.11	Small signal field effect mobility as a function of frequency.	230
Fig. 5.12	Variation of large signal field effect mobility with induced surface charge at different times in film 40.79 (solid lines : T = 299 K, broken line: T = 343 K).	232
Fig. 5.13	Decay of field effect mobility as a function of induced surface charge in film 40.79.	233
Fig. 5.14	Decay of field effect modulation with time at T = 298 K and 343 K (film thickness = 520Å, $Q_g/e = -3.7 \times 10^{11}$ cm^{-2}).	234

Page

Fig. 5.15 The field effect mobility in film 30.9 as a function of time at T = 298 K and 343 K ($Q_g/e = -3.7 \times 10^{11}$ cm^{-2}, thickness = 520Å). 236

Fig. 5.16(a) Model used to compute the potential distribution due to a plane of charge near the interface in an MIS system

(b) Definition of a unit cell in a square array of charge. 247

Fig. 5.17 $\phi(x,y)$ in units of $e/4\pi\varepsilon\varepsilon_o$ computed in various z-planes. 250

Fig. 5.18 $\phi(x,y,z)$ vs. $|z-b|$ as a function of (x,y) using $\varepsilon=8.8$ and a = 164Å. 252

Fig. 5.19 ΔV vs. $|z-b|$ in film 30.9, using equation 3.26, for the points in the unit cell shown. 254

Fig. 5.20 The space charge region due to the potential $\Delta V(a/2, a/2, z)$ in film 30.9. 256

Fig. 5.21 $F_p = \sum_{m=1}^{\infty} \frac{(-V_s)^m}{m.m!}$ vs. V_s . 266

Fig. 5.22 Trap parameters computed for film 40.79 using the A.C. field effect data and the discrete charge model. 267

Chapter 1

Introduction

An amorphous solid may be defined as one whose long range atomic structure is non-periodic, although short range order over a few atomic distances may be preserved.

Recent research interest in the electrical properties of amorphous solids followed Ovshinsky's 1968 publication [1] in which he reported two types of reversible switching in these materials. The pioneering work on amorphous solids was carried out, however, by B.T. Kolomiets [2] and coworkers in Russia in the 1950's and early 1960's. They discovered that chalcogenide glasses - that is glasses containing one or more of the chalcogen elements of group VIB of the Periodic Table - could be prepared over a large range of compositions by quenching the molten ingot. They also found these glasses to be electronic conductors, which were insensitive to doping with pinned Fermi energies and semiconducting properties.

Non-crystalline inorganic semiconductors may be divided into two distinct categories. The first are the transition metal oxide semiconductors which are ionic in nature, and the second are the covalent amorphous semiconductors. The latter may be subdivided into tetrahedral amorphous solids which may only be obtained in thin film form (e.g. Si, Ge, GaAs), tetrahedral II-IV-V glasses (e.g. $CdGe_xAs_2$, $ZnSi_xP_2$), and lone pair (chalcogenide) semiconductors (e.g. Se, Te, As_2Te_3, ternary glasses in the system Se-As-Ge, and quaternary glasses in the Si-Ge-As-Te system). Some chalcogenide semiconductors may only be obtained as thin films

(e.g. Te), while others may be prepared in both bulk and thin film forms. Other types of covalent amorphous solids which also exist are for example, amorphous boron and arsenic. Organic and mixtures of organic and inorganic amorphous solids are also possible, but these will not be discussed here.

1.1. Switching and Other Applications of Chalcogenide Glasses.

Over the past decade, the theoretical understanding of electronic transport processes in amorphous semiconductors has increased considerably, and the use of these materials in technological applications has become more feasible over the same period. The best known of these is the use of amorphous selenium in xerography. Many review articles on the potential applications of amorphous semiconductors have been written (see, for instance, refs. 3-9), and therefore only a brief outline will be given here.

The two types of switching observed in chalcogenide glasses are of the "threshold" and the "memory" type. Threshold switching is a monostable phenomenon, in which the semiconductor is transformed into a low resistance "ON" state after the application of a field greater than a threshold value. If the current in then allowed to fall below a minimum "holding" value, the switch will revert to its high resistance "OFF" state. The memory switch, on the other hand, is bistable, and the ON state is maintained after the removal of the field. The switch may only be turned off by the application of a second current pulse.

Memory switching is generally associated with reversible structural changes from the amorphous OFF state to the crystalline ON state. Two theories have been proposed to explain threshold switching

in thin films. The first, which is a thermal one [10], is based on the thermistor action. It depends on the joule heating of the semiconductor causing an increase in the current. The second model, which is electronic [11], operates on a non-equilibrium increase in the free carrier density. The controversy as to which of the above two is correct seems to have been resolved by the observation of very fast switching times [12], and an estimated 60°C maximum temperature rise in the conducting filament [13], both of which favour an electronic mechanism.

The type of switching observed depends on the chemical composition of the chalcogenide glass. Threshold switching materials have heavy cross-linking of the chalcogen chain structure by elements from groups IV and V of the Periodic Table; memory materials have fewer cross-links, and longer, more flexible chain structures with weaker bonds, which may lead to crystallisation under excitation. Ovshinsky and Sapru [14] have proposed a structure dependent model which explains the two switching mechanisms. They follow Kastner's suggestion [15] that in chalcogen atoms (electronic configuration s^2p^4) two of the outer electrons form a non-bonding lone pair (LP) orbital at the top of the valence bond, and they propose that these LP electrons are responsible for the reversible switching properties of chalcogenide glasses. The ON state of the threshold switch then comes about from the excitation of an electron from the LP (leaving a hole behind) as a result of the applied electric field. Because of the heavy cross-linking, no structural changes occur, and the OFF state is restored by the recombination of the excited carrier with the hole after the removal of the field. In the memory switch, on the other hand, the hole left behind by the excitation of the electron is much more reactive because of the weaker and looser structure of the material.

Here, the hole may be taken up by a nearby dangling bond resulting in the localised rearrangement of the structure acting as a nucleation centre for crystallisation (i.e. the ON state). The switch is returned to the OFF position by the melting of the material using a high current pulse. As a result, chalcogenide memory devices are used in "read mostly memory" applications (RMM) where the read-time is extremely fast (a few nanoseconds) but writing-in takes a few milliseconds. A 1024-bit RMM is being developed for production [6]. These memory devices have lifetimes of more than 10^8 cycles, are very rugged (operating temperature - 50°C to 125°C), radiation resistant, and above all have non-volatile memories. Threshold devices have also found applications as control elements in display systems [5].

An amorphous-crystalline reversible transition may be induced optically as well as electrically or thermally. This has led to applications [4],[5] for chalcogenide glasses in the fields of computer-controlled multiple copy printing (ovography), optical and electron beam mass memories, and dry film processes. Compositionally graded alloys of Se, As and Te have also been used by Hitachi [16] recently in the target element of a colour TV camera pickup tube called SATICON.

With the recent success in doping of amorphous silicon films [17], it has become possible to produce an all amorphous pn junction [17b]. This has led to the development of amorphous silicon solar cells with efficiencies of up to 5.5% using doped amorphous silicon [18].

1.2. Localised States in Amorphous Solids.

In contrast to crystalline solids, there is no long range order in amorphous materials, and therefore no unit cell may be defined. Consequently an electron may not be described by a Bloch wave function. The density of states function, $N(E)dE$, and the Fermi distribution function, $f(E)$, are, however, still valid concepts in non-crystalline solids.

The most important concept in understanding the electronic transport properties of amorphous solids is that of localisation. Mott [21],[22], who has been largely responsible for formulating the theory of localised states in amorphous solids, used the earlier work of Anderson's [20] which considered impurity conduction in doped and compensated semiconductors. A crystalline array of potential wells was envisaged, and the potential at each well was varied at random over a range V_o. It was shown that, with increasing V_o, a critical value was reached above which an electron in a given well would not diffuse away at absolute zero of temperature, and would thus become localised. At temperatures above zero, charge transport was via phonon assisted hopping of carriers (i.e. thermally activated) from one localised state to another* as first described by Miller and Abrahams[23]. Mott, and Cohen etal [24] argued that a tail of localised states would be expected in a conduction or valence band. An energy E_c was defined in the conduction band below which all the states were localised. For energies above E_c, charge transport took place in the extended states via a diffuse random process similar to Brownian motion in a gas[25]. It was noted that the extended states

---

*See Section 3.7.1, Chapter 3, for a more detailed description.

in this regime ($E > E_c$) were not Bloch states because of lack of long range order, and the electron mean free path, L, was short and of the order of the interatomic spacing, a - the so-called 'random phase model', because phase coherence is lost over a. A similar situation also prevailed in the valence band: an energy E_v was defined above which all states were localised. The energies E_v and E_c were called the "mobility edges"[24], across which a drop in the magnitude of mobility, μ, of the order of about 1000 was expected in going from the extended, diffusive regime ($E > E_c$ or $< E_v$, $\mu \sim 10$ $cm^2V^{-1}s^{-1}$) to the localised, hopping transport regime ($E_v < E < E_c$, $\mu \sim 10^{-2}$ $cm^2V^{-1}s^{-1}$). A "mobility gap" was thus defined between E_v and E_c.

Many models have been proposed for 'states in the gap' of amorphous solids. One feature common to all has been the existance of mobility edges at E_v and E_c. These models will now be examined in approximate chronological order.

1.2.1. The Cohen-Fritsche-Ovshinsky (CFO) Model.

This model was proposed[24] to explain the electrical properties of amorphous covalent alloys like the chalcogenide glasses. It is based on a speculation by Mott that the valence requirements of atoms in these glasses are locally satisfied[26]. This tends to explain the insensitivity to doping observed in this group of amorphous solids. Because of compositional and translational disorder, high densities of localised states are assumed to tail-in from the conduction and valence bands (Figure 1.1(a)) and to overlap. In this situation, the electrons at the top of the valence band tail are at a higher energy than the states at the bottom of the conduction tail, and they therefore fall

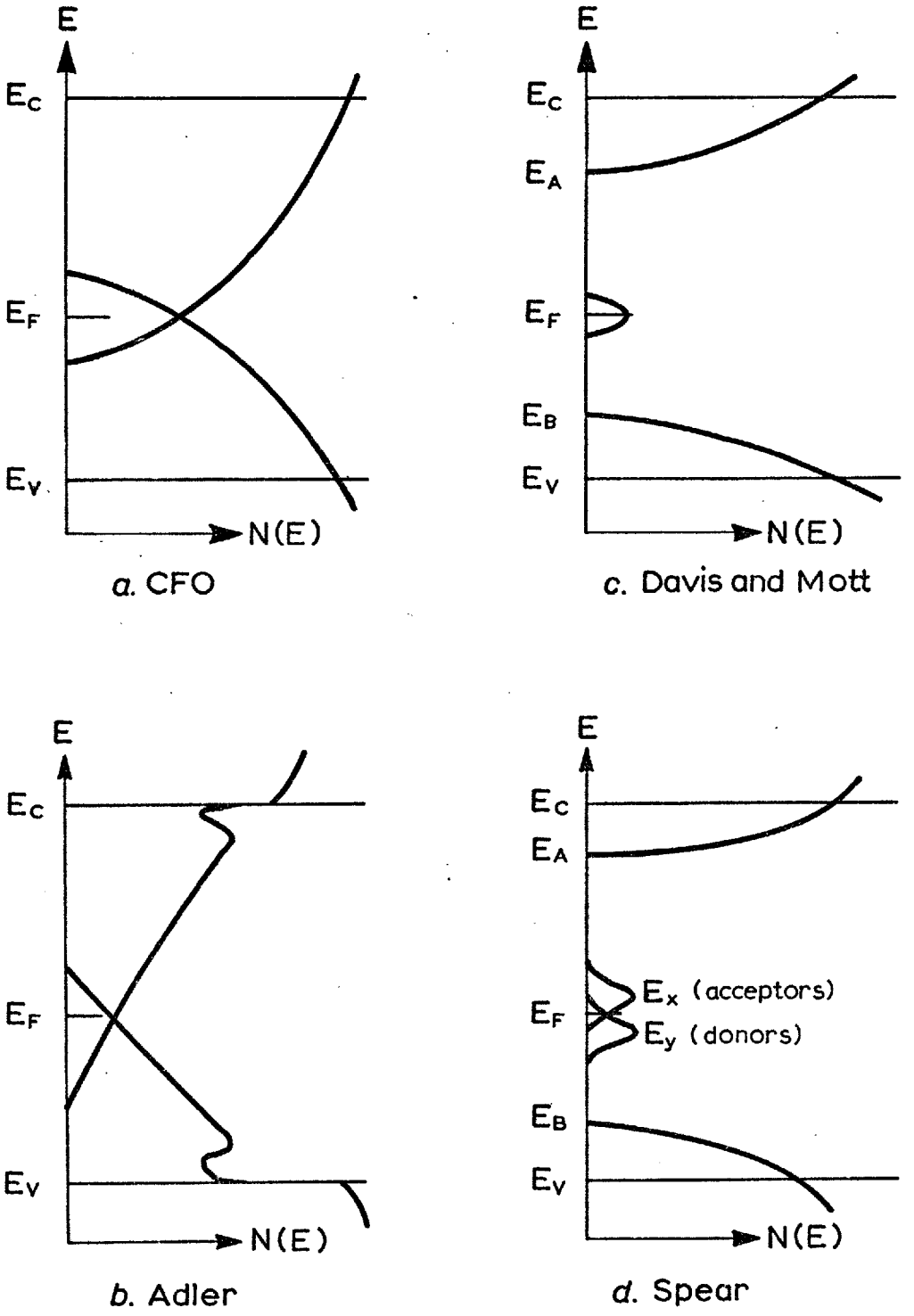


Fig.1·1: Proposed band models for amorphous semiconductors. States with energies $E_V<E<E_C$ are localised

into the latter states. The Fermi level, E_F, is then situated in the region of overlap with respective positively and negatively charged electron and hole traps above and below it, which cause E_F to be effectively pinned near the middle of the gap. The density of states at the Fermi level is high and estimated to be about 5×10^{19} $cm^{-3}eV^{-1}$.

The CFO model explained the singly activated, 'intrinsic' like conductivity which had been observed in many chalcogenide alloy glasses. The high density of states also provided explanations for the absence of rectifying contacts to chalcogenide glasses and the observed decay of photoconductivity[27].

Adler[28] modified the CFO model by considering electron correlation effects by including the influence of occupation of localised states on neighbouring states. His suggested model is shown in Figure 1.1(b).

1.2.2. The Davis and Mott Model[29],[30].

This model is shown in Figure 1.1(c), and is significantly different from the CFO model. It has been used, with some modifications, to explain many of the observed properties in chalcogenide glasses and tetrahedral amorphous films like Si and Ge.

In this model, a band of compensated states about 0.1 eV wide is assumed to exist near the middle of the band gap which effectively pins the Fermi level. The localised states at the band edges ($E_V < E < E_B$ and $E_A < E < E_C$) are due to lack of long range order, whereas the states at E_F are associated with defects such as dangling bonds.

Davis and Mott's argument against the CFO model stemmed from the radiative recombination spectra in As_2Se_3 and As_2S_3[30a], which peaked in intensity at about half the band gap. In the CFO model, this emission would be due to transitions to charged states near E_F. Davis and Mott proposed that with a continuous distribution of localised states, it was more likely for the electrons to jump down from one localised state to another with phonon emission. The similarity in the shapes of spectra from crystalline and glassy specimens also indicated that the same types of localised states were present in both structures.

In the light of more recent photo-luminescence studies as a function of As concentration (0.3 - 40% at.) in As-Se glasses, Street etal[41] associated the recombination centres with charged defects (As dangling bonds). Bishop etal[43] have, however, identified both As and chalcogen dangling bonds from ESR studies. Further evidence against the CFO model for, at any rate, simple chalcogenide alloys, has come from drift mobility measurements, where trapping levels with well defined energies have been detected.

The density of defects at E_F in the Davis-Mott model would be sensitive to the method of sample preparation and treatment, whereas the extent of localised states at the band edges would be dependent upon the degree of disorder present in the solid, which would vary with composition. This has been observed experimentally [36],[44b].

Various forms of DC conduction according to this model are given elsewhere[29],[30], and are also summarised in Section 3.7.1, Chapter 3. Briefly, conduction is by three possible mechanisms:

(1) Excitation of carriers to the extended states beyond E_v or E_c.

(2) Thermally activated hopping of carriers at E_A (for electrons), or E_B (for holes).

(3) Nearest neighbour hopping of carriers at E_F, leading to variable range hopping at lower temperatures.

A modification to the above model has been proposed by Mott [31] and also by Spear[32], as shown in Figure 1.1(d). Mott assumed that the dangling bond can act as a deep donor and as an acceptor. The donors (E_y) lie below the Fermi level, and the acceptors (E_x) above it. These states are broadened into bands, and they strongly overlap giving rise to charged states around E_F just as in the CFO model. However, Spear's field effect experiments on RF glow discharge deposited silicon films on substrates that were held at a high temperature, T_d, during the deposition (T_d > 310 K) show that there is a well defined minimum in the density of states between E_y and E_x. The density of states at the Fermi level is reduced from about 5×10^{18} $cm^{-3}eV^{-1}$ for specimens deposited at T_d = 310 K, to about 10^{17} $cm^{-3}eV^{-1}$ for T_d = 570 K specimens with a shift in E_F towards E_c with increasing T_d over about 0.4 eV.

Spear suggested that the defects at E_y and E_x might be similar to divacancies in crystalline silicon[33]. These would be equivalent to <u>pairs</u> of dangling bonds in Mott's model. The divacancy can produce a centre which can act as a donor <u>and</u> an acceptor just as in Mott's model. This centre is neutral in the ground state with

two electrons of opposite spins in its orbital. Therefore, the spins are paired and no ESR signal is observed. If, however, an extra electron is introduced from the valence band, the centre becomes negatively charged; removing an electron from it (to the conduction band) will make it positively charged (i.e. a donor like level). The ionisation energies are such that the accepter like level (negative when full) is above the donor like level (neutral when full). These levels are broadened into bands, which overlap (Figure 1.1(d)) and produce charged states with free spins.

This model has been used quite successfully in amorphous silicon. Chalcogenide glasses behave quite differently, however. No ESR without optical excitation[34] or variable range hopping has been observed in these glasses (except for unannealed, sputtered films deposited at 77 K[35]). These properties are difficult to explain for a finite density of states at E_F which manages to pin the Fermi level, but does not produce unpaired spins. Marshall and Owen[36a], however, use a model similar to that of Figure 1.1(d) in which they assume that the overlapping of E_y and E_x centres is not sufficient to produce an ESR signal. The origins of these centres in chalcogenide glasses would, nevertheless, remain uncertain in such a model.

1.2.3. The Chemical Bond Approach.

Anderson[37] suggested an alternative model to Marshall and Owen's where, in agreement with experimental observations, the pinning of E_F without producing ESR was made possible. He assumed that all bonding states in a chalcogenide glass are either occupied

by two electrons (one with spin up (↑) and one with spin down (↓)) or they are empty. This was made possible by assuming that the distortion energy released by the contraction of a bond because of the two electrons is larger than repulsive Coulomb interaction. This results in an atttractive (i.e. negative) correlation energy (the Hubbard U), which is the sum of the repulsive Coulomb term ($= \frac{e^2}{4\pi\varepsilon\varepsilon_o r}$, where r is the distance between the two electrons, and ε is the relative permittivity of the medium), and the attractive term resulting from the distortion of the lattice. Anderson proposed that the localised gap states arose because of disorder in the chalcogenide glass and avoided the concept of defects in a glass (see below). He argued that a CFO type model was possible, except that the effect of the variation in bond length giving rise to overlapping tails of localised states would be greatly reduced [37],[38].

Street and Mott [39], and Mott, Davis, and Street [40] (MDS) followed the above ideas of Anderson to propose a model where the localised gap states were due to well defined defects identified with dangling bonds on chalcogen atoms. A dangling bond (D^o) is a broken chemical bond with one unpaired electron (Figure 1.2), and is therefore electrically neutral. MDS assumed that the distortion energy gained by bringing two electrons together in a dangling bond, and making it negatively charged (D^-), was more than the repulsive energy between the two electrons, and therefore for two distant dangling bonds, the reaction,

$$2D^o \rightarrow D^+ + D^- \qquad 1.1$$

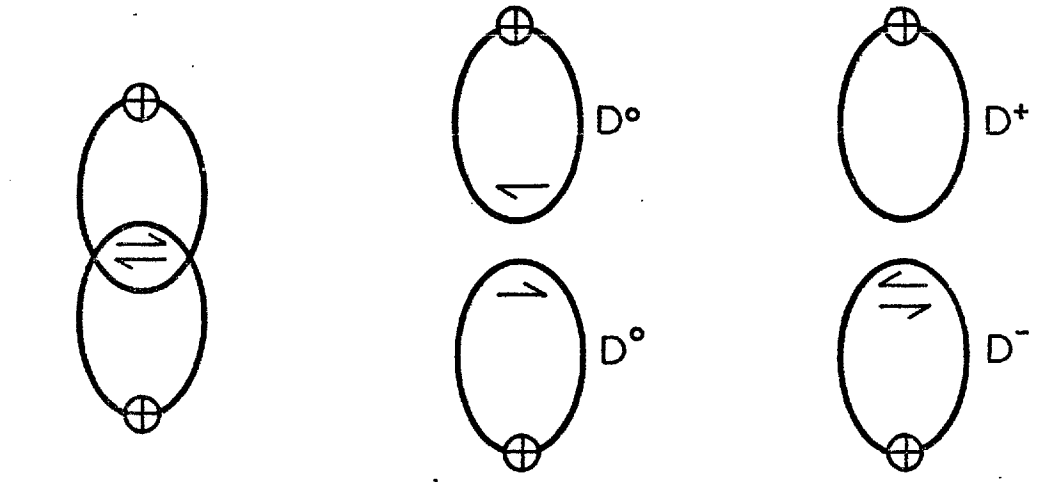


Fig. 1.2

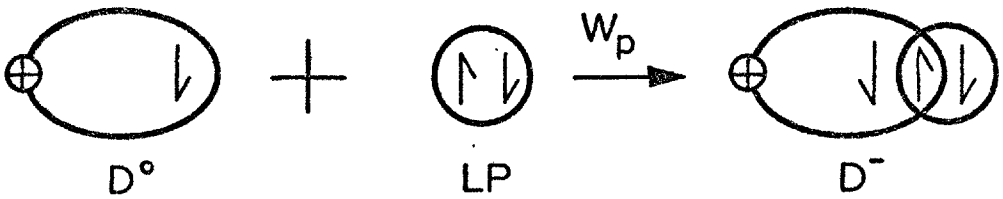


Fig. 1.3

Delete Fig. 1.3.

would be exothermic, where D^+ is an empty, positively charged dangling bond. In the ground state, then, the states below the Fermi level are the two electron $D^-(\uparrow\downarrow)$ "bipolaron" states, and those above it are the unoccupied D^+ states, and hence no ESR is observed. It is important to note that it is not possible to assign a single energy to a localised state here, and that the thermal and optical transition energies differ by a polaron energy term because of lattice distortion. MDS's outline of this is described below.

MDS follow the already mentioned suggestion by Kastner [15] that lone pair (LP) states form the top of the valence band. Thus, in the absence of distortion, a neutral dangling bond (D^o) would be a singly occupied LP acting as a shallow acceptor at an energy E_{el}(0.1 eV) above the valence band. If D^o were to bond to a LP (~~as shown in Figure 1.3~~) to form a D^-, this would require an energy W_p. Thus the thermal energy, W_1, to turn a D^o into D^- by taking an electron from the valence band is,

$$W_1 = E_{el} + W_p \qquad 1.2$$

D^+ can also form a bond with a neighbouring LP causing distortion of its environment. The LP electrons form deep bonding states during this process and release much energy. An electron added to D^+ would occupy the antibonding orbital, which, because D^+ is charged, would be in a shallow donor of binding energy E'_{el} below the conduction band. However, because of further change in distortion by the addition of the electron, the electron energy is lowered by an

amount W_p'. Hence, conversely, the thermal energy, W_2, to take an electron from D^o to the conduction band (i.e. $D^o \rightarrow D^+ + e$) is,

$$W_2 = W_p' + E_{el}' \qquad 1.3$$

For reaction (1.1) to be exothermic,

$$W_1 + W_2 - B < 0$$

where B is the band gap. To take two electrons from D^- to the conduction band requires an energy $B - W_1 + W_2$ ($B-W_1$ for this first electron, W_2 for the second). Therefore, for each electron, the energy is $\frac{1}{2}(B-W_1 + W_2)$. This determines the position of E_F below the conduction band, which will be pinned for a high enough density of defects. Furthermore, for $W_1 \sim W_2$, E_F will be near the mid-gap.

The above theory has been used to describe many of the observed properties in chalcogenide glasses like drift mobility and optical absorbtion measurements (including low absorption below the edge). It was, however, first developed to account for the observed Stokes shift (the energy difference between the absorbed and emitted radiation) in chalcogenide glasses[41]. The mechanism for this is now briefly described.

To observe luminescence, the sample is illuminated at low temperatures with radiation of band-gap energy (about 2 eV for As_2Se_3). This is absorbed by D^- centres producing a trapped hole (i.e. a D^o centre with a weakly bound electron). This electron would usually

escape, except at low temperatures, where it will recombine and emit radiation. Before emission, however, the distortion (because of the movement of the D° centre) results in a lowering of the energy of emitted radiation (to about leV in As_2Se_3), and hence causes a Stokes shift. This shift is equivalent to about $2W_p$ in equation 1.2.

Emin[42] proposed a small polaron model which would also explain the Stokes shift. He envisaged an electron polaron level below the conduction band, and a hole polaron level above the valence band. During optical excitation, the position of the atoms remain unaltered by the rapid electronic transition (Franck-Condon Principle). However, during to carrier-lattice interaction, atomic deformation occurs in which the carrier is "self-trapped" leading to small polaron formation, and the above mentioned polaron levels result. These levels affect the luminescence spectrum which will peak at a lower energy than the excitation energy. Small polaron formation also has important consequences when electrical conduction in chalcogenide glasses is considered. This is examined further in Chapter 3.

Kastner etal[43] and Adler[7] have considered the MDS model in the light of the energy configurations of the various bonding arrangements in a chalcogen network as reporduced in Figure 1.4. In the energy level diagrams illustrated, the energy of a non-bonding (σ) orbital is $-E_B$, and that in an antibonding (σ^*) orbital is $E_B + \Delta$, where Δ (always > 0) is the difference in the energies of σ^* and σ compared to the LP level. The increase in energy due to electronic correlation because of addition of an extra electron

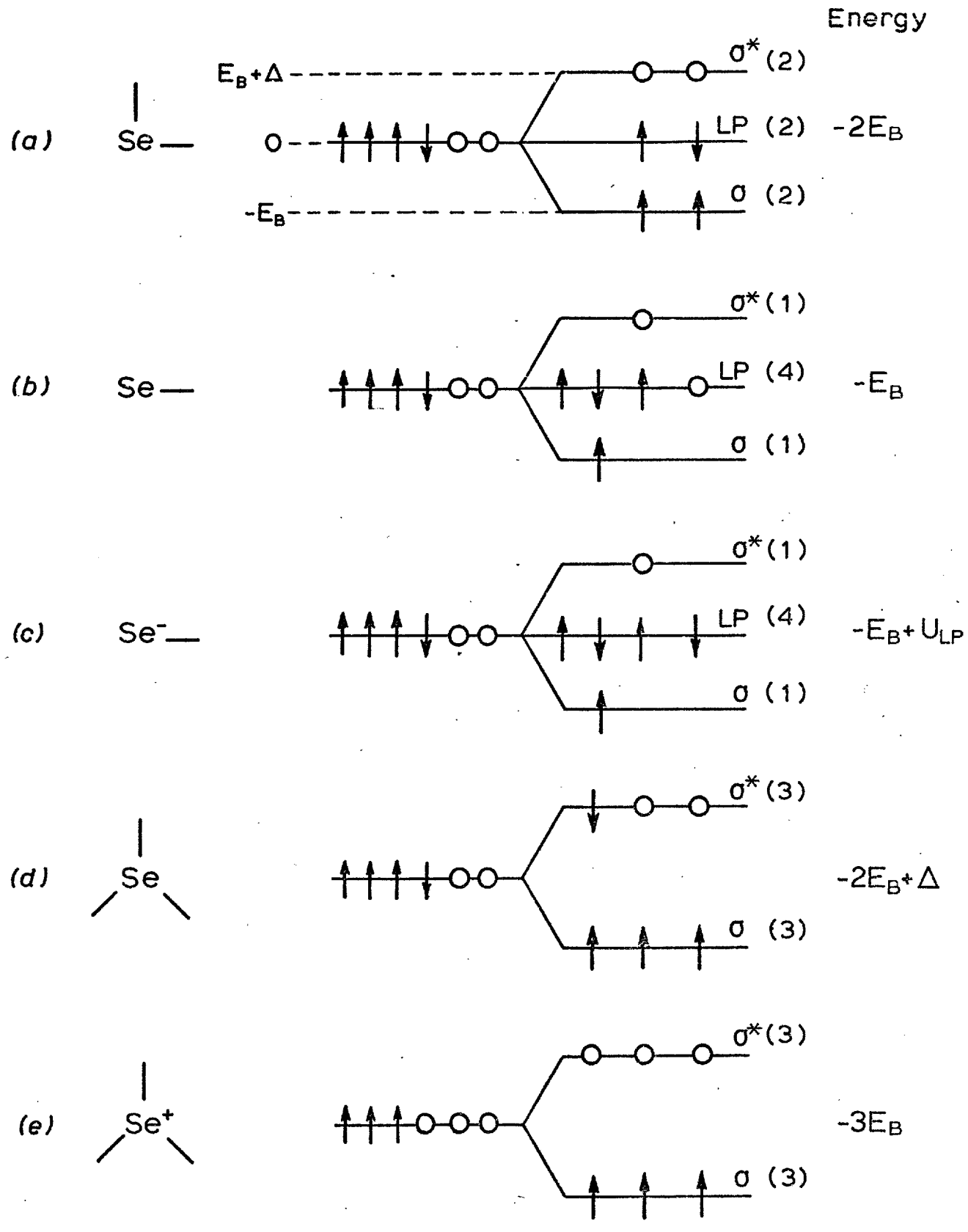


Fig. 1.4: Bonding configuration and energies of a chalcogen atom (e.g. Se).

is designated by $U_{\sigma*}$ and U_{LP} depending on whether the extra electron is in a σ^* state or in a LP. E_B is considered to be much larger than Δ, $U_{\sigma*}$, or U_{LP}. They conclude that a singly coordinated dangling bond (Figure 1.4(b)) is energetically unfavourable. Instead, the valence alternation pair (VAP) model is proposed. It is argued that a combination of positively charged trigonally coordinated (Figure 1.4(e)) and negatively charged singly coordinated (Figure 1.4(b)) chalcogen atoms would have an energy almost as low as two chalcogen atoms in two-fold coordination (Figure 1.4(a)). Neither of these centres have unpaired spins, which would explain the absence of ESR. The trigonally coordinated chalcogen atom would act as a cross-link between chalcogen chains, and the singly coordinated Se^- would terminate a chain, being similar to a halogen atom in its lowest energy configuration (s^2p^5). The charged centres arise through the transfer of an electron from one trigonally coordinated centre to another, thereby breaking the bond on the latter, and lowering the energy of the system. The VAP model also explains why tetrahedrally bonded amorphous solids like silicon do not behave in the same manner, since it is impossible to form five bonds with s and p electrons only.

Bishop etal [44] have observed an ESR signal in arsenic chalcogenides under optical excitation. This optically induced ESR would be due to D^o centres formed via the trapping of free electrons and holes by the D^+ and D^- centres in the MDS model. Bishop etal, however, identify two specific types of D^o: one is an electron localised on an As atom, and the other a hole localised on a chalcogen.

The observation of optically induced, metastable paramagnetic centres in amorphous arsenic is also not explained by the MDS model, since there is no evidence for the existence of lone pair orbitals in this material.

It is thus apparent that whilst models based on localised gap states arising from charged centres in an amorphous solid go a long way toward explaining the observed electrical and optical properties, some questions still remain unanswered.

In this introduction, it has been attempted to give a brief insight into the possible mechanisms suggested for some of the observed properties of chalcogenide glasses. The review presented here is by no means exhaustive, and for further information the reader is referred to various published articles and books on the subject[45].

1.3 General Layout of the Thesis

In Chapter 2, the preparation of bulk Se-Te-As-Ge (SeTAG) glasses in the series Ch_xY_{100-x}, where Ch = $Se_{19.7\%}Te_{80.3\%}$, Y = $As_{74.4\%}Ge_{25.6\%}$, and X = 45, 61, and 71% is described (all values quoted are atomic percentages). The glassy nature of the glasses is confirmed by scanning electron microscopy and X-ray diffraction. The compositions and homogeneities of the glasses are examined by electron probe microanalysis technique. Softening temperature measurements as a function of composition are also examined in this Chapter.

Chapter 3 deals with the electrical bulk properties of Ch_xY_{100-x} SeTAG glasses. DC resistivity and thermoelectric power

measurements as a function of temperature and composition are reported together with the temperature coefficient of the optical gap in $Ch_{61}Y_{39}$ glass. The data are examined in terms of various models.

Chapter 4 is a comparative study of thin film preparation methods using DC sputtering, Knudsen cell evaporation, and flash evaporation. The composition and structure of the films are briefly studied using electron microprobe analysis, electron spectroscopy for chemical analysis, and transmission electron microscopy.

In Chapter 5, the electrical properties of flash evaporated thin films of SeTAG ($Ch_{61}Y_{39}$ nominal bulk composition) are discussed in the light of DC resistivity measurements as a function of temperature and film thickness, and DC and AC field effect measurements at room temperature and 343K.

Chapter 6 is a general discussion and summary of the observed properties of SeTAG glasses.

Chapter 1 - References

1. S.R. Ovshinsky, Phys. Rev. Lett., 21 (1968) 1450.
2. B.T. Kolomiets, Phys. Stat. Solidi., 7 (1964) 359.
3. See articles by C.H.L. Goodman, H. Fritsche, and J. Mort in Section 5 of Electronic and Structural Properties of Amorphous Semiconductors, edited by P.G. LeComber and J. Mort, Academic Press, London, 1973.
4. S.R. Ovshinsky, J. App. Photographic Eng., 3 (Winter 1977) 35.
5. J. Allison, M.J. Thompson, Radio and Electr. Eng. 46 (1976) 11.
6. R. Allan, IEEE Spectrum, 14 (May 1977) 41.
7. D. Adler, Scientific American, 236 (May 1977) 36.
8. J. Tauc, Physics Today, Oct. 1976, 23.
9. H. Fritsche, Jap. J. App. Phys., 43 (1974) 32.
10. A.C. Warren, J. Non-Cryst. Sol., 4 (1970) 613.
    A.C. Warren, J.C. Male, Electron. Lett., 6 (1970) 567.
11. H.K. Henisch, E.A. Fagen, S.R. Ovshinsky, J. Non-Cryst. Sol., 4 (1970) 538.
12. R.W. Pryor, H.K. Henisch, J. Non-Cryst. Sol., 7 (1972) 181.
13. K.E. Petersen, D. Adler, J. App. Phys., 47 (1976) 256.
14. S.R. Ovshinsky, K. Sapru, p.447, Vol. I, Amorphous and Liquid Semiconductors, edited by J. Stuke and W. Brenig, Taylor and Francis, 1974.
15. M. Kastner, Phys. Rev. Lett., 28 (1972) 355.
16. T. Fujita, E. Maruyama, Hitachi Rev., 25 (1976) 141.

17a. W.E. Spear, P.G. LeComber, Phil. Mag., 33 (1976) 935.

17b. W.E. Spear, P.G. LeComber, S. Kinmond, M.H. Brodsky, App. Phys. Lett., 28 (1976) 105.

18. C.R. Wronski, IEEE Trans. Electr. Dev., ED 24 (1977) 351, and references 1-5 therein.

20. P.W. Anderson, Phy. Rev., 109 (1958) 1492.

21. N.F. Mott, Phil. Mag., 17 (1968) 1259.

22. N.F. Mott, Phil. Mag., 22 (1970) 7.

23. A. Miller, E. Abrahams, Phys. Rev., 120 (1960) 745.

24. M.H. Cohen, H. Fritsche, S.R. Ovshinsky, Phys. Rev. Lett., 22 (1969) 1065.

25. M.H. Cohen, J. Non-Cryst. Sol., 4 (1970) 391.

26. N.F. Mott, Adv. Phys., 16 (1967) 49.

27. H. Fritsche, E.A. Fagen, S.R. Ovshinsky, Bull. Am. Phys. Soc., 14 (1969) 311.
E.A. Fagen, H. Fritsche, J. Non-Cryst. Sol., 4 (1970) 480.

28. D. Adler, Amorhpous Semiconductors, Butterworths, London, 1972.

29. E.A. Davis, N.F. Mott, Phil. Mag., 22 (1970) 903.

30 N.F. Mott, E.A. Davis, Electronic Processes in Non-Crystalline Solids, Clarendon Press, Oxford, 1971.

30a. B.T. Kolomiets, T.N. Mamontova, A.A. Babaev, J. Non-Cryst. Sol., 4 (1970) 289.

31. N.F. Mott, Phil. Mag., 24 (1971) 911.

32. W.E. Spear, p.1 of ref. 14.

33. G.D. Watkins, J.W. Corbett, Phys. Rev. A, 138 (1965) 543.

34. S.C. Agarwal, Phys. Rev. B, 7 (1972) 685.

35. J.J. Hauser, R.S. Hutton, Phys. Rev. Lett., 37 (1976) 868.

36a. J.M. Marshall, A.E. Owen, Phil. Mag., 31 (1975) 1341.

36b. J.M. Marshall, F.D. Fisher, A.E. Owen, Phys. Stat. Sol. A, 25 (1974) 419.

37. P.W. Anderson, Phys. Rev. Lett., 34 (1975) 953.

38. N.F. Mott, Contemporary Phys., 18 (1977) 225.

39. R.A. Street, N.F. Mott, Phys. Rev. Lett., 35 (1975) 1293.

40. N.F. Mott, E.A. Davis, R.A. Street, Phil. Mag., 32 (1975) 961.

41. For a review of luminescence in amorphous semiconductors see R.A. Street, Adv. Phys., 25 (1976) 397.

42. D. Emin, p. 261 of ref. 3.

43. M. Kastner, D. Adler, H. Fritsche, Phys. Rev. Let., 37 (1976) 1504.

44. S.G. Bishop, U. Strom, P.C. Taylor.
(a) Phys. Rev. Lett., 34 (1975) 1346.
(b) Sol. State Comm., 18 (1976) 573.
(c) Phys. Rev. Lett., 36 (1976) 543.
(d) Phys. Rev. B, 15 (1977) 2278.

45 See books in refs. 3, 14, 28, 30. For review articles see, for instance :
(a) K. Weiser, Prog. Sol. State Chem., 11 (1976) 403.
(b) A.E. Owen, W.E. Spear, Phys. Chem. Glasses, 17 (1976) 174.
(c) Ref. 7 and 8.

Chapter 2

Preparation, Classification, and Physico-Chemical Properties of Bulk Se-Te-As-Ge Glasses

2.1. Introduction.

In this chapter, the method used in preparing Se-Te-As-Ge bulk glasses (henceforth called "SeTAG") is described. Glasses of three compositions in the series Ch_xY_{100-x}, where Ch ≡ $Se_{19.7\%}Te_{80.3\%}$, Y ≡ $As_{74.4\%}Ge_{25.6\%}$ (all values quoted are atomic percentages), and x = 45%, 61% and 71%, were prepared during the course of this work.

The reason for choosing the above atomic ratios was that at the commencement of this project, it was known that Se-Te-As-Ge alloys of composition $Se_{12}Te_{49}As_{29}Ge_{10}$ (≡ $Ch_{61}Y_{39}$) had been successfully prepared in the glassy state [1]. It was therefore decided to prepare glasses of this composition to begin with, and the subsequent bulk measurements as a function of composition were carried out by preparing glasses in the series Ch_xY_{100-x}, where the atomic ratios of the elements present in the chalcogen (Ch) complex, had been determined (and kept unaltered) by the ratios used in preparing the first ingot mentioned above *.

Apart from describing the method of glass preparation used, this chapter also covers the following topics:

(1) The glass forming regions of the Se-As-Ge and Te-As-Ge as investigated by other workers. The influence of the presence of

---

*One glass outside the Ch_xY_{100-x} series was also prepared and its electrical properties investigated. See Figure 2.1 and Section 2.5.2.

various additives on glass properties will also be reviewed.

(2) The use of X-ray powder techniques and scanning electron microscopy (S.E.M.) to check the amorphous nature of the prepared ingots, and to ensure the absence of any secondary macrophases.

(3) Compositional analyses and homogeneity investigations of the prepared ingots by the electron probe microanalysis (E.P.M.A.) technique.

(4) A brief description of the physical and chemical properties of SeTAG glasses.

(5) Measurement of the softening temperature of SeTAG glasses as a function of composition. Investigation of possible trends in the variation of the softening temperature of chalcogenide glasses with composition as illustrated on a pseudo-ternary compositional diagram.

2.2. Glass Forming Regions of (Se,Te)-As-Ge Ternary Compounds.

Figure 2.1 shows the glass forming regions of Se-As-Ge ternary complexes as investigated by Savage and Nielson [2], and Nemilov [3]. Superimposed on the same diagram, the glass forming regions of Te-As-Ge complexes determined by three independent groups of workers are shown [4],[5],[6]. The main compositions studied in this work have also been marked on this diagram by treating SeTAG as a pseudo-ternary alloy in which the Se and Te components are treated as one chalcogen unit in the compositional triangle *.

---

* The $Se_9Te_{32}Ge_{6.5}As_{52.5}$ composition in Figure 2.1 was outside the Ch_xY_{100-x} series.

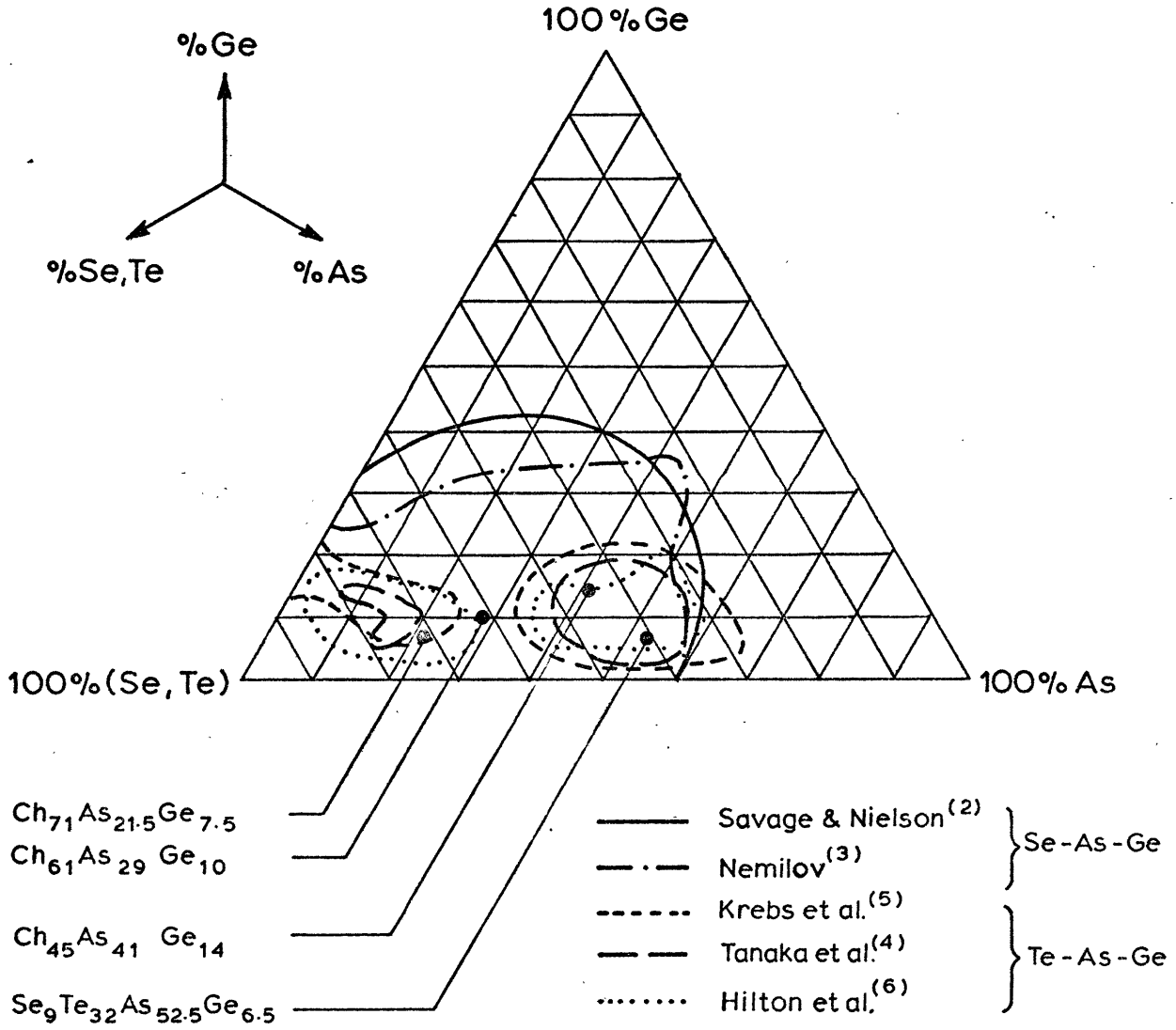


Fig. 2·1: Glass forming regions of Se-As-Ge and Te-As-Ge ternary systems together with the compositions selected in this work.

It should be noted that the above glass forming regions were plotted by air quenching of the molten alloys.

It can be seen from Figure 2.1 that the various glass forming regions reported by research workers from different laboratories agree quite closely with each other, and that, generally speaking, the glasses are reasonably chalcogen rich, and Ge and As deficient. Haisty and Krebs [7] have investigated the effects of various additives on the glass forming ability of Se. They conclude that addition of Te reduces the stability of the Se glass, as the incorporation of Te in Se chains, where Se-Te bonds are weaker than Se-Se bonds, makes thermal dissociation easier. This is interpreted to mean that a few Se atoms can form a nucleation centre, which would enhance crystallisation. The addition of Ge and As has a stabilising effect on the Se network by acting as branching and cross-linking agents between the Se chains. Thus the effect is to introduce more disorder into the Se network, which is maintained on cooling. As more As and Ge atoms are added, however, the nature of bonding in the melt changes from sp hybrid bonding (not favouring atomic motion) to pσ bonding (i.e. weaker non-directional one-electron bonds) which allows free motion of atoms in the melt that can form themselves into a crystalline state on cooling.

Hilton etal. [6] have examined the glass forming tendencies of ternary systems with constituent elements from groups IVA, VA, and VIA of the Periodic Table. They suggest that, in the melt, these ternary glasses are composed of mixtures of stoichiometric molecules, and so long as one binary molecule is not present in the excess to act as a nucleation centre during cooling, the molecules from the

three binaries prevent crystallisation by acting as diluents for each other. Hence, the larger the number of different molecular complexes the three elements can form, the larger is the glass forming region for that system. Based on this theory, these authors have been able to predict the glass forming regions of various ternary systems quite well.

2.3. Method of Bulk Glass Preparation.

Bulk ingots of SeTAG were prepared from their 99.999% pure constituent elements by weighing out the relative amount of each element into a quartz ampule. The elements were crushed in an agate mortar and pestle to dimensions of about 1-5 mm to keep any surface oxides to a minimum. The weighing accuracy was better than ± 0.01 gm, and since 30 gms of ingot were made each time, this meant a weighing accuracy of better than ± 1% for the element which was present in the smallest quantity. The quartz ampule was about 12 mm I.D., and it had a constriction near the top for sealing purposes under vacuum. Before weighing the elements into the ampoule, the ampoule was thoroughly washed in distilled water, and then etched in a 3:1 by volume concentrated HF/HNO_3 solution for at least two hours. The ampoule was again thoroughly washed in distilled water after it had been etched, and left in a hot oven to dry completely.

The ampoule, with the correct amount of the elements in it, was then evacuated to a pressure of less than 10^{-5} mm Hg. Before sealing off under vacuum, it was gently heated to get rid of any residual water vapour which might have been present.

The sealed ampoule was then placed in a vertical brick furnace,

whose temperature could be controlled by a "Eurotherm" temperature controller. The ampoule was attached to an agitator which was driven electrically. This ensured the thorough mixing of the components in the molten state. The temperature of the furnace was raised at a rate of 150° - 200°C per hour to 900°C, where it was kept for about 24 hours. After this period, the ampoule was taken out of the furnace and air quenched. Finally the ampoule was broken and the freshly made ingot was taken out. It was found that, in instances with the higher chalcogen content ampoules in particular, the ingot tended to stick to the quartz tube walls, which meant that taking the out ingot in one undamaged piece was sometimes impossible. The ingot was metallic grey in colour, and it appeared homogeneous. Because of the rapid cooling, it had a vortex at the top. All the ingots prepared in this way underwent concoidal fracture , and they all had several voids in them. This was attributed to the evolution and trapping of dissolved gases during the rapid quench from 900°C to room temperature. "Cleaved" ingots had a very shiny, mirror like appearance, and all the ingots were quite brittle, which made their processing and cutting into parallelpiped "timbers" for bulk electrical measurements quite difficult.

Samples taken from the different regions of the ingot (typically about 5 cm long) were numbered in the following way: the ingot was divided into four approximately equal portions along its length, and these were numbered from one to four from the top to the bottom of the ingot. The ingot itself was also given an identification number. For example, sample 3.4 refers to a sample taken from ingot number three, and the sample came from the bottom quarter of the ingot. The samples for the bulk electrical measurements were always taken from

along the length of the ingot, so that in case of any compositional gradients present, they were as representative of the mean composition as possible.

2.4. Material Classification.

The SeTAG compositions prepared in this work were classified as glasses if:

(1) They exhibited concoidal fracture.

(2) They showed no structure in their X-ray powder patterns.

(3) They appeared homogeneous, and structureless under examination by SEM (typical maximum resolution about 200 Å).

As already mentioned in the previous section, all the compositions that were prepared satisfied condition (1) above.

X-ray powder patterns, taken using a Debye-Scherrer type camera, showed a very diffuse ring typical of multicomponent glasses. An X-ray powder photograph of a STAG glass of $Si_{12}Te_{49}As_{29}Ge_{10}$ composition was very similar to those of SeTAG glasses studied in this work.

Scanning electron microscopy was used to check the homogeneity of SeTAG ingots. Figure 2.2 is a typical SEM micrograph taken, at 50 K magnification, of the surface of a broken ingot. It can be seen that no secondary phases and /or structure is present in this sample of $Ch_{71}Y_{29}$ composition - a feature which was common to all the compositions studied. Small pieces of dirt on the surface, shown in the photograph, were used for focusing purposes, as it was very difficult to focus on a completely structureless surface.

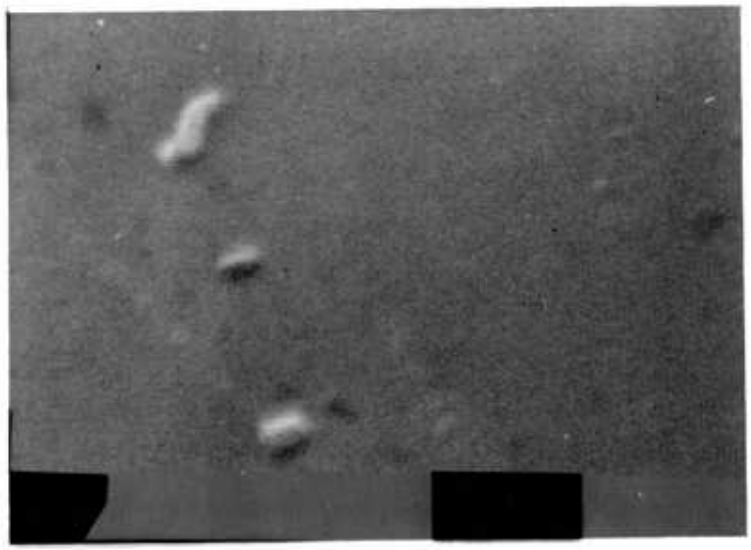


Fig. 2.2. SEM micrograph of broken ingot of SeTAG.

2.5 Material Compositional Analysis.

2.5.1. Introduction.

When an electron beam interacts with a solid, the processes which are of special interest in material characterisation are:

(1) The generation of secondary X-rays used in EPMA.

(2) The generation of secondary electrons used in Auger electron spectroscopy.

The EPMA technique was used by Imperial College Analytical Services Laboratory in examining thin films and bulk samples of SeTAG. Although this is a basically non-destructive technique, it was found that normal beam currents (~ 100 nA) over a spot of area 1 μm square caused beam damage to the samples. As a result, the beam current was reduced to about 15 nA, and area scans of about 100 μm square were used in the measurements. This meant, however, that the reported results had a relative accuracy of only about ± 5%.

By looking at the backscattered electron intensity (BEI), some information about the topography and presence of secondary phases may be obtained, which would be equivalent to the kind of information obtained by SEM. Since BEI is a function of the atomic number, it is very difficult to obtain BEI pictures for Ge, As, and Se separately because of their close proximity in the Periodic Table (all in the fourth row). It is, however, possible to obtain one BEI for the above group, and one for Te (in the fifth row of the Periodic Table), which is a much heavier element. On this basis, all the samples sent for analysis appeared homogeneous, and devoid of any secondary phases.

2.5.2. Results of EPMA on SeTAG.

Table 2.1 lists the analytical results obtained on the bulk samples examined. In this Table, 'N' and 'A' depict the 'Nominal'

x%	Sample No.	Se(atomic %) N	A	Te(atomic %) N	A	As(atomic %) N	A	Ge(atomic %) N	A
61	1.2	12	12	49	47	29	30	10	11
61	2.3	12	11	49	45	29	32	10	11
61	3.3	12	11	49	47	29	32	10	10
61	3.4	12	11	49	48	29	31	10	10
45	5.3A	9	9	36	32	41	52	14	7
45	5.3B	9	9	36	31	41	53	14	7
61	7.3	12	11	49	47	29	32	10	11
45	8.2	9	7	36	37	41	41	14	15
45	8.3	9	7	36	34	41	43	14	16
61	10.2	12	11	49	47	29	31	10	11
71	13.2	14	13	57	53	22	23	7	9
71	13.3	14	12	57	57	22	23	7	8
45	14.1	9	8	36	32	41	44	14	16
45	14.1	9	8	36	36	41	41	14	15
71	15.1	14	12	57	48	22	23	7	17
71	15.4	14	13	57	54	22	25	7	8

Table 2.1. EPMA Results for Ch_xY_{100-x} SeTAG Glasses

and 'Analysed' compositions respectively. All the compositions listed are quoted in atomic percentages and to the nearest atomic percent.

Comparing the results of the analysis with the nominal compositions, it can be seen that, with the exception of ingots 5 and 15,

the EPMA results relative to the nominal compositions are in agreement to within about ± 4%. In ingot 5, it is believed that weighing errors were responsible for the large differences in the 'N' and 'A' values. This was confirmed by the electrical measurements, where the thermopowers and conductivities of samples from this ingot were quite different from those obtained from other ingots of the same nominal compositions. In the case of ingot 15, the results are slightly puzzling, and the possibility of operator error in making the analytical measurments is not ruled out. This is justified by the fact that no such large variations in composition from the top to the bottom of an ingot is recorded in any of the other cases (compare, for example, samples 14.1 and 14.4 from ingot 14).

Although the relative accuracy of the EPMA results are ± 5%, it can be seen, within these limits, that there are no compositional gradients in any of the ingots where more than one sample was analysed (i.e. ingots 3, 8, 13, 14, 15). Samples 5.3A and 5.3B were taken from the same position in ingot 5 in order to check the reliability of the analyses - the resulting correspondence between the two sets of analysed compositions is very good.

2.6. Physical and Chemical Properties of SeTAG.

As mentioned earlier, ingots of SeTAG prepared during the course of this work were metallic grey in appearance, and they underwent concoidal fracture. They were found to be quite brittle, which made their cutting and polishing a very delicate task, as they were very susceptible to chipping and cracking.

SeTAG glasses were found to have no sharp melting points, but instead they were found to 'soften' upon heating - a process which is described more fully in Section 2.7, where softening tempera-

ture measurements on SeTAG are discussed.

SeTAG glasses were chemically inert to all normal organic cleaning reagents like acetone, trichloroethylene, ethyl and isopropyl alcohols, and chloroform. They did, however, etch very rapidly in concentrated hydroflouric acid, and more slowly in concentrated HNO_3. In both cases, a brown pungent gas was given off, which was thought to be hydrogen selenide because of its strong odour.

Hilton and Hayes [8] have measured some of the physical properties of multicomponent selenium and sulphur based chalcogenide glasses, where elements from groups IVA (Ge), VA (As and Sb), and VIA (S, Se and Te) of the Periodic Table were used in the synthesis of their glasses. One SeTAG glass of $Se_{25}Te_{30}As_{25}Ge_{20}$ composition was studied by these authors. It was found to have a density of about 5 g/cm^3, Young's modulus of 3×10^6 psi, shear modulus of 1.18×10^6 psi, Poisson's ratio of 0.27, hardness of 150 Knoop, and a thermal conductivity of about 1.9×10^{-3} W cm^{-1} K^{-1}.

The above authors also found that there is an approximate linear relationship between the density and the molecular weight of chalcogenide glasses. The forms of the relationship were different, however, for sulphur and selenium based glasses. Since the molecular weights of Ch_xY_{100-x} SeTAG glasses may be calculated, the densities of these glasses may be extrapolated from the results of Hilton etal. These (approximate) densities are given in Table 2.2.

Molecular volumes ($= \frac{\text{Molecular Weight}}{\text{Density}}$) of the glasses have also been calculated and listed in this Table. These compare to molecular volumes of 16.4 cm^3 for Se, 20.5 cm^3 for Te, 13.0 cm^3 for As, and 13.3 cm^3 for Ge. It can be seen that Ch_xY_{100-x} glasses have molecular

	Composition	Molecular Weight (g)	Density (gcm^{-3})	Molecular Volume (cm^3)
$Ch_{45}Y_{55}$	$Se_{8.9}Te_{36.1}As_{40.9}Ge_{14.1}$	94.0	5.3	17.1
$Ch_{61}Y_{39}$	$Se_{12}Te_{49}As_{29}Ge_{10}$	101.0	5.6	18.0
$Ch_{71}Y_{29}$	$Se_{14}Te_{57}As_{21.6}Ge_{7.4}$	105.3	5.8	18.2

Table 2.2. Densities of Ch_xY_{100-x} SeTAG Glasses Extrapolated from Hilton etal's data

volumes that are somewhere in between those of Se and Te. This seems to indicate quite an open structure in SeTAG glasses in which the basic helical chain configurations of crystalline Se and Te held together with van der Waals forces are maintained.

2.7. Softening Temperature of SeTAG Glasses.

2.7.1. Introduction.

Consider a substance in the liquid state being cooled, whilst one of its first order thermodynamic properties like volume (or enthalpy or entropy) is monitored (Figure 2.3). As the temperature is lowered, the volume of the liquid decreases linearly. A certain temperature is finally reached when either:

(1) there is a discontinuous change in the volume of the material under study, and the liquid freezes into a crystalline solid, at its freezing point, T_F,

or (2) the volume continues to decrease linearly with temperature, in which case the substance is now termed a "super-cooled" liquid.

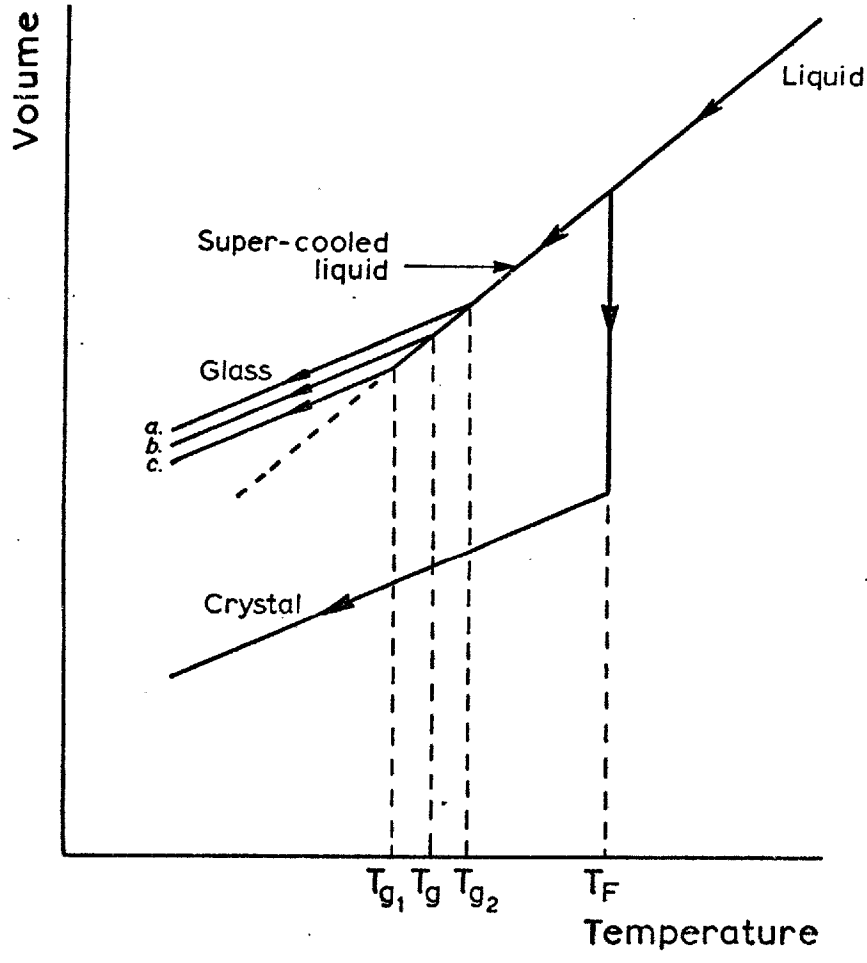


Fig. 2.3: Variation of volume with temperature at the liquid-crystal and liquid-glass transitions. Curves marked *a*, *b*, and *c* refer to fast, normal, and slow cooling rates respectively.

If the temperature of this supercooled liquid is reduced further, a point is reached where there is a sudden decrease in the slope of volume vs temperature plot. This point marks the transition from the supercooled liquid into a glass, and is called the glass transformation temperature, T_g [10]. Second order thermodynamic properties such as the expansion coefficient or the specific heat are, however, discontinuous at T_g. The viscosity of the substance in case (2) above, will show a continuous increase with a decrease in temperature until eventually the material becomes rigid at a viscosity of about 10^{15} poise.

T_g is a "kinetic" property of the glass in the sense that its value depends on the cooling rate and any subsequent heat treatment the glass may be subjected to: its value changes by about 10 - 20 K for a two order of magnitude change in the cooling rate in the case of amorphous Se, As_2Se_3, and As_2S_3 [9]. It should, therefore, be really regarded as a range of temperatures (see Figure 2.3).

The transformation temperature, T_g, should not, however, be confused with the softening tempearture, T_m. This is loosely defined as the temperature at which the viscosity of the glass falls below about 10^{11} - 10^{12} poise * as the glass is heated. It is usually some 10 - 30 degrees higher than T_g. If the fractional linear expansion of the glass is measured as a function of temperature, it will increase and reach a maximum at T_m as the temperature of the glass is raised [10]. This is basically due to the failure of the conventional experimental techniques, because at T_m the glass is no longer rigid, and it will deform under the action of a small force and hence a

---

*This is a very arbitrary definition, and viscosities of the order 10^{13} - 10^{11} poise have been used by different workers [13].

maximum in the plot of fractional linear expansion vs temperature is observed.

Whilst T_g is a much more significant parameter, the measurement of T_m is still quite useful in examining the origins of the glassy state. The softening temperature of a glass is indicative of its structure, and is a useful quantity in design of glass devices since the rigidity of the device at its operating temperature is of importance. Broadly speaking, a glass with a low softening point would have quite an open structure compared to one with a higher T_m.

Hilton, Jones, and Brau [6] have made extensive softening point measurements on multicomponent chalcogenide glasses. They found that, generally, the softening point increases with atomic weight, i.e.,

$$S > Se > Te$$

$$P > As > Sb$$

$$Si > Ge > Sn$$

By substituting Ge for Si in Si-As-Te glasses, it was found that T_m changes by the largest amount in compositions containing the greatest amount of group IVA elements. In contrast, glasses rich in Te showed little variation in their T_m. They also observed that the higher the softening point, the harder the glass and the smaller its thermal coefficient of expansion. The weak, low softening point and soft nature of non-oxide chalcogenide glasses as compared to the oxide glasses is interpreted by these authors in terms of the electronegativity differences of the constituent elements of the glasses: electronegativity difference is taken as a rough measure of the bond

energy between two atoms. The larger this difference, the more likely the bond formation, and the smaller the difference, the more the covalent nature of the bond. Hence, the strong nature of oxide glasses is interpreted in these terms, where the Pauling electronegativity of oxygen is 3.5 compared to 2.5 for S, 2.4 for Se, and 2.1 for Te. Although covalent bonding in itself does not produce weak solids (Si, for example, is a hard solid), but, in the case of amorphous chalcogenides, a strong solid is formed if the amorphous chalcogen rings and chains are broken down, and a strong three dimensional network is formed in its place. This will only occur if the bond energy between other elements and the chalcogens is much greater than those of the elemental covalent solids themselves.

The results of Kolomiets [11] are of interest here. He observed an increase in T_m when Ge was added to amorphous As_2Se_3 and As_2S_3, while addition of iodine reduced T_m: Ge replaces the weak van der Waals bonds between chains of chalcogen atoms with the relatively stronger covalent bonds, whereas iodine, which does not form covalent bonds with the chalcogens, has the reverse effect.

2.7.2. Experimental Procedure.

Figure 2.4 is a schematic drawing of the experimental set-up used to measure the softening temperature of SeTAG glasses as a function of temperature. The apparatus consisted of a press, which had a circular cross-sectional area of about 0.03 cm^2 (0.2 cm diameter) at its end. The load applied by the press could be monitored on a chart recorder. The press was housed in an enclosed chamber whose temperature could be varied. The parallel faced SeTAG specimen, whose T_m was to be

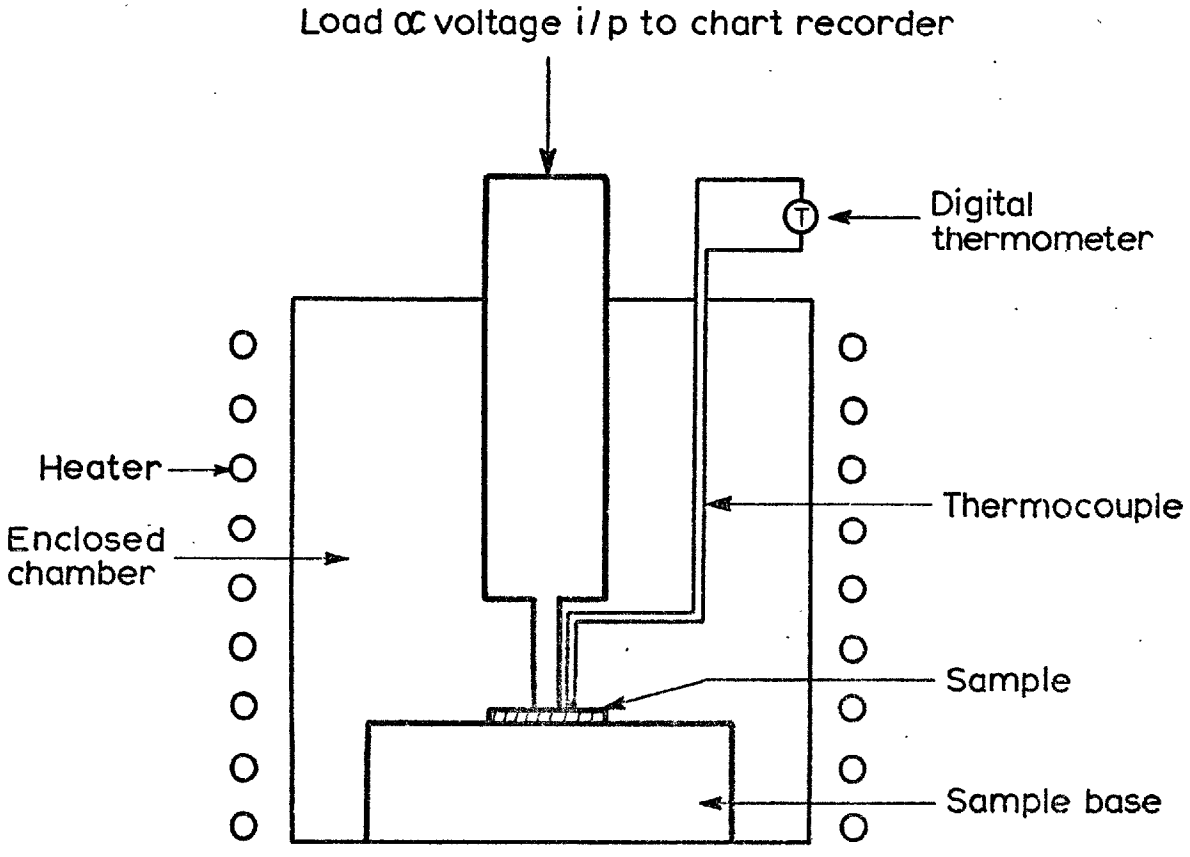


Fig. 2·4: Schematic drawing of the softening temperature apparatus

measured, was placed inside this chamber, and a load of about 2 kg (i.e. a pressure of about 6×10^4 g/cm^2) was applied to it. A thermocouple attached to the press, and in contact with the sample in the close vicinity of the area of application of the load, enabled the direct measurement of the specimen temperature. Thermally conducting silicon grease* was used to improve the thermal contact between the thermocouple and the sample. The temperature was raised at a rate of about 3-5°C per minute, although this could not be controlled very accurately.

The load on the specimen, as recorded on the chart recorder, increased slowly as the temperature inside the chamber increased. This was due to the thermal expansion of the press with temperature, and subsequently, the load had to be readjusted to 2 kg periodically. At a certain temperature, a sudden drop in the applied load was observed on the chart recorder. The temperature at which this occurred was taken to be the softening point, T_m. Becuase of the uncertainty introduced into the measurements by the expansion of the press itself, it is estimated that T_m could only be recorded to about $\pm$ 5 K. As mentioned in the previous section, however, this lack of accuracy is relatively unimportant, because of the arbitrary nature of softening point measurements, and their dependence on heating rates, and the chosen value of viscosity for defining T_m. Although a measure of the absolute value of T_m is desirable, the interest here is more in the change in T_m with composition. So long as the same procedure is employed in measuring the softening point in different specimens, a general idea about the variation of T_m with composition is obtained.

---

*Supplied by RS Components Ltd., London - See Chapter 3.

The method which has been described in this section is quite similar to those used by Hilton etal [12] and Levy [1].

2.7.3. Results.

Using the procedure outlined above, the softening tempeartures of two specimens from each of the three prepared compositions in the series Ch_xY_{100-x} were measured. The results are summarized in Table 2.3.

Composition	Sample No.	T_m(°C)	T_m(K)
$Ch_{45}Y_{55}$	8.2	218	491
$Ch_{45}Y_{55}$	14.3	213	486
$Ch_{61}Y_{39}$	1.2	175	448
$Ch_{61}Y_{39}$	9.4	167	440
$Ch_{71}Y_{29}$	13.2	140	413
$Ch_{71}Y_{29}$	13.3	135	408

Table 2.3. Softening Temperature in Ch_xY_{100-x} SeTAG Glasses

Figure 2.5 shows the variation of softening temperature with the atomic % of chalcogen atoms present in the SeTAG glasses investigated.

From Table 2.3 and Figure 2.5 it can be seen that there is a reduction in T_m with increasing % chalcogen content of the glass, and hence with decreasing amount of cross-linking additives As and Ge present in the glass.

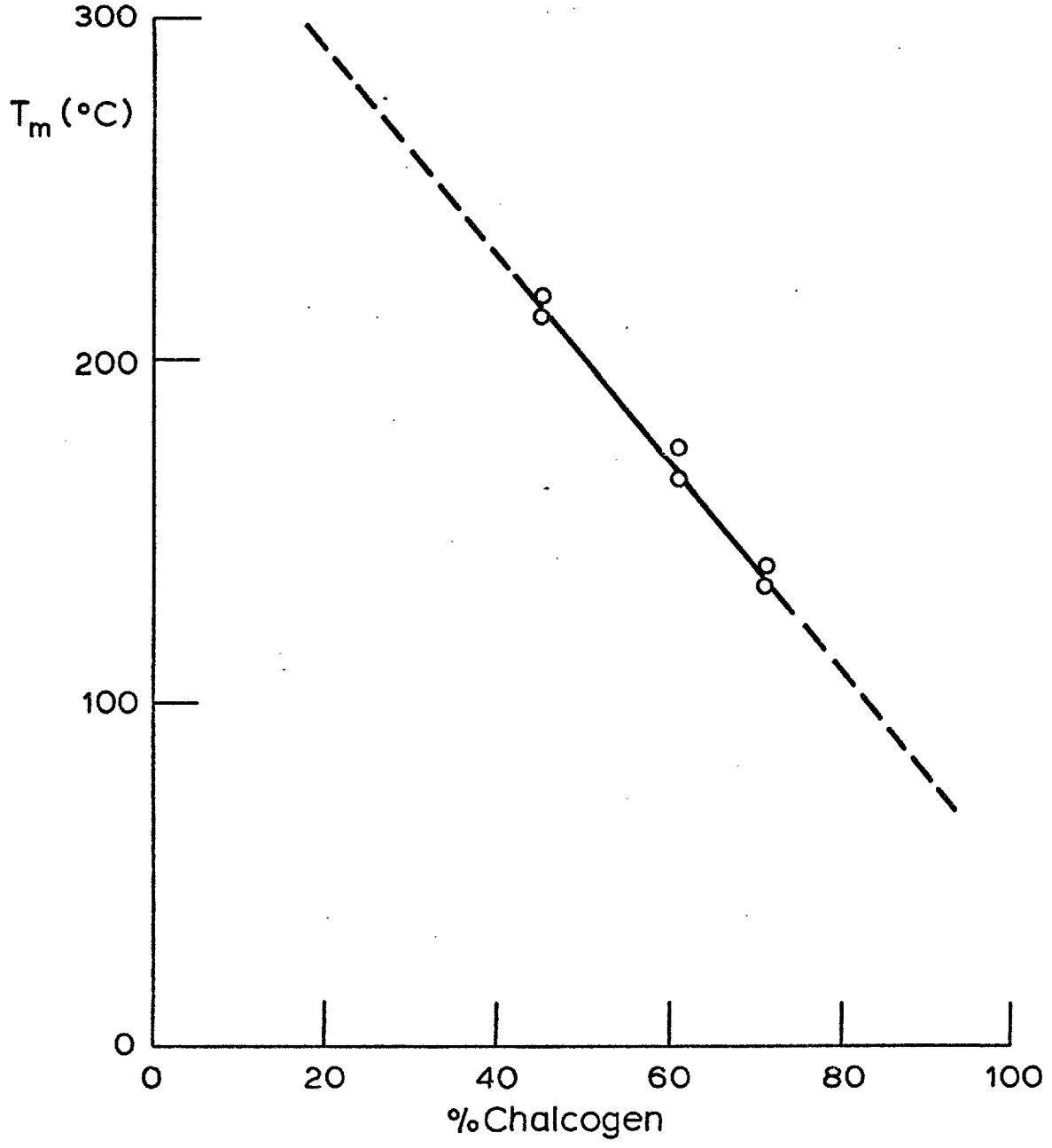


Fig. 2·5: Softening temperature as a function of % Chalcogen in Ch_XY_{100-X}SeTAG glasses.

The results of Levy [1] on STAG glasses are of interest here. He found a similar behaviour, and observed a linear decrease in T_m with increasing Te content from 39% to 74%. In SeTAG, where the Si component in STAG glasses has been replaced by Se, there is a marked reduction of 90 - 100°C in T_m if glasses of the same Te content are compared in the two cases. This confirms the results of Hilton etal and Kolomiets [11] who observed an increase in T_m as more cross-linking elements are introduced into the chalcogen network.

2.8. Discussion and Conclusions.

SeTAG glasses in the series Ch_xY_{100-x} (X = 45%, 61%, and 71%) were prepared. The amorphous nature of these glasses were checked by SEM and X-ray techniques. Concoidal fracture and the absence of any sharp melting points confirmed the glassy nature of the prepared ingots. The EPMA method was used to compare the nominal and actual compositions of the prepared ingots. In most cases studied, the two were in agreement to within the quoted accuracy of the analytical results. EPMA studies also indicated that no secondary phases were present in the prepared ingots, and that there were no significant compositional gradients within the ingots.

The approximate densities and molecular volumes of SeTAG glasses, computed using the results of Hilton etal [8], indicate that the structure of SeTAG is quite an open one, since the molecular volumes of these glasses are quite close to those of Se and Te.

The above conclusions are confirmed by the low softening temperatures of SeTAG glasses which vary from about 215°C for 45% chalcogen content to about 137°C for 71% chalcogen content in these glasses.

These results are in agreement with the proposition [6],[11] that chalcogenide glasses retain the helical chain structure of the pure chalcogens to a large extent, and that the introduction of additives such as As and Ge "strengthens" their structure by replacing the weak van der Waals bonds between these chains with the stronger covalent bonds, thus producing a more three dimensional network which is harder and has a higher softening temperature (where T_m gives one an idea of the ease with which atomic motion can take place in a glassy structure).

The above model of the chalcogen network being cross-linked, and thus strengthened, by Ge and As additives, is satisfactory when these additives are present in small quantities. With larger percentages of As and Ge (up to 50%), however, this model would imply that almost all the chalcogen atoms are cross-linked, at which point the model must break down.

Figure 2.6 shows the variation of softening temperature with composition in the ternary Ge-Se-As system. The data in Weber and Savage's paper [13] were used to draw the isothermal softening temperature contours of this diagram. The softening temperatures at various compositions were estimated from the average value of the temperatures at which the viscosities were 10^{11} and 10^{12} poise. Again, a general decrease in T_m with increasing Se content is observed, whereas the addition of As, and Ge in particular, tends to raise the softening point.

It is believed that a diagram such as that in Figure 2.6 may also be constructed for the pseudoternary SeTAG, and in fact for all other multi-component glasses. Weber and Savage have already done this in Se-Ge-As glass by considering other properties such as the

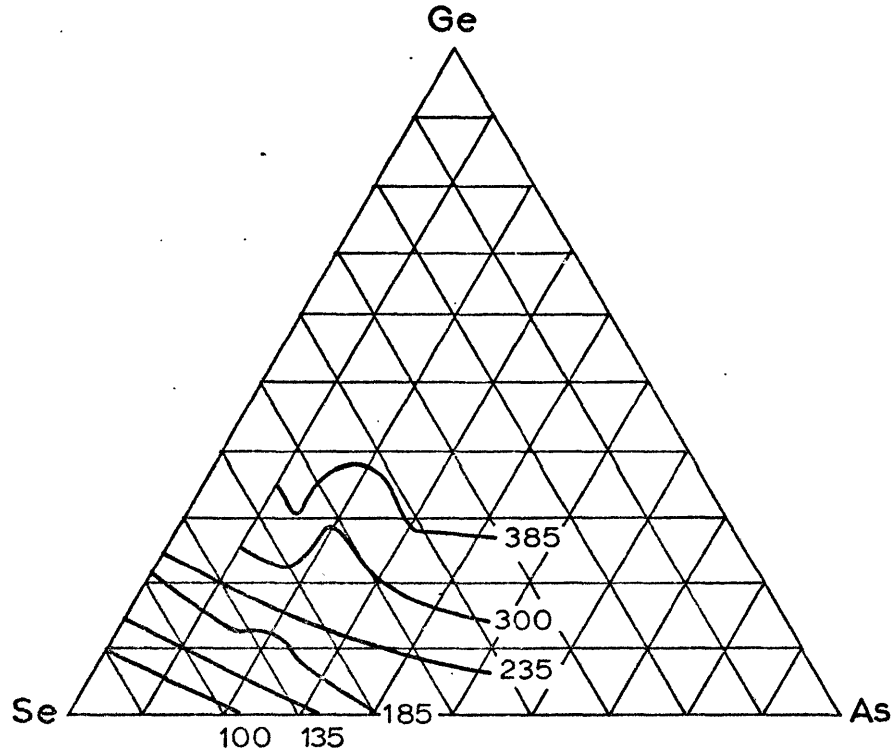


Fig 2·6: Softening temperatures in °C in Ge - As - Se system (calculated from Weber and Savage's data[13])

density, the thermal expansion coefficient, and the glass transformation temperature. Diagrams such as these would be useful in predicting the properties of glasses of different compositions, and in the study of glass structures in general.

Chapter 2. References.

1. A.W. Levy, Ph.D. Thesis, Council for National Academic Awards, 1972.
2. J.A. Savage and S. Nielson, Infrared Physics, 5 (1965) 195, Phys. Chem. Glasses, 5 (1964) 82, Ibid., 6 (1965) 90.
3. S.V. Nemilov, Zh. Prikl. Khim., 37 (1965) 1452, 1699.
4. K. Tanaka, Y. Okada, M. Sugi, S. Izima, M. Kikuchi, J. Non-Cryst. Solids, 12 (1973) 100.
5. H. Krebs, P. Fischer, Disc. Faraday Soc., 50 (1970) 35.
6. A.R. Hilton, C.E. Jones, M.Brau, Phys. Chem. Glasses, 7 (1965) 105.
7. R.W. Haisty, H. Krebs, J. Non-Cryst. Solids, 1 (1969) 399 and 427.
8. A.R. Hilton, D.J. Hayes, J. Non-Cryst. Solids, 17 (1975) 339.
9. A.E. Owen in Electronic and Structural Properties of Amorphous Semiconductors, edited by P.G. Le Comber and J. Mort, Academic Press, London, 1973.
10. G.O. Jones, Glass, Chapman and Hall Ltd., 1971.
11. B.T. Kolomiets, Phys. Stat. Solidi, 7 (1964) 359.
12. A.R. Hilton, C.E. Jones, M. Brau, Infrared Physics, 4 (1964) 213.
13. P.J. Weber, J.A. Savage, J. Non-Cryst. Solids, 20 (1976) 271.

Chapter 3

Electrical Transport in Bulk Se-Te-As-Ge Glasses

3.1. Introduction.

In amorphous semiconducting solids, as in their crystalline counterparts, the determination of the electrical transport parameters plays a central role in understanding the electronic nature of the solids.

In the case of crystalline materials, techniques such as conductivity, Hall and drift mobility, thermoelectric power, photoconductivity, optical absorption, and luminescence measurements have been used to investigate the electronic transport mechanisms. In investigating the physical properties of amorphous semiconducting materials, generally similar methods have been employed with encouraging results.

Conventional theories have not, however, been applicable in the interpretation of the transport data in non-crystalline semiconductors, and, as a result, new models and theories have been developed.

The multicomponent semiconducting chalcogenide glasses have been found to have properties, which, in general, distinguishes them from other groups of semiconducting amorphous solids [1].

As a reasonable approximation, the temperature dependent dc conductivity, σ , in amorphous multicomponent chalcogenides follows general Arrhenius relation [1],

$$\sigma = C \exp \left[- E_{\sigma o} / kT \right] \qquad 3.1$$

where $E_{\sigma o}$ is a simple activation energy extrapolated to OK, and C is a constant.

The thermoelectric power in multicomponent chalcogenide glasses is of the order of 1000 - 2000 $\mu V\ K^{-1}$ at room temperature, and it has been found to have a linear, or near linear, variation with the inverse

of absolute temperature. The sign of thermoelectric power is positive over the experimental temperature range, and it therefore indicates conduction dominated by holes [1].

Hall mobilities in chalcogenide glasses are of the order of 10^{-1} cm^2 $V^{-1}s^{-1}$ at 300 K. The Hall coefficient, with the exception of $Tl_2Te.As_2Te_3$ [16], is negative, and, therefore, apparently anomalous when compared with Seebeck coefficient data. This 'n-p anomaly' has been treated by Holstein [3] for the case of hopping type transport in general (e.g. in the case of small polaron hopping, or hopping in doped semiconductors), and by Friedman [3] for the case of the random phase model (R.P.M.)* of amorphous solids in the diffusive, short mean free path (L ~ a) regime. It is assumed that the applied magnetic field modifies the phase of the transfer integral between sites, and it is found that charge transfer processes involving at least three sites (instead of two, i.e. the initial and final sites) are necessary to obtain a Hall effect. These sites are nearest neighbours with a finite transfer integral between each pair of sites. Only when the three site interactions are large+, is the Hall coefficient negative. The four site interactions are found to make a positive, but small, contribution to the Hall coefficient. In other words, the Hall mobility, unlike the conductivity mobility, ~~is~~ maybe a function of the short range order of the material. Friedman's theory gives a Hall mobility which is typically one-tenth of the conductivity mobility in the diffusive regime, in general agreement with the experimental evidence. Friedman's model results, however, in a temperature insensitive Hall mobility, which

---

*The RPM is based on the Anderson model (already discussed in Chapter 1), in which electronic motion in the extended states (which are not, incidentally, Bloch states because of lack of long range order) is assumed to be diffusive, and a random site-to-site walk takes place. Phase coherence is lost over the interatomic spacing, a, where L ~ a.

+ Compared to 4-site interactions

is in apparent contradiction to the experimental evidence, where thermal activation energies of 0.03 - 0.06 eV [4],[8] are observed. Emin etal [4] attribute this weak activation energy to conduction associated with small polaron hopping. Their theory results in a Hall mobility activation energy which is one-third of the conductivity mobility activation energy due to hopping of small polarons in the extended state. Nagels etal [8], on the other hand, in a model discussed in more detail in Section 3.7.3., consider the parallel conduction of carriers in the extended and localised states. The experimental Hall mobility they obtain for Si-As-Te glasses is also weakly activated, but they assume that the localised Hall mobility contribution is negligibly small compared to the extended states Hall mobility, and they obtain a temperature independent Hall mobility due to carriers in the extended states, which is in agreement with Friedman's model.

Electrical contacts to multicomponent bulk chalcogenide glasses are generally ohmic. This has been attributed by Fritzsche [5] to the 'intrinsic' nature of the material with the Fermi level near the middle of the mobility gap. Wallace and Robertson [6] have also investigated contacts to chalcogenide glasses. They attribute the ohmic nature of these materials to a very high density of states in the gap (10^{20} $cm^{-3}eV^{-1}$) giving rise to quasi-intrinsic behaviour and narrow depletion regions. The carriers can, therefore, tunnel through any thin barriers present, and the contacts will appear ohmic.

The experimental sections of this chapter give detailed accounts of measurements on the temperature dependence of dc conductivity and thermoelectric power as a function of composition for Ch_xY_{100-x} (x = 45%, 61%, 71% atomic) glasses. The temperature dependence of the optical gap for the $Ch_{61}Y_{39}$ glass is also reported.

The formation of a conducting 'skin' due to heating in air, as reported in the literature [12] for STAG glasses, is briefly reported for the case of SeTAG. The results are presented and compared with binary and multicomponent glasses of other compositions reported in the literature. Particular reference is made to the widely investigated Si-Te-As-Ge (STAG) glasses.

The later sections examine the results with reference to three models in particular. These are the models as proposed by Mott and Davis [1], Green, Levy and Gee [7], and Nagels, Callaerts and Denayer [8] (N.C.D.). A number of other conduction models have also been proposed by various authors (see for example (9), (10), (13), (17), (18)). These will be commented upon where appropriate. It must be noted, however, that some of these [9],[10] have been deduced from generally different sets of experiments than those undertaken in the present study, which makes direct comparison difficult, whilst others have performed their experiments at entirely different temperatures [13], or the temperature range has been too limited [9] for the results to be conclusive with regards to the nature of the temperature dependence of dc conductivity and especially thermoelectric power.

The reasons for choosing the three particular conduction models mentioned above are the following:

(1) The Mott and Davis Model.

This model has been widely used and accepted by a large number of experimentalists to compute the various parameters for their materials. Although, in its simplest form, it does not satisfactorily explain the temperature dependence, in SeTAG, of dc conductivity and thermoelectric power as obtained in the present study, the evaluation of the various transport parameters in terms of this model does provide a basis for comparing the bulk electrical properties of SeTAG with that of other

chalcogenide glasses which have been investigated by other workers.

(2) The Green-Levy-Gee Model.

The present study has been the direct follow-up of the work carried out by Green etal on STAG glasses. In their paper they proposed a conduction model assuming a density of states distribution $N(E) \propto E^n$, where n is a positive number. This leads to an expression for dc conductivity of the form

$$\sigma = CT^n \exp\left(-\frac{E_{\sigma o}}{kT}\right) \qquad 3.2$$

where C is a constant. $E_{\sigma o}$ is the activation energy for conduction. Detailed analysis of dc conductivity and thermoelectric power data shows that this model is not totally satisfactory either - the reasons are given in a later section. A more detailed derivation of equation (3.2) is given in Appendix 3 A at the end of this Chapter.

(3) The NCD Model.

This model, based on that proposed by Mott and Davis, postulates that conduction can take place by the simultaneous thermal excitation of carriers into the extended states, and thermally assisted hopping of carriers in the "tail" of localised states within the mobility gap.

$$\text{i.e.} \quad \sigma = \sigma_{ext} + \sigma_{loc} \qquad 3.3$$

Similarly, the expression for the Seebeck coefficient, S, becomes,

$$S = \frac{S_{ext}\sigma_{loc} + S_{loc}\sigma_{loc}}{\sigma} \qquad 3.4$$

where the subscripts 'ext' and 'loc' refer to the extended and localised state contributions respectively.

Expressions (3.3) and (3.4) predict slight curvatures in plots of $\ln\sigma$ viz $^1/T$ and S viz $^1/T$, which is indeed what is obtained experimentally in SeTAG. There are, however, some shortcomings in the model, which will be discussed later.

It should be noted that all of the above models, as presented here, assume single carrier type conduction. This will be broadly assumed in this Chapter as well.

3.2. Experimental Apparatus.

All the temperature dependent dc conductivity and thermoelectric power measurments were carried out in a modified variable temperature liquid N_2, stainless steel BOC MRC -1, cryostat. A conventional rotary and diffusion pump set up was used to achieve pressures of less than 5×10^{-6} mm Hg in the cryostat chamber. Figure 3.1 is a simplified schematic drawing of the cryostat. The inset shows details of the heater and sample holder assembly. Different sample holders were used in the conductivity and thermoelectric power measurements. The heater consisted of a one watt (~ 500Ω) carbon resistor painted over by 'Silver-Dag' and inserted into the copper block. The Silver-Dag was used to improve thermal contact between the heater and the copper block. PTFE insulated copper leads via short lengths of 0.001" diameter gold or platinum wire were used to make electrical contacts to the samples. All

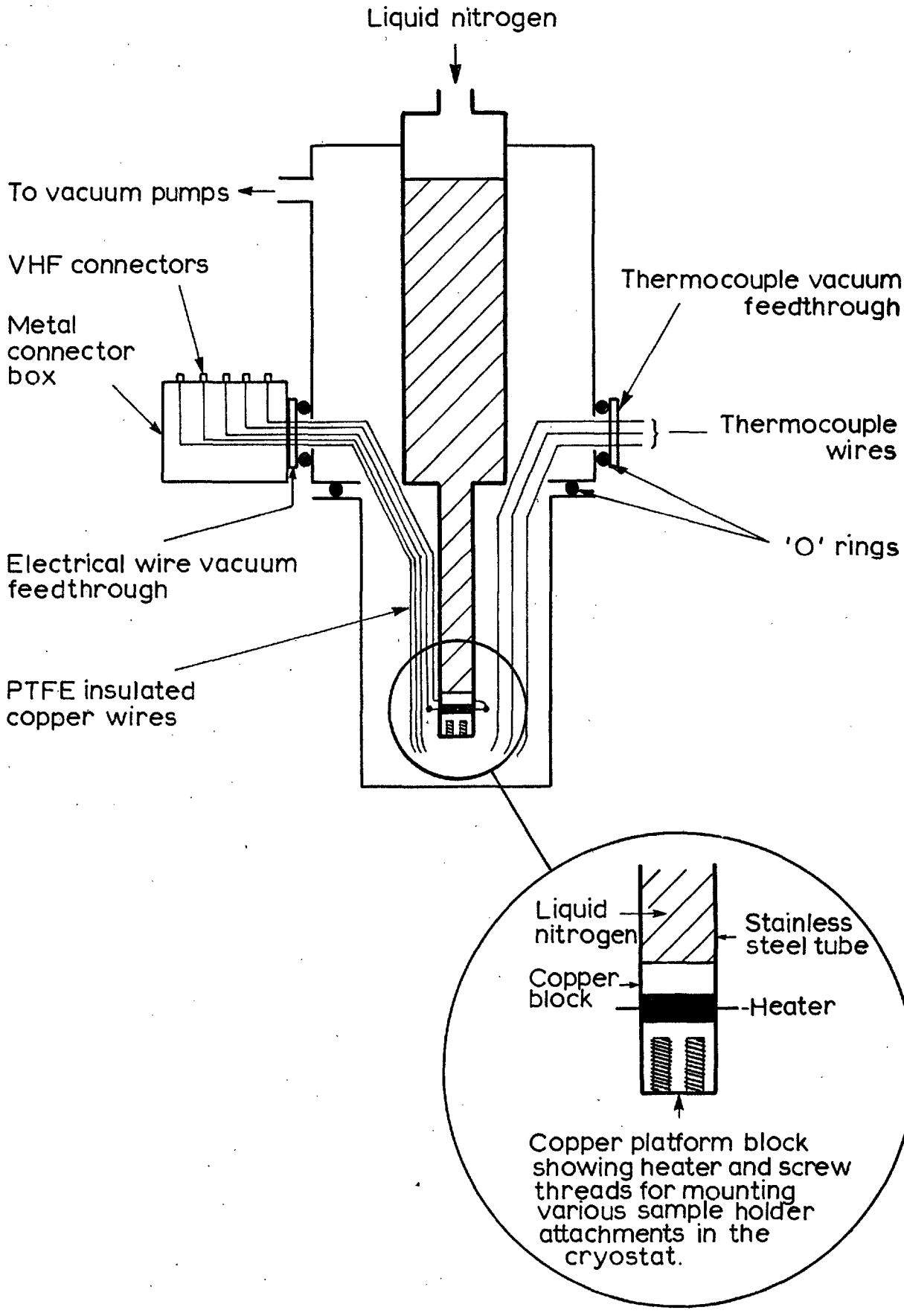


Fig. 3·1: Schematic drawing of the cryostat

electrical connections were kept clean to ensure their ohmicity. The leakage resistance between the different leads was greater than $10^{14}\Omega$. The system was designed so as to obtain effective electrical shielding from the outside, and the external metal casing of the cryostat was connected to an earth common with the electrical instruments to avoid earth loops. It was found that a dc power supply to the heater was necessary in order to avoid interference with the low signal levels from the sample.

Three sets of Chromel/Alumel thermocouples were used to monitor the temperature. The thermocouples were not broken at the air-vacuum feed-through. This was in order to minimise errors in the readings due to any thermal emf's generated at this interface. Araldite and black vacuum wax (Edwards W) were used to form the vacuum seals at the feed-throughs.

All the samples studied were kept in the dark for at least twelve hours prior to the measurements - a precaution which, subsequently, proved to be unnecessary, as no notable change in the experimental readings could be detected.

3.2.1. Thermocouple Calibration.

All the thermocouples used (Chromel/Alumel) had independent cold junctions held at $0^{\circ}C$ (melting ice); they were electrically insulated along their lengths, and their junctions were welded. One of the thermocouples was calibrated against a standard platinum resistance thermometer*, and it was in turn used to check the calibration of the other two thermocouples.

---

* Supplied by Cryogenics Ltd., Pitchcott, Nr. Aylesbury, Bucks. Platinum resistance thermometer calibrated to ± 0.04 K from 77-273 K against IPTS (68) HMSO SBN 11 4800057 Tables II and III

The readings from all three thermocouples were in agreement with the platinum resistance thermometer to within ± 0.6 K over the entire temperature range employed. It was therefore felt feasible to use the standard thermocouple calibration tables (IPTS-68)* for all the measurements. Four fixed temperature points were used [11] during the calibration:

(1) Boiling point of liquid nitrogen (77.4 K)

(2) Sublimation temperature of Co_2 (194.6 K)

(3) Melting point of ice (273.15 K)

(4) Boiling point of water (373.15 K)

All the values quoted above are at one atmosphere pressure, and corrections were applied where neccessary. In addition, further calibration points against the platinum resistance thermometer were obtained using a mixture of methanol and water cooled by liquid nitrogen. The thermocouple readings were taken during the calibration and the experiments using a Solartron LM 1420 L D.V.M. (reading accuracy ± 2.5 μV).

A more detailed account of the thermocouple calibration procedure, and the subsequent error analysis, is given in Appendix 3B.

3.3. Temperature Dependence of DC Conductivity.

3.3.1. Experimental Procedure.

SeTAG specimens for DC conductivity measurements were cut into parallel-pipeds of approximate 8 x 1.5 x 1.5 mm dimensions. The ingot

---

*British Standards Institution, London W1A 2BS, Publication No. BS 4937/Part 4/1973 - ISBN 0 580 079325.

was first mounted on to a glass slide using a low melting point (~ 60°C) modelling wax *, which was soluble in trichloroethylene or chloroform. The low melting temperature was desirable in order to avoid inducing chemical changes at the surface of the specimen [12]. The ingot was then cut into the desired dimensions using a 0.01" diamond saw + and a Mullard ultrasonic drill. An attempt was made to cut the parallel-piped out from along the length of the ingot. This was done in order to make the specimen more representative of the composition under study, and to minimise any effects due to possible compositional variations along the length of the ingot. The 'timber' thus obtained was polished, and then washed in trichloroehtylene, and acetone. The dimensions of the timber were measured with a micrometer screwgauge capable of reading to ± 0.001 mm.

Contacts were made to the ends of the timber using gold or platinum 0.001" diameter wire painted over, and held in position by "Silver-Dag". Four point resistivity measurements gave identical results to two terminal measurements. It was therefore concluded that the contacts were ohmic.

The conductivity measurements were carried out using a Keithley 616 Digital Electrometer Multimeter. This had an input impedence of greater than 2×10^{14} Ω in the resistance (constant current) measuring mode. The voltages applied across the specimen in this mode of operation varied from 0.1 to 200 volts depending on the value of resistance being measured. Great care was taken, however, to keep the power dissipation in the specimen below 10^{-4} W in order to avoid joule heating. Measuring the resistance by using the Keithley as a voltmeter/ammeter gave identical results as the direct resistance measurements.

---

*Ash modelling wax No. 2 supplied by Cottrell & Co. of London, W1P 2AA.

+Supplied by Kristalap Ltd., London, E.C.1.

A schematic cross section of the sample holder designed for the conductivity measurements is shown in Figure 3.2. The wedge-shaped sample clamps ensured good thermal contact between the sample and the base. The clamps also held the sample rigidly in position. The position of the thermocouple with respect to the sample is shown in Figure 3.3. The thermocouple was held firmly in position, and in good thermal contact, with the sample.

The problem of good thermal contacts, especially between the thermocouple and the sample, was found to be non-trivial. As a result a layer of the RS Heat Sink Compound * was applied at all mating faces from the sample to the cryostat stem, and between the thermocouple and the sample. The Heat Sink Compound is composed of zinc oxide impregnated silicone grease with a room temperature resistivity of 2×10^{15} Ω cm. It did not, therefore, interfere with any of the electrical measurements by shunting the sample. Its resistivity was, however, checked at room temperature and at liquid nitrogen temperature. It was found to be greater than $\sim 2 \times 10^{14}$ Ω cm in both instances. The use of the Heat Sink Compound greatly reduced the temperature equilibration times, and hence speeded up the measurements.

The sample was allowed to remain at thermal equilibrium for at least ten minutes before taking any temperature and resistance readings. To ensure that equilibrium values had been reached, both the temperature and the output from the Keithley were monitored on a chart recorder. As a spot check on the reliability of the temperature readings, the resistance of all the specimens studied were first recorded in air, and the room temperature was noted. The specimen was then mounted in the cryostat, and

---

*Supplied by RS Components Ltd., London EC2P 2HA - Room temperature thermal conductivity 7×10^{-3} W K^{-1} cm^{-1}.

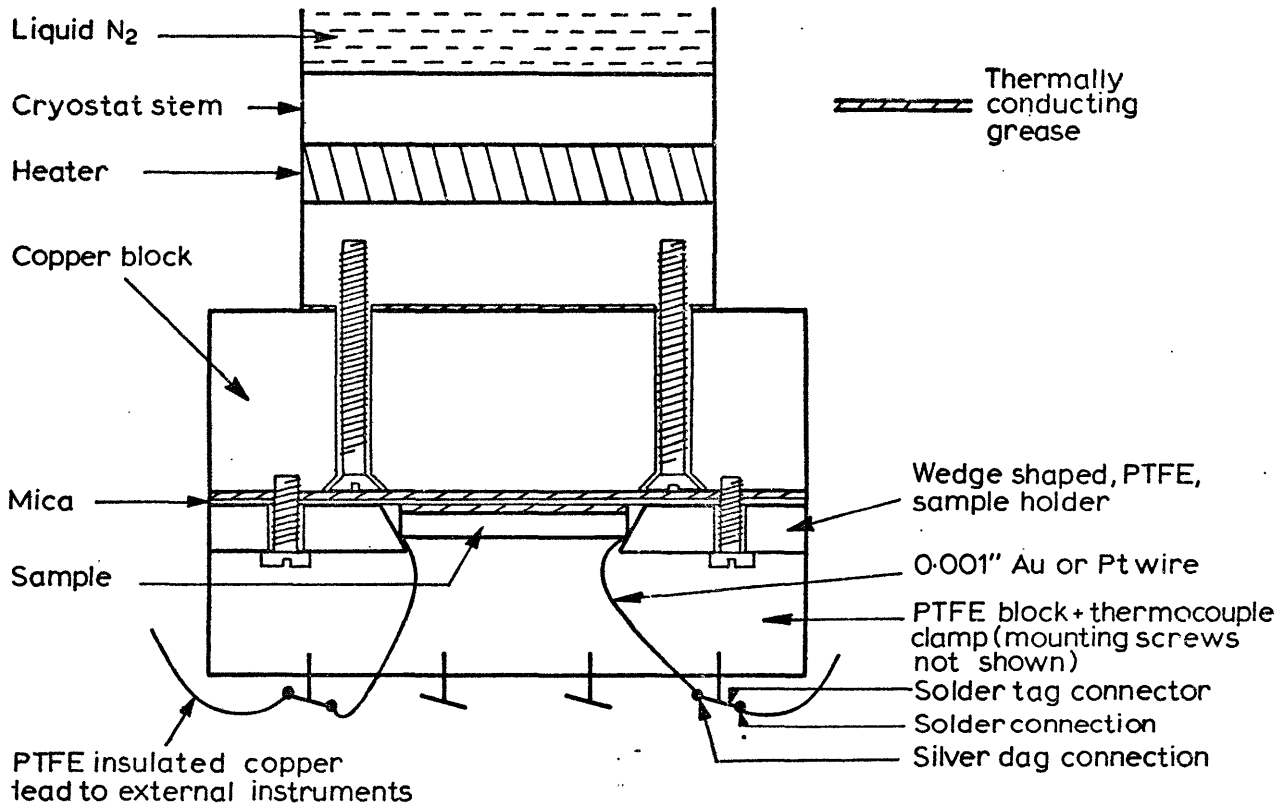


Fig. 3·2. Schematic cross-sectional drawing of the cryostat sample holder used for the conductivity measurements

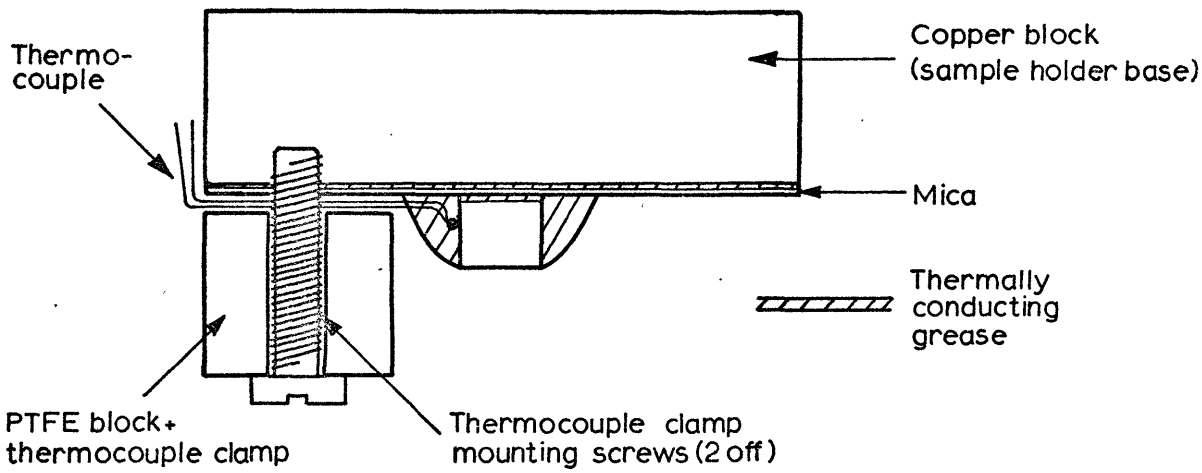


Fig. 3·3. Schematic diagram showing the thermocouple clamp and the position of the thermocouple with respect to the sample

and put under vacuum. With liquid nitrogen used as a coolant, the sample was heated to the temperature of the ambient. The sample resistance under these conditions was then compared to the previous value taken in air. If the compatibility between the two readings was worse than 2%, the thermocouple in the cryostat was repositioned until agreement was obtained. This, however, was rarely necessary. The resistivity, ρ, was calculated using the relation $\rho = \frac{RA}{L}$ where R is the sample resistance, A is the cross-sectional area of the sample, and L is the sample length.

Finally, the conductivity of the specimens as a function of the position of the sample within the ingot was checked in a few cases where the length of the timber was along the circular cross-section of the ingot. The sample resistivities thus obtained agreed to within $\pm$ 15%. The agreement obtained with the timbers cut along the length of the sample was in general better than $\pm$ 5%, although not many measurements of this kind were made.

3.3.2. Results.

The temperature dependence of resistivity in the Ch_xY_{100-x} series of SeTAG glasses in the range 145 K to 330 K (~ -128°C to 56°C) was investigated. Five ingots were used for the detailed resistivity measurements. In the case of $Ch_{45}Y_{55}$, only one ingot was examined, whilst two ingots in each of the compositions $Ch_{61}Y_{39}$ and $Ch_{71}Y_{29}$ were studied. In addition, an ingot of nominal composition $Ch_{45}Y_{55}$, but whose actual composition was found to be $Se_9Te_{32}As_{52.5}Ge_{6.5}$ (see Chapter 2), and therefore compositionally outside the Ch_xY_{100-x} series, was also investigated.

A typical current-voltage characteristic, for a $Ch_{45}Y_{55}$ glass specimen, is shown in Figure 3.4. A linear, ohmic behaviour is observed.

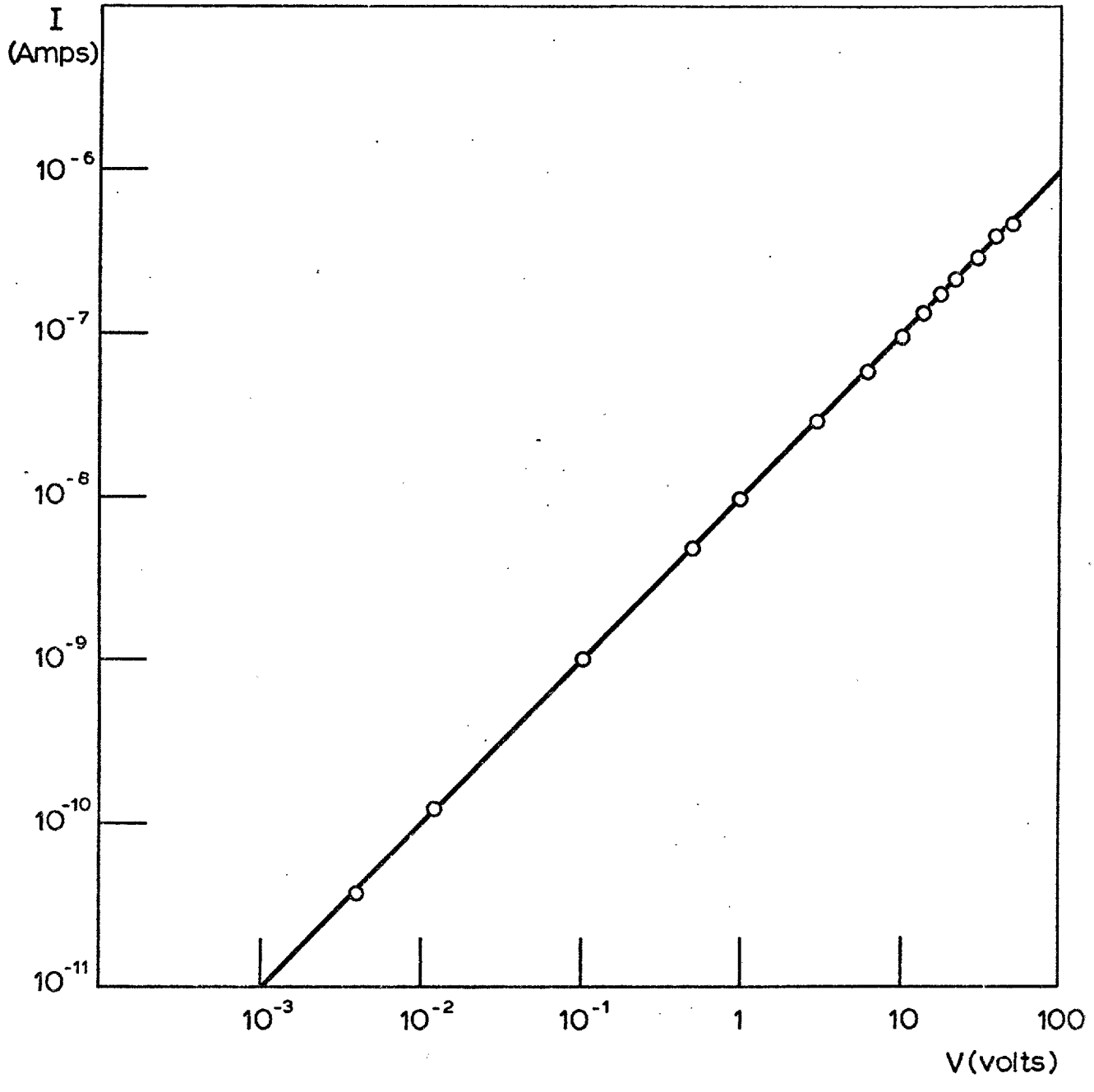


Fig. 3.4: Current voltage characteristic in bulk specimen of $Ch_{45}Y_{55}$ composition. (Specimen length = 7·25 cm.)

Figure 3.5 shows the variation of resistivity as a function of temperature and composition for three representative specimens in the series Ch_xY_{100-x}. Table 3.1 lists the variation of room temperature (298 K) resistivity as a function of composition for the various ingots studied. The activation energy, $E_{\sigma o}$, and the pre-exponential factor, C,

Specimen	Composition	$\rho_{298\ K}$ Ωcm	$\sigma_{298\ K}$ $\Omega^{-1}cm^{-1}$	$E_{\sigma o}$ eV ($\pm$ 0.01 eV)	C $\Omega^{-1}cm^{-1}$
8.2	$Ch_{45}Y_{55}$	6.8×10^{6}	1.5×10^{-7}	0.55	309
8.3	"	---	---	0.56	---
14.2	"	4.9×10^{6}	2.0×10^{-7}	---	---
3.3	$Ch_{61}Y_{39}$	3.9×10^{5}	2.6×10^{-6}	0.48	155
2.3	"	4.5×10^{5}	2.2×10^{-6}	0.49	425
10.2	"	6.9×10^{5}	1.4×10^{-6}	0.49	276 (estimated)
7.3	"	---	---	0.49	---
13.2	$Ch_{71}Y_{29}$	1.5×10^{5}	6.1×10^{-6}	0.45	476
13.3	"	---	---	0.46	---
15.4	"	1.3×10^{5}	7.7×10^{-6}	0.46	385
15.3	"	---	---	0.47	---
5.3	$Se_9Te_{32}As_{52.5}Ge_{6.5}$	4.9×10^{5}	2.0×10^{-6}	0.48	221
5.4	"	---	---	0.50	---

Table 3.1 Conductivity Parameters for SeTAG glasses according to equation 3.1

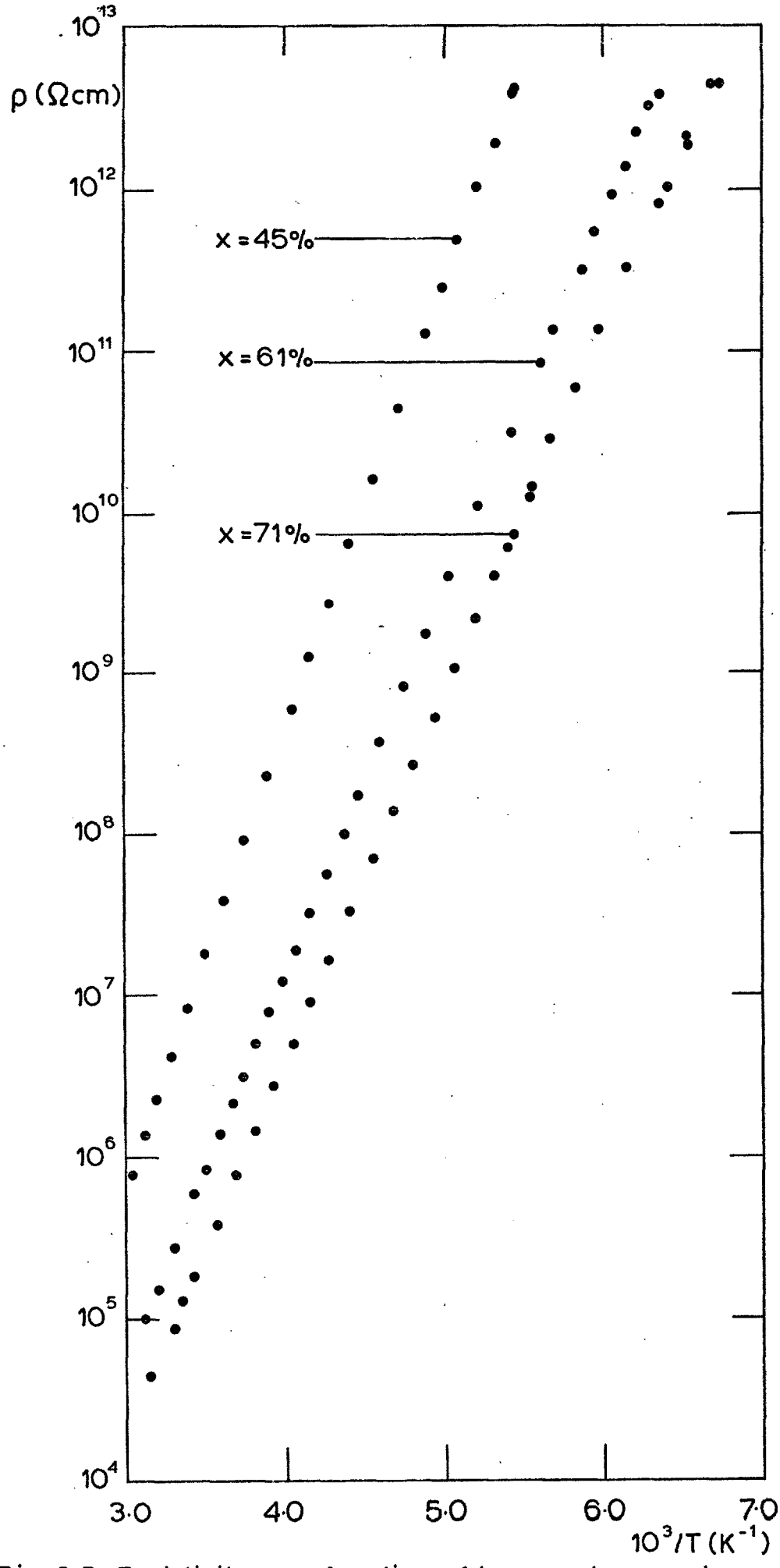


Fig. 3·5: Resistivity as a function of temperature and composition for SeTAG glasses in the series Ch_xY_{100-x}

for each sample are also calculated using equation 3.1. In each sample, $E_{\sigma o}$ was calculated (to $\pm$ 0.01 eV) from the slope of the best straight passed through the experimental points. C was given by the value of conductivity at $^1/T = 0$ as extrapolated using this straight line. A general increase in resistivity and activation energy with decreasing chalcogen content, x, is apparent from Figure 3.5 and Table 3.1. It will be noticed that, for some of the samples, only $E_{\sigma o}$ has been listed. These were obtained by the simultaneous temperature dependent measurements of the sample resistance and the thermoelectric emf on specimens used for the Seebeck coefficient experiments. Since the exact dimensions for these samples were not known only $E_{\sigma o}$ could be calculated. In sample 10.2, the pre-exponential factor, C, was estimated by measuring the room temperature resistivity of another specimen of known dimensions from the same ingot. The notation for numbering the samples has already been given in Chapter 2.

Thermal cycling at pressures of less than 5×10^{-5} mm Hg between about 100 K and 330 K produced no annealing effects in the specimens, and all the experimental points were fully reproducible within the experimental error.

Examining the data of Figure 3.5, a small degree of curvature can be observed in all the curves. In other words, there is some deviation from the straight line, singly activated process as predicted by equation 3.1. This curvature was present for all the samples that were examined. Its magnitude generally decreased with increasing chalcogen content.

Figure 3.6 shows the variation of room temperature resistivity with chalcogen content and conductivity activation energy. Figure 3.7 shows the variation of the conductivity activation energy with the atomic

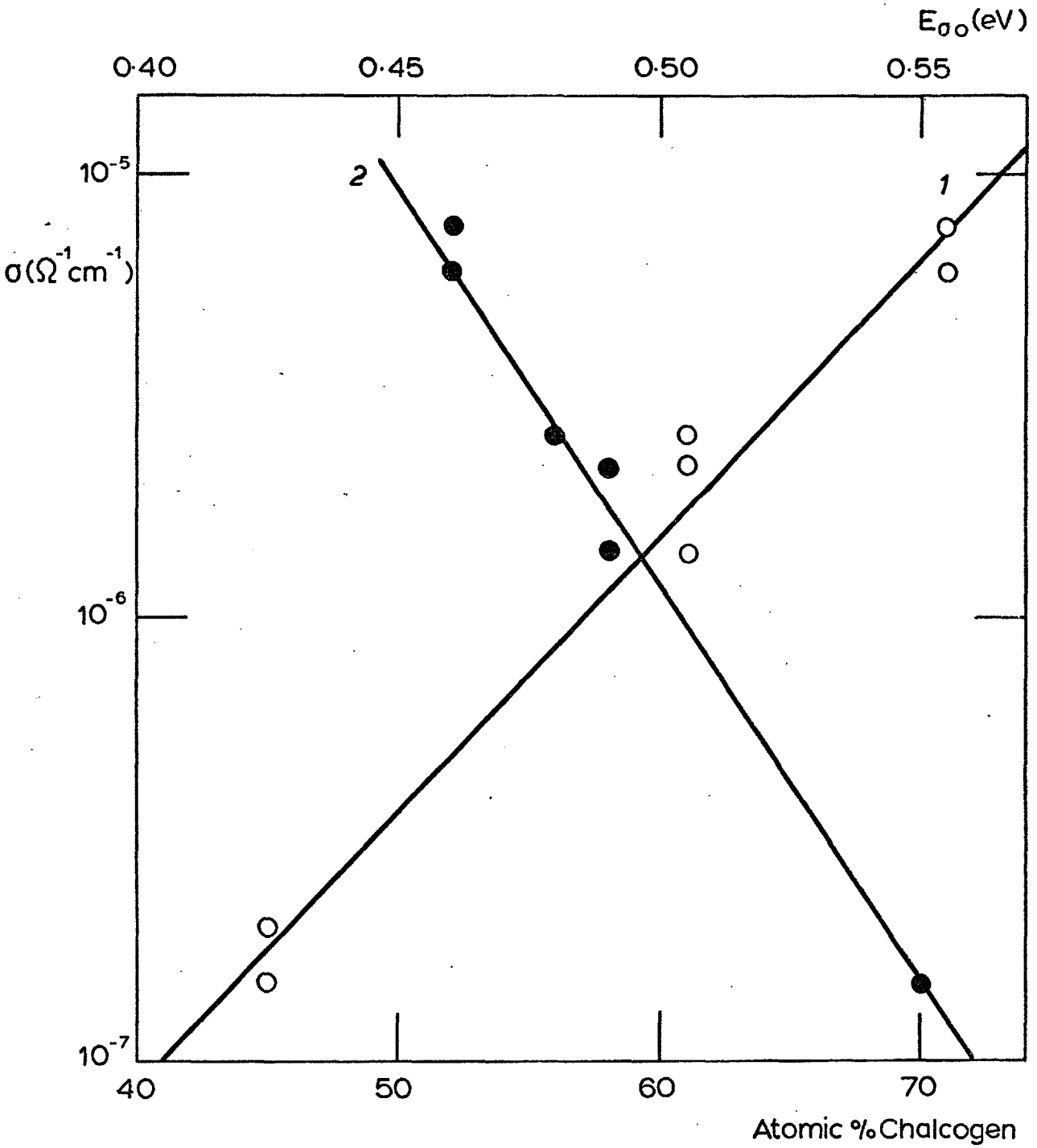


Fig. 3·6: Variation of room temperature conductivity with
1. The atomic fraction of chalcogen elements present O
2. Conductivity activation energy ●

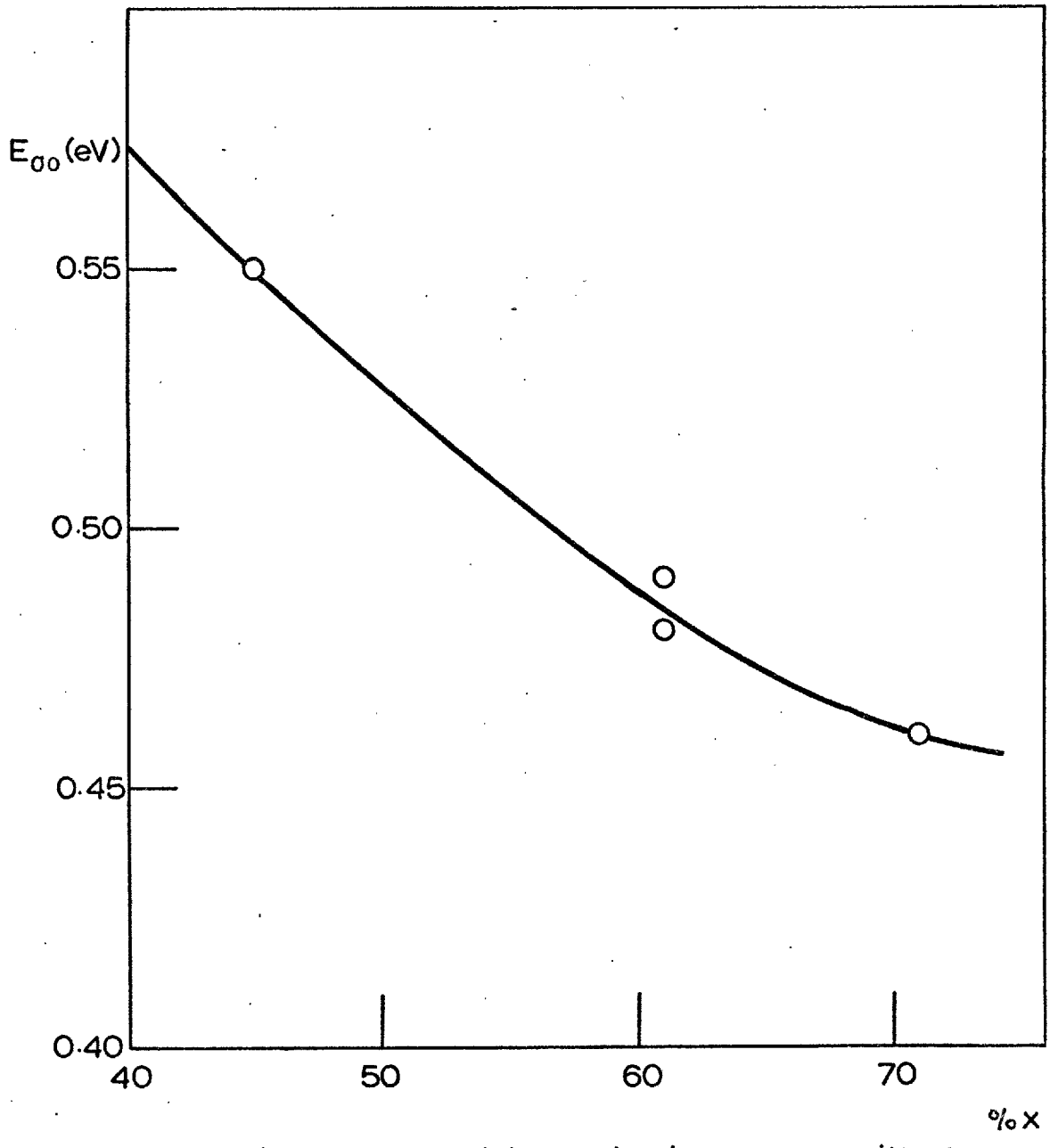


Fig. 3·7: Variation of conductivity activation energy with % chalcogen content.

fraction of chalcogen elements present. A general decrease in the activation energy with the addition of more chalcogen atoms is observed.

3.4. Ambient Effects and the Electrical Conductivity of SeTAG Glasses.

3.4.1. Introduction.

It has been shown [12],[14] that excessive heating of chalcogenide glasses in poor vacuum, or in an atmosphere where oxygen and water vapour are present, leads to the formation of a conducting 'skin' which, in the case of STAG glasses, is composed mainly of crystalline tellurium[15]. The presence of skin in STAG glasses leads to an enhanced conductivity, and a drastic change in the variation of thermoelectric power, S, with temperature: there is a reduction in thermoelectric power with decreasing temperature, i.e. $\frac{dS}{d(\frac{1}{T})} < 0$, which is the reverse of what is usually observed in the absence of skin.

It was therefore felt appropriate briefly to investigate the likelihood of skin formation in SeTAG glasses.

3.4.2. Experimental Procedure and Results.

A 'timber' of $Ch_{61}Y_{39}$ was mounted onto a glass substrate, which was heated on a hot plate. A Chromel/Alumel thermocouple was used to monitor the temperature of the sample to $\pm$ 5 K. Thermally conducting silicone grease improved the thermal contacts at the sample/substrate and sample/thermocouple interfaces.

The resistance of the sample was noted at room temperature. The temperature was then progressively cycled between room temperature (298 K) and 323 K (50°C), 373 K (100°C), and 423 K (150°C). Cycling took place twice at each of the latter two temperatures. The sample was kept at

the selected 'hot point' for five or thirty minutes and its resistance noted before being allowed to cool down to ambient temperature, when its new resistance was also measured. The results, as summarised in Table 3.2, indicate increasing skin growth.

Temperature (K)	Resistance (Ω)	Comments
298	6.8×10^6	Original room temperature resistance (No skin).
323	1.8×10^6	T = 323 K for about 5 minutes before cooling.
298	6.6×10^6	Resistance after first temperature cycle.
373	2.1×10^5	T = 373 K for about 5 minutes before cooling.
298	5.8×10^6	Resistance after second temperature cycle.
373	2.1×10^5	T = 373 K for about 30 minutes before cooling.
298	5.6×10^6	Resistance after third temperature cycle.
423	2.7×10^4	T = 423 K for about 5 minutes before cooling.
298	4.5×10^6	Resistance after fourth temperature cycle.
423	2.4×10^4	T = 423 K for about 30 minutes before cooling.
298	2.7×10^6	Resistance after fifth temperature cycle.
298	6.7×10^6	Resistance after removal of conducting skin.

Table 3.2 - The Effect of Skin Growth on the Electrical Resistance of a $Ch_{61}Y_{39}$ SeTAG Specimen

Finally the sample was lightly braded to remove a thin (several microns) layer of its surfaces. The new room temperature resistance was found to be the same as the original one with no skin effects.

The above experiments were , however, quite crude in so far as their insufficiency to compare the origins of skin formation to that in STAG glasses.

Figure 3.8 and 3.9 are scanning electron micrographs of flash evaporated thin films of $Ch_{61}Y_{39}$ showing no skin and the extent of skin formation after heating in air at 423 K for about one hour.

The structure, which results on the surface of these films because of skin growth, can be clearly seen in Figure 3.9. It should be noted that the photographs of Figures 3.8 and 3.9 were both taken at the same magnification.

3.5. Temperature Dependence of Thermoelectric Power.

3.5.1. Introduction.

Thomas Seebeck discovered in 1821 that an emf could be produced by heating the junction between two metals, after whom the Seebeck coefficient, which is synonomous with thermoelectric power, has been named.

Considering a circuit consisting of two dissimilar materials A and B, and connected in the order A-B-A, then a temperature gradient ΔT between the junctions of A-B produces an open circuit emf, V, given by the relation

$$S_{AB} = \frac{V}{\Delta T} \qquad 3.5$$

where S_{AB} is the differential Seebeck coefficient of the two materials.

Thermoelectric power in chalcogenide glasses has been found to be positive, which would indicate conduction dominated by holes.

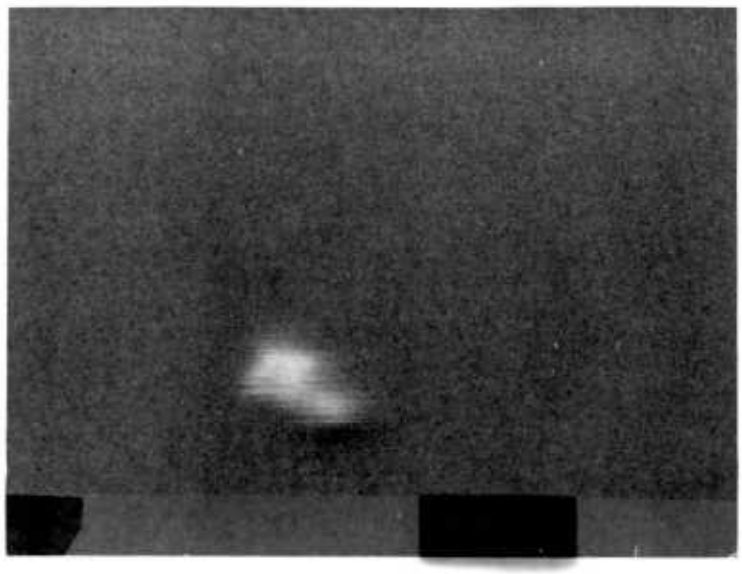


Fig. 3.8. Flash evaporated SeTAG thin film with no heat treatment

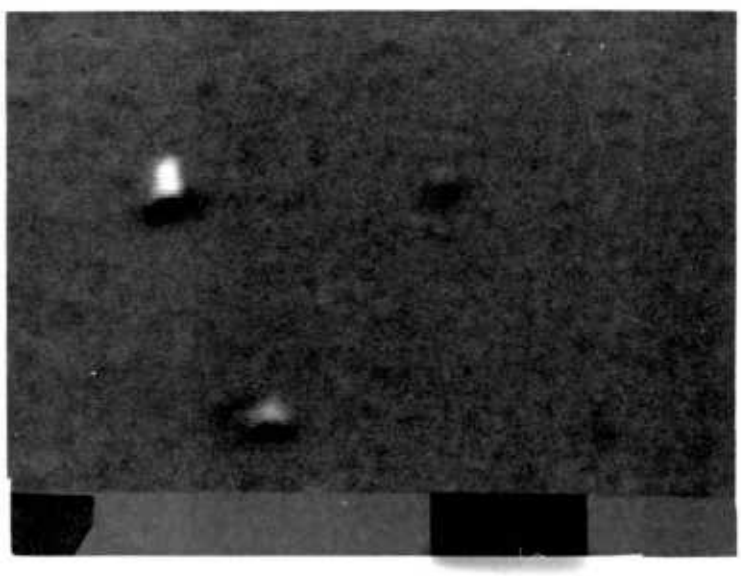


Fig. 3.9. Flash evaporated SeTAG thin film after heating in air at 423 K for one hour.

Bulk and thin film temperature dependent thermoelectric power measurements in chalcogenide glasses have, on the whole, been quite limited because of the high resistivity of the materials, and the difficulty in obtaining accurate and reproducible data. The high resistivity has also meant that a large number of measurements have been carried out above room temperature [7],[13],[14],[17],[19],[20],[21],[28] and with only about half the reported measurements being performed below ambient temperature [8],[9],[16],[21]-[27]. With one exception [8] all the data have been interpreted as a linear variation of S with $^1/T$. Examining some of the thermoelectric power data in the literature, it should be noted that the functional relation between S and T is indeterminate from these experiments, because there is either too much scatter in the results [14],[25] or the temperature range is too narrow [14],[20],[21] to observe any deviation from straight line in the S vs. $^1/T$ plots, or the experimental points are not shown [17],[28]. The variation of the Seebeck coefficient with temperature has been given as [1],[29],

$$S = -\frac{k}{e}\left[\frac{E_{so}}{kT} - \frac{\gamma}{k} + A\right] \qquad 3.6$$

for p-type conduction. Here A is a constant of the order of unity [29],

$E_{so} = (E_F - E_V)_{T=0}$ * for extended states conduction,

$E_{so} = (E_F - E_B)_{T=0}$ for hopping conduction in the tail of states,

and $\gamma = \frac{d(E_F - E_V)}{dT} = \frac{d(E_F - E_B)}{dT} \simeq \frac{1}{2}\frac{dE_g}{dT}$

where E_g is the optical band gap of the material. It is assumed here

---

*See the MD model (Section 3.7.1.) and Figure 3.23 for the definitions of E_F, E_V and E_B.

that the energies E_V and E_B have the same temperature coefficients.

Most of the Seebeck coefficient data have been interpreted in terms of equation (3.6), which assumes single carrier, hole conduction. Although two band conduction models have also been examined [17], this is very unlikely because of the strong evidence against it from the field effect measurements [7],[30], which indicate conduction totally dominated by holes.

Thermoelectric power measurements were made on SeTAG glasses in the series Ch_xY_{100-x}, where x = 45,61,71%, and on a sample of composition $Se_9Te_{32}As_{52.5}Ge_{6.5}$ during the course of this work.

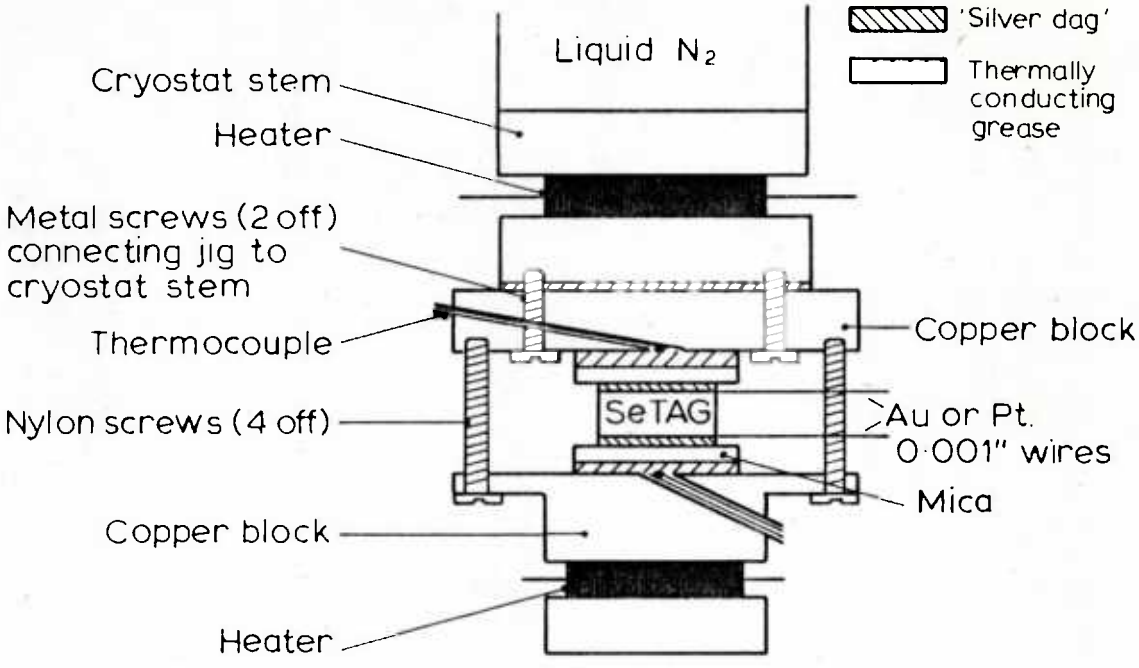
3.5.2. Experimental Procedure.

As the main limitation in measuring the Seebeck coefficient is the generally high resistivity of chalcogenide glasses, it was decided to hot-press bulk specimens to a thickness of about 0.5 mm between two parallel metal electrodes. This was performed under a vacuum of about 10^{-3} mm Hg to minimise skin formation. The full hot pressing procedure is described in Section 3.6. The edges of the prepared samples were lightly braded to remove any residual skin. These samples could not, however, give reproducible results, because the maximum temperature gradient that could be maintained between the two faces was less than about 3 K under equilibrium conditions. As the error in reading each temperature was $\pm$ 0.6 K, very large errors were introduced, which made the results totally irreproducible.

It was, therefore, necessary to make the measurements on much thicker samples, which could support much larger temperature gradients across their faces, but would also limit the low temperature range of the measurements. This was done on parallel faced samples of 6 mm typical thickness, and of uniform but arbitrary cross-sectional area. The faces of the sample across which the temperature gradient was to be applied were painted over with "Silver-Dag" whilst a 0.001" diameter gold or platinum wire was stretched

across each face. A thin (less than 30 μm) sheet of mica was pressed on to each face while the "Silver-Dag' was still wet, and it was held in position under slight pressure until the "Dag" contacts were completely dry. The mica insulators were found to be necessary to completely isolate the sample electrically from the heaters and the thermocouples. Without this electrical insulation, erroneous results were obtained. The sample was then mounted in a copper jig with carbon resistor heaters on either side of the specimen. A thin layer of thermally conducting silicone grease was used to improve thermal contact between the mica and the copper faces of the jig. The jig consisted of two copper parts, which were held together by four nylon (electrically insulating) screws, and with the sample held firmly in position inbetween. A fine hole was drilled right through to the face of each copper piece which was, via the sheet of mica, in thermal contact with the sample. This allowed a thermocouple to be pushed right through until it was in good thermal contact with the mica insulator. The thermocouples were electrically insulated along their lengths using twin bore ceramic tubing of 1 mm overall diameter, through which the thermocouple wires were fed before their ends were welded together. The tubing also made the thermocouples very rigid, which meant that they could be pushed right through to the mica faces without bending or 'doubling up'. A schematic cross sectional drawing of the thermoelectric power sample holder is shown in Figure 3.10(a). Figure 3.10(b) is an actual photograph, which shows the jig and the specimen mounted on to the cryostat stem.

With the specimen mounted as described in the above paragraph, the cryostat was evacuated to a pressure of less than 5×10^{-5} mm Hg. The variation of thermoelectric power with temperature was measured in the range 223 K to 356 K (-50°C to 83°C). The temperature gradient across the faces, which was controlled manually using two dc power supplies to the heaters of Figure 3.10(a), was kept to 15 K to 20 K in all the measurements. The Seebeck potential vaired linearly with the temperature



a. Schematic cross-section of the thermopower jig mounted onto the cryostat system.



b. Mounted thermopower specimen

Fig. 3.10

difference between the two faces of the specimen, so long as this difference was not too small for the errors in the temperature readings to become significant.

The thermoelectric emf of the sample was measured using a Keithley 616 digital electrometer in the voltmeter mode of operation. One side of the input to the Keithley was at a common earth with other electrical equipments in use. The input impedance of the Keithley could be varied in decade steps, with a value of 2×10^{14} Ω as a maximum. The input impedance of the Keithley was always selected so that it was at least 1000 times higher than the sample resistance. The Keithley readings were typically accurate to $\pm$ 2% under steady state conditions. The emf's generated by the thermocouples monitoring the temperatures of the two faces of the specimen were measured using a Solartron LM 1420 L D.V.M. The D.V.M. could be switched from one thermocouple to the other by using a high quality 2 pole, 2 way ceramic switch. Both the temperatures, and the Keithley recorder output were monitored on a chart recorder to ensure that thermal equilibrium had been reached. The sample was kept under thermal equilibrium conditions, with the thermocouple and the Keithley readings steady for at least fifteen minutes before any measurements were made. By switching the Keithley to the ohmmeter mode, the resistance of the sample at various temperatures was also measured at the same time. Figure 3.11 shows the circuit used for thermopower measurements.

Contact and/or annealing effects were found to be an important consideration. It was found that by keeping the sample at a temperature of about 363 K under vacuum for periods longer than half an hour, the low temperature thermoelectric emf could be changed, with a corresponding increase in the slope of the Seebeck coefficient plotted against $^1/T$. This seemed to affect the resistance readings as well, but to a much

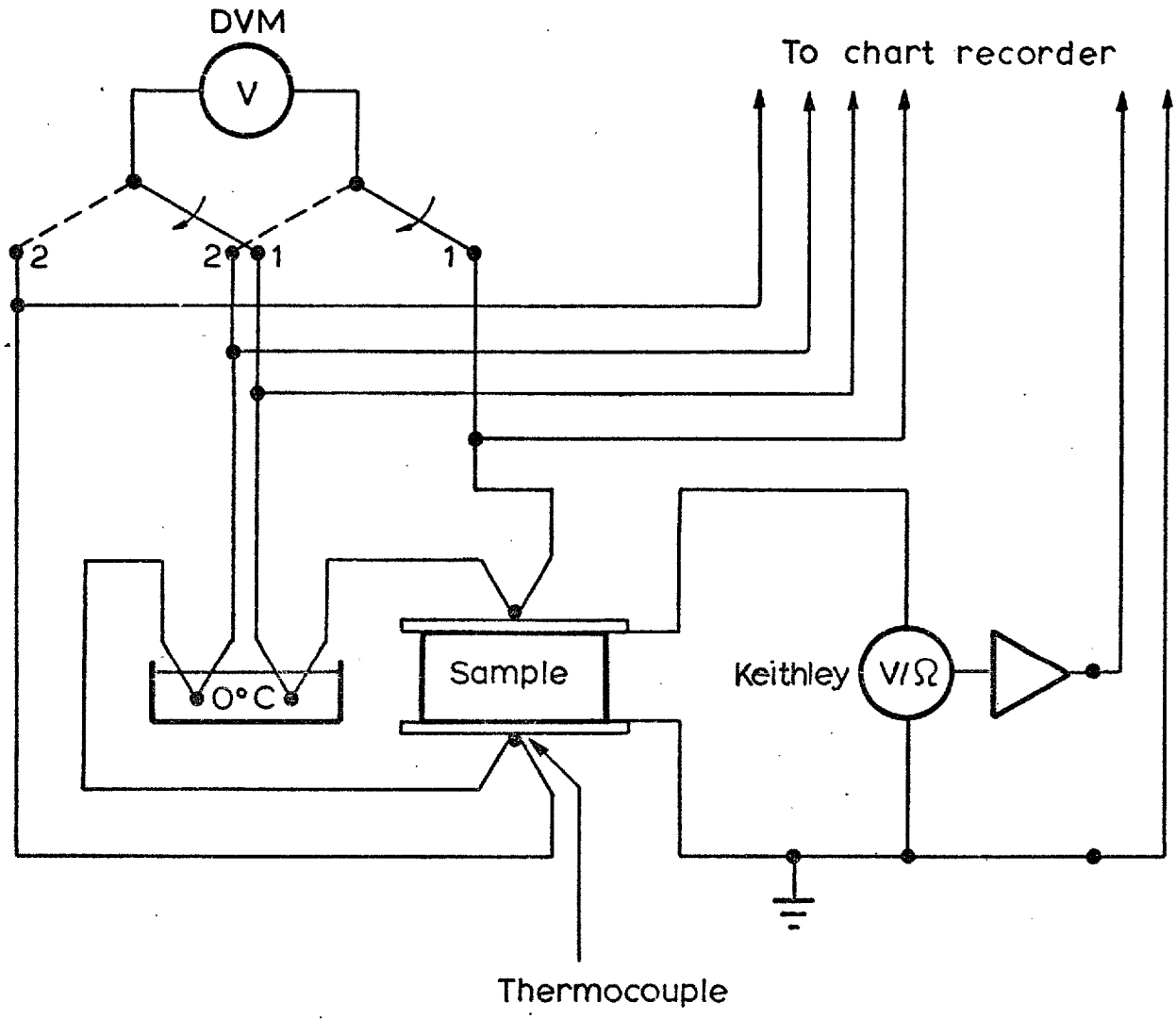


Fig. 3·11: Circuit diagram for thermoelectric power measurements

smaller degree. If heating at 363 K was repeated for further periods, the Seebeck coefficient increased further in each cycle, until a 'steady state' was reached, when further heat treatment would have no effect either upon the Seebeck coefficient or on sample resistance. The heat treatment did not affect different samples in the same way. It was found that in some specimens, the effect was totally absent, whilst in others different durations of heat treatments were necessary to reach the 'steady state'. These observations were not composition dependent either. All the samples selected for thermopower measurements were heat treated at 363 K, and if this affected the Seebeck measurements, the samples were subjected to further heating until the Seebeck potentials were reproducible on recycling.

Figures 3.12 and 3.13 illustrate the above phomenon as it was observed in a sample of $Ch_{61}Y_{39}$ composition, where the effects of successive heat treatments on the Seebeck coefficient and the resistance of the sample are demonstrated.

'Annealing' effects have also been observed by Nagels etal [8], where an increase in bulk resistance of Si-As-Te glasses was observed upon heating at 383 K for one hour.

It is not believed, however, that annealing is the responsible factor in the present observations for the following reasons:

(1) The presence and the magnitude of the effect seems to vary from sample to sample.

(2) The observations on skin (Section 3.4) where the samples were heated to 423 K also rule out annealing, since the resistivity of the sample could be restored to its original value by polishing a thin layer of the material off the surface.

It seems likely, in fact, that contact preparation is the most likely

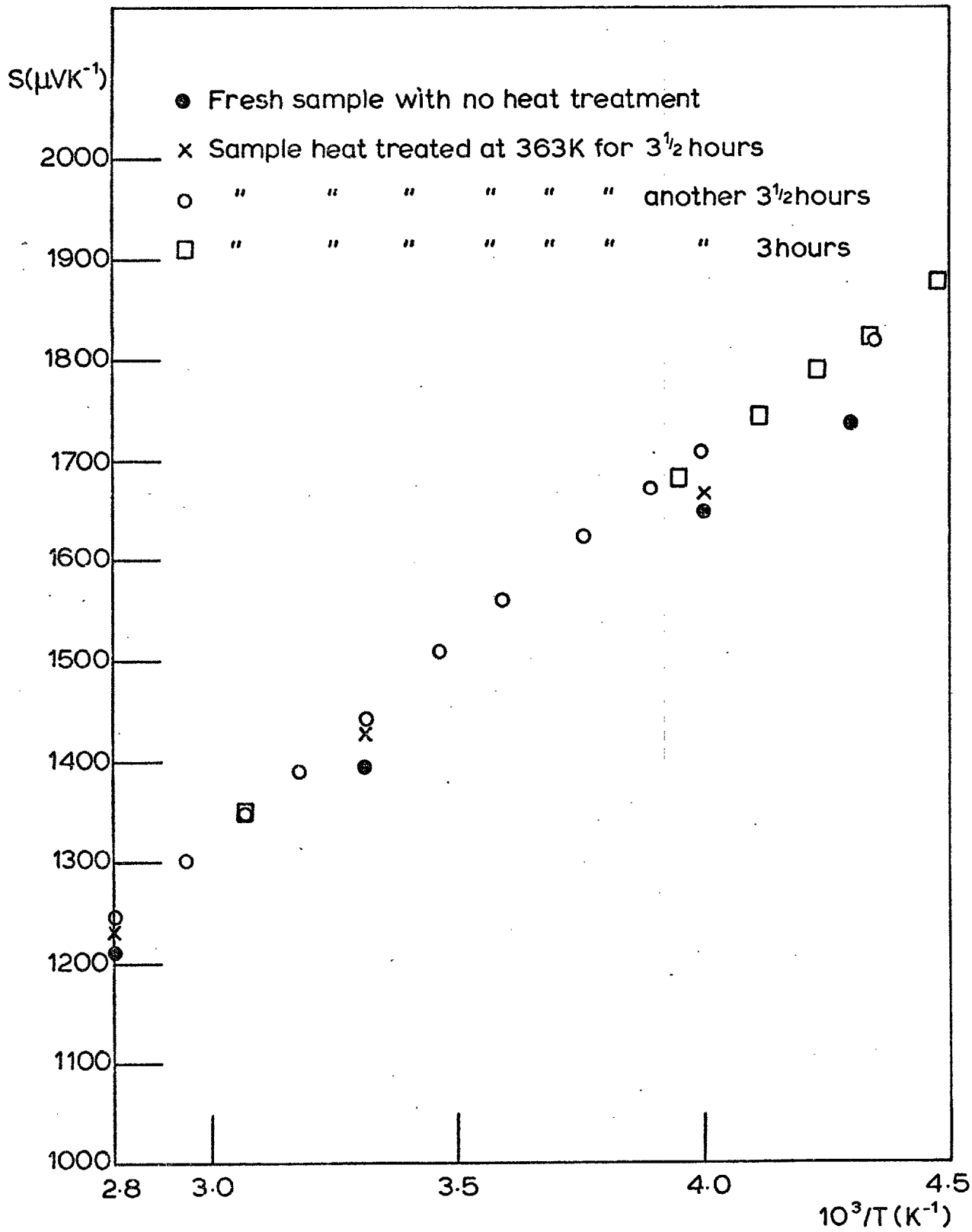


Fig.3·12: Seebeck coefficient of sample 7·3 as a function of heat treatment at 363K.

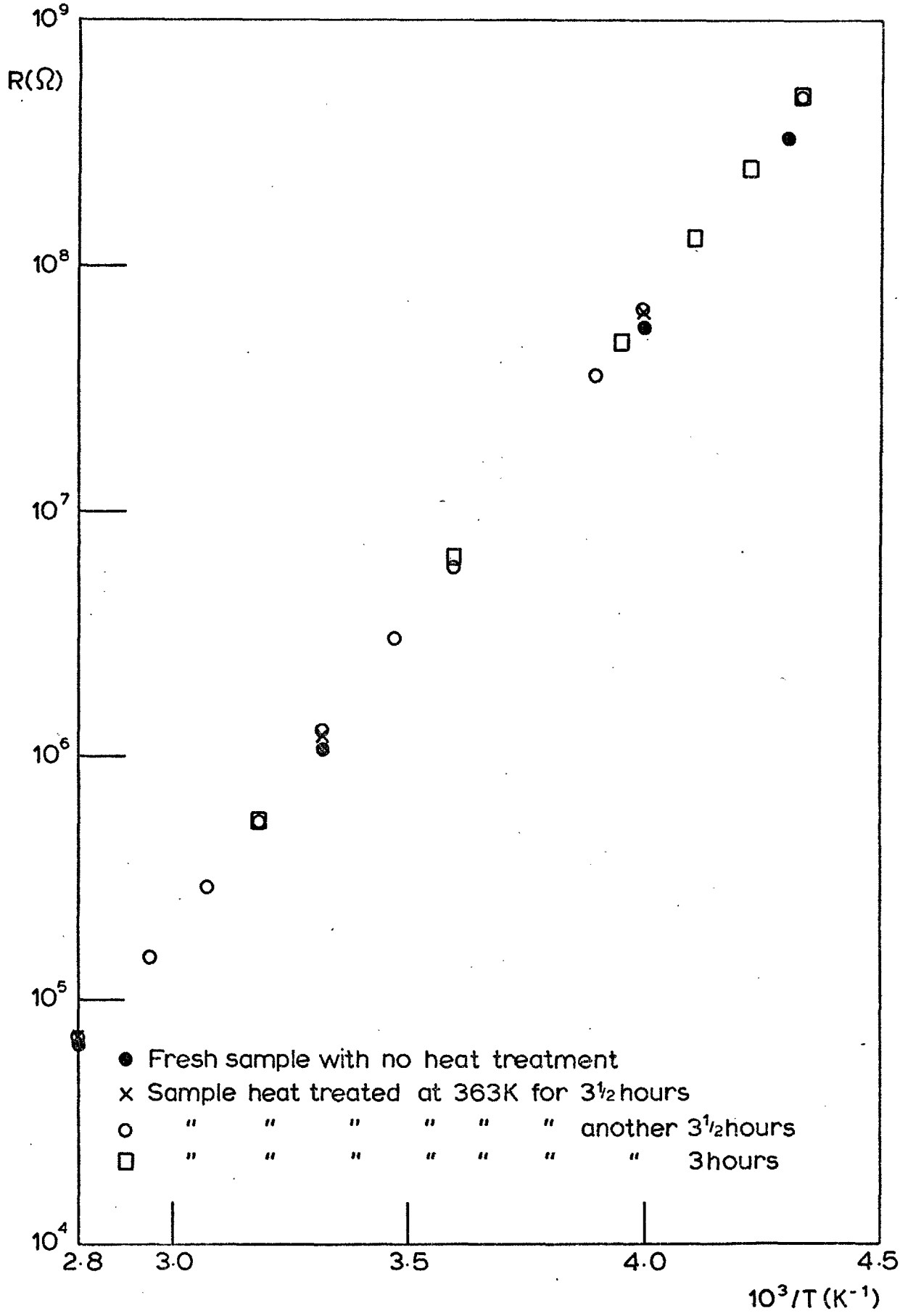


Fig. 3·13: Resistance of Sample 7·3 as a function of heat treatment at 363 K.

explanation for the effects observed in the present study. Although no concrete evidence is avaliable, it is possible that the slightly varying amounts of "Silver-Dag" and thermally conducting grease used in making electrical and thermal contacts to the different specimens needed varying amounts of outgassing before becoming stable. These could introduce errors in the measured temperatures of the two faces of the sample, which would in turn influence the Seebeck and Resistance data. The samples were checked for errors introduced into the readings because of the thermal resistances of layers of "Silver-Dag", mica, and thermally conducting grease that existed between each face of the sample and the thermocouple monitoring the temperature of that face. This was done by bringing the temperature of both faces , as displayed on the D.V.M., to the same value, and measuring the Seebeck potential with a zero temperature gradient. The thermoelectric emf's thus measured were always less than 150 μV. This is a very reasonable value if it is considered that the accuracy in each thermocouple reading was $\pm$ 0.6 K, and that a typical Seebeck potential was about 2500 μV when the temperature difference between the faces was about 20 K. It was not possible, however, to establish any link between heat treatment effect, and its influence on the thermal resistance of "Silver-Dag", say, which would, in turn, modify the Seebeck potential readings. The zero temperature difference thermoelectric emf did not vary much with heat treatment, and any variation was in a random manner. This could be because of the fact that experimentally it was very difficult to keep the temperatures of both faces at exactly the same value while allowing the system to reach thermal equilibrium. Invariably, there would be slight temperature drifts, which at small temperature differences would cause large percentage changes in the Seebeck potential reading.

A theoretical estimate of errors introduced in measuring the temperature of slab faces due to the presence of thin layers of thermally

conducting grease, mica, and "Silver-Dag" may be made: there is a finite temperature drop in these layers, because of the thermal resistance, R_t, in each layer, where

$$R_t = \frac{1}{k} \cdot \frac{\Delta x}{A} \qquad 3.7$$

k is the thermal conductivity, Δx the thickness, and A the cross-sectional area.

Levy [14] has calculated the thermal resistance of "Silver-Dag" for a particular configuration, from which a value of 5×10^{-2} W K^{-1} cm^{-1} at room temperature can be estimated for the thermal conductivity of this material. In the present set-up, a maximum thickness of 0.5 mm of "Silver-Dag" is estimated at each face (i.e. total "Dag" thickness of 0.1 cm). The cross sectional area of the slabs were typically 0.25 cm^2 (0.5 cm x 0.5 cm). It therefore follows from equation 3.7 that,

$$R_{t\ \text{"Silver-Dag"}} = \frac{1}{0.05} \times \frac{0.1}{0.25}$$

$$= 8\ \text{W}\ K^{-1}$$

Estimating the thickness of thermally conducting grease at each face to be 0.25 mm, then,

$$R_{t\ \text{grease}} = \frac{1}{7 \times 10^{-3}} \times \frac{0.05}{0.25}$$

$$= 28\ \text{W}\ K^{-1}$$

where $k_{\text{grease}} = 7 \times 10^{-3}$ W K^{-1} cm^{-1} at room temperature as already quoted in Section 3.3.1.

Mica has a typical ambient temperature thermal conductivity of

5×10^{-3} W K^{-1} cm^{-1} normal to the basal plane. Typical thicknesses used were always less than 30 μm.

$$\text{i.e. } R_{t\ \text{mica}} = \frac{1}{5 \times 10^{-3}} \times \frac{60 \times 10^{-4}}{0.25}$$

$$= 4.8 \text{ W } K^{-1}$$

SeTAG specimens were always more than 5 mm in thickness. Taking the thermal conductivity of SeTAG to be 1.9×10^{-3} W K^{-1} cm^{-1} (31), we obtain

$$R_{t\ \text{SeTAG}} = \frac{1}{1.9 \times 10^{-3}} \times \frac{0.5}{0.25}$$

$$= 1.1 \times 10^{3} \text{ W } K^{-1}$$

It can be seen that the total thermal resistance of thermally conducting grease, mica, and "Silver-Dag" is about 40 W K^{-1}, which is the 'worst possible case' value. Comparing to $R_{t\ \text{SeTAG}} \sim 10^{3}$ W K^{-1}, the maximum error due to the above is 4% at room temperature.

3.5.3. Results.

The temperature variation of the Seebeck coefficient was measured* in six samples from six different ingots. In the Ch_xY_{100-x} series of SeTAG glasses, two ingots with x = 71%, two with x = 61%, and one with x = 45% were examined. In addition, an ingot of composition $Se_9Te_{32}As_{52.3}Ge_{6.5}$ was also studied. The temperature range of measurements was 223 - 356 K (-50°C to 83°C), except for the sample of composition $Ch_{45}Y_{55}$, where because of the higher resistivity of the material, measurements could only be made down to a temperature of 248 K (-25°C).

*Errors due to the thermoelectric emf's of the leads (< 10 μVK^{-1}) are very small compared to the Seebeck coefficients of the sample (> 1000 μVK^{-1}), and, therefore, no corrections were deemed necessary.

The results which are reported in this section were those obtained after the samples had been heat treated, and they are, therefore, the reproducible, and thermally stable data.

The results for all six specimens that were studied are shown in Figure 3.14. The experimental points for curve 6, which lie very close to the broken line, have been omitted for clarity.

The data of Figure 3.14 suggest the presence of significant degrees of curvature in all the plots of S against $10^3/T$. An increase in the magnitude of S and the slope of each plot with decreasing chalcogen content may also be observed, although the sample of composition $Se_9Te_{32}As_{52.5}Ge_{6.5}$ is a notable exception.

If the results of Figure 3.14 are interpreted in terms of equation 3.6, the thermopower activation energies, E_{so}, in Table 3.3 are obtained.

Sample	Composition	$S_{298\ K}$ μVK^{-1}	E_{so} (eV) ($\pm$ 0.01 eV)	$E_{\sigma o}$ (eV) ($\pm$ 0.01 eV)	$E_{\sigma o} - E_{so}$ (eV)
8.3	$Ch_{45}Y_{55}$	1560	0.42	0.56	0.14
10.2	$Ch_{61}Y_{39}$	1435	0.38	0.49	0.11
7.3	$Ch_{61}Y_{39}$	1475	0.39	0.49	0.10
15.3	$Ch_{71}Y_{29}$	1370	0.36	0.47	0.11
13.3	$Ch_{71}Y_{29}$	1350	0.37	0.46	0.09
5.4	Se_9Te_{32} $As_{52.5}Ge_{6.5}$	1425	0.39	0.50	0.11

Table 3.3 Seebeck Coefficient Parameters for SeTAG Glasses According to Equation 3.6

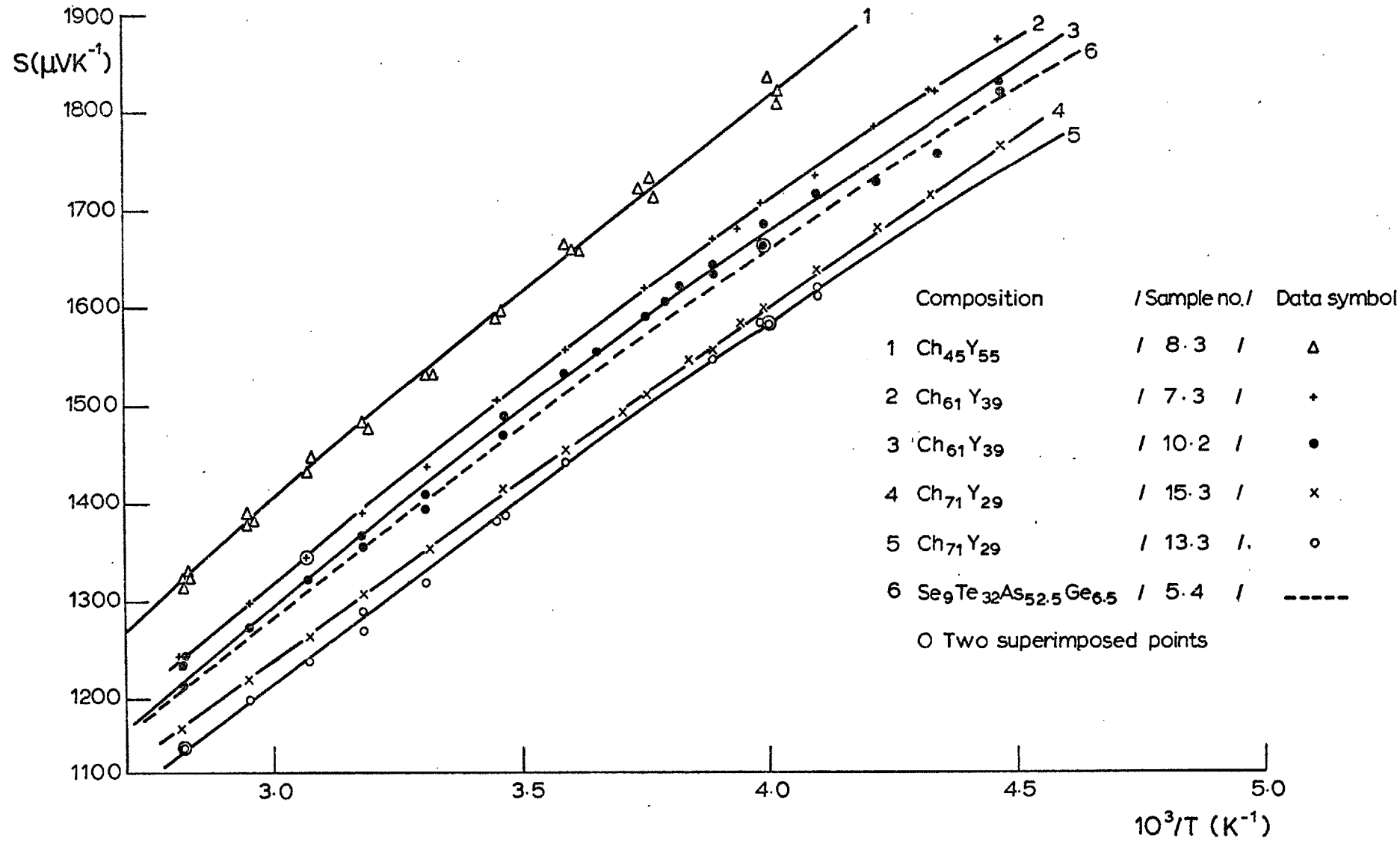


Fig. 3.14: Variation of thermoelectric power with temperature and composition

E_{so} was calculated from the slope of a straight line passed through the experimental points. The conductivity activation energies, $E_{\sigma o}$, which were calculated by measuring the resistance of the thermopower samples, are also listed. Room temperature Seebeck coefficients, $S_{298\ K}$, are included in this table as well.

The intercepts of straignt line plots of S viz $^{1}/T$, at $\frac{1}{T} = 0$, which give the values of $\left[-\frac{\gamma}{k} + A \right]$ are not calculated here. This will be deferred until Section 3.7.1, where all the conductivity and Seebeck coefficient data are discussed in terms of the Mott and Davis model.

In Figure 3.15, the Peltier coefficient π (= ST) is plotted against T for three representative specimens from each composition in the series Ch_xY_{100-x} that was studied.

3.6. Temperature Dependence of the Optical Gap in $Ch_{61}Y_{39}$ Bulk Glass.

3.6.1. Introduction.

Several groups of crystalline materials have an absorption constant that increases as the exponential of the photon energy. This type of behaviour, as observed in alkali halides for example, is called the Urbach rule, and it follows the relation

$$\alpha = \alpha_o \exp \left[\text{Const.} \ (\hbar\omega - E_g)/kT' \right] \qquad 3.8$$

where α is the absorption coefficient, $\hbar\omega$ is the photon energy, E_g is the optical gap at temperature T and T' is the absolute temperature at high temperatures, and is a constant below about 100 K. The optical gap at 0 K, E_{go}, is determined by assuming E_g to be a linear function of temperature

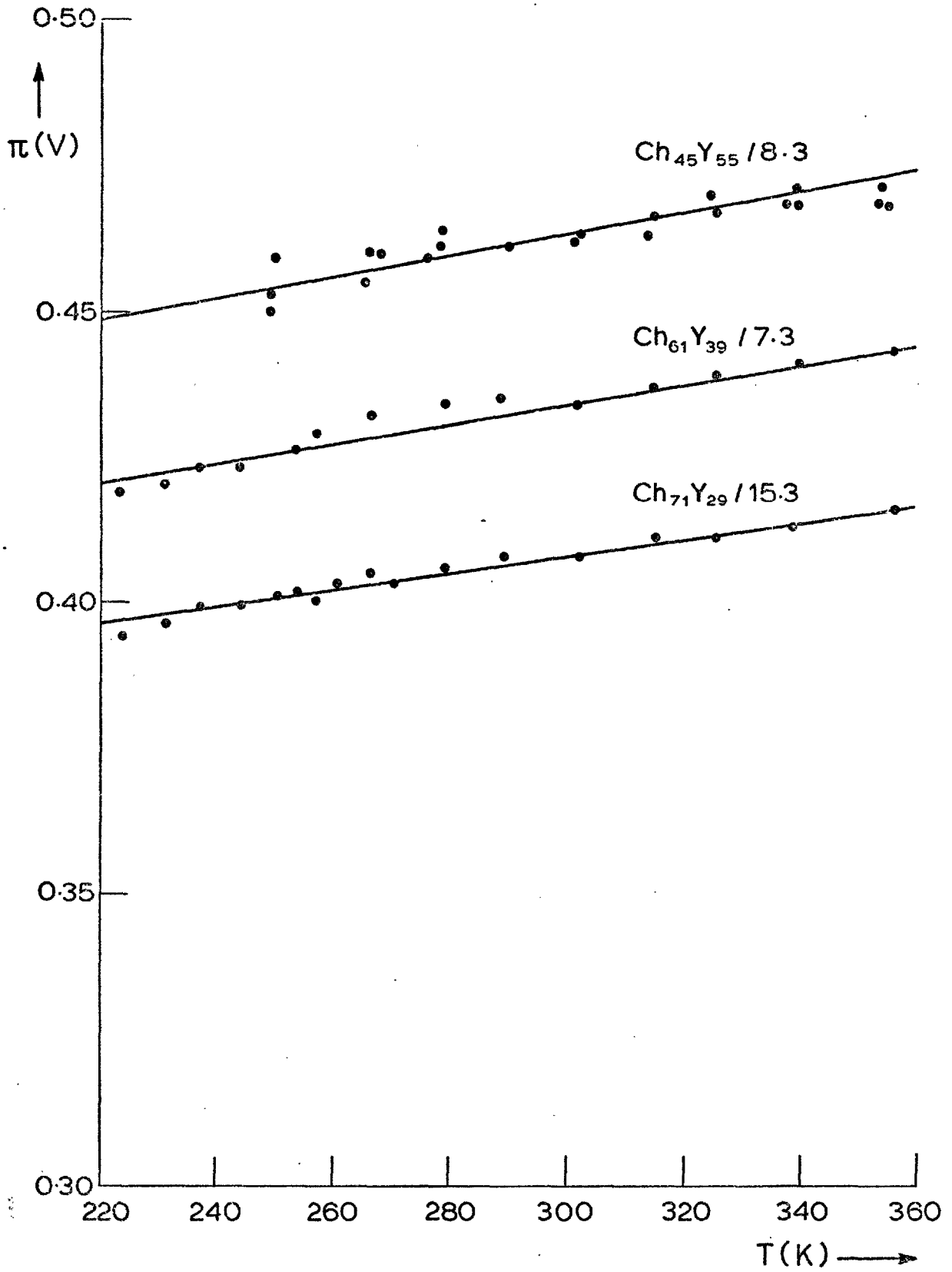


Fig. 3·15: Temperature variation of Peltier coefficient with composition in $Ch_x Y_{100-x}$ glasses.

$$\text{i.e. } E_g = E_{go} - \beta T \qquad 3.9$$

which when substituted back in equation 3.8 gives a temperature independent α at $\hbar\omega = E_{go}$. Thus by measuring α at various temperatures, the value of E_{go} may be determined. This is illustrated graphically in Figure 3.16 (after Mott and Davis [1]).

The k-selection rule, $\underline{k} \pm \underline{q} = \underline{k}'$ (where $\underline{k}$ and $\underline{k}'$ are the wave vectors before and after an electronic transition, and $\underline{q}$ is the wave vector of the photon) maybe applied in crystalline materials. In the case of optically induced transitions in amorphous semiconductors, however, charge carriers experience strong scattering at the valence and conduction band edges, and the mean free path is short, so that $\Delta\underline{k} / \underline{k} \sim 1$: $\underline{k}$ is no longer a good quantum number, and the above rule breaks down [1],[35]. This, though, may not be the case at energies well away from the absorption edge.

In amorphous chalcogenides, an exponential absorption edge is observed, but its shift with temperature is as shown in Figure 3.17: an almost parallel shift is noted *, which means that equation 3.8 cannot be used to determine E_{go}. A change in the slope of the edge with T is only observed at temperatures above the ambient. This deviation from Urbach's rule is explained [1] by writing equation 3.8 in the form

$$\ln\alpha = \text{Constant} + \frac{\hbar\omega - E_{go}}{kT'} + \frac{\beta T}{T'}$$

which for constant T' reduces to

$$\ln\alpha = \text{Constant} + \frac{\beta}{T'} \cdot T \qquad 3.10$$

---

*a-Se is an exception

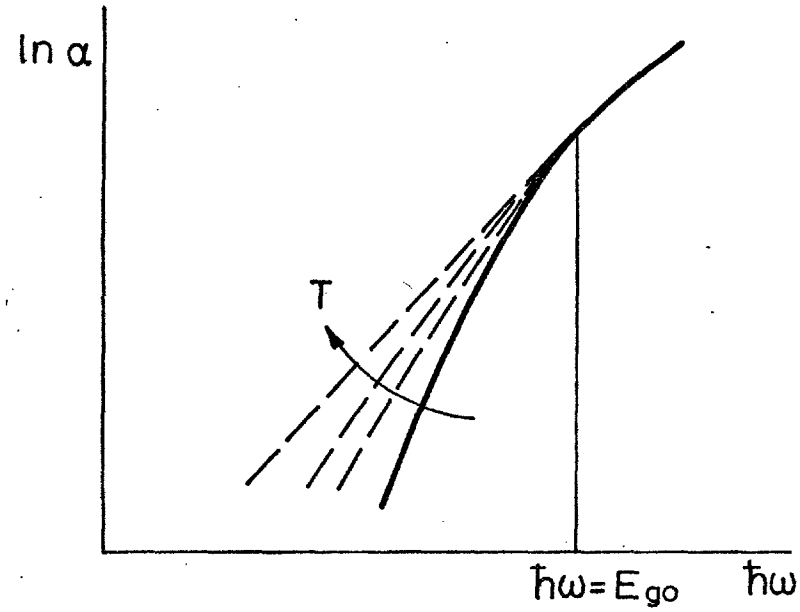


Fig. 3·16: Temperature variation of the Urbach edge in alkali halides (as typically observed)

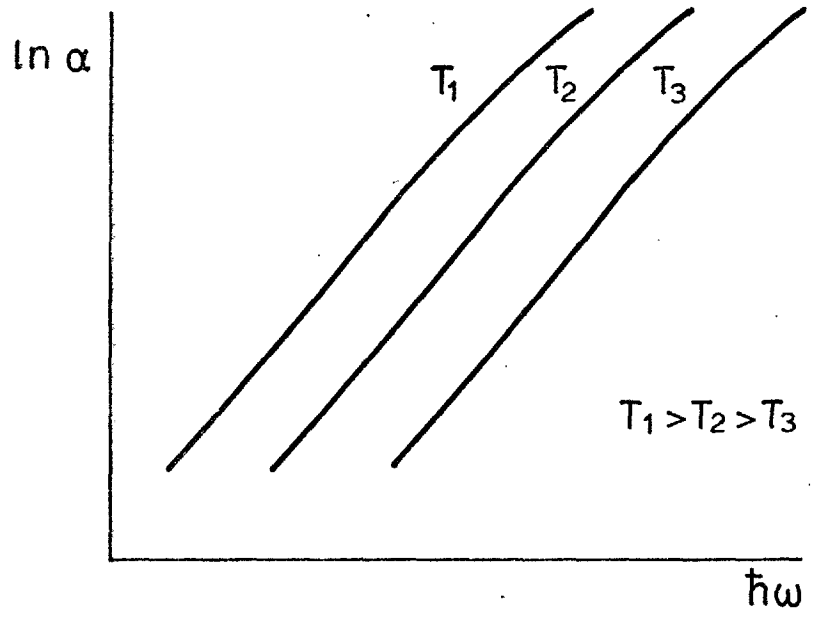


Fig. 3·17: Temperature variation of the absorption edge in amorphous chalcogenides.

at any given photon energy. The above equation would give a straight line by plotting $\ln\alpha$ against T, which would have a slope of β/T'. In other words, if in amorphous chalcogenides, the critical temperature below which T' is a constant is increased considerably, the parallel shift of $\ln\alpha$ with T would be explained.

A widely accepted theory to explain the Urbach edge has been put forward by Dow and Redfield [32]. They proposed the existance of 'micro-fields' in the solid, and derived an expression of the same form as equation 3.8 for the absorption coefficient by considering direct excitonic transitions in the presence of a uniform electric field [33]. The electric field broadens the sharp exciton peak, which in turn results in the exponential nature of the edge. It was shown that the absorption edge broadened with increasing electric fields, and that fields of the order of 10^7 V/cm were required to explain the exponential behaviour. Dow and Redfield [32] have also shown that when random fields are present, as is indeed very likely in amorphous solids, the exponential behaviour can still be explained by their theory if a Gaussian electric field distribution is assumed.

Olley [34] has demonstrated the effect of disorder on single crystal PbI_2, which has a sharp exciton absorption peak in the undamaged state. If disorder is introduced by the helium ion bombardment, the exciton peak is broadened with increasing disorder, and the leading absorption edge becomes exponential. In amorphous chalcogenides at energies below the exponential edge, a weak absorption tail is observed. Its shape, which is not well defined, is a function of preparation, homogeneity, and thermal history of the material [36],[39],[41].

For $\alpha \gtrsim 10^4$ cm^{-1}, i.e. at energies above the exponential tail, the

edge is no longer exponential. Its behaviour is described by

$$\alpha(\omega)\,\hbar\omega = \text{Constant}\,(\hbar\omega - E_g)^n \qquad 3.11$$

where n = 2 has been predicted by Davis and Mott [35] by assuming linear density of state distributions at the band edges (i.e. $n(E)\alpha E$), and neglecting localised to localised transitions. n = 2 has been found in simple binary chalcogenide alloys As_2Se_3, As_2S_3, As_2Te_3, and GeTe. In multicomponent chalcogenide alloys, however, n = 3 has been found [40]. This value of n can be derived, according to Mott and Davis [1], if localised to localised transitions are not neglected in their model.

In the brief review presented above, no attempt has been made to cover the wide range of theoretical and experimental work done on chalcogenide glasses. Much more detailed reviews of optical absorption in particular, and optical properties in general, of amorphous solids are to be found in the literature. (See, for example, Refs.(1),(36),(38).)

The optical absorption measurements presented in this section were carried out in order to determine the value of γ in the thermoelectric power expression 3.6. If it is assumed that all the critical energies at the band edges have the same temperature coefficients, then

$$\gamma = \frac{d(E_F - E_V)}{dT} = \frac{d(E_F - E_B)}{dT} \simeq \tfrac{1}{2}\frac{dE_g}{dT} \qquad 3.12$$

By measuring $\alpha(\hbar\omega)$ at various temperatures, the value of γ may be estimated from the above equation.

3.6.2. Experimental Procedure.

The temperature dependence of the optical gap was measured in a hot pressed sample of $Ch_{61}Y_{39}$ composition. The sample (softening temperature ~ 440 K) was raised to a temperature of about 460 K in a modified, evacuable, 13 mm pressure die supplied by Specac * (Figure 3.18). The sample was then pressed between two stainless steel pellets, whose faces had been polished to an optical finish of 1 μm. The whole die assembly was heated externally. The temperature of the sample was monitored by inserting a thermocouple through a hole drilled into the plunger (see Figure 3.18). In this way, the temperature of the sample could be monitored very approximately. The pressure in the die was quite low prior to pressing (~ 10^{-5} mm Hg), but during the pressing process the pressure increased to ~ 10^{-2} mm Hg. This increase in pressure was probably due to the poor quality of the vacuum 'O' ring seal between the plunger and the die cylinder. A load of about five tons was necessary to produce a 30 μm thick specimen. The thickness of the specimen was uniform across its diameter to $\pm$ 1 μm. The optical finish of the sample, however, was not as good as the stainless steel pellets used in the pressing process, and small surface imperfections were visible under examination by an optical microscope.

Room temperature transmission and reflection measurements were made on the above prepared sample in a Beckman DK2A double beam recording spectrophotometer over the range 600 - 2500 nm (~ 2 - 0.5 eV).

Transmission measurements as a function of temperature were carried out in a Cary 14 double beam recording spectrophotometer in the range 0.7 - 1.2 eV. As this spectrometer was not equipped for temperature

---

*Spectroscopic Accessory Co., 241 Main Raod, Sidcup, Kent, DA14 6QS.

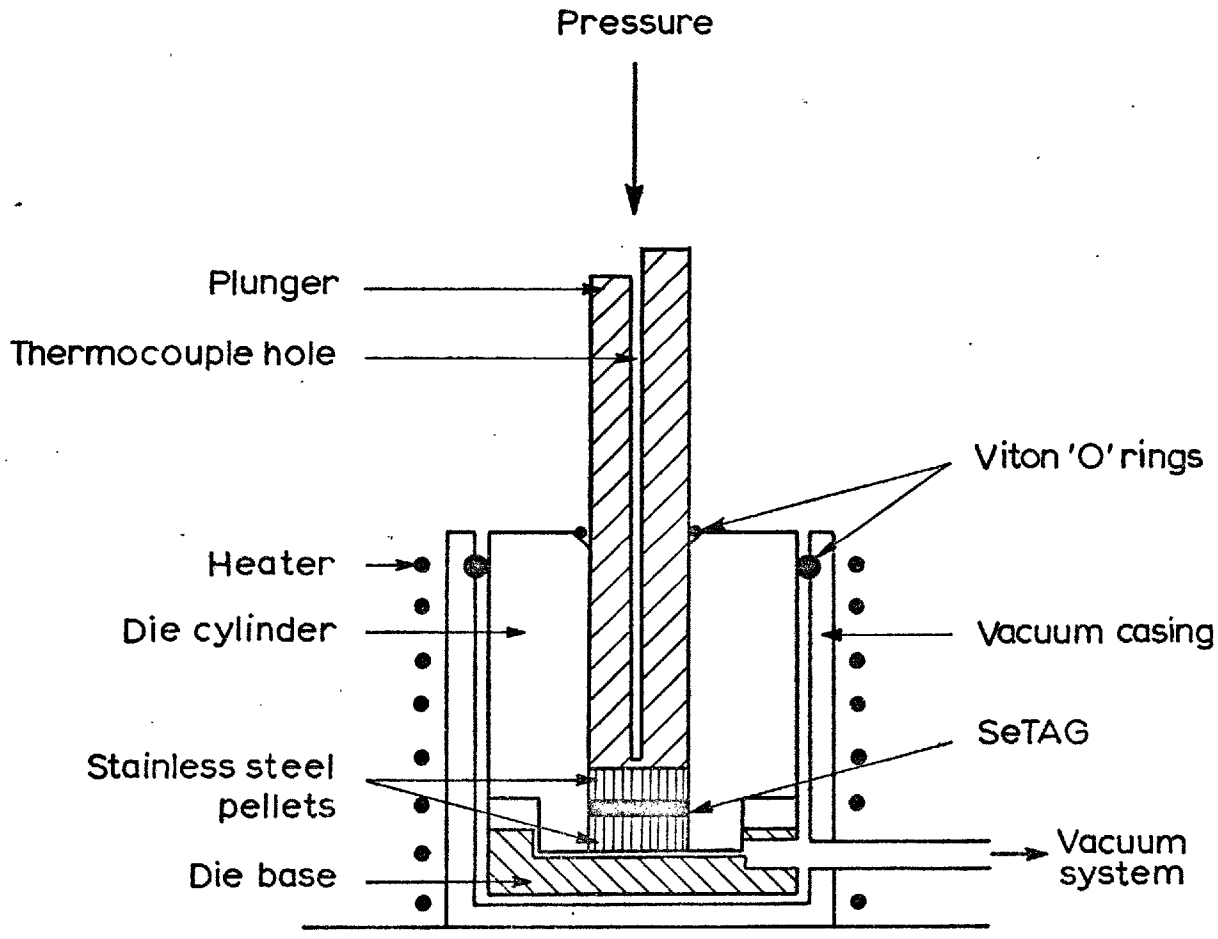


Fig. 3·18: Schematic cross-section of the pressure die

dependent measurements, a variable temperature optical cryostat * was used to measure the % transmission at various temperatures. The experimental set-up was not as good as could be expected, however, because of the difficulty of aligning the cryostat windows with the beam. This was done manually by adjusting the position of the cryostat without the sample with the spectrometer slits fully open until maximum transmission could be seen on a piece of paper held in front of the spectrometer detector. The transmission for minimum slit opening was then checked to make sure that the beam was central with respect to the area under illumination. The cryostat was then fixed in this position for all the measurements.

In all the transmission measurements, the spectormeters were checked for 0% and 100% transmission with the shutters fully closed and fully open.

Because of the small area of the sample, a black, non-reflecting mask was constructed to cut out all radiation not incident on the sample. All the above adjustments were carried out with this mask in the measuring beam.

3.6.3. Results.

The room temperature reflectivity, R, of $Ch_{61}Y_{39}$ glass, measured at near normal incidence (angle of incidence = 6°), is shown in Figure 3.19. The total reflectivity, R_T, of a given material is composed of two components, namely the diffuse component, R_D, and the specularly reflected component, R_s, where,

$$R_T = R_s + R_D \qquad 3.13$$

---

*Beckman VLT-2 Variable Temperature Cryostat

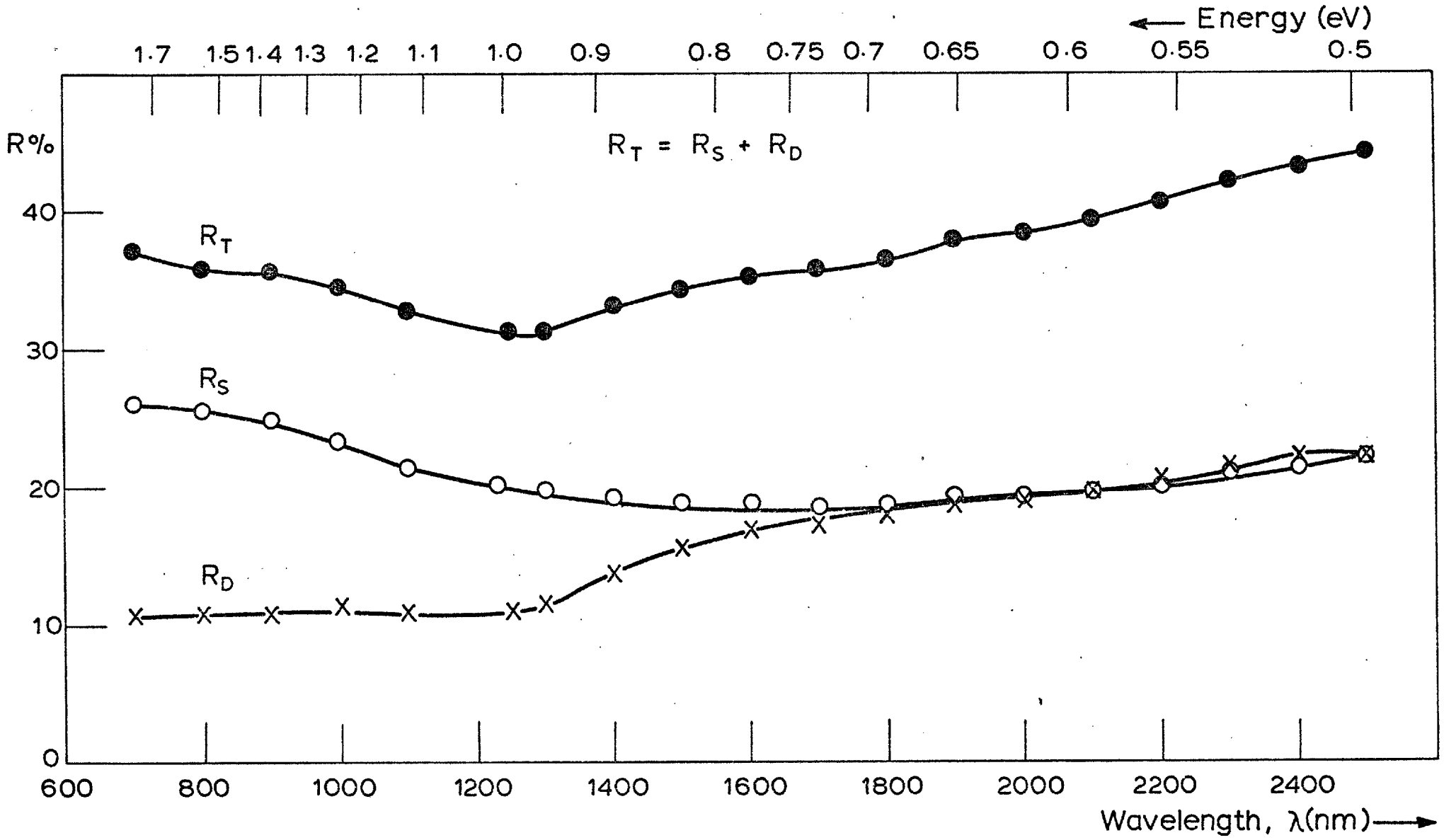


Fig.3.19: Reflection spectrum of $Ch_{61}Y_{39}$ glass

The diffuse component, R_D, depends on the surface roughness, and increases with the bulk inhomogeneity of the material. It is also wavelength dependent.

The specular term, R_s, at normal incidence, is given by

$$R_s = \frac{(n - 1)^2 + k^2}{(n + 1)^2 + k^2} \qquad 3.14$$

for reflection from the front face of slab of strongly absorbing material, so that the contribution to R_s from the second face may be neglected. In this equation n and k (sometimes known as the extinction coefficient) are the real and imaginary parts of the refractive index respectively.

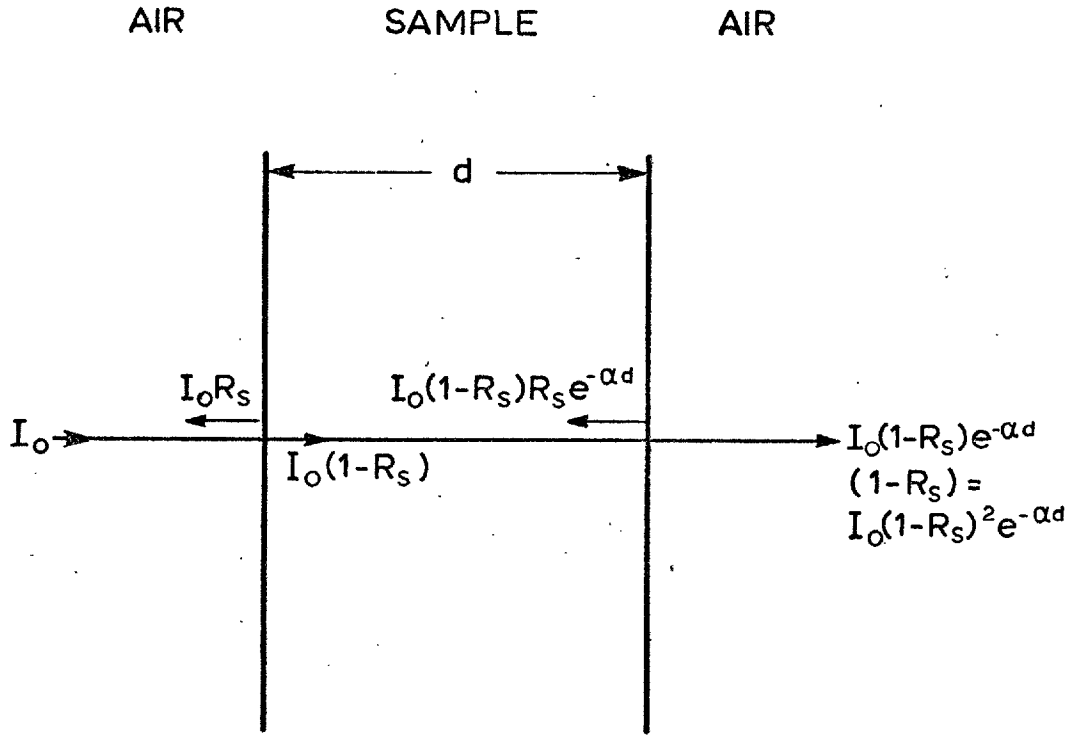
Since the maximum transmission for the sample under investigation was less than 25%, it was deemed possible to use equation 3.14.

In the specular reflectivity spectrum of Figure 3.19, however, there is little variation in reflectivity with energy, and for lower energies (i.e. longer wavelengths > 1250 nm) below and in the region of the absorption edge, its value in approximately constant at 20% ($\pm$ 2%). This means that $k^2 \ll (n - 1)^2$ over this entire region, and equation 3.14 becomes,

$$R_s \approx \frac{(n - 1)^2}{(n + 1)^2} \qquad 3.15$$

From the value of R_s (= 0.2), the high frequency dielectric constant ε_∞ (= n^2) is calculated to be 6.9.

The transmission coefficient, $T(= \frac{I_{incident}}{I_{transmitted}})$, of a parallel faced slab of material of thickness, d, and absorption coefficient, α, can be calculated for an incident beam of intensity I_o as shown in Figure 3.20. If the effects of multiple reflections from the faces, and the diffuse reflection term are neglected, the transmission coefficient is given by



$$T = \frac{I_o(1-R_s)^2 e^{-\alpha d}}{I_o} = (1-R_s)^2 e^{-\alpha d}$$

Fig. 3.20: Transmission of light through specimen of thickness, d, and absorption coefficient, α. The effects of multiple reflections are neglected.

$$T = (1 - R_s)^2 \, e^{-\alpha d} \qquad 3.16$$

Since d is known, and R_s has already been measured, (taken to be 0.2 independent of wavelength), then by recording the value of T at various beam energies, α may be plotted as a function of energy using equation 3.16. This is shown in Figure 3.21 for a $Ch_{61}Y_{39}$ specimen at four different temperatures from liquid nitrogen to room temperature. There is a slight difference in room temperature absoprtion spectra taken with the Cary and Beckman spectrophotometers.

Neglecting multiple reflections in equation 3.16 is unlikely to give rise to any significant errors in calculating the absorption coefficient at a particular frequency: even for a totally non-absorbing specimen in which $R_s = 0.2$ for both the front and the back face, only 2.7% of the transmitted radiation is neglected if multiple reflections are ignored.

The errors involved in neglecting the diffuse reflection term in equation 3.16 are likely to be significant, since between 11% and 18% of the total incident radiation is diffusely reflected in the energy range 1.15 - 0.7 eV. It has been shown in appendix 3C that the fraction of the transmission lost through diffuse scattering is given by

$$T_D = \frac{2(\alpha d)^2 e^{-\alpha d} R_D}{(1 - e^{-\alpha d})^2} \qquad 3.17$$

by considering an average diffuse scattering depth into the specimen, whose magnitude is a function of the wavelength of incident radiation

Combining equations 3.16 and 3.17 gives,

$$T_{measured} = (1 - R_s)^2 \, e^{-\alpha d} - T_D \qquad 3.18$$

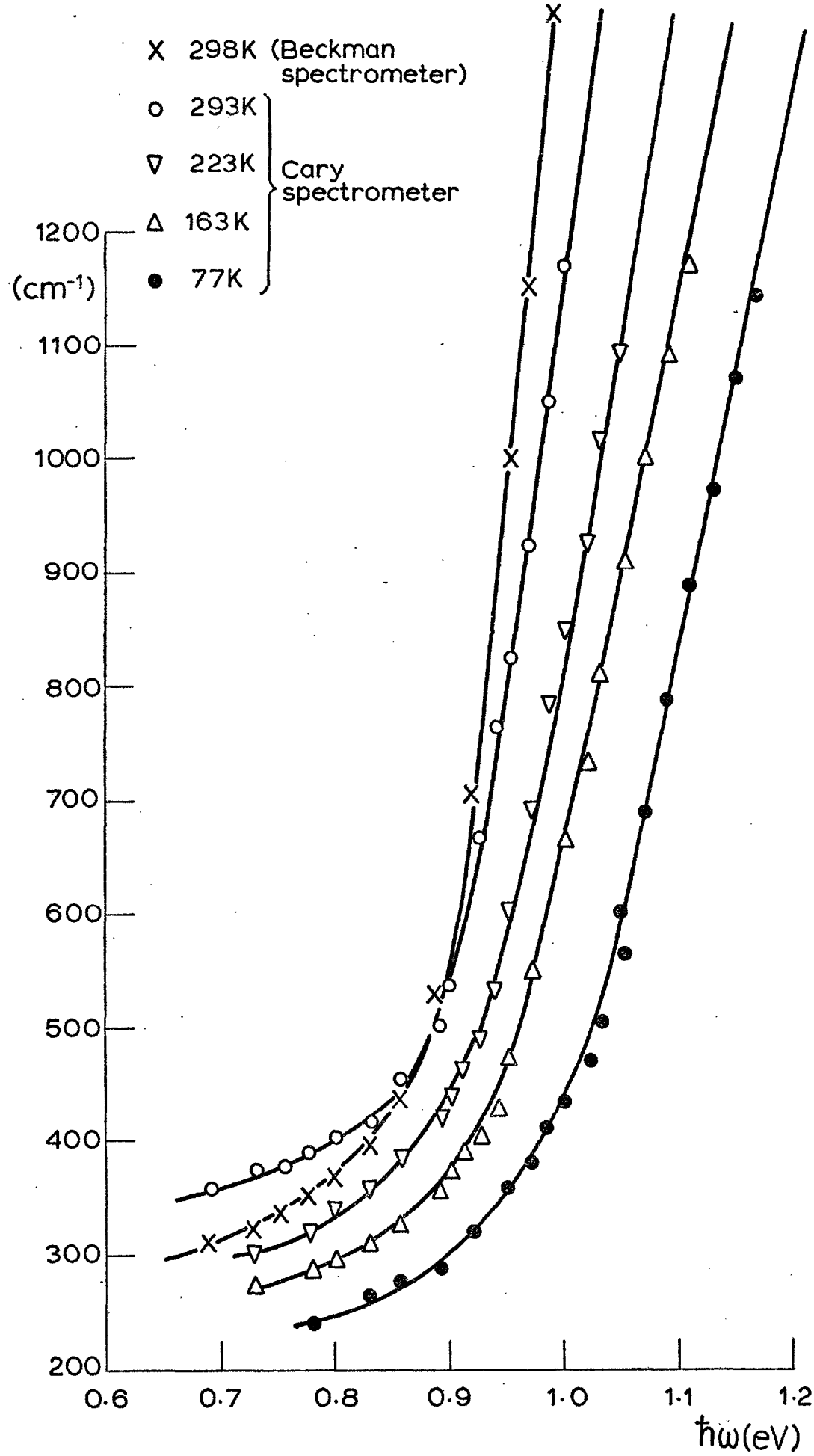


Fig.3.21: Absorption spectrum of $Ch_{61}Y_{39}$ as a function of temperature according to equation 3.16 (no diffuse reflectivity correction).

An iterative procedure was employed in finding an estimate of α which takes account of diffuse scattering: the value of α calculated from equation 3.16 was used in equation 3.17 to find a 'first estimate' of T_D, which when substituted in equation 3.18, yielded an improved estimate of α. The procedure was repeated, and after about five iteration steps, the value of α was found to converge.

By correcting the data of Figure 3.21 in the above manner, the values of α were found to be significantly reduced. Figure 3.22 shows the shift in the absorption edge with temperature, when diffuse scattering is not ignored.

Because of the thickness of the specimen, no absolute values of the optical energy gaps could be obtained, as it was not possible to go to high enough energies.

The temperature coefficient of the optical gap is therefore calculated by measuring the near parallel shift in the absorption edge with temperature at an arbitrarily chosen value of α (α = 1000 cm^{-1} was used in Figure 3.21, and α = 300 cm^{-1} was chosen in Figure 3.22). As can be seen from Table 3.4, the temperature coefficient of the optical gap, $\frac{dE_g}{dT}$, is almost independent of the temperature at which the measurements were made, although a slight increase in its value with decreasing temperature is apparent. It is not possible here to speculate in a useful manner upon this variation: the experimental apparatus used to measure the temperature coefficient of the gap was such that it was only possible to obtain an <u>estimate</u> of the value of $\frac{dE_g}{dT}$. Certain approximations were also made, which may have affected the accuracy of the results. For instance, the reflectivity measurements were carried out at room temperature only, and the α vs $\hbar\omega$ curves of Figures 3.21 and 3.22 were obtained by making the same room temperature reflectivity corrections in all cases

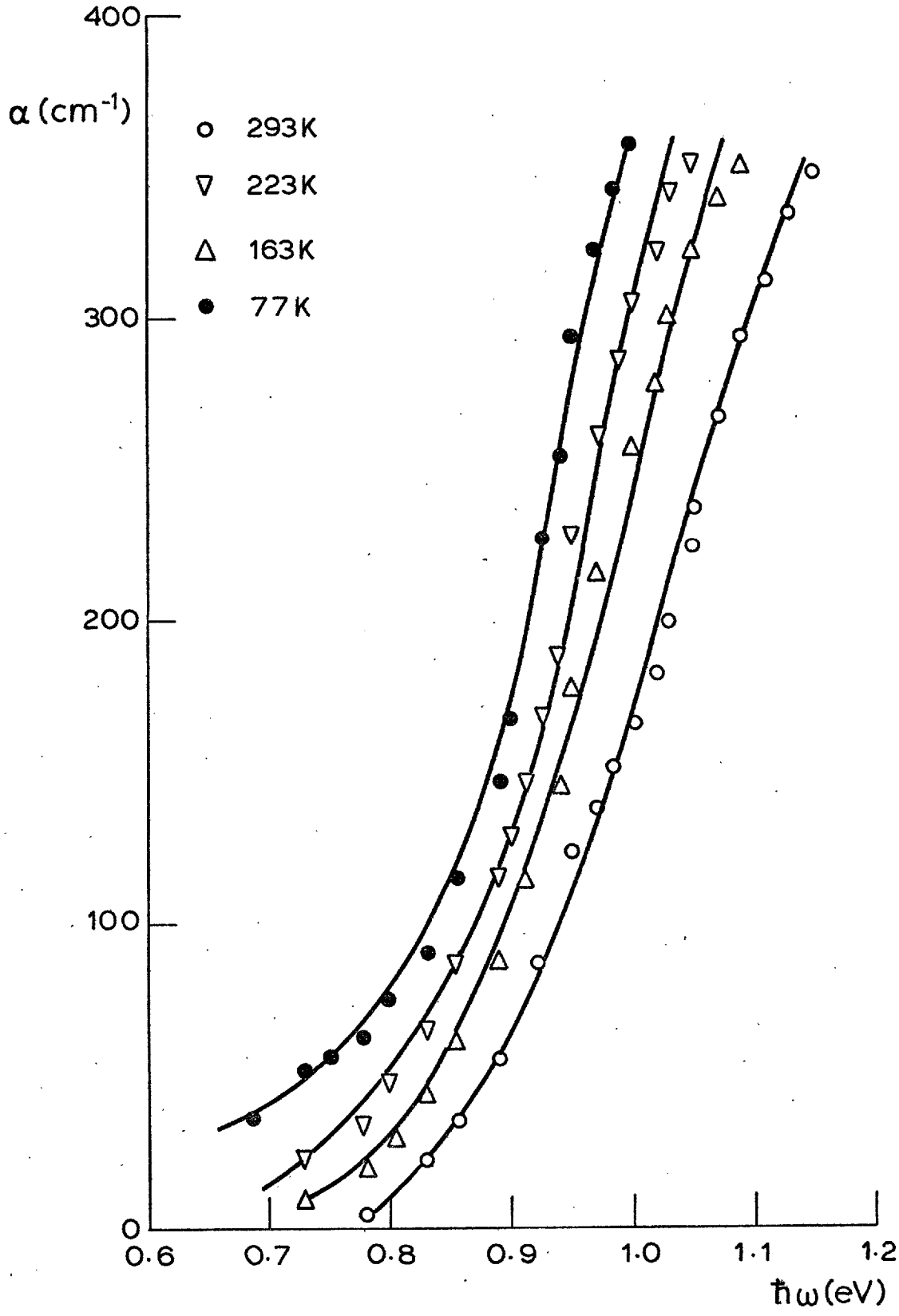


Fig. 3.22 : Absorption spectrum of $Ch_{61}Y_{39}$ as a function of temperature according to equations 3.17 and 3.18 (diffuse reflectivity correction included)

T_1(K)	T_2(K)	ΔT(K) ($=T_1-T_2$)	$\frac{dE_g}{dT}$ (eV K^{-1}) (at α=1000 cm^{-1})	Mean Value of $\frac{dE_g}{dT}$
293	223	70	6.4×10^{-4}	7.2×10^{-4} eV K^{-1}
293	163	130	6.9×10^{-4}	
293	77	215	7.2×10^{-4}	
223	163	60	7.5×10^{-4}	
223	77	145	7.6×10^{-4}	
163	77	85	7.65×10^{-4}	

(a) $\frac{dE_g}{dT}$ calculated ignoring diffuse reflection

T_1(K)	T_2(K)	ΔT(K) ($=T_1-T_2$)	$\frac{dE_g}{dT}$ (eV K^{-1}) (at α= 300 cm^{-1})	Mean Value of $\frac{dE_g}{dT}$
293	223	70	5.1×10^{-4}	6.2×10^{-4} eV K^{-1}
293	163	130	5.6×10^{-4}	
293	77	215	6.2×10^{-4}	
223	163	60	6.2×10^{-4}	
223	77	145	6.2×10^{-4}	
163	77	85	7.1×10^{-4}	

(b) $\frac{dE_g}{dT}$ calculated by including diffuse reflection correction

Table 3.4

irrespective of the temperature at which transmission measurements were made. It is, therefore, not possible to say whether there is a genuine shift in $\frac{dE_g}{dT}$ with temperature, or whether what has been observed is an experimental artifact.

It can be seen from Table 3.4 that the diffuse reflectivity correction reduces $\frac{dE_g}{dT}$ by about 14% from 7.2×10^{-4} eV K^{-1} to 6.2×10^{-4} eV K^{-1}. The values compare quite favourably with Weiser and Brodsky's 5×10^{-4} eV K^{-1} for As_2Te_3 (45), and with Green etal's value of 7.6×10^{-4} eV K^{-1} for $Si_{10}Te_{59}As_{23}Ge_8$ (7).

The value of γ ($\simeq \frac{1}{2} \frac{dE_g}{dT}$ from equation 3.12) is therefore found to be 3.1×10^{-4} eV K^{-1} (or 3.6×10^{-4} eV K^{-1} if the above correction is not included).

3.7. Analysis of Results.

As mentioned already in Section 3.1, the thermopower and conductivity results will be analysed mainly in terms of three models, namely the Mott and Davis (MD) model, the Green-Levy-Gee (GLG) model, and the Nagels etal (NCD) model.

Before more detailed analysis using the above models, however, it should be mentioned that any models based on a two band conduction mechanism will not be considered here. Such models have been considered by Rockstad etal (17), and by Moustakas etal (13).

The former authors have considered the effects of annealing on thermopower in amorphous chalcogenide films. In $Ge(Te_{0.7}Se_{0.3})_2$, for instance, they found that, upon annealing, a plot of S vs $^1/T$ gave a large negative intercept at $\frac{1}{T} = 0$. However, the four component alloys that they considered showed no annealing effects. Moustakas etal

interpret the results of Rockstad etal in terms of a two band conduction model, although they conclude that for unannealed specimens, conduction is by one band hopping, as this is the only mechanism in which the intercept in a plot of S vs $^{1}/T$ gives reasonable values.

The evidence from field effect measurements also indicate conduction strongly dominated by holes [7],[14],[30].

The results will now be examined in the light of the above mentioned models.

3.7.1. The MD Model.

The density of states model for amorphous semiconductors proposed by Mott and Davis, and already discussed in Chapter 1, is shown in Figure 3.23: E_c and E_v are the conduction and valence band mobility edges respectively. The shaded regions between E_c and E_A, and E_v and E_B are the localised band tails. A narrow region of localised states (< 0.1 eV wide) also exists at the Fermi level, E_F.

Considering conduction by holes only, the following conduction mechanisms are possible:

(1) Conduction by excitation of carriers into the extended states below E_V. The conductivity is given by,

$$\sigma_{ext} = \sigma_{o,ext} \exp - (E_F - E_V)/kT \qquad 3.19$$

where $\sigma_{o,ext}$ is a constant independent of temperature.

Since in general,

$$\sigma = ne\mu$$

where n is the number of carriers, e the electronic charge, and μ the mobility, $\sigma_{o,ext}$ can be written as,

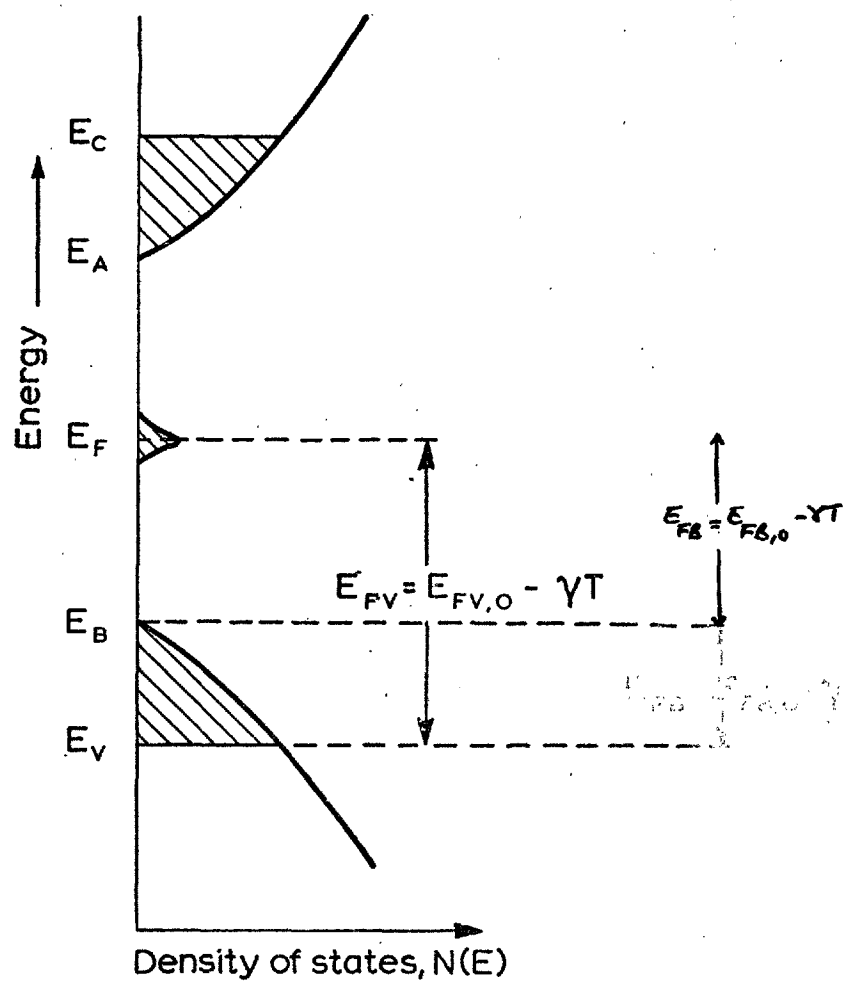


Fig. 3.23: The density of states in amorphous semiconductors as a function of energy as proposed by Mott and Davis [1]

$$\sigma_{o,ext} = eN_V\mu_{ext}$$

where N_V is the effective density of states (cm^{-3}) at the valence band mobility edge, and μ_{ext} is the extended states mobility.

If $E_F - E_V$ varies linearly with temperature, so that,

$$E_F - E_V = E_{FV,O} - \gamma T \qquad 3.21$$

then substituting 3.20 and 3.21 in 3.19, we get,

$$\sigma_{ext} = eN_V\mu_{ext}e^{\gamma/k} \exp - E_{FV,O}/kT$$

$$= C_{ext} \exp - E_{FV,O}/kT \qquad 3.22$$

where $C_{ext} = eN_V\mu_{ext}e^{\gamma/k}$. $E_{FV,O}$ in the above expression is the value of $(E_F - E_V)$ extrapolated to 0 K. The pre-exponential constant, C_{ext} in (3.22) is of the order of $10^3\ \Omega^{-1}\ cm^{-1}$.

The mobility below E_V is considered to be diffusive, and it is written as,

$$\mu_{ext} = \frac{1}{6}\ e\nu_{el}R^2/kT$$

$$\sim 10\ cm^2\ V^{-1}\ s^{-1} \qquad 3.23$$

where ν_{el} ($\sim 3 \times 10^{15}\ s^{-1}$) is an electronic frequency, and R is distance between nearest neighbours.

(2) Conduction by hopping of carriers between nearest neighbour sites in the tail of localised states between E_V and E_B. In this regime, the mobility due to hopping is given by,

$$\mu_{hop} = \frac{1}{6}\nu_{ph}\frac{eR^2}{kT}\exp\left(-\frac{E_\mu}{kT} - 2\alpha R\right) \qquad 3.24$$

$$= \mu_{0,hop}\exp\left(-\frac{E_\mu}{kT}\right)$$

where ν_{ph} ($\sim 10^{12}$ s^{-1}) is a phonon frequency, E_μ is the activation energy due to hopping, and α is the localisation parameter. Because of the value of ν_{ph} compared to ν_{el}, μ_{hop} is estimated to be about 10^{-2} cm^2 V^{-1} s^{-1}. In equation 3.24, E_μ has been taken to be constant and independent of temperature, except at low temperatures, although the validity of this assumption has been questioned [42].

Using expression 3.24 for the mobility, the conductivity in the tails of localised states is given by,

$$\sigma_{loc} = C_{loc}\exp - (E_{FB,0} + E_\mu)/kT \qquad 3.25$$

where $$C_{loc} = eN_B\,\mu_{0,hop}e^{\gamma/k} \qquad 3.26$$

Equations 3.25 and 3.26, in which $E_{FB,0} = (E_F - E_B)_{T=0}$, and N_B is the effective density of states at E_B, have been derived in a similar manner to equation 3.22 by assuming a linear variation of $E_F - E_B$ with temperature.

(3) Conduction by hopping of carriers between localised states near E_F. In this regime (not observed in chalcogenide glasses) the conductivity is given by,

$$\sigma_F = \sigma_{0,F}\exp\left(-\frac{\Delta W_F}{kT}\right) \qquad 3.27$$

where the hopping energy $\Delta W_F \sim 0.05$ eV, and $\sigma_{0,F}$ is a constant.

The above equation describes hopping between nearest neighbour sites at E_F. At lower temperatures, however, variable range hopping by tunnelling of carriers to more distant sites may dominate. Mott [43] has shown that the conductivity in this regime is given by

$$\ln\sigma_F = A - BT^{-1/4} \qquad 3.28$$

In SeTAG glasses examined here, and in chalcogenide glasses in general, mechanism (3) is not observed, and this will not be considered any further.

Culter and Mott [29] have derived an expression for thermoelectric power when the current is carried in the extended states. The expression may be written as

$$S = \frac{k}{|e|}\left[\frac{E_F - E_V}{kT} + A\right]$$
$$= \frac{k}{|e|}\left[\frac{E_{FV,0}}{kT} - \frac{\gamma}{k} + A\right] \qquad 3.29$$

A in the above expression is a constant of the order of unity. The above expression is also used in crystalline semiconductors, and the constant A, known as the scattering parameter, has a value which depends on the scattering processes involved.

Similarly, for currents carried in the localised tail of states,

$$S = \frac{k}{|e|}\left[\frac{E_{FB,0}}{kT} - \frac{\gamma}{k} + A\right] \qquad 3.30$$

where A is again a small constant.

Hence if the plot of S vs $^1/T$ is a straight line, its intercept with the S axis at $^1/T = 0$ would give the value of $\left[-\frac{\gamma}{k} + A\right]$. If A

is taken to be unity, the value of γ may be obtained from the intercept. Alternatively, if γ is estimated from the temperature dependence of the optical gap, the value of A may be calculated.

If the conductivity and thermoelectric power data of Sections 3.3.2. and 3.5.3. are treated in terms of the MD model, the parameters of Table 3.5 are obtained. From the values of the pre-exponential factors, C, which are in the range 200 - 500 Ω^{-1} cm $^{-1}$, it is likely that conduction is taking place in the extended states (mechanism (1)), since the C values are too large for conduction in the localised tail of states.

Assuming conduction to be taking place via the above mechanism, then the difference between the conductivity activation energy, $E_{\sigma o}$, and the thermoelectric power activation energy, E_{so}, of about 0.1 eV (column 7, Table 3.5) may be explained in terms of Emin etal's small polaron theory[4] In this theory, $E_{\sigma o}$ is the sum of the energy required to generate the carriers, $E_{FV,O}$ (see equation 3.22), and the activation energy required for small polaron hopping of hole-like carriers, W_H,

$$\text{i.e. } E_{\sigma o} = E_{FV,O} + W_H \qquad 3.31$$

Since the activation energy from the thermoelectric power is still $E_{so} = E_{FV,O}$, the difference between the conductivity and thermopower activation energies gives W_H. W_H is zero only if there are no small polaron effects.

Although the above theory, as combined with the MD model, suggests a very attractive explanation for the difference in $E_{\sigma o}$ and E_{so} with the conduction still taking place in the extended states, it is not adequate in explaining the curvatures observed in the conductivity and thermo-

1	2	3	4	5	6	7	8	9	10	11	12	13	14	15
SAMPLE	%Chalcogen	$\sigma(298K)$ $\Omega^{-1}cm^{-1}$	$S(298K)$ μVK^{-1}	$E_{\sigma o}$ (eV)	E_{So} (eV)	$E_{\sigma o}-E_{So}$ (eV)	$C(\Omega^{-1}cm^{-1})$	$-\frac{\gamma}{k}+A$	$\gamma(A=1)$ (eVK^{-1})	$\gamma(A=2)$ (eVK^{-1})	$\gamma(A=3)$ (eVK^{-1})	$\gamma(A=4)$ (eVK^{-1})	$A(\gamma=3.6\times10^{-4}$ $eVK^{-1})$	$A(\gamma=3.1\times10^{-4}$ $eVK^{-1})$
8.2	45	1.5×10^{-7}	---	0.55	---	0.13 (8.3)	309	---	---	---	---	---	---	---
8.3	45	---	1560	0.56	0.42	0.14	---	1.72	-6.2×10^{-5}	2.4×10^{-5}	1.1×10^{-4}	2.0×10^{-4}	5.9	5.3
3.3	61	2.6×10^{-6}	---	0.48	---	0.09 (7.3)	155	---	---	---	---	---	---	---
2.3	61	2.2×10^{-6}	---	0.49	---	0.10 (7.3)	425	---	---	---	---	---	---	---
10.2	61	1.4×10^{-6}	1435	0.49	0.38	0.11	276	1.8	-7.1×10^{-5}	1.5×10^{-5}	1.0×10^{-4}	1.9×10^{-4}	6.0	5.4
7.3	61	---	1475	0.49	0.39	0.10	---	1.9	-7.8×10^{-5}	8.3×10^{-6}	9.4×10^{-5}	1.8×10^{-4}	6.1	5.5
13.2	71	6.1×10^{-6}	---	0.45	---	0.08 (13.3)	476	---	---	---	---	---	---	---
13.3	71	---	1350	0.46	0.37	0.09	---	1.2	-2.0×10^{-5}	6.6×10^{-5}	1.5×10^{-4}	2.4×10^{-4}	5.4	4.8
15.4	71	7.7×10^{-6}	---	0.46	---	0.10 (15.3)	385	---	---	---	---	---	---	---
15.3	71	---	1370	0.47	0.36	0.11	---	1.9	-7.4×10^{-5}	1.2×10^{-5}	9.9×10^{-5}	1.8×10^{-4}	6.0	5.5
5.3	$Se_9Te_{32}As_{52.5}Ge_{6.5}$	2.0×10^{-6}	---	0.48	---	0.09 (5.4)	221	---	---	---	---	---	---	---
5.4	''	---	1425	0.50	0.39	0.11	---	1.3	-2.8×10^{-5}	5.8×10^{-5}	1.4×10^{-4}	2.3×10^{-4}	5.5	4.9

Table 3.5 Transport Parameters in Bulk SeTAG obtained using the Mott and Davis Model

power plots. It should also be noted that Austin and Mott [46] have shown that for conduction in the extended states with a small polaron effect, a value of A < 1 is expected, whereas inspection of Table 3.5 shows this not to be the case.

Using the thermopower expression (3.29), the experimental values of $\left[-\frac{\gamma}{k} + A \right]$ have been worked out for the various samples studied. These have been listed in column 9 of Table 3.5. In columns 10 to 13, the values of γ, assuming integral values of A from 1 to 4, have been calculated. It can be seen that only if A = 4, will the experimentally determined value of $\gamma = 3.1 \times 10^{-4}$ eVK^{-1} be approached, although even with this high value of A, an average value of only $\gamma = 2 \times 10^{-4}$ eVK^{-1} is obtained.

If , on the other hand, the value of A is calculated by assuming the experimental value of γ, A is found to be generally between five and six (columns 14 and 15 in Table 3.5), which do not compare well with Cutler and Mott's predicted value of unity. It should be noted that other authors [7,9,13], using the MD model, also obtain values of A which generally lie between three and five.

3.7.2. The GLG Model.

In the MD model, the equation for conductivity in the extended states beyond the mobility edge, and for conduction in the localised band tail, have been derived by making the following assumptions:

(1) The majority of carriers contributing to the conduction process (i.e. $n = \int N(E)f(E)dE$) are concentrated at an effectively single energy level at E_B (for conduction in the localised valence states), and at E_V (for conduction in the extended valence states) and are of the order kT in energy band width. Hence it is assumed

that other carriers, of higher energies in the relevant set of states under consideration, do not make a significant contribution to the total conductivity.

(2) The mobility is assumed to vary as $^{1}/T$ in the extended states, and as $^{1}/T \exp(-E_{\mu}/kT)$ in the localised states. In other words, no significant mobility variation with energy is considered in either of the above sets of states, because otherwise, in the localised states, the current would not be carried at E_B, but possibly in the range of energies between E_B and E_V. This would result in curvature in $\ln\sigma$ vs $^{1}/T$ plots.

(3) Starting with the number of carriers, n, in a given energy interval, the conductivity in the extended states is written as,

$$\sigma_{ext} = eN(E_V)\ kT\ \mu_{ext} \exp\left[-(E_F - E_V)/kT\right]$$

Similarly, the conductivity in the localised states may be written as,

$$\sigma_{loc} = eN(E_B)\ kT\ \mu_{hop} \exp\left[-(E_F - E_B)/\ kT\right]$$

It can be easily be shown that the above equations may only be obtained by assuming constant, but not equal, densities of states in the extended and localised levels. If the density of states is allowed to vary with energy, this would make the pre-exponential factors in the above expressions functions of temperature, and they would no longer be constants as derived by Mott and Davis (equation 3.22 and 3.25), and subsequently used in the NCD model (see Section 3.7.3.).

In the GLG model, it has been attempted to incorporate the energy dependence of the density of states, and possibly that of the mobility, into the expression for conductivity.

If, therefore, it is assumed that the density of states and the mobility are both functions of energy, so that,

$$\left.\begin{array}{l} \left.\begin{array}{l} N(E) \propto (E_B - E)^m \\ \text{and} \\ \mu(E) \propto (E_B - E)^n \end{array}\right\} \text{ in the localised band} \\ \\ \left.\begin{array}{l} \text{or } N(E) \propto (E_V - E)^m \\ \text{and } \mu(E) \propto (E_V - E)^n \end{array}\right\} \text{ in the valance band} \end{array}\right\} \qquad 3.32$$

where $p = m + n$, then the conductivity can be shown to obey the relation,

$$\sigma = CT^p \exp(-E_{\sigma o}/kT) \qquad 3.33$$

where C is a constant. Equation 3.33 has been derived more fully in Appendix 3A.

Equation 3.29 for thermoelectric power is, however, still valid in the GLG model, although the value of the constant A would now depend on the quantity p in equation 3.33[44].

Two independent sets of data have been analysed using this model. The first is the conductivity vs temperature data obtained on sample 3.3 of $Ch_{61}Y_{39}$ composition. The second is a set of data obtained from Dr. A. Levy who made his measurements on STAG glasses as part of his Ph.D. programme at Zenith Radio and Research Corporation (U.K.) Ltd [14]. The STAG composition used in these measurements was $Te_{69}R_{31}$, where $R = (Si_{0.24}Ge_{0.20}As_{0.56})$.

A computer program was written to fit the above data to equation 3.33, in which the parameter p could be varied until a best straight line fit to the experimental points was obtained in a plot of $\ln (\sigma T^{-p})$ vs $^{1}/T$. The program also computed the activation energy $E_{\sigma o}$ from the slope of this plot.

In both compositions p was found to be about four. The activation energies for the best straight line fits were 0.39 eV for the $Ch_{61}Y_{39}$ SeTAG glass (E_{so} = 0.38 - 0.39 eV), and 0.35 eV for the $Te_{69}R_{31}$ STAG glass (E_{so} = 0.41 eV).

Assuming Mott and Davis's expression for mobility in the extended states (equation 3.23), then p = 4 means that $N(E) \propto E^{4}$, which seems highly unlikely. Unfortunately using this method, it is not possible to distinguish between the energy dependence of the mobility and the density of states. It is not likely, however, that the mobility in the extended states will be strongly energy dependent. This still leaves a very strongly energy dependent N(E).

It should also be noted that the computer program which was developed for the above fitting purposes, distinguished the best fit value of p from all the other values by working out and comparing the correlation coefficient and the standard deviation in each case. The model, however, is not particularly sensitive to variations in p. For instance, for both sets of data, the correlation coefficient was unchanged up to the fourth decimal place, and any variation in the goodness of fit for various p values only became apparent at this point. It was not, therefore, possible to deconvolute the data in a positive manner by using the GLG model. Furthermore, although this model attempts to explain the curvature

in the $\ln\sigma$ vs $^{1}/T$ plots, it still gives a linear dependence of S vs $^{1}/T$, which is not what is observed experimentally in SeTAG.

3.7.3. The NCD model.

This model [8], as already briefly outlined in Section 3.1, assumes conduction to take place by two parallel mechanisms (in the case of conduction by holes only):

(a) The excitation of hole carriers into the extended valence states below the mobility edge at E_V.

(b) The nearest neighbours hopping of carriers in the localised states at E_B.

If the conductivity contributions due to (a) and (b) are summed together, then expression 3.3 of Section 3.1 is obtained,

$$\text{i.e.} \quad \sigma = \sigma_{ext} + \sigma_{loc} \qquad 3.3$$

$$\text{where} \quad \sigma_{ext} = C_{ext} \exp\left(- E_{FV,0}/kT\right) \qquad 3.22$$

$$\text{and} \quad \sigma_{loc} = C_{loc} \exp\left[-(E_{FB,0} + E_{\mu})/kT \right] \qquad 3.25$$

where equations 3.22 and 3.25 are the expressions given in the MD model for extended and localised state conduction respectively. Also, as in the case of the MD model, the energy distribution of the localised states is replaced here by a constant value. In fact, only through this approximation, together with the assumption of a single, energy and temperature independent, hopping activation energy, E_{μ}, can the singly activated process of equation 3.25 be obtained.

Similarly, the total thermoelectric power for the system is given by equation 3.4 of Section 3.1,

$$\text{i.e.} \quad S = \frac{S_{ext}\sigma_{ext} + S_{loc}\sigma_{loc}}{\sigma} \qquad 3.4$$

where, again, S_{ext} and S_{loc} are given by equations 3.29 and 3.30 of the MD model.

$$\text{i.e.} \quad S_{ext} = \frac{k}{|e|}\left[\frac{E_{FV,0}}{kT} - \frac{\gamma}{k} + A_{ext}\right] \qquad 3.29$$

$$\text{and} \quad S_{loc} = \frac{k}{|e|}\left[\frac{E_{FB,0}}{kT} - \frac{\gamma}{k} + A_{loc}\right] \qquad 3.30$$

From equations 3.3 and 3.4, using equations 3.22, 3.25, 3.29, and 3.30, a series of 'best fits' may be obtained to the various sets of conductivity and thermopower data, from which the following parameters are calculated: $E_{FV,0}$, $E_{FB,0}$, E_{μ}, C_{ext}, C_{loc}, A_{ext}, and A_{loc}.

The fitting procedure is now described: equation 3.3 is the sum of two exponentials, and it may be written as,

$$y = A\, e^{-\alpha x} + B\, e^{-\beta x} \qquad 3.33$$

where $\alpha = E_{FV,0}/k$, $\beta = (E_{FB,0}+E_{\mu})/k$ and $x = {}^{1}/T$.

Choosing four values of x in such a way that,

$$x_4 - x_3 = x_3 - x_2 = x_2 - x_1 = \Delta,$$

then four equations for y_1, y_2, y_3, and y_4 may be written down. These four equations may be reduced to a single quadratic equation, which is given by,

$$(y_z^2 - y_2y_4)z^2 - (y_2y_3 - y_1y_4)z + (y_2^2 - y_1y_3) = 0 \qquad 3.33a$$

Solving the above equation for z, the two solutions give $e^{\alpha\Delta}$ and $e^{\beta\Delta}$. Since Δ is known, α and β, and hence $E_{FV,0}$ and $(E_{FB,0} + E_\mu)$, may be calculated.

Substituting the above values of α and β in any two of the expressions for y, the pre-exponential factors A and B (i.e. C_{ext} and C_{loc}) may be calculated.

Using the method described above, various estimates of the two pre-exponential constants and the two activation energies were obtained. The actual values of the parameters, however, varied slightly by choosing different x and/or Δ values at the start of the fitting procedure. The x and Δ values were usually selected so as to cover as broad a temperature range as possible, so that the resultant calculated parameters would be as representative of the material properties as could be obtained in the given experimental temperature span. The different sets of parameters thus obtained, however, fitted the experimental conductivity vs temperature data equally well.

The corresponding y value for each value of x selected was read off a smooth representative curve drawn through the given set of data points. A weakness of this procedure was that it was imperative to make sure that the representative curve was as smooth as possible with no sharp discontinuities in it. In case of even a relatively slight deviation by, for example, introducing a small kink in the curve at some point, it was sometimes found that absurdly large or small values were obtained for the four parameters of equation 3.33.

The value of A and B in this equation were particularly sensitive to the detailed shape of the curve drawn through the data points. This shortcoming in the analytical method is illustrated in Table 3.6 for the case of sample 8.2. Three pairs of selected sets of data points, together with their calculated conductivity parameters, are shown. Curve I in each pair had a slight discontinuity in it. Curve II was much smoother, although the actual variation in the value of σ for a given x is rather small (on a logarithmic scale in particular) compared to the value obtained from Curve I. Examining the last four columns of Table 3.6, the large variation in the values of the conductivity parameters calculated from the two curves can be noted especially in the first pair of data sets shown.

Applying the curve fitting procedure already described, a variety of sets of slightly different values for the four conductivity parameters (i.e. $E_{FV,0}$, $(E_{FB,0} + E_\mu)$, C_{ext}, and C_{loc}) were obtained from the conductivity vs temperature data collected in the case of each sample that was studied.

The next step in the calculation procedure was to discover which of the above sets of parameters fitted the thermopower data just as well. In each case this was done by substituting the already calculated parameters into equation 3.4 for the thermopower. Examining expressions 3.29 and 3.30 for S_{ext} and S_{loc}, it will be noticed that a knowledge of the values of E_μ (so that $E_{FB,0}$ may be obtained from $(E_{FB,0} + E_\mu)$), A_{ext}, and A_{loc} is necessary. In fact the values of these three parameters were continuously changed until either a good fit to the experimental thermopower data was obtained,

Curve No.	$10^3/T_1$ K^{-1}	σ_1 $\Omega^{-1}cm^{-1}$	$10^3/T_2$ K^{-1}	σ_2 $\Omega^{-1}cm^{-1}$	$10^3/T_3$ K^{-1}	σ_3 $\Omega^{-1}cm^{-1}$	$10^3/T_4$ K^{-1}	σ_4 $\Omega^{-1}cm^{-1}$	$E_{FV,0}$ eV	$E_{FB,0} + E_{eV^{\mu}}$	C_{ext} $\Omega^{-1}cm^{-1}$	C_{loc} $\Omega^{-1}cm^{-1}$
I	3.0	1.79×10^{-6}	3.7	1.56×10^{-8}	4.4	1.79×10^{-10}	5.1	2.08×10^{-12}	0.95	0.55	8.9×10^{7}	259
II	3.0	1.67×10^{-6}	3.7	1.56×10^{-8}	4.4	1.67×10^{-10}	5.1	2.08×10^{-12}	0.60	0.50	1609	12
I	3.2	4.31×10^{-7}	3.9	4.29×10^{-9}	4.6	4.95×10^{-11}	5.3	6.13×10^{-13}	0.66	0.53	6762	115
II	3.2	4.31×10^{-7}	3.9	4.17×10^{-9}	4.6	4.76×10^{-11}	5.3	6.13×10^{-13}	0.62	0.52	2922	41
I	3.2	4.31×10^{-7}	4.0	2.27×10^{-9}	4.8	1.39×10^{-11}	5.6	1.11×10^{-13}	0.57	0.45	782	0.5
II	3.2	4.31×10^{-7}	4.0	2.17×10^{-9}	4.8	1.35×10^{-11}	5.6	1.11×10^{-13}	0.59	0.47	1212	1.7

Table 3.6. Variation of Conductivity Parameters with Conductivity Curve Selection in Sample 8.2

or it was found that no theoretical fit was possible. In all the cases studied, only one or two sets of conductivity parameters were found to fit both the experimental conductivity and thermopower data just as well. In the cases where two sets of conductivity parameters could be fitted to the Seebeck data, it was found that the values of $E_{FB,O}$ and $E_{FV,O}$ computed from them were the same to the second decimal place, and that the C_{ext}, C_{loc}, A_{ext}, A_{loc} values computed from the two different fits were similar in their magnitudes.

In all the fitting calculations, the experimental value of $\gamma = 3.1 \times 10^{-4}$ eVK^{-1}, which had been corrected for diffuse reflection losses, was used. Using the uncorrected value of $\gamma = 3.6 \times 10^{-4}$ eVK^{-1} will not, in any case, make a significant difference to the thermopower parameters: in equations 3.29 and 3.30, the quantities $\left[\frac{E_{FB,O}}{kT} + A_{loc}\right]$ and $\left[\frac{E_{FV,O}}{kT} + A_{ext}\right]$ are both considerably larger than the change introduced into the value of $(-\frac{\gamma}{k})$ by using the uncorrected γ. Hence the net effect would be slightly larger A_{loc} and A_{ext} values to off-set the use of the larger γ.

Figures 3.24 and 3.25 show the computed conductivity and thermopower curves (full lines) as fitted to the experimental points. In both figures, the fitted data for one sample from each of the three compositions in the series Ch_xY_{100-x} is shown. The fits to the data from the other samples were equally as good as those illustrated in the above figures.

Figure 3.26 summarizes, in the form of a flow chart, the method used in the NCD analysis.

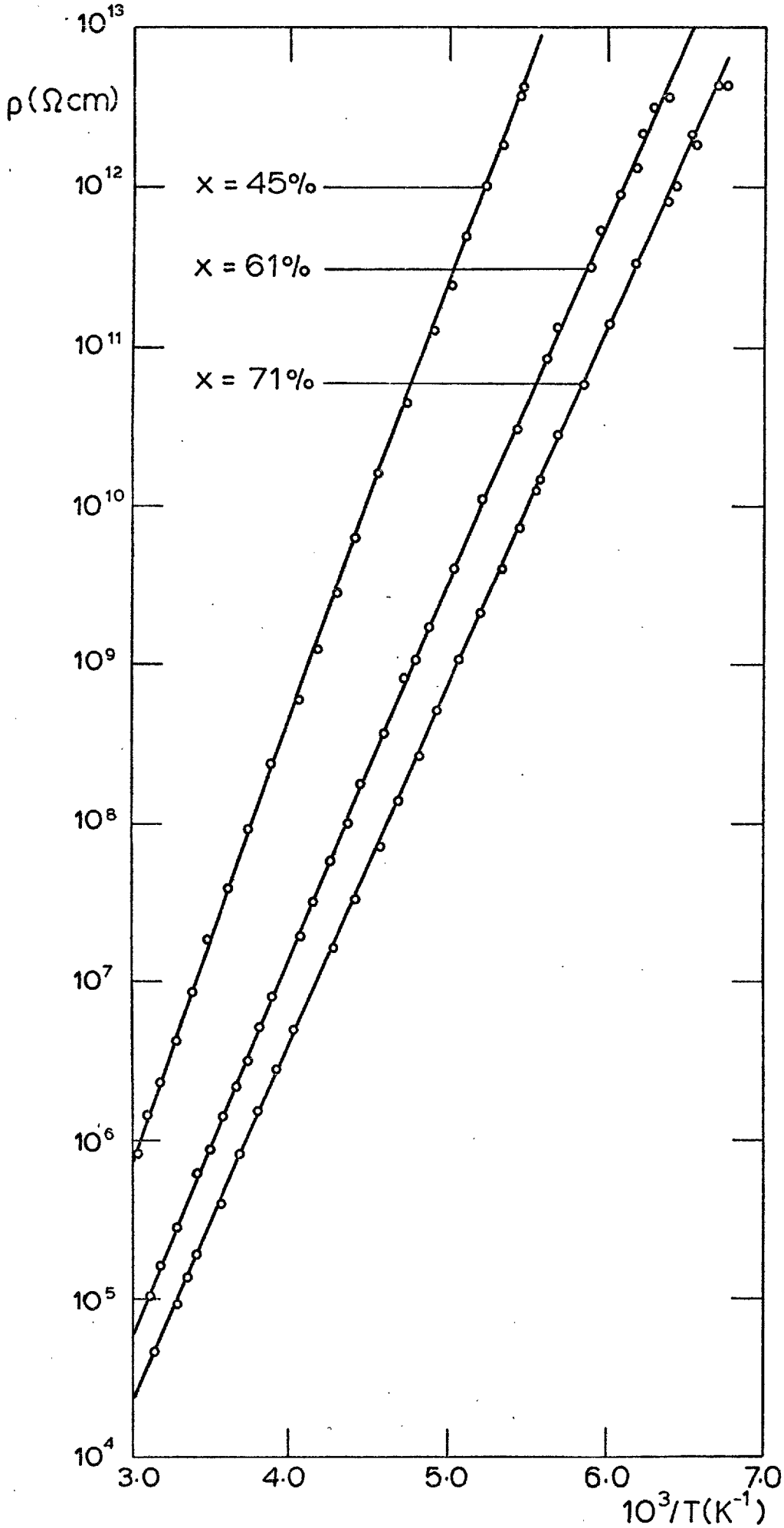


Fig. 3·24: Curved fits (solid lines) to the experimental resistivity *vs.* temperature data of Ch_xY_{100-x} SeTAG glasses using the NCD model

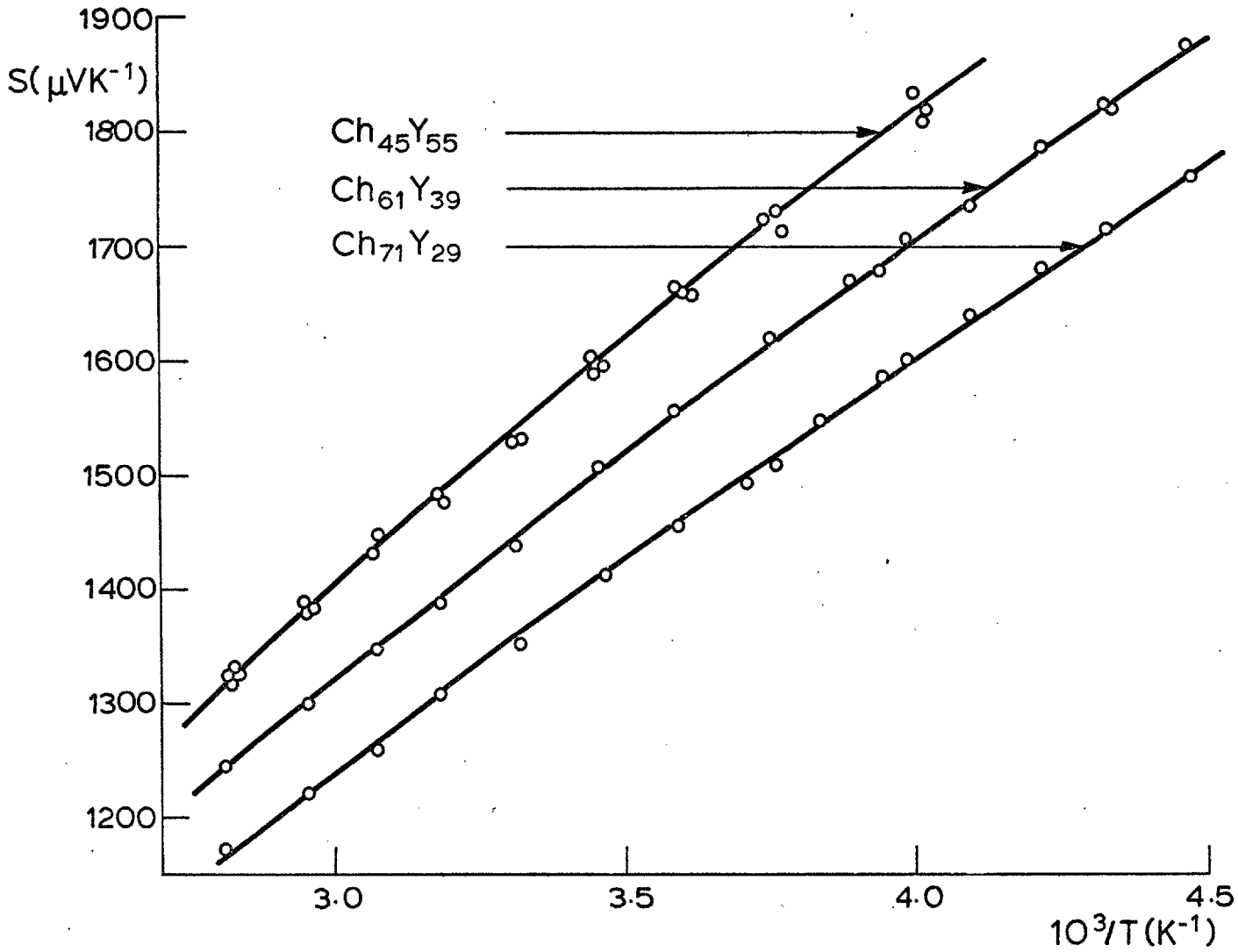


Fig.3·25: Curved fits (solid lines) to the experimental thermoelectric power *vs.* temperature data of Ch_XY_{100-X}SeTAG glasses using the NCD model.

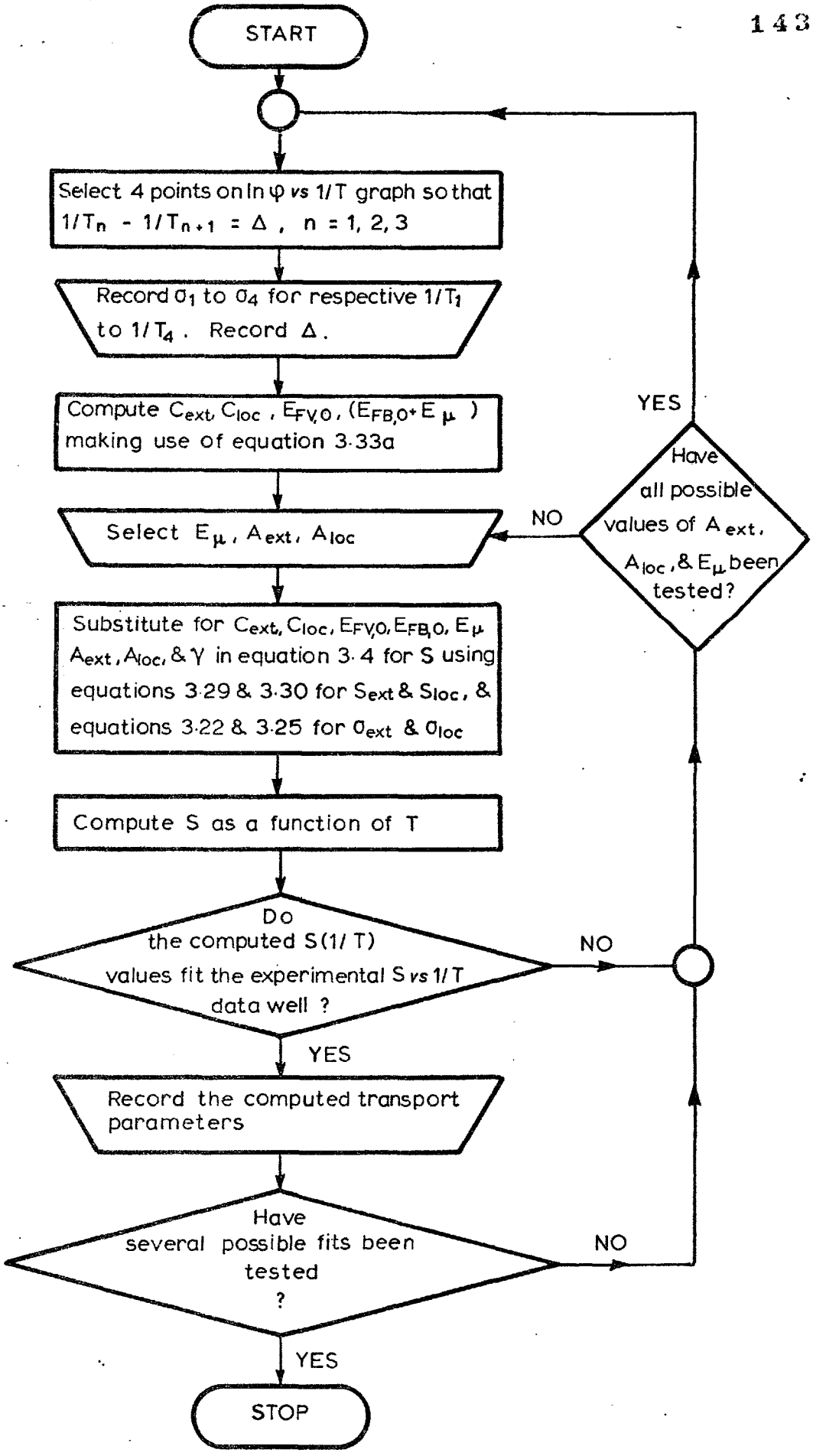


Fig. 3·26: A flow chart of method used in the NCD analysis

It would be interesting to examine how much the localised states contribute to the overall conduction process in SeTAG glasses. Figure 3.27 graphically illustrates this contribution, where, the ratio σ_{loc}/σ is plotted against the inverse of absolute temperature for all the samples whose data were analysed by the NCD model. Although a broad general trend is evident, the data are insufficient to illustrate any definite trends in the contribution of hopping conduction to the overall conduction process. In Figure 3.27, it can be seen that the hopping conductivity term contributes from about 38% at 333 K, to about 95% at 145 K, to the total measured conductivity in SeTAG glasses. The most important point about this plot is that even above room temperature, a substantial proportion of conduction takes place in the localised states. In Nagels etal's Si-As-Te glasses, it was found that at 370 K roughly 29% of the total conductivity was due to σ_{loc}, whilst σ_{ext} contributed about 25% to the total conductivity at 210 K, which is approximately the same as SeTAG glasses.

In Table 3.7, the values of various conductivity and thermopower parameters, computed using the NCD model, are listed. In the case of glasses of $Ch_{61}Y_{39}$ composition, no comprehensive set of conductivity and thermopower data were obtained from the same ingot. Consequently, the transport parameters computed from the conductivity vs temperature data of ingot 3 were fitted to the thermopower vs temperature results of ingots 7 and 10 (both of $Ch_{61}Y_{39}$ composition). Also, it was found that in some cases, it was possible to obtain equally good theoretical fits to the Seebeck coefficient data by assuming different values of E_μ, the activation energy for hopping. The instances, in which the value of E_μ could be varied without a significant deterioration

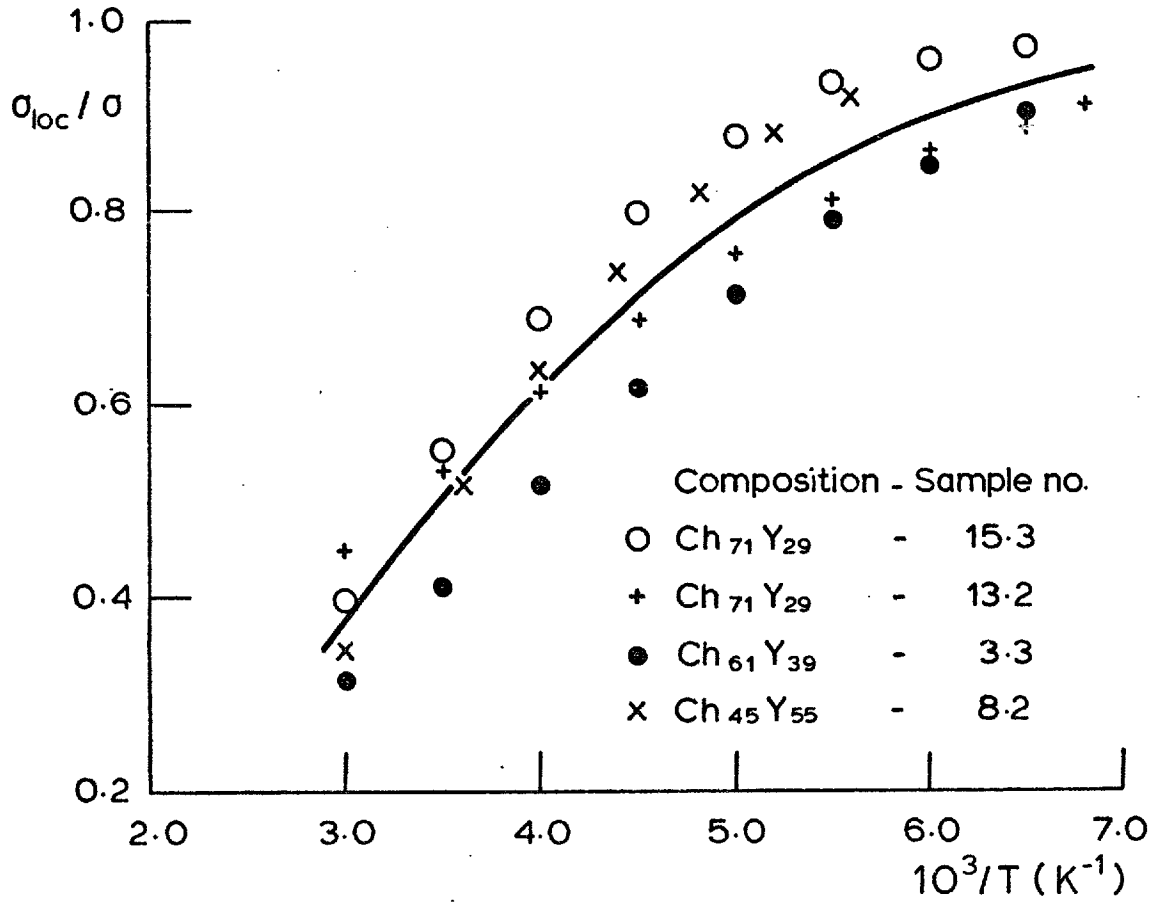


Fig. 3·27: The ratio of localised band tail hopping conductivity to total conductivity as a function of temperature in SeTAG glasses computed using the NCD model.

Composition	Ingot No.	$E_{FV,0}$ (eV)	$E_{FB,0}+E_{\mu}$ (eV)	E_{μ} (eV)	$E_{FB,0}$ (eV)	$(E_B-E_V)_{T=0}=E_{FB,0}-E_{FV,0}$ (eV)	C_{ext} ($\Omega^{-1}cm^{-1}$)	C_{loc} ($\Omega^{-1}cm^{-1}$)	A_{ext}	A_{loc}
$Ch_{71}Y_{29}$	15	0.50	0.41	0.01	0.40	0.10	5017	91	0.9	0.8
$Ch_{71}Y_{29}$	13	0.49	0.43	0.02	0.41	0.08	753	83	2.8	0.7
$Ch_{71}Y_{29}$	13	0.49	0.43	0.03	0.40	0.09	753	83	2.6	1.3
$Ch_{61}Y_{39}$	3 + 10	0.51	0.44	0.02	0.42	0.09	849	31	2.3	0.6
$Ch_{61}Y_{39}$	3 + 10	0.51	0.44	0.03	0.41	0.10	849	31	2.2	1.1
$Ch_{61}Y_{39}$	3 + 7	0.51	0.44	0.02	0.42	0.09	849	31	2.5	1.0
$Ch_{61}Y_{39}$	3 + 7	0.51	0.44	0.03	0.41	0.10	849	31	2.5	1.5
$Ch_{45}Y_{55}$	8	0.62	0.52	0.04	0.48	0.14	2493	37	0	0

Table 3.7. Transport Parameters in Bulk Ch_xY_{100-x} SeTAG Glasses computed using the NCD Model

in the goodness of fit to the Seebeck coefficient data, are also listed in Table 3.7. It was not possible, however, to obtain any theoretical fits to the experimental results if the value of E_μ was allowed to increase above 0.04 eV.

The computed values of A_{ext} and A_{loc} are also listed in this table. There does not seem to be any systematic variation in the values of these parameters, except that in all instances $A_{ext} \geq A_{loc}$, which is what is to be expected. This lack of any coherence in the variation of the values of A_{ext} and A_{loc} between ingots of nominally the same composition (compare, for example, the values obtained for ingots 13 and 15), and with various compositions, is quite puzzling. It can certainly be said that this is not due to any errors in the experimental determination of the Seebeck coefficient which would influence the A values. Ingots 7 and 10 have different Seebeck coefficients (see Figure 3.14), but their A_{ext} and A_{loc} values are quite similar. It should be mentioned that NCD's values of $A_{ext} = 1$ and $A_{loc} = 0$ did not give any good fits at all to the experimental results.

Examining the values of C_{ext} and C_{loc} in Table 3.7, it is noted that, although the values are quite reasonable, ratios of C_{ext}/C_{loc} are rather smaller than the theoretical estimates of about 100-1000. As already mentioned, the values of these two pre-exponentials are very sensitive to the detailed shape of the curve which is passed through the experimental conductivity vs temperature points. It is thought that any conflict between theoretical predictions and calculated values of $\frac{C_{ext}}{C_{loc}}$ is possibly due to the failure to pass the "best"

curve through the experimental points.

Finally, inspecting the variation in the energy separation of E_B and E_V from E_F, it can be seen from Table 3.7 that there is a general increase in $(E_F - E_B)$ and $(E_F - E_V)$ with increasing percentage of As and Ge atoms in the glass composition. There is also a general, though small, increase in $(E_B - E_V)$ with increasing non-chalcogen content of the glass. This behaviour has also been observed by Nagels etal[8] in Si-Te-As glasses, and by Marshall etal[10] in As_2Te_3 and $Si_{12}Te_{48}As_{30}Ge_{10}$ glasses. In SeTAG, as in the materials studied by the two groups of workers cited above, there is a general increase in the width of the localised band tail as more disorder is introduced into the chalcogen network.

From the values of the pre-exponential constants listed in the above Table, the effective densities of extended and localised states may be calculated.

From equations 3.20 and 3.22 for conduction in the extended valence states,

$$C_{ext} = N_V . e . \mu_{ext} \; e^{\gamma/k}$$

where N_V is the effective density of states (cm^{-3}) in the valence band. Therefore,

$$N_V = \frac{C_{ext} \; e^{-\gamma/k}}{e\mu_{ext}} \qquad 3.34$$

where μ_{ext} is given by equation 3.23, i.e.,

$$\mu_{ext} = \frac{1}{6} \, e \, \nu_{el} R^2/kT$$

Taking T = 300 K, R = 3 Å, $\nu_{el} = 3 \times 10^{15}\ s^{-1}$, and $\gamma = 3.1 \times 10^{-4}$ eVK^{-1},

$$\mu_{ext} = 17.4\ cm^2\ V^{-1}\ s^{-1} \qquad 3.35$$

$$\text{and } N_V = 9.8 \times 10^{15}\ C_{ext} cm^{-3} \qquad 3.36$$

Similarly, using equations 3.24 to 3.26 for μ_{hop}, σ_{loc}, and C_{loc} respectively, the effective density of states, N_B, in the localised valence states is,

$$N_B = \frac{C_{loc} \cdot e^{-\gamma/k}}{e\mu_{o,hop}} \qquad 3.37$$

Using the above given values for T, R, and γ, and taking $\nu_{ph} = 10^{12}\ s^{-1}$,

$$\mu_{o,hop} = 5.8 \times 10^{-3}\ cm^2 V^{-1} s^{-1} \qquad 3.38$$

$$\text{and} \quad N_B = 2.9 \times 10^{19} . C_{loc}\ cm^{-3} \qquad 3.39$$

It should be noted that the effective densities of states, N_V and N_B, are both functions of temperature. For example, if the density of valence states varied as E^m, then N_V would vary as $(kT)^{m+1}$. In other words, for a constant density of states (i.e. m = 0), N_V will vary linearly with kT. The same argument would also apply to N_B.

Using equations 3.36 and 3.39, the N_B and N_V values listed in Table 3.8 are obtained. N_B and N_V have also been computed from NCD's data [8] on Si-As-Te glasses*. Examining these parameters, $N_V \sim 2.2 \times 10^{19}$ cm^{-3}, and $N_B \sim 1.8 \times 10^{21}\ cm^{-3}$ are obtained in SeTAG glasses. For

---

*NCD's value of $\gamma = 2.5 \times 10^{-4}$ eV K^{-1} was used here.

Composition	Sample No.	C_{ext} ($\Omega^{-1}cm^{-1}$)	C_{loc} ($\Omega^{-1}cm^{-1}$)	$N_V \times 10^{19}$ (cm^{-3})	$N_B \times 10^{21}$ (cm^{-3})
$Ch_{71}Y_{29}$	15.3	5017	91	4.9	2.7
$Ch_{71}Y_{29}$	13.2	753	83	0.74	2.4
$Ch_{61}Y_{39}$	3.3	849	31	0.83	0.91
$Ch_{45}Y_{55}$	8.2	2493	37	2.4	1.1
$Si_{15}As_{34}Te_{51}$	---	3200	70	6.3	4.2
$Si_{10}As_{36}Te_{54}$	---	3000	90	5.9	5.3
$Si_{5}As_{38}Te_{57}$	---	3800	92	7.5	5.5
$Si_{2}As_{39.2}Te_{58.8}$	---	2700	90	5.3	5.3
$Si_{1}As_{39.6}Te_{59.4}$	--	3200	90	6.3	5.3

Table 3.8. Room Temperature Effective Densities of Extended and Localised Valence States in Ch_xY_{100-x} SeTAG Glasses, and in Si-As-Te Glasses (Calculated from the Results of Nagels etal [8]).

NCD's Si-As-Te glasses, the corresponding values are $N_V \sim 6 \times 10^{19}$ cm^{-3} and $N_B \sim 5.1 \times 10^{21}$ cm^{-3}. It can be seen that, for both these glasses, N_B is greater than N_V by roughly two orders of magnitude, which is highly unexpected. Even if it is assumed that the computed C_{loc} values (and hence N_B) are too high, and the predicted [1] value of $C_{loc} \sim 1$ $\Omega^{-1}cm^{-1}$ is used instead, one would still obtain $N_B \sim 2.9 \times 10^{19}$ cm^{-3}

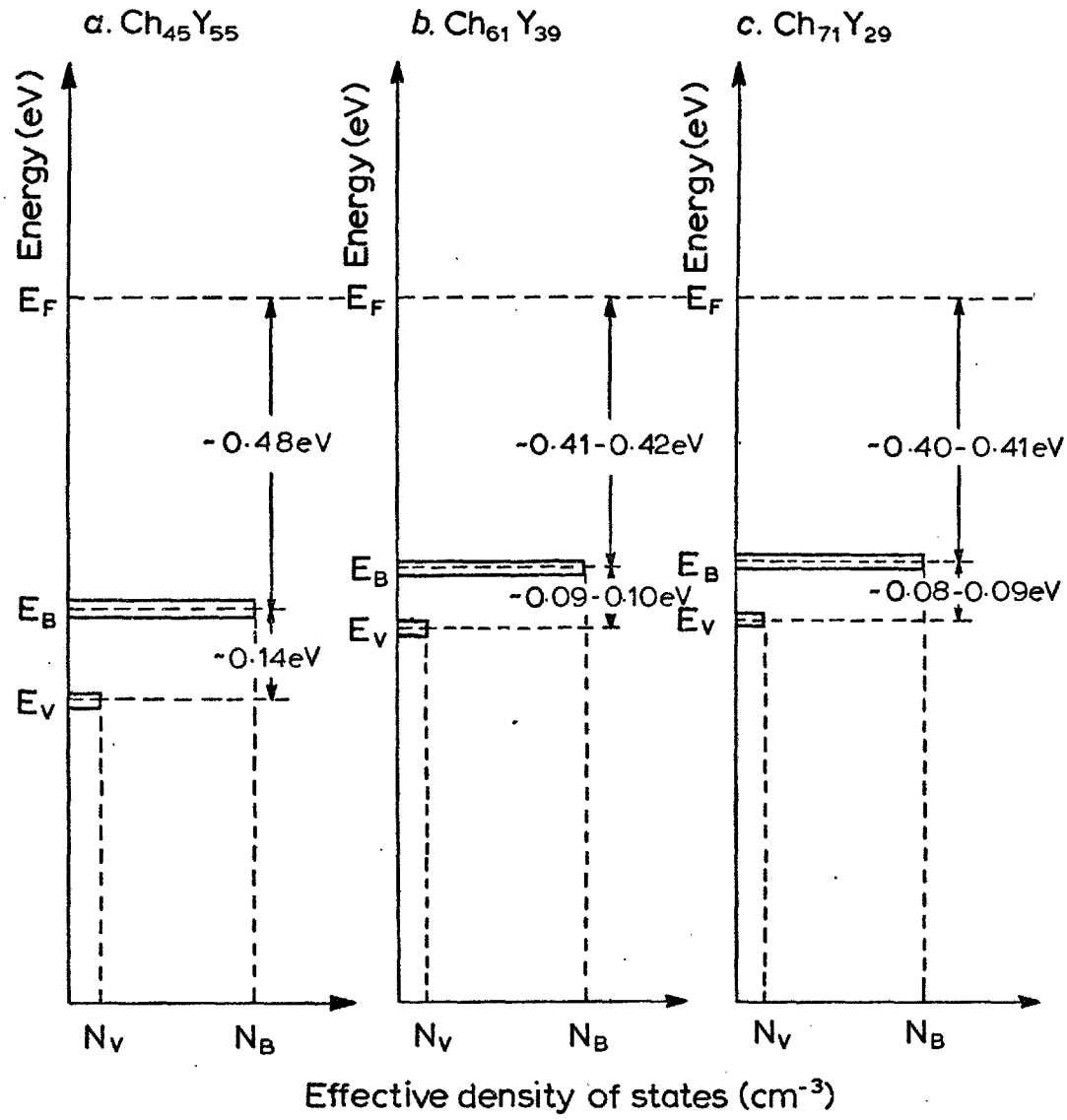
for SeTAG, and $N_B \sim 5.9 \times 10^{19}$ cm^{-3} for Si-As-Te glasses, which are still quite high.

It is, therefore, evident that the Mott and Davis model, where a continuous decrease in the density of states from the mobility edge at E_V to the localised band edge at E_B is envisaged, would be in conflict with the N_V and N_B values calculated for SeTAG and Si-As-Te glasses. In other works, since $N_B > N_V$, the density of states would peak at some energy close to the top of the localised band tail at E_B.

Figure 3.28, which summarizes the experimental data as analysed by the NCD model, shows the effective state densities dominating the conduction processes in the extended valence band and the localised states. The variation in the energy distributions of the above two sets of states with composition is also shown.

3.8. Discussion and Conclusions.

The electrical properties of bulk SeTAG glasses in the series Ch_xY_{100-x} have been investigated by making dc conductivity, thermoelectric power, and optical absorption and reflection measurements on these glasses. The optical measurements on the $Ch_{61}Y_{39}$ glass, from which the temperature coefficient of the gap was deduced, were used in the subsequent calculations on all three different compositions in the Ch_xY_{100-x} glasses that were studied. If, however, the variation of the temperature coefficient of the gap with composition is large, this would seriously affect the subsequent analysis of the results. Such large variation is not likely if one considers that the temperature coefficients of most amorphous alloys containing two or more of the constituent elements of SeTAG which have been



$N_V \sim 2{\cdot}2 \times 10^{19} cm^{-3}$

$N_B \sim 1{\cdot}8 \times 10^{21} cm^{-3}$

Fig. 3·28: The energy distribution of the states dominating the conduction processes and their effective densities at 300K as a function of composition in Ch_xY_{100-x}SeTAG glasses determined using the NCD model.

measured, lie approximately in the 4-8 x 10^{-4} eV K^{-1} region.

Examining the temperature dependence of conductivity and thermopower in SeTAG (Figures 3.5 and 3.14), it is clear that both sets of results show some curvature.

Analysing the above data in terms of the GLG model, where the energy dependence of the density of states and of the mobility were accounted for by the introduction of a temperature dependent pre-exponential factor in the conductivity expression (3.32), three difficulties are encountered:

(1) Changing the parameter p in the above expression, has little effect on the fit of the theoretical curve to the experimental data.

(2) It is impossible to separate the energy dependence of the density of states and that of the mobility.

(3) The energy dependence of the mobility and the density of states enter expression (3.6) for thermopower in the form of an additional constant independent of temperature, as has been shown by Fritzsche [38],[44]. He finds A = 1 in equation (3.6) if both the mobility and the density of states are independent of energy, A = 2 for $N(E)_{\mu}(E) \propto E$, and A = 3 for $N(E)_{\mu}(E) \propto E^2$. Under these circumstances, the thermopower should still give a straight line when plotted against $^1/T$, which would be incompatible with the experimental data on SeTAG.

In examining the data in terms of the Mott and Davis model, it should be noted that these authors point out [1] that equations 3.22 and 3.25 for extended states and localised band conductivity, and expressions 3.29 and 3.30 for extended and localised states thermopower, respectively, are in general only valid over a limited

range of temperature, and the possibility of parallel conduction taking place in the above two sets of states is not ruled out. The so called NCD model, used to analyse the experimental results of this Chapter, sets out exactly to take account of this possibility.

The transport parameters, evaluated by analysing the data in terms of the NCD model, raise a number of important points, which will now be discussed in turn:

(1) The method of analysis used in the NCD model is rather unreliable: any slight deviations from the smooth curves drawn through the plots of ln σ vs. $^{1}/T$, could result in widely different, and sometimes totally unrealistic, estimates of C_{ext}, C_{loc}, $E_{FV,0}$, and $(E_{FB,0} + E_{\mu})$ - Table 3.6 illustrates this point. It is suggested that, in any future calculations using the NCD model, the possibilities of an alternative method which is independent, or at least less dependent, on the four experimental points selected for the evaluation of the above parameters, should be seriously examined.

(2) The ratios C_{ext}/C_{loc} vary from 9 to 67, which are lower than the theoretical estimates [1],[35] of about 1000. This may be due to the weakness in the analytical method described above, although Mott, Davis, and Street [47] point out that continuous and smooth curvatures (as opposed to a sharp 'kink') in plots of ln σ vs $^{1}/T$ and S vs $^{1}/T$ would result only if the C_{ext}/C_{loc} ratio is small.

(3) The computed values of A_{ext} and A_{loc} are quite inconsistent, and no systematic variation is observed. No positive explanation can be given for this behaviour, especially since there seems to be quite large variations in the 'A' values in different ingots of the

same composition (see Table 3.7). The only concrete conclusions which may be drawn are that $A_{ext} \geq A_{loc}$, and that $0 \leq A_{ext} \leq 3$.

(4) The evaluation of the effective densities of states N_V and N_B, at E_V and E_B respectively, yields $N_B > N_V$ for both SeTAG and NCD's Si-As-Te glasses ($N_V \sim 2.2 \times 10^{19}$ cm^{-3}, $N_B \sim 1.8 \times 10^{21}$ cm^{-3} in SeTAG, and $N_V \sim 6 \times 10^{19}$ cm^{-3}, $N_B \sim 5.1 \times 10^{21}$ cm^{-3} in Si-As-Te). As already pointed out in paragraph (2) above, the ratio C_{ext}/C_{loc} is small. This would explain the rather large N_B values listed in Table 3.8, because of the large C_{loc} values compared to the predicted $C_{loc} \sim 1\ \Omega^{-1}$ cm^{-1}.

The fact that N_B has been found to be larger than N_V by approximately two orders of magnitude in two rather different groups of chalcogenide glasses, points to an important weakness in the NCD model, especially that $N_B \sim 1.8 \times 10^{21}$ cm^{-3} is too large to be physically realistic at an energy which is only 0.1 eV higher than N_V.

At this point, it might be appropriate to comment upon the work of Marshall and Owen [10] on thin films of α - As_2Te_3 and STAG glasses where measurements of dc conductivity and drift mobility (using a transient photo-conductive method) were made. They conclude that at high temperatures ($T > 200$ K), charge transport is via holes moving at the mobility edge ($E_{FV,0} = 0.54$ eV for STAG, 0.44 eV for As_2Te_3) with occasional trapping by a set of localised states (0.22 eV from the Fermi level), which may or may not be part of the localised band tail. At low temperatures, carrier hopping, with a mobility activation energy of about 0.05 eV, takes place in a second set of localised levels 0.13 eV from E_F.

Mott etal.[47] have examined the results of Nagels etal. and Marshall and Owen in some detail. They conclude that the deep localised levels observed by the latter are due to the "extrinsic" nature of the material (i.e. due to dangling bonds, which are sensitive to the method of preparation and heat treatment). They support this argument by the straight line $\ln \sigma$ vs $^{1}/T$ plots observed in bulk STAG glasses as reported by Marshall and Owen (c.f. the curvature observed in thin films of STAG), which they also interpret as evidence against small polaron hopping proposed by Emin etal.[4]. In the small polaron picture, the decrease in the slope of $\ln \sigma$ vs $^{1}/T$ plot would no longer be associated with any defects, which would be sensitive to the method of preparation of the glass, but it would simply be due to the disappearance of the polaron hopping energy terms at low temperatures. Levy[14] has measured the dc conductivity of bulk STAG glasses of near identical compositions to Marshall etal's, and he observes a significant degree of curvature in the $\ln \sigma$ vs $^{1}/T$ plot in a similar temperature range. If Levy's results are correct (and, therefore, Marshall etal's incorrect), it would support the theory that any observed curvature in the above plots is "intrinsic" to the material, and independent of preparation methods etc. But, whether the change of slope is due to small polarons, or connected with the type of conduction envisaged in the NCD model, remains uncertain. Indeed, Mott etal. interpret the data of Nagels etal. as being associated with the intrinsic nature of the chalcogenide glass under study: any deep lying levels, which may be present, are not detected in the conductivity and thermopower measurements, except at very low temperatures, where, up to the present, no such measurements have been possible.

In all three conduction models (i.e. GLG, MD, and NCD) examined in this Chapter, one basic assumption made in all cases has been that the hopping activation energy is constant and independent of temperature except at very low temperatures. Grant and Davis [42], however, have argued that variable range hopping may be expected in the localised band tail. These authors assume, for the conduction band, an electronic density of states given by,

$$N(E) = C(E - E_A)^n$$

where C is a proportionality constant.

The maximum in the density of occupied states is given by,

$$E_m = E_A + nkT$$

Assuming a jump frequency of the form $\nu_{ph}\exp(-2\alpha R - E_\mu/kT)$, where both the average hopping length, R, and the hopping energy, E_μ, are functions of T, they find that, for various values of n, R is a decreasing function of T, whereas E_μ increases with T, and in both cases the temperature dependence increases with increasing n. It is found that the variation of mobility with $1/T$ may be written as,

$$\frac{d \ln\mu}{d(1/kT)} = -(n + 1) E_\mu$$

where $\ln\mu = A - BT^{-(n + 1)/4}$,

and B is a function of $(E_C - E_A)^{n/4}$.

It is apparent from the above expressions, that if variable range hopping prevails in the localised band tail, then from Arrhenius plots of $\ln\mu$ vs $1/T$, the computed hopping activation energies are

larger than the actual values by a factor depending on the value of n. Only in the case of a constant density of states, would the correct value of E_μ be computed from the above plots.

At this point, it should be noted that, in the NCD model, a constant density of states is effectively assumed. Otherwise, as shown in the GLG model, a temperature dependence in the pre-exponential factor would be expected. This is, in fact, probably the reason why the computed values of E_μ are of the order of 0.03 eV in SeTAG and Si-As-Te glasses, and in general agreement with the values predicted by Grant and Davis.

As mentioned earlier, the large values of N_B computed using the NCD model, tend to argue against parallel conduction taking place in the extended and localised valence states considering the basic assumptions envisaged in this model (i.e. constant densities of states in the extended and localised valence states, and a singly activated, temperature independent, hopping mobility activation energy). The possibility of parallel conduction is not totally ruled out, however, if some other form of energy dependent density of states and/or hopping mobility is assumed. In considering any such model, the resultant parameters should, nevertheless, be carefully examined to make sure that they are physically reasonable quantities. Ideally, new experiments should be designed in order uniquely to determine the energy dependence of the density of states and mobility. Conductivity and thermopower experiments alone do not allow one to determine these energy relationships.

The curvature in the conductivity and thermopower plots may possibly be explained by examining the temperature dependence of $(E_F - E_V)$.

In all the models that have been examined, it has been assumed that $(E_F - E_V)$ varies linearly with temperature, i.e.,

$$E_F - E_V = E_{FV.O} - \gamma T$$

where γ has been equated to be roughly equal to one-half the temperature coefficient of the optical gap.

Let us, for a moment, assume that the shift in the above energies is not linear with temperature, but that it varies as,

$$E_F - E_V = E_{FV,O} - \alpha\, T^n \qquad 3.40$$

where α is in eV K^{-n}, and n is the exponent determining the temperature dependence of $(E_F - E_V)$.

For conduction in the extended valence states, the expressions for conductivity and thermopower would then be given by,

$$\sigma = \sigma_{o,ext} \exp\left(\frac{\alpha T^{n-1}}{k}\right) \exp(-E_{\sigma o}/kT) \qquad 3.41$$

i.e. $$\ln\sigma = \ln\sigma_{o,ext} + \frac{\alpha T^{n-1}}{k} - \frac{E_{\sigma o}}{kT} \qquad 3.42$$

and $$S = \frac{k}{e}\left(\frac{E_{so}}{kT} - \frac{\alpha T^{n-1}}{k} + A\right) \qquad 3.43$$

Assuming that the type of temperature dependence given by equation 3.40 prevails, then for the correct values of α and n, plots of $(\ln\sigma - \frac{\alpha T^{n-1}}{k})$ vs $\frac{1}{T}$ using equation 3.42, and $(\frac{e}{k}S + \frac{\alpha T^{n-1}}{k})$ vs $\frac{1}{T}$ using equation 3.43, should give straight lines provided that conduction is taking place in the extended valence states only.

Such a fitting procedure was carried out on the experimental data of ingot 8 of $Ch_{45}Y_{55}$ composition. It was attempted to obtain straight line fits in the above plots by continuously varying

α and n, and using the experimental α and S values at various temperatures. The value of A in (3.43) was kept between one and two. It did not prove possible, however, to obtain satisfactory fits to the data by using this method. Two particular difficulties were encountered:

(1) Although the fits to S vs $^1/T$ data were reasonable, but using the same α and n values resulted in much poorer fits to the experimental ln σ vs $^1/T$ points.

(2) The values of α and n were not found to be unique for equally good fits to the experimental data. α could be varied numerically from 1×10^{-5} to 1×10^{-8}, while n varied from 1.1 to 1.9 for comparable fits.

It is interesting to note, however, that in all these fits, the computed value of $E_{\sigma o}$ was about 0.55 eV, while E_{so} was about 0.41 eV. The values of the pre-exponential constant, $\sigma_{o,ext}$, varied between 185 and 320 Ω^{-1} cm^{-1}.

In equation 3.40, the simplest possible form of temperature dependence for $(E_F - E_V)$ has been assumed, where the number of variable parameters, α and n, has been kept to a minimum. It is likely that using a different, and more elaborate form of temperature dependence, the fits to the experimental data could be greatly improved. All that can be said at this stage, is that there is no reason why $(E_F - E_V)$ should vary linearly with temperature. Indeed, it is likely that incorporating the above type of temperature variation into a parallel conduction model which considers conduction in both the localised and extended states, and which takes account of the energy dependence of the density of states and of the hopping mobility, would be able to explain conduction in multicomponent chalcogenide glasses in a satisfactory manner.

Appendix 3 A.

The GLG Model of the temperature Dependence of Conductivity in Amorphous Chalcogenide Semiconductors

The conductivity in a continuous band of states may be expressed as the integral

$$\sigma = e \int \mu(E) N(E) f(E)\, dE \qquad 3A.1$$

where the limits of the integral are determined by the energy limits of the band of states under consideration.

In the above expression, e is the electronic charge, $\mu(E)$ is the mobility, $N(E)$ is the density of states, and $f(E)$ is the Fermi factor.

In the MD model, it is effectively assumed that, for conduction dominated by electrons, the maximum denstiy of occupied states occurs at the localised band edge, E_A, for the case of conduction in the localised tail of states between E_A and E_C, and that the density of occupied states has its maximum at E_C when conduction takes place in the extended states above E_C. It is thus assumed that one of the two narrow bands of states at E_A or E_C dominate the conduction process, and that the other states in the localised band tail or in the extended conduction band make a negligible contribution to total conductivity, and they therefore treat the density of states in the localised band tail and in the conduciton band as being constant and independent of energy. It is also assumed that the mobility in the extended states is diffusive ($\mu \propto \frac{1}{T}$), and that it is thermally activated in the localised band tail, i.e. $\mu \propto \frac{1}{T} \exp(-E_\mu/kT)$.

In the GLG model it is attempted to account for the energy dependence of the density of states, and the possible variation of μ with energy,

The conductivity in the GLG model is computed by assuming a density of states shown in Figure 3A.1, where it is assumed that, for the purposes of the calculations, the extended and localised states can be defined by two separate bands, in which the tail of localised states are still confined to the range of energies between E_A and E_C in the conduction band tail (and E_B and E_V in the valence band tail). In computing the extended states conductivity, it is assumed that the number of occupied localised states at E_C (or E_V) are much smaller than the number of occupied extended states, and they may therefore be neglected.

Considering electron conduction in the localised states between E_A and E_C, the GLG model assumes $N(E)$ and $\mu(E)$ to be both function of energy, so that,

$$N(E) = A(E - E_A)^m$$

$$\mu(E) = B(T)(E - E_A)^m$$

where A and B(T) are proportionality constants, with B(T) being a function of temperature.

Assuming $E_A - E_F >> kT$, we can apply Boltzmann statistics,

$$\text{i.e.} \quad f(E) = \exp\left[-(E - E_F)/kT\right] \qquad (E \geq E_A)$$

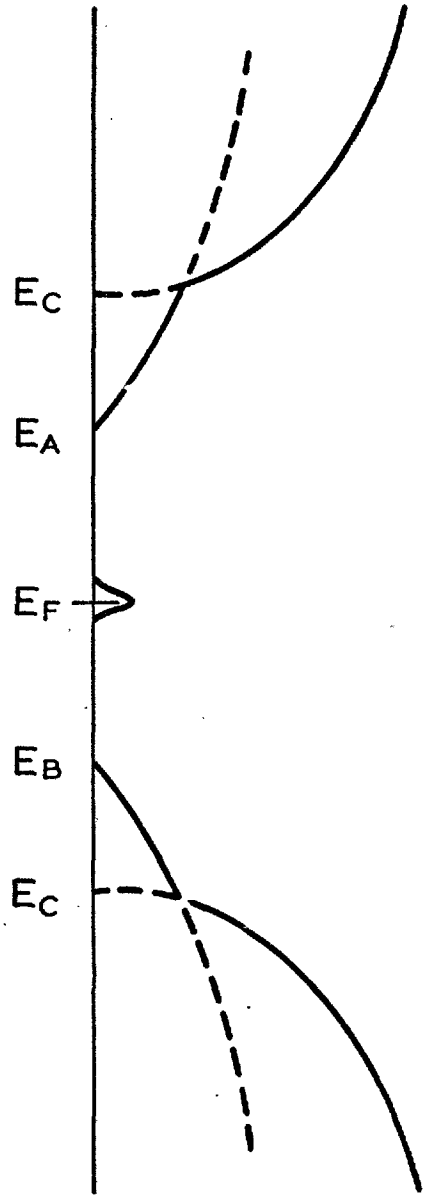


Fig.3a.1: The density of states model used in GLG's derivation of the expression for conductivity

Therefore, from equation 3A.1,

$$\sigma = \text{constant} \times \int_{E_A}^{E_C} (E - E_A)^{m+n} \exp\left[-(E - E_F)/kT\right] dE$$

where the "constant" outside the integral is a function of temperature.

Since most of the electrons in the band lie in the range of energies between E_A and E_C, replacing the upper limit of integration by infinity will introduce negligible errors into the calculations. Therefore,

$$\sigma = \text{constant} \times \int_{E_A}^{\infty} (E - E_A)^{m+n} \exp\left[-(E - E_F)/kT\right] dE$$

Let $\dfrac{E_A - E_F}{kT} = -\eta$

and $\dfrac{E - E_A}{kT} = X$

then $-\left(\dfrac{E - E_F}{kT}\right) = -(X - \eta)$

and $dE = kT\, dX$.

Making the above substitutions into the integral for σ, we get

$$\sigma = \text{constant}.e^{\eta}.\ (kT)^{m+n+1} \int_0^{\infty} X^{m+n}\, e^{-X}\, dX \qquad 3A.2$$

The above integral is the gamma function, which is defined as,

$$\Gamma(j) = \int_0^{\infty} X^{j-1}\, e^{-X}\, dX$$

where $\Gamma(j+1) = j\Gamma(j)$ $\Big)$ $j > 0$

In our case, $j - 1 = m + n$

i.e., $j = m + n + 1$

The gamma function has been tabulated for various j values. In Table 3A.1, below, the values of $\Gamma(j)$ for $0 \leq j \leq 5$ are given

j	j-1 = m+n	(j)
1	0	1
1.5	0.5	0.886
2	1	1
2.5	1.5	1.329
3	2	2
3.5	2.5	3.322
4	3	6
4.5	3.5	11.629
5	4	24

Table 3A.1. Variation of $\Gamma(j)$ with j for $0 \leq j \leq 5$

Therefore, substituting for $\Gamma(j = m + n + 1)$ from expression 3A.3 in equation 3A.2 for σ, we obtain,

$$\sigma = \text{constant} \times \exp\left[-(E_A - E_F)/kT\right] \cdot \Gamma(m+n+1) \cdot (kT)^{m+n+1} \qquad 3A.4$$

Similarly, for the case of conduction in the extended states above E_C, it can be shown that,

$$\sigma = \text{constant}.\exp\left[-(E_C - E_F)/kT\right] \cdot \Gamma(m+n+1)(kT)^{m+n+1} \qquad 3A.5$$

Now the pre-exponential "constant", which contains the temperature dependence of the mobility, is examined. Using the MD expressions for extended states and localised states mobility (equations 3.23 and 3.24),

$$\mu_{ext} \propto \frac{1}{T}$$

and

$$\mu_{hop} \propto \frac{1}{T} \exp\left(-\frac{E_\mu}{kT}\right)$$

For conduction in the extended states,

$$\sigma \propto T^{m+n} \exp\left[-\left(\frac{E_{\sigma o}}{kT}\right)\right] \qquad 3A.6$$

where $E_{\sigma o} = (E_C - E_F)_{T=0}$ 3A.7

The expression for conduction in the localised tail of states is identical to the above, except that $E_{\sigma o}$ is now written as,

$$E_{\sigma o} = (E_A - E_F)_{T=0} + E_\mu \qquad 3A.8$$

In writing equation 3A.6, it is assumed that $\Gamma(j)$ is a slowly varying function of j for small j, and it may therefore be treated as a constant, resulting in equation 3A.9 below.

i.e. $$\sigma = CT^p \exp\left[-\left(\frac{E_{\sigma o}}{kT}\right)\right] \qquad 3A.9$$

where C is a constant, and $p = m + n$

It can be seen from Table 3A.1, however, that this assumption may not be valid as j becomes larger than 3.

Identical expressions to 3A.9 may be derived for the case

of hole conduction in the extended and localised valence states. In these cases, $E_{\sigma o}$ is expressed as,

$$E_{\sigma o} = (E_F - E_V)_{T=0}$$ for hole conduction in the extended valence states.

$$E_{\sigma o} = (E_F - E_\mu)_{T=0} + E_\mu$$ for hole conduction in the localised tail of the valence band.

Appendix 3 B.

Thermocouple Calibration Procedure and Error Analysis

3B.1. Method of Calibration.

The ratio of the resistance of a standard platinum resistance thermometer at T K, $R_{Pt}(T)$, to its resistance at 273.15 K, $R_{Pt}(273.15)$, has been tabulated* from 13 K to 273 K.

The platinum resistance thermometer, and the Chromel/Alumel thermocouple which was to be calibrated, were mounted on a copper block, making sure that good thermal contact existed between the copper block, the thermocouple, and the resistance thermometer.

The copper block was mounted in the centre of a vacuum dewar flask, but it was kept well away from the dewar walls. The flask was equipped with a stirrer to minimise any temperature gradients when the measurements commenced, by stirring the contents of the dewar.

The thermocouple was first calibrated against the fixed temperature points already mentioned in Section 3.2 The measured resistance of the platinum thermometer at the ice point (273.15 K)

---

*International Practical Temperature Scale (1968), HMSO Publication No. SBN 11 480005 7.

was found to be 25.494 Ω (compared to the quoted value of 25.497 Ω in the IPTS (68) tables). The resistance of the thermometer was measured by applying a small voltage (a few mV) to it and measuring the voltage drop across it and the current passing through it.

Intermediate calibration points against the platinum resistance thermometer were obtained by filling the dewar with a mixture of methanal and water, and cooling the contents by small additions of liquid nitrogen. Continuous stirring ensured short equilibration times for temperature inside the flask, and also small temperature gradients.

It was found that over the range investigated (from 273.15 K down to 77.4 K), the thermocouple and platinum resistance thermometer readings agreed to within ± 0.6 K. During all the calibration procedure, the thermocouple "cold junction" was held at 273.15 K by immersing it in a container of melting ice, whose temperature was monitored by means of a calibrated mercury in glass thermometer.

3B.2. Calculation of Errors in the Platinum Resistance Thermometer Readings.

Since the variation of the resistance of the platinum thermometer with temperature is very nearly linear over the temperature range of interest, the temperature may be expressed as,

$$T = k \frac{R_{Pt}(T)}{R_o} \qquad 3B.1$$

where $R_o = kR_{Pt}(273.15)$, and k is a proportionality constant.

Let the voltage drop across the thermometer be V when a current I is passing through it. I was calculated by measuring the

voltage drop V, across a resistance R, connected in series with the platinum thermometer.

Equation (3B.1) may therefore be written as,

$$T = k' R_{Pt}(T) \qquad k' = \frac{k}{R_o}$$

$$= k' . V . R_1 . (V_1)^{-1} \qquad 3B.2$$

Therefore, the uncertainty, δT, in measuring the temperature, T, is given by,

$$\delta T \simeq k' \left[\frac{\partial T}{\partial V} . \delta V + \frac{\partial T}{\partial R_1} . \delta R_1 + \frac{\partial T}{\partial V_1} . \delta V_1 \right]$$

Differentiating the terms in the above equation using expression (3B.2),

$$\delta T \simeq k' \left[\frac{R_1}{V_1} . \delta V + \frac{V}{V_1} . \delta R_1 - \frac{V R_1}{V_1^2} . \delta V_1 \right] \qquad 3B.3$$

Dividing equation (3B.3) by (3B.2),

$$\frac{\delta T}{T} = \frac{\delta V}{V} + \frac{\delta R_1}{R_1} - \frac{\delta V_1}{V_1} \qquad 3B.4$$

Typical values of the above parameters and their uncertainties are,

$$R_1 = 10\ \Omega \pm 0.1\%$$

$$= 10\ \Omega \pm 0.01$$

$$V \simeq 4\ mV \pm 2.5\ \mu V$$

$$V_1 \simeq 2.5\ mV \pm 2.5\ \mu V$$

$$T \simeq 200\ K$$

Substituting the above in equation (3B.4),

$$\delta T = 200 \left[\pm \frac{2.5 \times 10^{-6}}{4 \times 10^{-3}} \pm \frac{2.5 \times 10^{-6}}{2.5 \times 10^{-3}} \pm \frac{0.01}{10} \right]$$

i.e. $\underline{\delta T \leq \pm 0.55 \text{ K.}}$

3B.3. To calculate the Errors in the thermocouple readings.

Assuming the thermocouple e.m.f., E, to vary linearly with temperature referred to the ice point, T_o, we can write,

$$E \simeq \alpha(T - T_o)$$

where α is the proportionality constant. Therefore,

$$\frac{dT}{dE} = \alpha^{-1}$$

$$dT = \alpha^{-1} dE$$

$$\frac{\delta T}{T - T_o} \simeq \frac{\delta E}{E}$$

$$\delta T \simeq (T - T_o) \frac{\delta E}{E}$$

Assuming the coldest temperature during the experiments to be $-150^{\circ}C$, where $E \simeq 4.8$ mV, and with $\delta E = \pm 2.5$ μV,

$$\delta T \simeq -150 \times \frac{\pm 2.5 \times 10^{-6}}{4.8 \times 10^{-3}}$$

i.e. $\underline{\delta T \leq \pm 0.1^{\circ}C}$

It follows, therefore, that since the platinum resistance thermometer readings were only accurate to about ± 0.55 K, and that the maximum recorded deviations between the thermocouple readings (accurate to $\pm 0.1^{\circ}C$) and the platinum thermometer readings were less than ± 0.6 K, then errors in the temperature measurements were less than ± 0.6 K.

Appendix 3 C.

The Effect of Diffuse Reflectivity losses on the Absorption Coefficient

It is desirable to account for the effect of neglecting transmission losses due to the diffuse reflectivity term, R_D.

Since R_D shows quite a pronounced wavelength or energy dependence (see Figure 3.19), it is reasonable to assume to a first approximation that the scattering centres giving rise to R_D are at an effective distance $\ell(\lambda)$ from the front face of the specimen, where $\ell(\lambda)$ is a function of the wavelength, λ, of the incident radiation. As shown in Figure 3C.1, the reflection from such a centre would be $(1 - R_S)e^{-\alpha\ell(\lambda)}$ and the fraction transmitted from the same centre would be $(1 - R_S)e^{-\alpha(d - \ell(\lambda))}$.

Hence the fraction of transmission lost through diffuse scattering would be,

$$T_D = \frac{2R_D}{(1 - R_S)e^{-\alpha\ell(\lambda)}} \cdot (1 - R_S)e^{-\alpha(d - \ell(\lambda))}$$

$$\text{Therefore,} \quad T_D = 2\,R_D e^{-\alpha(d - 2\ell(\lambda)}, \qquad 3C.1$$

The factor 2 in the above expression is to account for the fact that the diffuse reflectivity is being measured over π radians.

Examining the attenuation of radiation in the specimen, as illustrated in Figure 3C.2, $\ell(\lambda)$ is taken as an average distance into the specimen, so that,

$$T_\ell . d = \text{Area under the curve } (0 \leq x \leq d)$$

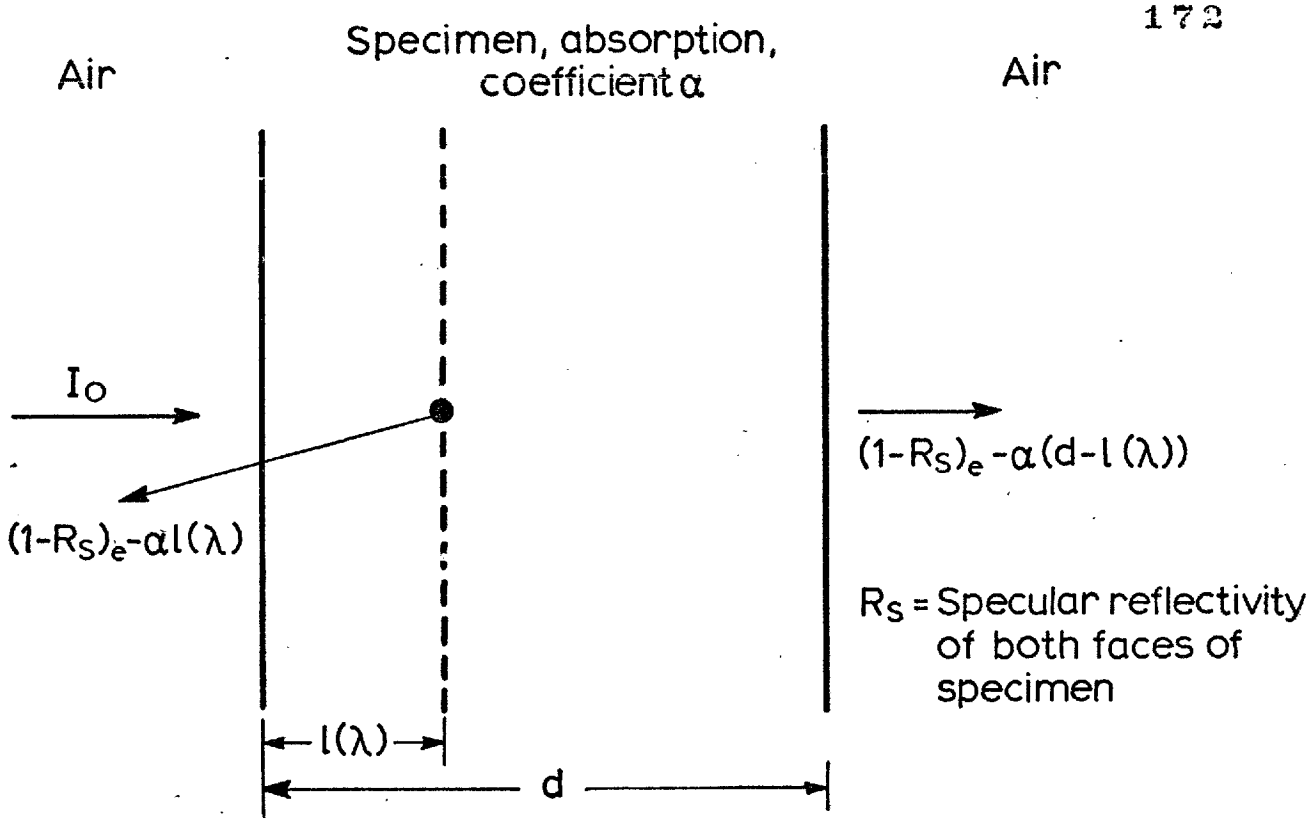


Fig. 3c.1: The fractions of reflected and transmitted radiation from a scattering centre of distance $l(\lambda)$ into a parallel faced slab of material of thickness d

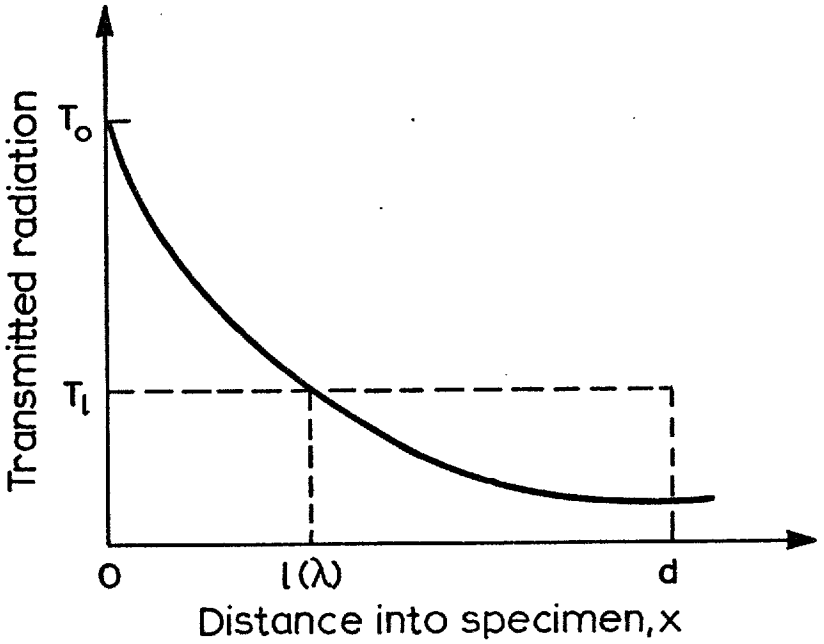


Fig. 3c.2: Attenuation of transmitted radiation in specimen of *Fig. 3c.1.*, showing the choice of $l(\lambda)$ so that $T_l \cdot d$ = Area under the curve $(0 \leqslant x \leqslant d)$.

where T_ℓ is the amount of transmission at $\ell(\lambda)$.

$$\text{i.e.} \quad T_\ell . d = T_o \int_0^d e^{-\alpha x} dx$$

where $$T_\ell / T_o = e^{-\alpha \ell(\lambda)}$$

$$\text{then,} \quad e^{-\alpha \ell(\lambda)} = \frac{1}{d} \left[- \frac{e^{-\alpha d}}{\alpha} \right] + \frac{1}{\alpha}$$

$$\text{and,} \quad e^{-2\alpha \ell(\lambda)} = \frac{1}{(\alpha d)^2} \left[1 - e^{-\alpha d} \right]^2 \qquad 3C.2$$

Substituting for $e^{-2\alpha \ell(\lambda)}$ from (3C.2) into (3C.1),

$$T_D = 2R_D e^{-\alpha d} \cdot \frac{(\alpha d)^2}{(1 - e^{-\alpha d})^2}$$

Now T_D is the correction to the <u>measured</u> transmission, T_m,

$$\text{i.e.} \quad T_m = (1 - R_S)^2 \, e^{-\alpha d} - T_D \qquad 3C.3$$

$$\therefore \quad \alpha = - \frac{\ln \left[(T_m + T_D)/(1 - R_S)^2 \right]}{d} \qquad 3C.4$$

where $T_m + T_D = T_{actual}$

An iterative procedure is developed, whereby α is calculated from $T = (1 - R_S)^2 \, e^{-\alpha d}$ and substituted in equation 3C.3, from which a new α value is found. This is substituted back in equation 3C.3 and the process repeated until, after a few iteration steps, the value of α is found to converge.

Chapter 3 - References.

1. N.F. Mott, E.A. Davis, Electronic Processes in Non-Crystalline Materials, Clarendon Press, Oxford, 1971.
2. M.H. Cohen, H. Fritsche, S.R. Ovshinsky, Phys. Rev. Lett., 22 (1969) 1065.
3. T. Holstein, Phil. Mag., 27 (1973) 225.
   L. Friedman, J. Non-Cryst. Solids, 6 (1971) 329.
   L. Friedman in Electronic and Structural Properties of Amorphous Semiconductors, edited by P.G. Le Comber and J. Mort, Academic Press, London, 1973.
4. D. Emin, C.H. Seager, R.H. Quinn, Phys. Rev. Lett., 28 (1972) 813.
5. H. Fritsche in Book of Ref. 3.
6. A. Wallace, J. Robertson, Inst. Phys. Conf. Ser., 22 (1974) 237.
7. M. Green, A.W. Levy, W. Gee, J. Phys. C., 7 (1974) 352.
8. P. Nagels, R. Callaerts, M. Denayer in Amorphous and Liquid Semiconductors, Taylor and Francis, 1974, Vol.II, 867.
9. T.C. Arnoldussen, C.A. Menezes, Y. Nakagawa, R.H. Bube, Phys. Rev., B 9 (1974) 3377.
10. J.M. Marshall, A.E. Owen, Phil. Mag., 31 (1975) 1341.
11. International Critical Tables, McGraw Hill Book Co. Inc., New York 1927, Vol.II, 53.
12. M. Green, A.W. Levy, W. Gee, Ming, P., J. Phys. D 5 (1972) L55.
13. A.J. Grant, K. Weiser, T.D. Moustakas, T. Penney III, Localised and Extended State Transport in Amorphous As_2Te_3, IBM Research Report No. RC 4323 (April, 1973).

13.(con.) T.D. Moustakas, K. Weiser, A.J. Grant, Thermoelectric Power of Liquid and Amorphous Semiconductors, IBM Research Report No. RC 4324 (April, 1973).

14. A.W. Levy, Ph.D. Thesis, 1972 , Council for National Academic Awards.

15. M. Green, A.W. Levy, J. Phys.C; 7 (1974) L126.

16. P. Nagels, R. Callaerts, M. Denayer, J. Non-Cryst. Solids, 4 (1970) 295.

17. H.K. Rockstad, R. Flasck, S. Iwasa, J.Non-Cryst. Solids, 8 - 10 (1972) 326.

18. K. Weiser, A.J. Grant, T.D. Moustakas in Amorphous and Liquid Semiconductors, Taylor and Francis, 1974, Vol. I, 335.

19. R. Callaerts, P. Nagels, M. Danayer, Phys. Lett. 38A (1972) 15.

20. R. Strunk, J. Non-Cryst. Solids, 12 (1973) 168.

21. C.H. Seager, R.K. Quinn, J. Non-Cryst. Solids, 17 (1975) 386.

22. H.L. Uphoff, J. App. Phys., 32 (1961) 950.

23. T.D. Moustakas, K. Weiser, Phys. Rev. B, 12 (1975) 2448.

24. T.D. Moustakas, K. Weiser, R. Gambino, A.J. Grant, Am. Phys. Soc. Bull., Ser II, 18 (1973) 131.

25. L. Vescan, C. Popescu, M. Teluic, N. Croitoru in Amorphous and Liquid Semiconductors, Taylor and Francis, 1974, Vol.II,761.

26. H.K. Rockstad, R. Flasck in Amorphous and Liquid Semiconductors, Taylor and Francis, 1974, Vol. II, 1311.

27. A.M. Andriesh, B.T. Kolomeits,Soviet Physics-Solid State, 6 (1965) 2652.

28. B.T. Kolomeits, E.M. Raspopova, Soviet Physics - Semiconductors, 5 (1972) 1346.

29. M. Cutler, N.F. Mott, Phys. Rev., 181 (1969) 1336.

30. R.F. Egerton, App. Phys. Lett., 19 (1971) 203.

31. A.R. Hilton, D.J. Hayes, J. Non-Cryst. Solids, 17 (1973) 339.

32. J.D. Dow, D. Redfield, Phys. Rev.B, 5 (1972) 594.

33. J.D. Dow, D. Redfield, Phys. Rev.B, 1 (1970) 3358.

34. J. Olley, Solid State Communications, 13 (1973) 1437.

35. E.A. Davis, N.F. Mott, Phil. Mag., 22 (1970) 903.

36. Amorphous and Liquid Semiconductors, J. Tauc (Editor), Plenum Press, 1974.

37. E.A. Davis in Amorphous and Liquid Semiconductors, Taylor and Francis, 1974, Vol. I, 519.

38. Electronic and Structural Properties of Amorphous Semiconductors edited by P.G. LeComber and J. Mort, Academic Press, London, 1973.

39. J.T. Edmund, Brit. J. App. Phys., 17 (1966) 979.

40. E.A. Fagen, H. Fritsche, J. Non-Cryst. Solids, 2 (1970) 170, Ibid. 4 (1970) 480.

41. A. Vancu, St. Sladaru, R. Grigorovici in Amorphous and Liquid Semiconductors, Taylor and Francis, 1974, Vol.I,631.

42. A.J. Grant, E.A. Davis, Solid State Communications, 15 (1974) 563.

43. N.F. Mott, J. Non-Cryst. Solids, 1 (1968) 1.

44. H. Fritsche, Solid State Communications, 9 (1971) 1813.

45. K. Weiser, M.H. Brodsky, Phys. Rev. B, 1 (1970) 791.

46. I.G. Austin, N.F. Mott, Advances in Physics, 18 (1969) 41.

47. N.F. Mott, E.A. Davis, R.A. Street, Phil. Mag. 32 (1975) 961.

Chapter 4

Preparation of Amorphous Thin Films of Se-Te-As-Ge

4.1. Introduction.

Three methods of preparing thin films (TF) of SeTAG glasses of $Ch_{61}Y_{39}$ composition were examined during the course of this work. These were:

(1) Knudsen cell evaporation

(2) D.C. sputtering

(3) Flash evaporation

For various reasons, to be discussed later, the flash evaporation method was finally chosen for the preparation of thin films of SeTAG, subsequently used in thin film electrical measurements (see Chapter 5).

The following topics are covered in this chapter:

(1) Problems encountered in preparing TF specimens of multicomponent chalcogenide glasses.

(2) Experimental techniques used in fabricating thin film samples by the three methods cited above, together with the merits and disadvantages of each method.

(3) TF compositional analyses by EPMA (electron probe micro-analysis)*, and ESCA** (electron spectroscopy for chemical analysis).

---

*Carried out on evaporated films only.

**Carried out on sputtered films only.

(4) Thin film structural studies by transmission electron microscopy of flash evaporated specimens.

(5) Fabrication of structures for electrical measurements.

Since any chalcogenide glass device with potential technological applications will most likely have to be made in the thin film form, the electrical and structural characterisation of chalcogenide glass films is of importance. This is not possible, however, unless a technique is developed, which is capable of fabricating thin films of a particular composition and structure reproducibly.

The study of electronic processes in thin films of chalcogenide glasses is also important in that some experiments cannot be carried out on bulk samples. For instance, the optical gap in chalcogenide glasses may only be absolutly determined on specimens which are less than 10 μm thick, since absorption coefficients greater than about 10^3 cm^{-1} may only be observed in samples thinner than this value. Field effect measurements on chalcogenide glasses are only possible on thin film samples, as it is only here that the relative change in conductance is large. The same goes for any other experiment, which relies upon the injection of excess change into the surface region of the specimen.

There are, however, some difficulties in preparing thin films of multicomponent chalcogenide glasses from the parent bulk glasses. The more important amongst these are the following:

(1) The vapour pressures of the constituent elements may vary considerably. For Se, Te, As, and Ge, the temperatures at which the vapour pressures of these elements is 0.1 mmHg (a typical vapour pressure at the boat mouth required to obtain a reasonable evaporation rate) are listed in Table 4.1.

Element	T(K) for vapour pressure = 10^{-1}mmHg
Se	570
As	590
Te	706
Ge	1830

Table 4.1. Temperature at which the Constituent Elements of SeTAG have Vapour Pressures of 10^{-1}mmHg.

On evaporating a thin film of SeTAG from the bulk glass, it can be seen that Se, for example, will evaporate much more easily, and at much lower temperatures, than Ge. This could result in the problems of fractionation (i.e. a thin film, which is compositionally different from the bulk specimen from which it was prepared), and compositional gradients into the film. It should be noted, however, that the evaporation of chalcogenide glasses may not take place by the vaporisation of the constituent atomic species alone, but molecular complexes may also be present in the vapour phase, although the vapour pressures of these complexes would be quite varied as well.

The method of flash evaporation, in which small grains of the bulk glass are dropped into a very hot boat, tends to overcome this problem by "instantaneously" vaporising all the constituent elements of the grain (i.e. the evaporation rate is faster than bulk diffusional motion). Electron beam evaporation performs the same task less efficiently, by focussing an intense electron beam onto a small area of the bulk sample, causing it to melt and vaporise. Bunton etal [1] found, however, that thin films of STAG glass prepared by this technique had large random variations in their compositions. This was

ascribed to the sensitivity of the film composition to the conditions of evaporation, and the focussing of the electron beam in particular.

(2) The problem of fractionation may also be encountered in sputtering of multicomponent glasses. It arises because different elements have different sputtering yields and sticking coefficients. Bosnell and Thomas[2] found that in DC sputtering of STAG glasses of $Si_{12}Te_{48}As_{30}Ge_{10}$ composition, there is a relatively small gain in the Te content, and a loss in Si because of its low sputtering yield. Owen[3] also reports small compositional changes on RF sputtering of STAG glasses. Bunton[1], who found a loss of Te in RF sputtered STAG glass film, observed considerable compositional variations from one film to the next.

Bolker etal[4] have examined the effects of RF cosputtering and the control of film temperature and bias conditions on the composition of Ge-As-Te films. They found that in the low Ge content films, the composition could be controlled effectively by variation of the deposition parameters, and that Te had a lower sticking coefficient than As and Ge, and therefore resputtered preferentially.

(3) The high vapour pressures of the chalcogen elements and As cause the "spitting" of the unmolten grains from the source material onto the substrate. This phenomenon, observed both in open boat thermal evaporation, and in flash evaporation if no adequate precautions are taken, arises because of large pressure gradients built up across the powder grains in the evaporant source material, which are ejected at high speeds, and in solid form, in different directions. Some of these land directly onto the substrate, causing inhomongeneities and pinholes in the resultant film.

(4) Significant annealing effects have not been observed in four component chalcogenide films examined by making resistivity and

thermopower measurements on $Si_{18}Te_{40}As_{35}Ge_7$ and $Ge_{15}Te_{81}Sb_2S_2$ glasses (Rockstad etal [5]). Levy's [6] results did not show any annealing effects upon heating STAG glass films to 423 K in vacuum either. This is in contrast to binary and ternary chalcogenide alloys, and tetrahedral amorphous semiconductors like amorphous Si, which all show significant changes in their electrical properties upon annealing [5],[7]. The substrate temperature, however, should be kept below the glass transformation temperature, T_g, to prevent possible crystallisation of the film.

4.2 The Vacuum System and the Thin Film Deposition Assembly.

A CVC * vacuum coater system, as shown in Figure 4.1 with some auxilliary control equipment, was used to prepare the SeTAG thin film structures. The vacuum system consisted of an 18 in. diameter vacuum chamber, connected via a high vacuum valve and a liquid nitrogen cold trap to a six inch diameter diffusion pump. The pressure in the chamber could be reduced to about 6×10^{-7} mmHg after about one and half hours of pumping, and with the cold tap in operation. Without the cold trap a pressure of about 5×10^{-6} mm Hg could be achieved. The low pressure inside the chamber was monitored using an ionisation gauge. Electrical and rotary feed-throughs were available through the chamber base and top plates. A carousel divided the vacuum chamber into six equal sections, which meant that it was possible to carry out up to six different depositions in the same pump down. During the course of this work, however, only a maximum of two sections were used in any single pump down: one for electrode, and one for SeTAG deposition. Figure 4.2 is a schematic top plan view of the carousel,

---

*Consolidated Vacuum Corporation (U.K.) Ltd., Wokingham, Berks RG11 2PW.



Figure 4.1. Vacuum Apparatus and Auxilliary Control equipment

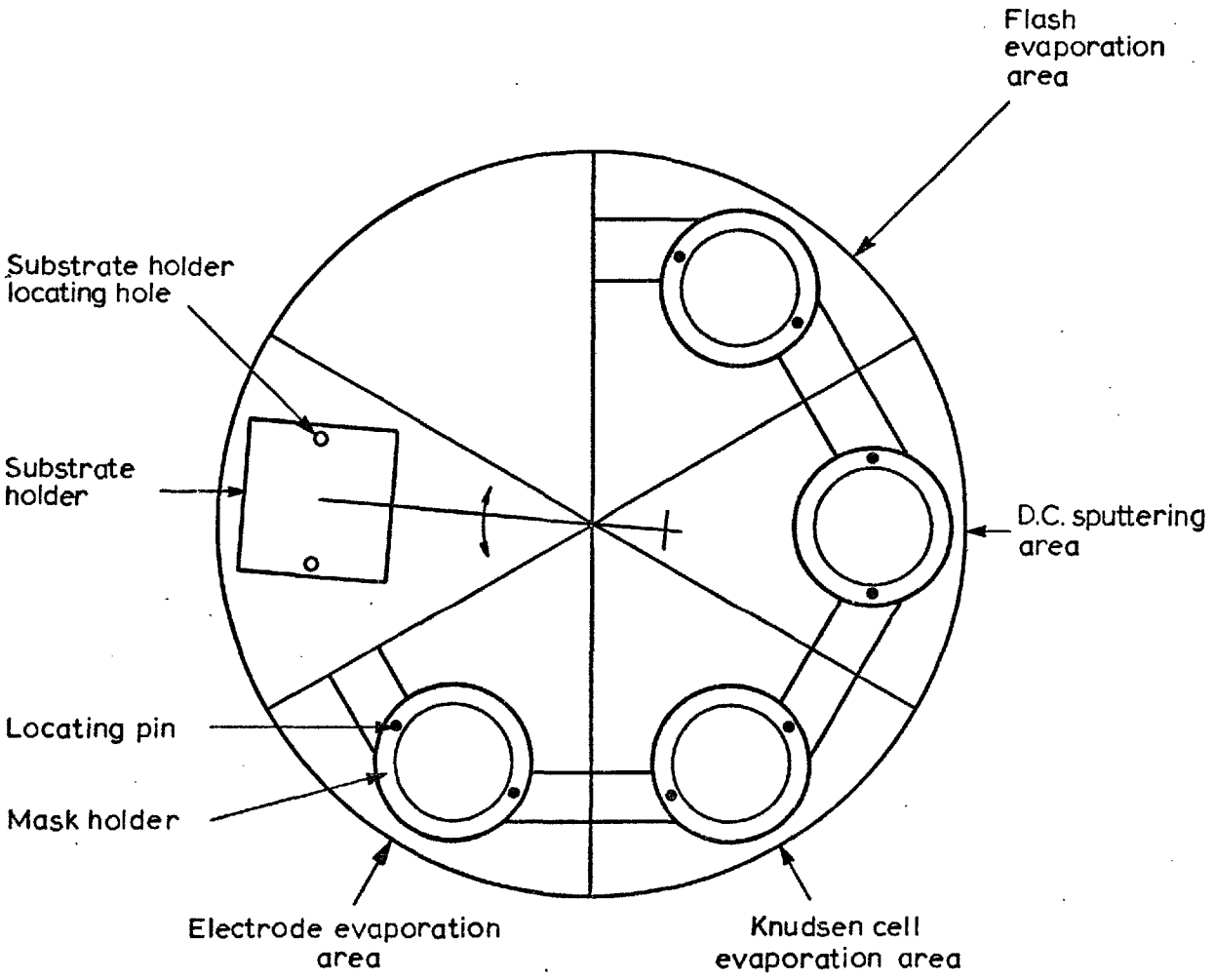


Fig.4.2: Top view of the carousel showing the various thin film deposition sections and the mask and substrate holders.

together with the substrate and mask holders. All the depositions were carried out in an upward direction, with the substrate facing downwards. The substrate was mounted onto a heatable substrate holder, which could be rotated in a plane parallel to the plane of the top plate, and about the central perpendicular axis of the carousel (see Figure 4.2). Figure 4.3 is a more detailed drawing of the substrate holder, and one of the thin film deposition sections. The locating pins shown ensured that the relative positioning of the substrate holder with respect to the mask was always the same. A Chromel/Alumel thermocouple inserted into the substrate holder, and in close vicinity to the back of the substrate, monitored the substrate temperature. The substrate-evaporation source separation was typically about nine inches (23 cm). All the thin film deposition sections had individual shutters, which were operated, via top or base-plate rotary feedthroughs from the outside. The metal components inside the bell jar, and especially those that were likely to be heated, were made of stainless steel to minimise any outgassing at high temperatures. The basic features of the carousel and the substrate holder were designed and constructed at Zenith Radio Research Corporation (U.K.) Ltd.

The thicknesses of the deposited films were measured using an Edwards Film Thickness Monitor (FTM-1). This operated on the principle that the frequency shift of a quartz crystal was proportional to the weight (and hence the thickness) of the material deposited on a well defined area of the crystal. Hence by placing the crystal in the direct "line of sight" of the boat (see Figure 4.3), and measuring the deposited film thickness by using optical interferometry techniques, the frequency shift of the crystal could be calibrated in Å kHz^{-1} for that particular material and geometry, and the thickness of any subsequent films was calculated to an estimated ±10%. This relatively

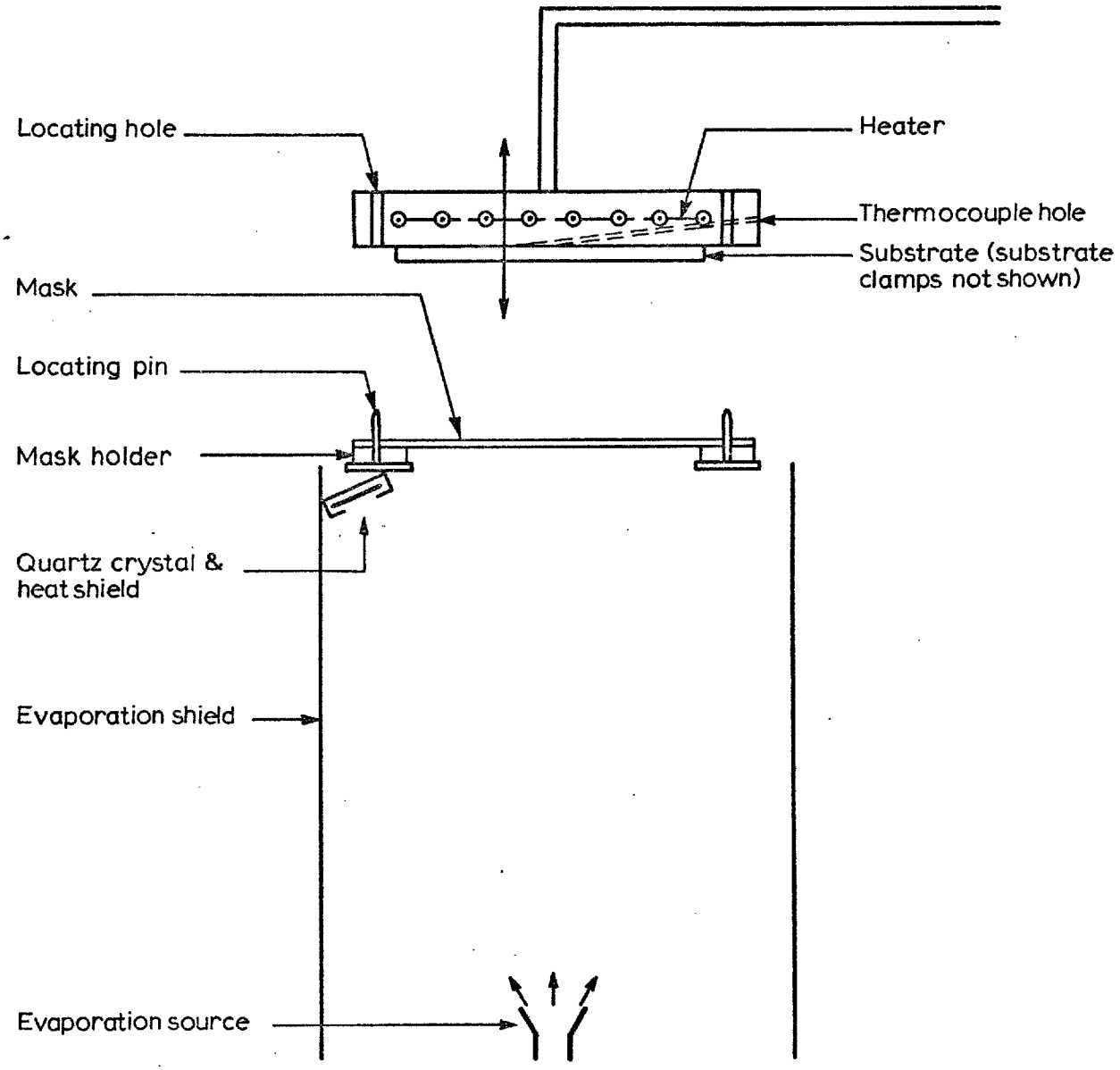


Fig. 4.3: Schematic drawing of a thin film deposition section showing the substrate and mask holders.

large error span was partly due to the errors in the calibration procedure, and partly due to the drifts in the frequency readings with time and temperature, although the latter was minimised by the thermal shielding of the crystal from the boat.

Most of the thin film structures that were fabricated were on freshly cleaved mica substrates, although a limited number of thin films were also deposited on 7059 Corning glass substrates. The latter were thoroughly washed in liquid detergent, and then degreased in an iso-propyl alcohol reflux condenser before being blow dried with nitrogen and placed in the vacuum system. All the substrateswere thoroughly outgassed in a vacuum of better than 5×10^{-6} mmHg for at least ten hours at a temperature of about $250^{\circ}C$, and then allowed to cool down to room temperature before any film deposition took place.

4.3. Preparation of $Ch_{61}Y_{39}$ SeTAG Glass Thin Films.

4.3.1. Knudsen Cell Evaporation Method.

In this method of thin film preparation, the material which is to be evaporated is usually placed in an open boat which is resistively heated in the vacuum system until the evaporation takes place. As already mentioned, this open boat technique is not suitable for the fabrication of chalcogenide glass films because of spitting. To overcome this problem, quartz boats of the type shown in Figure 4.5(d), were used. In order to avoid any spitting, a short length of about 0.5 mm bore quartz capillary tubing was used at the boat outlet. Some densely packed quartz wool was then inserted into the boat, before the boat was charged with powdered SeTAG (about 1 mm grain size). Finally some more quartz wool inserted into the boat in order to keep

the SeTAG charge in position. A rubber stopper was then inserted into the capillary tube end of the boat, which was evacuated and sealed under vacuum. Figures 4.4 (a to d) show the sequential steps in preparing a charged boat as described above.

The above boat was then placed in the Knudsen evaporation cell shown in Figure 4.5. This consisted of a ceramic tube housing, which enclosed the heater made of 0.001 in. Molybdenum foil. The ends of this heater were connected to stainless steel electrodes. The external boat diameter was selected so as to ensure good thermal contact with the heater. Three concentric cylindrical molybdenum heat shields (not shown in Figure 4.5) were placed around the evaporation unit to minimise radiation losses. A Chromel/Alumel thermocouple pushed through a hole in the bottom electrode allowed the temperature of the base of the boat to be measured. It was found, however, that a measured temperature of about 600°C at the boat base, corresponded to a temperature of about 860°C at a distance of 2 - 4 cm into the cell from the boat base. A measured temperature of 800°C ±50°C was used in all the evaporations. In order to minimise preferential loss of SeTAG components from the boat, the temperature was raised to this value very rapidly (in less than one minute), before the shutter was opened to expose the substrate to the vapour stream.

The use of the above method for the fabrication of SeTAG thin flims had the following disadvantages:

(1) The films made during different runs, but under the same conditions, did not have the same compositions. This was probably because of a combination of factors, which were due to trying to obtain films of a consistent composition in a system that did not operate under steady state conditions. These factors were:

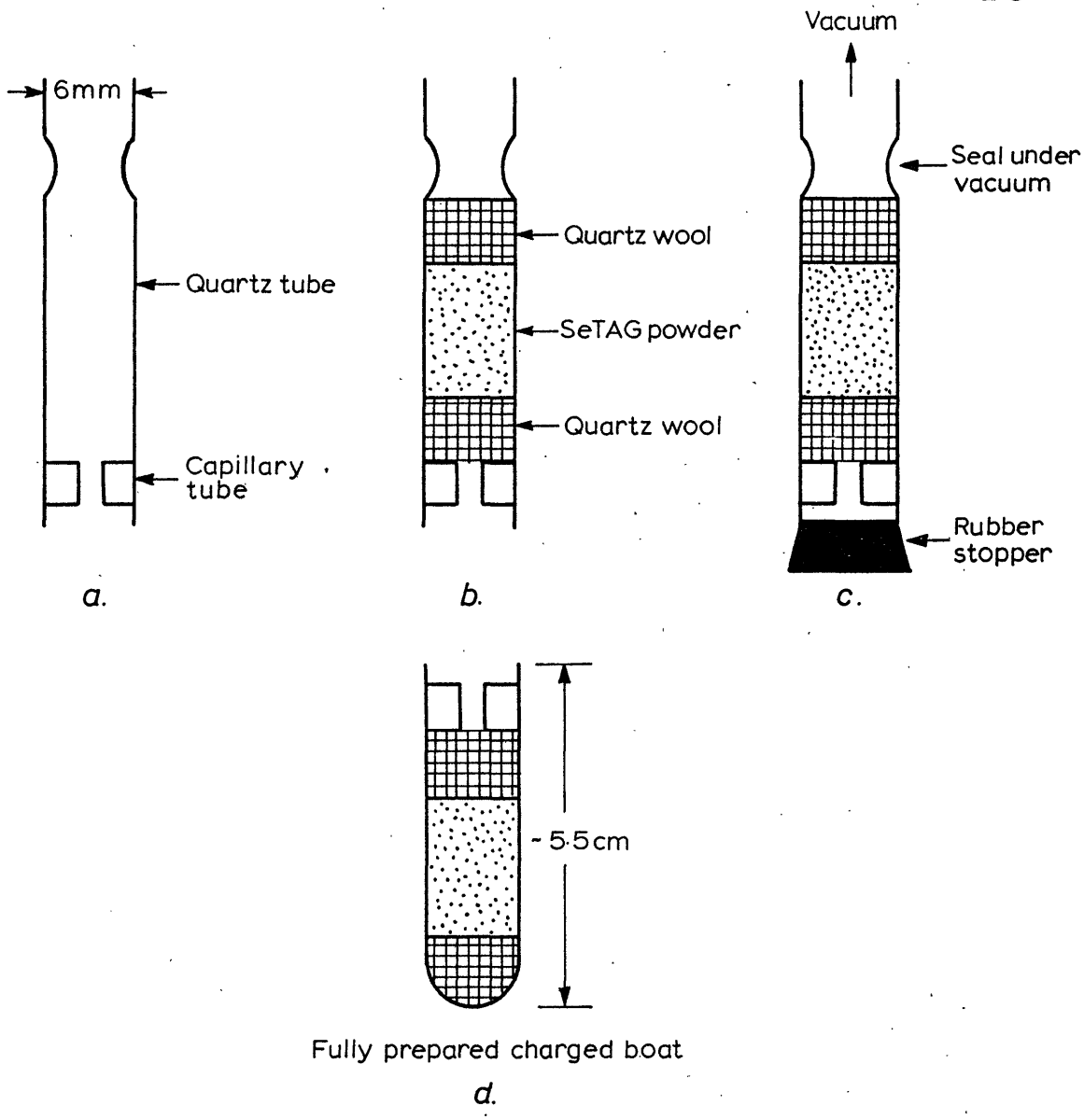


Fig. 4.4: Boat preparation and charging procedure

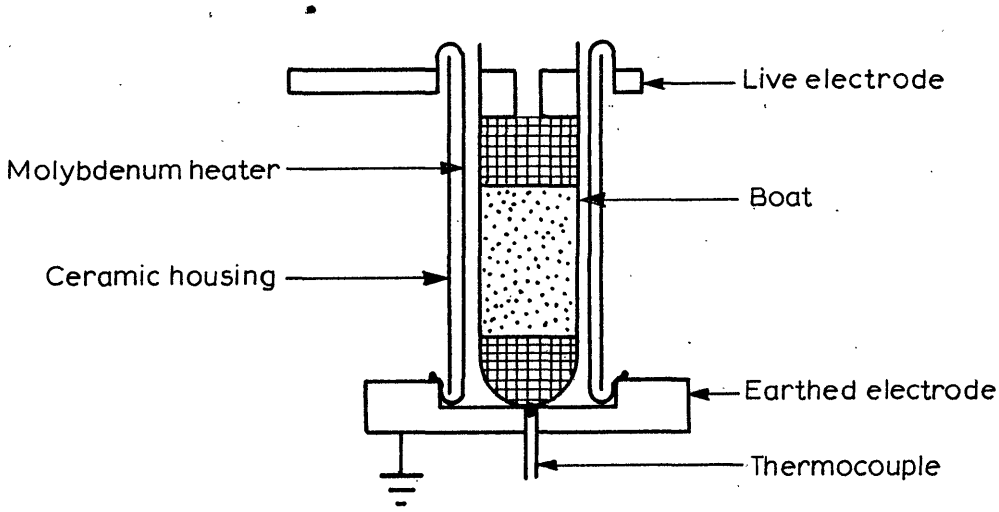


Fig. 4.5: Knudsen cell assembly

(a) A substantial preferential loss of material from the boat was incurred during the interval while the temperature of the boat was being raised to the selected evaporation temperature. The final film composition would be influenced by this, and also by any slight variations in the heating rates used in different runs.

(b) The substrate shutter, which was operated manually, could not be opened at exactly the same instant every time after the desired temperature had been reached. This would also result in vapour species of different compositions reaching the substrate during different runs.

(2) The film thickness could not be controlled very well. Typical deposition rates of 250 Å s^{-1} were observed. This method of evaporation was, therefore, particularly unsuitable for preparing thin film specimens of the order of 1000 Å thick, which would be suitable for field effect measurements.

For reasons of compositional irreproducibility, and a general lack of fine control over such parameters as the evaporation temperature, shutter opening times, and film thickness, it was decided that this method of SeTAG thin film preparation was unsuitable for the purposes of this project. The Knudsen cell technique did, however, produce pinhole free, homogeneous films, and it had the added advantage that typically the substrate temperature did not

increase by more than about 10 K above room temperature while a 1500 Å film was being deposited.

4.3.2. DC Sputtering Method.

DC as opposed to RF sputtering was selected because of the ease with which the former could be set up.

The main components of the DC sputtering facility were the following:

(1) Two inch diameter, 1 - 1.5 mm thick SeTAG target. This was prepared by cold pressing finely powdered SeTAG under a load of about 1 - 2 tons between two stainless steel pellets in a pressure die. The resulting pressed disc of SeTAG was then transferred onto a "Dural" or copper disc of the same diameter, which had been freshly painted over with 'Silver-Dag' to provide electrical and thermal contact between the two. This was then left to dry.

(2) Water-cooled, two inch diameter target holder. The mounted target was screwed onto this unit. Water-cooling was found to be necessary, because the poor thermal conductivity of SeTAG sometimes caused local melting or even cracking at the target surface during sputtering.

(3) A dark-space shield enclosed the above assembly to avoid the sputtering of any of the metal components.

(4) A high voltage DC power supply capable of supplying up to 5 kV at 1 A.

(5) The sputtering gas was 99.999% pure argon. This passed through a drying agent ($CaCl_2$), before being allowed into the vacuum system via a gas inlet valve. Once in the system, it passed over a tungsten getter to remove any residual oxygen impurities.

Typical argon pressures of 40 - 50 μm Hg were used for all the depositions. The pressure was monitored using an Edwards Pirani gauge which had been calibrated against a Macleod gauge for this purpose.

With the positive terminal of the power supply and the substrate holder at a common earth, typical sputtering voltages of 2 - 2.5 kV were applied to the target. This produced currents of the order of 2 - 2.5 mA. Application of higher voltages was not advisable because of the risk of cracking the target by overheating it.

SeTAG is a relatively poor electrical conductor, and, consequently, its dc sputtering yield is low. With a target-substrate separation of about 2.5 in, and under the conditions stated above, the deposition rate was about 10 Å/min. The substrate temperature did not increase significantly above room temperature during the sputter.

DC sputtering of SeTAG, using the methods described above, suffered the major shortcoming that all the films prepared in this way had large percentages of oxygen in them. This was probably closely related to the manner in which the targets were made. Since sufficient adhesion between the grains of SeTAG could only be achieved during the cold pressing process if finely powdered SeTAG was used, this meant that the proportion of surface oxide on each grain, and hence in the target as a whole, was high. This oxygen content was confirmed by the following observations:

(1) ESCA spectra* showed a large percentage of oxygen (as oxides) to be present in the thin films. No significant amount of oxygen could be detected in the spectra taken from the bulk samples. It should be noted, however, that the compositions of the

---

*ESCA measurements carried out by ICI Labs., Runcorn, Cheshire.

bulk and thin film samples calculated from the ESCA results, although very approximate, still do not seem very realistic. The composition of the bulk sample, from the ESCA data, for instance, was found to be $Se_{28}Te_{64}As_6Ge_2$ (c.f. a nominal composition of $Se_{12}Te_{49}As_{29}Ge_{10}$, confirmed by electron probe microanalysis). In the thin film analyses, it was found that the oxygen content was more than 50% in three out of the four films that were examined - this also seems unrealistic. The high oxygen impurity content could be explained if the spectra were those belonging to surfaces which have been exposed to air, and the observed oxygen belonged to a few monolayers of oxygen adsorbed on the surface. The fact remains, however, that in the absence of different treatments for the bulk and thin film surfaces before the ESCA spectra were taken, there was significantly more oxygen in the thin films of SeTAG as compared to the bulk.

(2) The electrical conductivity of the two sputtered SeTAG films that were prepared for electrical measurements were found to be about $10^{-8}\ \Omega^{-1}cm^{-1}$ compared to a bulk value of about $2 \times 10^{-6}\Omega^{-1}cm^{-1}$ for $Ch_{61}Y_{39}$ glasses.

(3) Very little field effect modulation could be observed in the prepared films, which was contrary to what was expected.

The electrical characteristics of these films, as commented on in(2) and (3) above, indicated that the film compositions were not typical of chalcogenide glasses, and since large amounts of oxygen were detected in these films it could only be concluded that their unusual electrical behaviour was related to the presence of oxide impurities, which made their use for the electrical measurements impracticable.

4.3.3. Flash Evaporation Method.

In this method of evaporation, small grains of material are introduced into the heated evaporation source, where the grains are instantaneously vaporised, and thus the stoichoimetry of the bulk starting material is preserved in the resulting thin film.

Flash evaporated thin films of SeTAG were prepared using an SG8 Single Grain Tantalum Box Source* as shown schematically in Figure 4.6. Powdered SeTAG (0.3 - 0.7 mm grain size) was fed into the heated box source via the inlet funnel. The baffle system inside this box prevented any grains which were not fully vaporised from reaching the vapour exit. The resulting films were, therefore, found to be pinhole free and homogeneous.

Figure 4.7 shows the flash evaporation assembly inside the vacuum system. The evaporant grains were introduced from a 'V' shaped trough, via a guiding glass funnel, into the material feed inlet funnel. The inlet was isolated from other parts of the vacuum system, and the substrate in particular, by the "anti-spit" and material feed/vapour outlet isolation shields shown, which restricted any unmolten material ejected from the inlet funnel to a small volume. The 'V' shaped trough was agitated manually from the outside as shown.

The source evaporation temperature, as measured using an optical pyrometer, was about 1000 ^{o}C at a power input of about 810 W (180 A @ 4.5 V). The pressure during evaporation was always less than or equal to 10^{-5} mm Hg.

---

*Supplied by Nordiko Ltd., Brockhampton Lane, Havant, Hants.

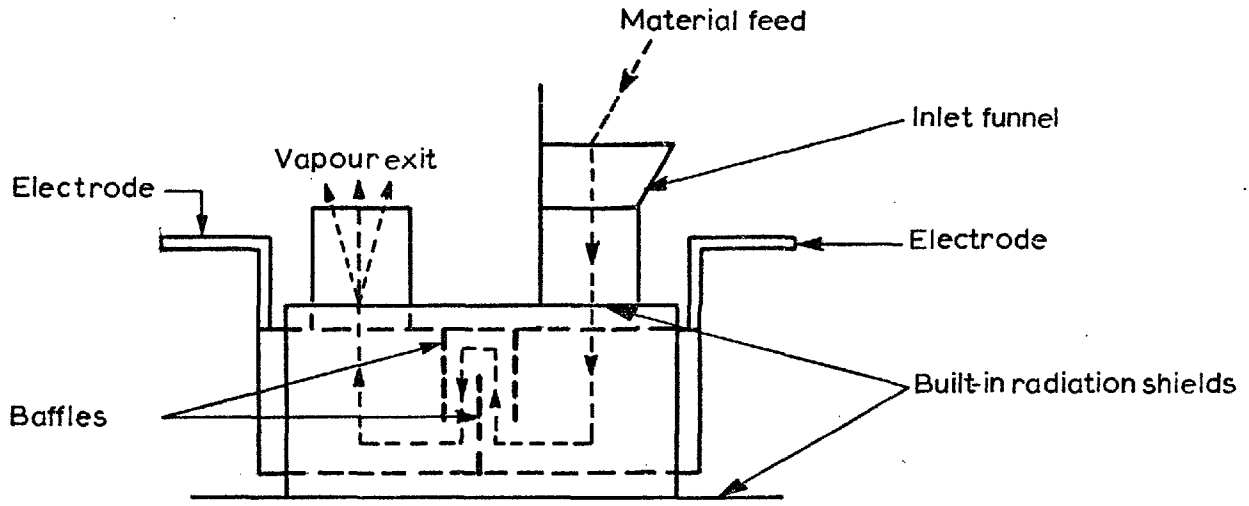


Fig. 4.6: SG8 single grain box source

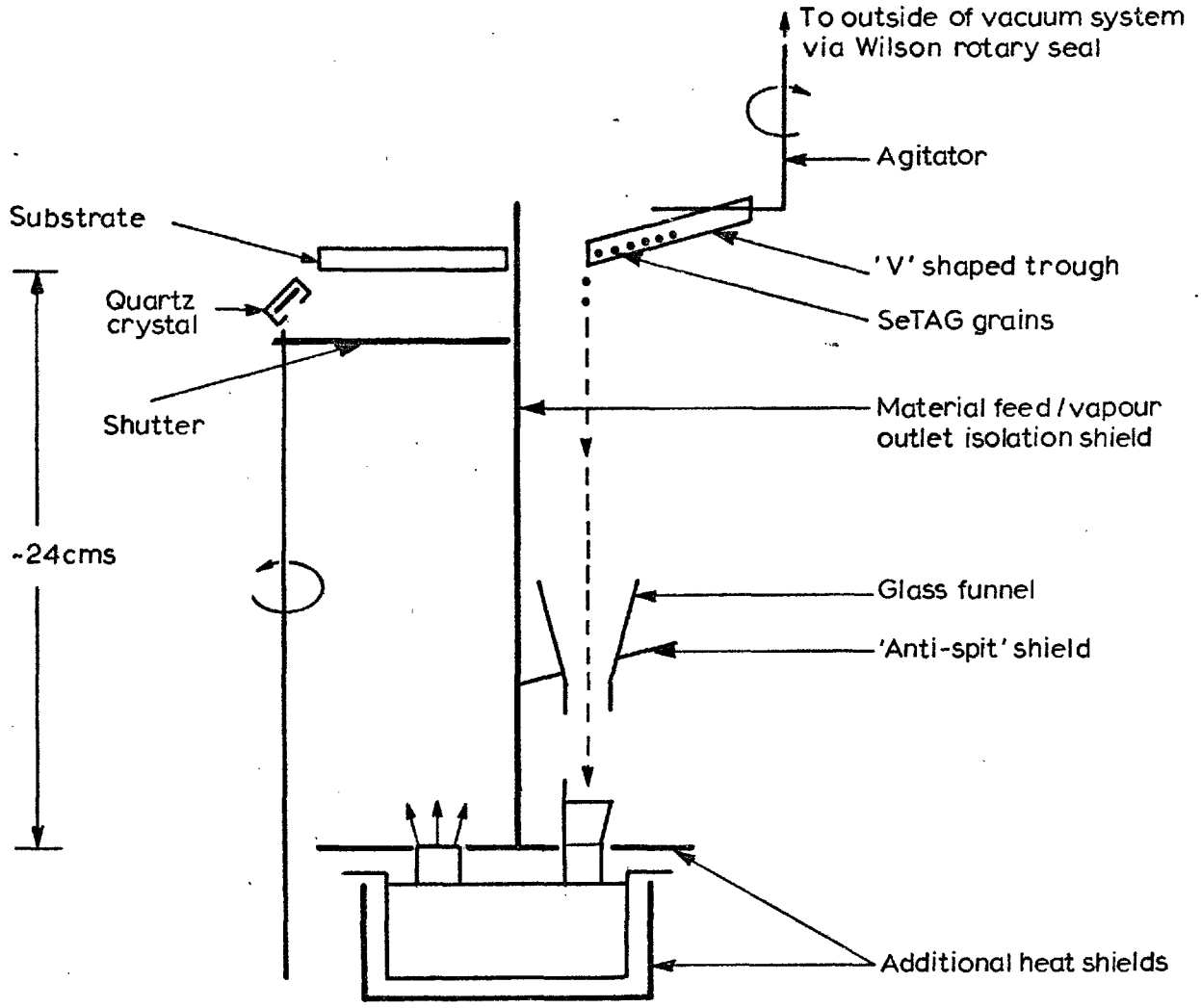


Fig. 4.7: Schematic drawing of the flash evaporation assembly

Despite the additional heat shields, the measured substrate temperature rose to about 200 °C during a typical evaporation run, which ususally took about ten minutes. This relatively high temperature did not, however, seem to affect the resulting films, which were still amorphous (see the transmission electron microscopy studies of Section 4.5). Once the evaporation was completed, the substrate temperature decreased to about 100 °C in less than five minutes. In other words, cooling to below the crystallisation temperature was quite rapid, and the substrate was only at a high temperature for a relatively short period.

The merits of the flash evaporation technique were as follows:

(1) The bulk composition was more or less retained in the thin films (see Section 4.4), with some fractional gain in Te content, and small losses in Se, As, and Ge contents of the films.

(2) The method of film preparation was rather simple compared to the two techniques already described.

(3) The film thicknesses were much more easily controled as compared to the Knudsen cell method.

The following disadvantages, which although not inherent to the technique, were, however, present in the set-up used in this study:

(1) The substrate temperature could not be controlled, and it was generally quite high. This, however, did not seem to affect the structure, or the electrical properties of the films.

(2) The agitator, which dispensed the SeTAG powder from the 'V' shaped trough into the source, was operated manually. As a result, the film deposition rates were not exactly uniform, nor were they finely controllable. It was therefore decided to keep this parameter as constant as possible. In all the film evaporations, the deposition rate, as monitored on the Edwards ratemeter, was about 7 Å s^{-1} ± 4 Å s^{-1}.

(3) It was difficult to deposit films thicker than about 2000 Å, because the ejected solid particles from the box source inlet funnel tended to block up the guiding glass funnel, and thus prevented other grains from reaching the evaporation source. Since the field effect measurements were best carried out on thin films, this limitation did not affect these measurements at all, but it did rather limit the attainable temperature range of the resistivity experiments.

4.4. Electron Probe Microanalysis (EPMA) of Thin Films.

EPMA was used to investigate the compositions of SeTAG thin films of $Ch_{61}Y_{39}$ (i.e. $Se_{12}Te_{49}As_{29}Ge_{10}$) nominal bulk compositions. The films were prepared by Knudsen cell or flash evaporation of the bulk powder. The conditions under which they were prepared have already been discussed in Sections 4.3.1 and 4.3.2.

The general comments made in Section 2.5, where the compositions of bulk samples, also analysed by EPMA, were reported, would also apply in the case of thin films. Analysis showed the films to be homogeneous, and the EPMA results, as listed in Table 4.2, were estimated to have an accuracy of about ±5%.

Film No.	Preparation Method	Substrate	Film Thickness (Å)	Atomic % Se	Te	As	Ge
3.3	KC	Mica	800	15	42	34	9
6.3	KC	Mica	1300	14	35	49	2
42.7	FE	Soda Glass	900	10	60	25	5
42.7	FE	Mica	900	13	57	24	6
43.7	FE	Soda Glass	1200	9	60	24	7
43.7	FE	Mica	1200	10	58	22	10
49.10	FE	Mica	2600	10	56	25	9

Table 4.2. EPMA on evaporated $Ch_{61}Y_{39}$ ($Se_{12}Te_{49}As_{29}Ge_{10}$) thin films - KC = Knudsen cell, FE = Flash evaporated.

The first column in Table 4.2 lists the film identification number: the number before the decimal point depicts the film deposition run number, and the one after it the ingot used in the evaporation.

Two Knudsen cell evaporated films were analysed, one of which was 800 Å, and the other 1300 Å thick. Both films were prepared under very similar conditions. Examining the results of the analysis, two observations may be made:

(1) The compositions of the two films are quite different. Both films, however, exhibit some gain in the As and Se contents, and some loss in Te and Ge compared with the parent ingot 3 of analysed composition $Se_{11}Te_{47}As_{32}Ge_{10}$.

(2) Film 3.3 was compositionally quite close to the bulk ingot, while film 6.3 showed a large compositional deviation from the parent ingot.

Of the flash evaporated films that were sent for analysis, two sets (films 42.7 and 43.7) were simultaneously evaporated onto mica and soda glass during the same runs in order to check the reliability of the results and/or to see whether the substrate had any significant effect on film homogeneity and composition. As can be seen from the Table, the substrate has little or no effect on film composition, with perhaps slight improvement in the compositions of the films on mica substrates when compared to the bulk values (both ingots 7 and 10 had analysed compositions of $Se_{11}Te_{47}As_{31}Ge_{11}$). The estimated relative accuracy of ±5% does not, however, allow any conclusions to be made in this respect. No changes in the degree of homogeneity with different substrates were observed either.

All the flash evaporated films showed an approximate 10% gain in the amount of Te present, with corresponding small losses in the Ge, As, and Se contents of the films. The important point is, however, that all the analysed films were compositionally very similar. In other words, the film compositions were reproducable during different runs. They also showed no compositional dependence on thickness.

4.5. Electron Microscopy of Flash Evaporated SeTAG Films.

Electron micrographs and selected area diffraction patterns (SADP) of an 1100 Å thick flash evaporated SeTAG film were taken in Imperial College's 1 MeV transmission electron microscope (TEM).

The thin film was deposited on a piece of mica substrate by the methods already described. A slightly dirty substrate was selected, so as to reduce the film adhesion to it. The film was then floated off the substrate (using water) onto clean electron microscope copper grids (grid size = 12 μm).

It was found that, under sharp focussing of the electron beam onto the SeTAG specimen, rapid crystallisation of the irradiated area, followed by loss of material, and eventual disintegration of the film occurred. Figure 4.8 (Magnification = 10,000, and beam energy = 700 keV) illustrates a beam damaged area. Figure 4.9 and 4.10 are SADP's of such a region in progressive stages of crystallisation respectively. Similar beam damage has also been reported in Si-As-Te glasses by Nagels [8] etal.

Figures 4.11 and 4.12 show respectively the electron micrograph and the SADP of a SeTAG specimen with the electron beam slightly out of focus. Both photographs indicate an amorphous structure, with the SADP of Figure 4.12 showing the typical diffuse rings. The small grains visible in Figure 4.11 may be characteristic of the thin films, although they may have arisen as a result of slight beam damage.

The beam damage arises because of the excessive heating of the film by the electron beam. The temperature rise in the thin film was estimated by considering two extreme cases:

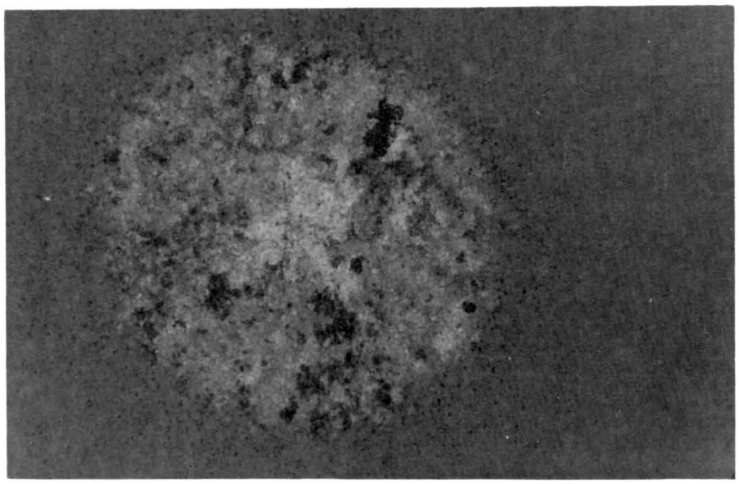


Fig. 4.8. Electron beam damage to SeTAG film (M = 10,000).

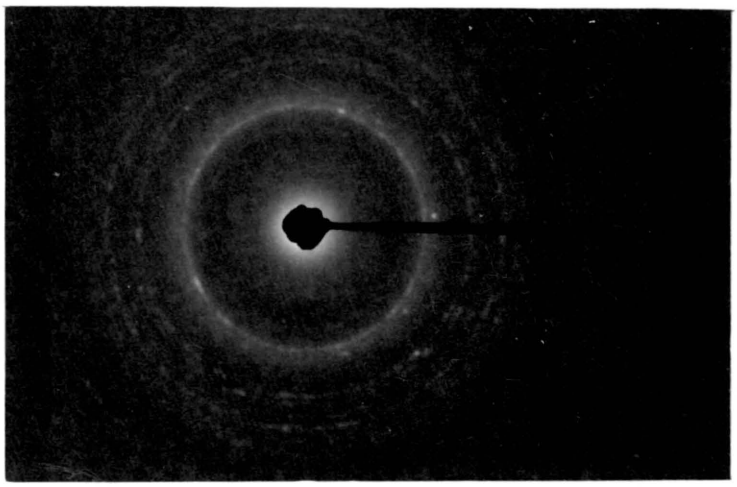


Fig. 4.9. SADP of beam damaged SeTAG film.



Fig. 4.10. SADP of heavily beam damaged SeTAG film.

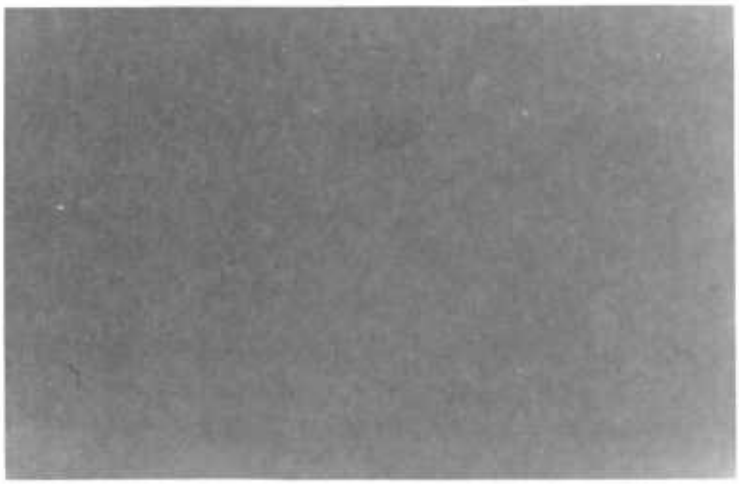


Fig. 4.11. Transmission electron micrograph of SeTAG film (M = 100,000).

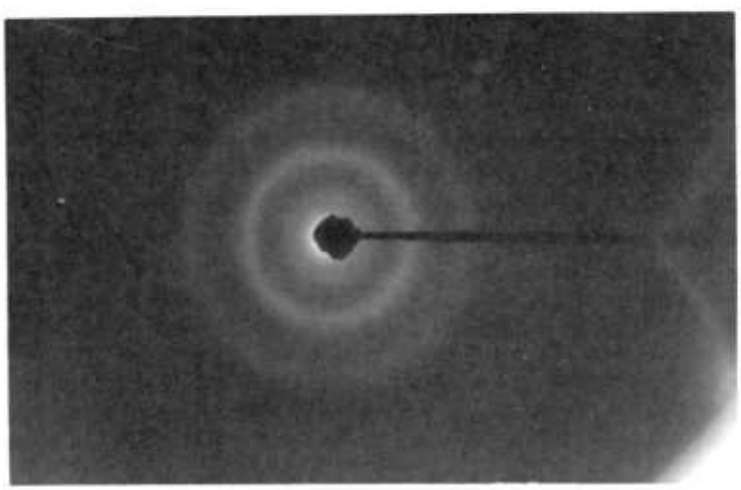


Fig. 4.12. SADP of SeTAG film.

(1) C.E. Hall [9] has estimated the maximum temperature rise in a microscope specimen of an element by assuming that all energy absorbed could only be lost through radiation. Using his results, and making the approximation of an average atomic number for SeTAG of about forty, it was found that the maximum temperature of the SeTAG film, under the specified conditions when the damage was observed, would be about 630 ^{o}C.

(2) S.B. Fisher [10] has estimated the temperature rise in thin metallic foils by assuming heat conduction to the grid, which is held at a fixed temperature, and is of infinite conductivity. He considers radiative losses to be negligible in comparison. He finds the temperature rise to be directly proportional to the electron beam intensity and the density of the film, and inversely proportional to the thermal conductivity of the specimen. By applying his results to the SeTAG film (using the bulk thermal conductivity value of 2×10^{-3} W cm^{-1} K^{-1}), a temperature rise of about 145 ^{o}C was estimated.

Since, in practice, heat losses by conduction and radiation take place in parallel, the actual temperature rise in the film would be somewhat less than 145 ^{o}C estimated above.

4.6. Device Fabrication.

Most of the electrical measurements were carried out on co-planar devices of the type shown in Figure 4.13. Chromium* electrodes were first evaporated onto freshly cleaved insulating mica substrates. The gap between the two electrodes was provided by stretching a (typically 50 μm dia) nichrome wire across the

---

*Cr electrodes were used because they were found to be ohmic and easy to evaporate. For further discussion see Chapter 5.

electrode mask. Good contact between the mask and the substrate ensured that a clear, well defined gap existed between the two electrodes (known as the source and the drain in a field effect device). The electrode evaporation source consisted of a Cr electroplated tungsten rod. Typical electrode thicknesses were about 5000 Å. SeTAG was subsequently deposited on top, over the entire source-drain gap region, to the desired thickness, by the techniques already described. The electrodes were always evaporated first to avoid possible contamination of the chalcogenide film. The devices thus fabricated were obtained without breaking the vacuum, and they were suitable for resistivity measurements. The gate electrode, which was necessary for the field effect experiments, was provided afterwards by painting the back face of the substrate with 'Silver-Dag', as shown in Figure 4.13. Thin gold or platinum wire connections to the electrodes were made via 'Silver-Dag'. Depending on the set of masks used, from three to twenty-four devices could be prepared in a single pumpdown. The widths of the source-drain electrodes varied from 1.1 to 1.56 mm.

A few co-planar devices were prepared, which used RF sputtered SiO_2 as the gate insulator. These were prepared in the following sequence:

(1) The evaporation of Cr gate electrodes onto clean and degreased Corning 7059 glass substrate.

(2) RF sputter deposition of 2000 - 5000 Å thick layer of SiO_2 on top of the gate electrode in a separate vacuum chamber. The substrate was again washed in an iso-propyl-alcohol reflux condenser, and blow dried with nitrogen before the SiO_2 was

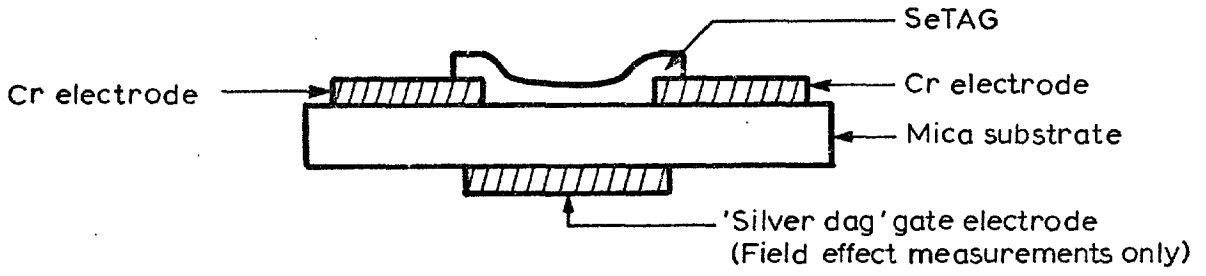


Fig. 4·13: Co-planar device using mica gate insulator

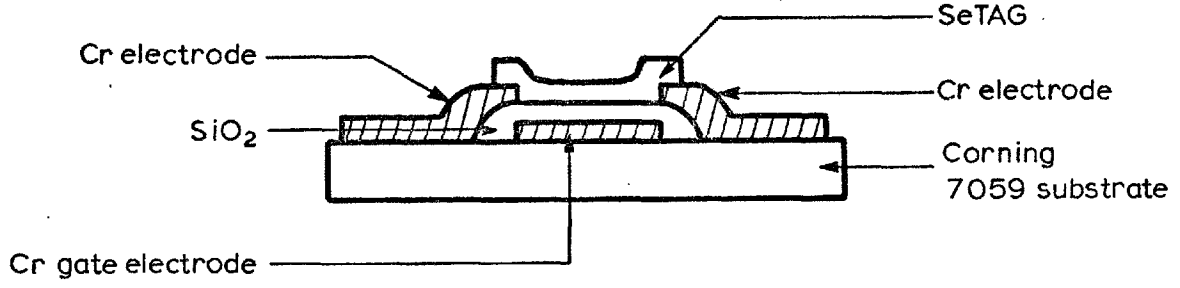


Fig. 4·14: Co-planar device using SiO_2 gate insulator

deposited. This was done to minimise the chances of dust particles causing a short-circuit between the gate and either of the source or drain electrodes.

(3) Transfer of the above from the RF sputtering system and back to the original vacuum system for the deposition of the source-drain electrodes and the SeTAG film. As before, the substrate was cleaned in transit, and then outgassed in the vacuum system before the above evaporations were carried out.

The geometry of the above prepared device is shown in Figure 4.14.

Despite the precautions taken, many of the above devices were found to be short circuited between the gate and the source-drain electrodes because of the presence of dust particles.

Apart from the above co-planar devices, two cross-over devices in a metal-semiconductor-metal (i.e. sandwich configuration) were also prepared. These were used to measure the low frequency dielectric constant of SeTAG films (see Chapter 5).

4.7. Summary and Discussion.

SeTAG thin films of $Ch_{61}Y_{39}$ nominal compositions were prepared by Knudsen cell evaporation, DC sputtering, and flash evaporation.

The flash evaporation method was found to be the only suitable technique through which thin films with reproducable compositions could be made.

Analysis by electron probe micro-analysis showed the flash evaporated films to be rich in Te, and slightly deficient

in Se, As, and Ge as compared to the bulk composition. They were also found to be homogeneous.

Examination of the films under the microscope indicated no pinholes to be present. Transmission electron microscopy found the films to be amorphous. The electron beam damaged the specimens very easily, and caused rapid cyrstallisation, which was ascribed to the excessive heating of the film by the electron beam.

Devices were fabricated for resistivity and field effect measurements, using evaporated chromium electrodes. The gate insulators used were mostly mica, although some sputtered quartz gate insulated devices were also made. The problem of pinholes due to dust particles made the latter unreliable, because the dirt tended to cause breakdown in the quartz insulator.

Although DC sputtering could be further developed to produce reliable SeTAG thin films, if the target is prepared by, say, hot pressing techniques in an inert atmosphere, it still has the disadvantage of very low sputtering rates (about 10 $\mathring{A}$ min^{-1}). RF sputtering of chalcogenide glasses, on the other hand, has been widely used elesewhere, although it is quite expensive and laborious to set-up because of the power supply, and the matching networks required.

On the whole, it is believed that the flash evaporation technique is the most suitable method of preparing thin multi-component films. Compared to RF sputtering, it is more economic, and easier to set-up. The film compositions are reproducible, and it is easy to prepare films of different compositions. In any future work, it would be advisable, however, to provide water cooling to the substrate, so that its temperature may be better controlled.

Chapter 4. References.

1. G.V. Bunton, S.C.M. Day, R.M. Quillam, P.H. Wisbey, J. Non-Crystalline Solids, 6 (1971) 351.
2. J. Bosnell, C.B. Thomas, Solid State Electronics, 15 (1972) 1261.
3. A.E. Owen in Electronic and Structural Properties of Amorphous Semiconductors, Edited by P.G. Le Comber and J. Mort, Academic Press, London, 1973.
4. B.F.T. Bolker, P.H. Sidles, J. Vac. Sci. Tech., 12 (1975) 114.
5. H.K. Rockstad, R. Flasck, S. Iwasa, J. Non-Cryst. Solids, 8 - 10 (1972) 326.
6. A.W. Levy, Ph.D. Thesis, 1972, Council for National Academic Awards.
7. See, for instance, A. Madan, P.G. Le Comber, W.E. Spear, J. Non-Cryst. Solids, 20 (1976) 239.
8. P. Nagels, R. Callaerts, M. Denayer in Amorphous and Liquid Semiconductors, Edited by J. Stuke and W. Brenig, Taylor and Francis, London, 1974.
9. C.E. Hall, Introduction to Electron Microscopy, McGraw Hill, 1953.
10. S.B. Fisher, Radiation Effects 5 (1970) 239.

Chapter 5

Electrical Properties of Thin Films of Se-Te-As-Ge

5.1 Introduction

In this Chapter, the results of resistivity and field effect measurements on flash evaporated thin films of SeTAG of approximate composition Se_{11} Te_{57} As_{24} Ge_8 (c.f. the nominal bulk value of Se_{12} Te_{49} As_{29} Ge_{10}) are reported.

Resistivity was measured as function of film thickness and temperature for co-planar structures with evaporated Cr electrodes. The current-voltage (I-V) characteristics and film resistance as a function of electrode separation indicated non-resistive "ohmic" contacts with Cr electrodes.

The field effect technique has been used successfully to study the surface properties of crystalline semiconductors by the application of a capacitatively induced field to the surface of the film, thus varying the extent and the shape of the space charge region. Early field effect experiments on complex chalcogenide films by Fritsche and Ovshinsky[1] were unsuccessful, and it was concluded that the density of states at the Fermi level was at least 6×10^{19} cm^{-3} eV^{-1}.

Barbe[2], using the CFO model in a somewhat simplified form, suggested that field effect measurements on amorphous materials should be possible provided that the density of surface states was less than 10^{14} cm^{-2}. Subsequently, Egerton[3], and Levy et al.[4] reported field effect modulations in SeTAG thin films by using A.C. gate voltages. Furthermore, in agreement with the results reported here on SeTAG, the above authors observed a

continuous decay in modulation with time to zero when a step voltage applied to the gate. Both the above authors analysed their A.C. field effect data by considering the states at the Fermi level using the Barbe analysis discussed in Section 5.4.2.1.

There have been some apparently succesful D.C. field effect measurements[5]-[8]. However, it is believed that the standing modulations observed by some workers[5],[6] may have been due to any of a number of experimental artifacts arising from the choice of the field effect configuration, the electrical circuitry, and/or the temperature range employed in the measurements.

With regard to Marshall and Owen's paper[6] on As_2Te_3 and STAG thin films, a number of experimental points of consideration arise, viz:-

(1) It was not mentioned whether the substrate was baked prior to sputter deposition of the semiconductor. Any adsorbed species, particularly water vapour, would affect the field effect data by causing a chemical change at the surface, as shown by Kastner and Fritsche[9a] in amorphous germanium, and Green et al.[9b] in chalcogenide glasses.

(2) The gate insulator was sputtered on top of the chalcogenide film. Apart from surface damage, this produces heating and possible incorporation of impurities in the semiconductor film. In the presence of water vapour and oxygen, a conducting Te "skin" may be formed which will produce a field effect signal.

(3) No details with regard to the circuit used in the measurements were given. In the presence of a slow decay in the field effect modulation (particularly below room temperature), a

circuit employing an ammeter to monitor the source-drain current would not be sensitive enough to register the small current changes. Instead, a balanced bridge network should be used to obtain the added sensitivity.

(4) The modulated source-drain currents in both As_2Te_3 and STAG films showed a linear dependence on gate voltage, V_g. However, for $V_g < 200V$, the gate voltage is comparable in magnitude to the source-drain voltage used (50V). This will introduce errors into the observed modulations, which have apparently not been corrected for.

The field effect results of the Stanford group[7] on chalcogenide glasses have been brought together in Mahan and Bube's paper[8]. They used a wheatstone bridge circuit to measure the out of balance voltage due to the modulated source-drain current after the application of a D.C. step gate voltage. As with Marshall and Owen, these authorse did not mention how the substrates were treated prior to semiconductor deposition.

Marshall and Owen identified a set of hole trapping centres 0.13 eV below the Fermi level which they associated with the linear variation of the source-drain current with V_g in the accumulation regime. As already mentioned, however, the validity of their data at low fields is questionable. Mahan and Bube, in contrast, did not identify any discrete hole traps in As_2Te_3 or other chalcogenide glass films. Instead, they proposed two separate mechanisms in the high and low temperature regimes: at high temperatures ($T \gtrsim 270K$), the observed field effect is controlled by the concentration of mobile charges available, while at low temperatures, the localised states at E_F are dominant.

As can be seen, therefore, there is no universal agreement on the electronic mechanisms which prevail in field effect measurements on chalcogenide thin films, and the results, and their interpretation, seem to be sensitive to the detailed methods of device preparation and measurements.

The only area of amorphous solids where the field effect technique has been used successfully is in amorphous tetrahedral films like silicon. Spear and co-workers[10] have made field effect measurements on pure[10a,b] and doped[10c] amorphous silicon prepared by R.F. glow discharge decomposition of silane ($SiH_4 \rightarrow Si + 2H_2$). They were able to "map" the density of states distribution as a function of substrate temperature during deposition, T_d, and they identified two peaks in the density of states distribution shown schematically in Fig. 1.1(d) (Chapter 1). It was also shown that the density of states at E_F decreased with increasing T_d. However, there is some evidence[18] to suggest that the films prepared by the above technique are not α-Si but α-SiH_x (where x $\sim$30% (atomic) for T_d = 298K), which causes the saturation of the Si dangling bonds by hydrogen.

5.2 Experimental Procedure

Thin film, coplanar, SeTAG structures were prepared by the method already described in Section 4.6, Chapter 4, and stored in a dry environment. Room temperature electrical measurements were carried out either inside a shielded metal box in dry air, or in the vacuum cryostat of Fig. 3.1. The results were not affected by the environmental conditions.

Electrical measurements as a function of temperature were all carried out in the vacuum cryostat at a pressure of less

than 5×10^{-6} mm Hg. The substrate (usually mica) was mounted on a copper substrate holder, which was screwed onto the copper platform block shown in Fig. 3.1 (Chapter 3). Zinc oxide impregnated silicone grease was used to improve the thermal contact between all mating surfaces. The temperature of the substrate was monitored using a Chromel/Alumel thermocouple fixed in good thermal contact with the front face of the substrate.

The field effect conductance measurements were carried out using the circuits shown in Figs 5.1 and 5.2. Since no standing field effect modulation could be observed, the change in surface conductance as a function of applied gate voltage was measured in three regimes:

(1) A.C. field effect

This was measured by using the circuit of Fig. 5.1. The sinusoidal A.C. gate voltage was applied via an oscillator-amplifier-HV transformer arrangement. Part of this applied voltage was used to drive the horizontal sweep of the C.R.O. The current, I_{sd}, in the source-drain circuit, which was provided by means of four sets of 9 volt batteries, was measured by observing the voltage drop across a series 2MΩ variable resistor, R_v, which was connected to the differential inputs of the Y plates of the C.R.O. (C.R.O. input impedance = 1 MΩ at each terminal). With the variable resistor balanced near its centre, a total resistance of 1 MΩ resulted.

With the gate voltage, V_g, applied, and the source-drain switches in position 1 (i.e. with no current flowing in the source-drain circuit) the resistor R_v was adjusted so that the displacement currents were balanced out (Fig. 5.3, trace A). A fine tune differential capacitor (about 1 pF) across the gate and source-drain

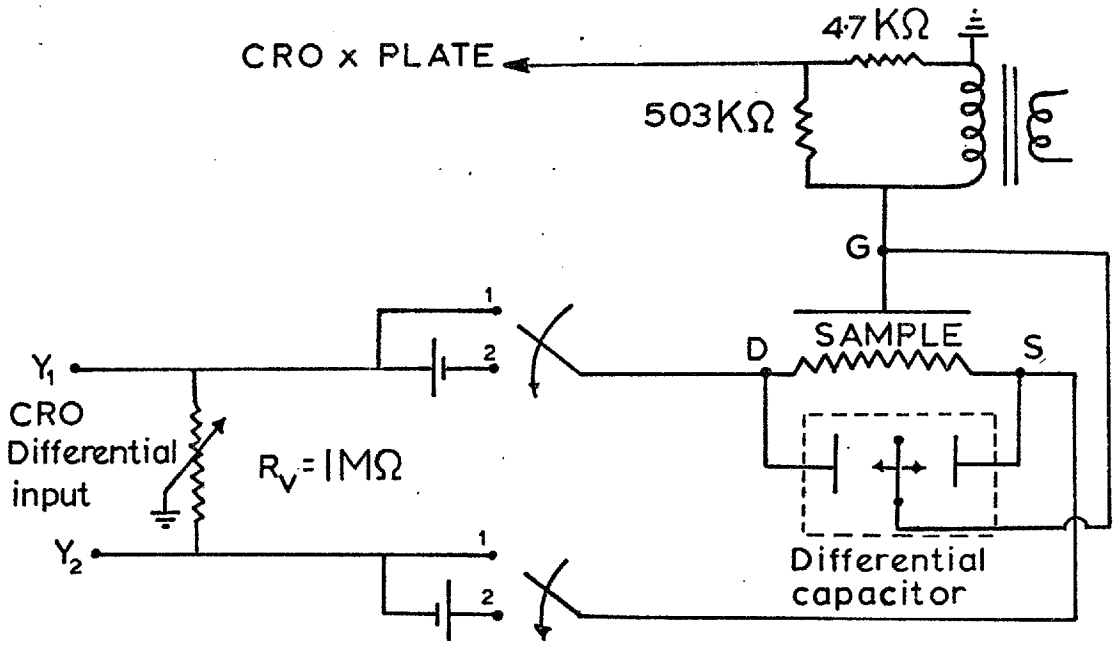


Fig. 5·1 AC Field effect circuit.

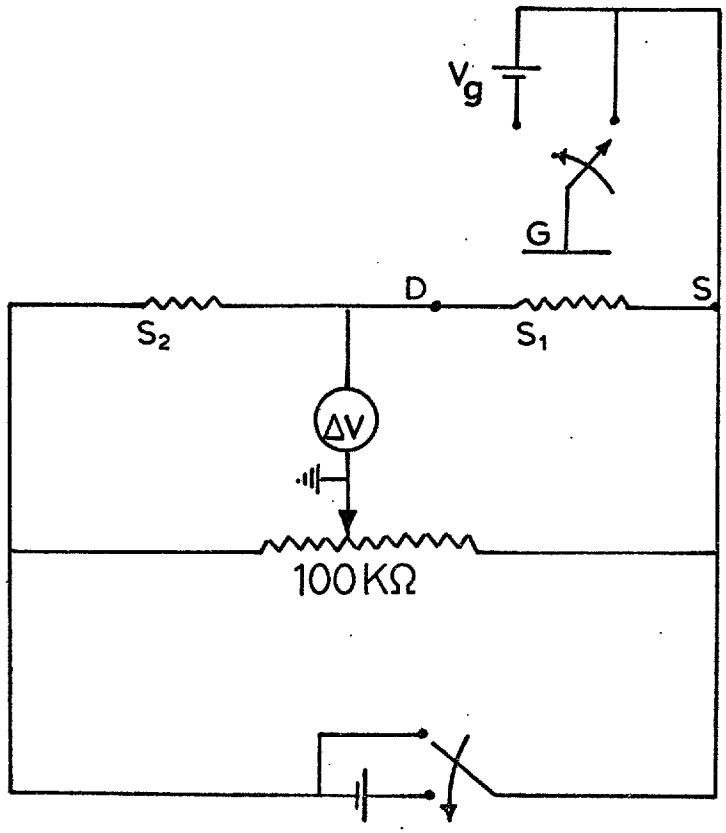


Fig. 5·2 Bridge circuit for measuring long time decay of field effect modulation.

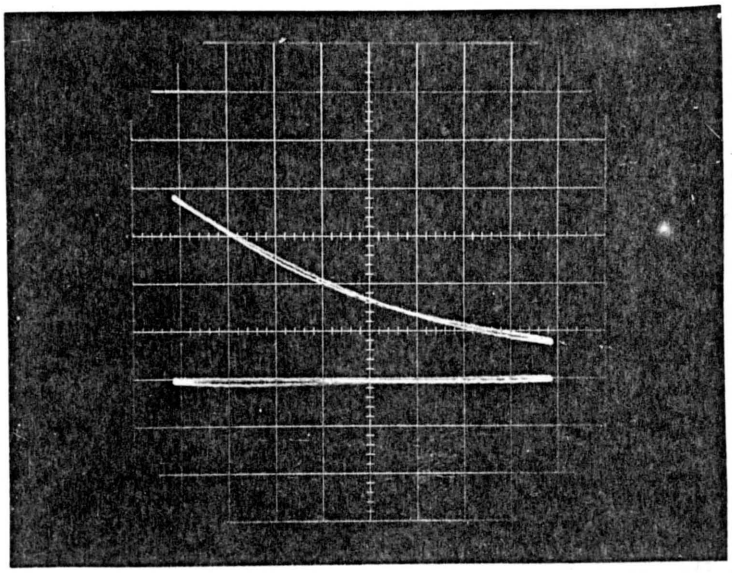


Fig. 5·3 AC Field effect trace(T=298K)

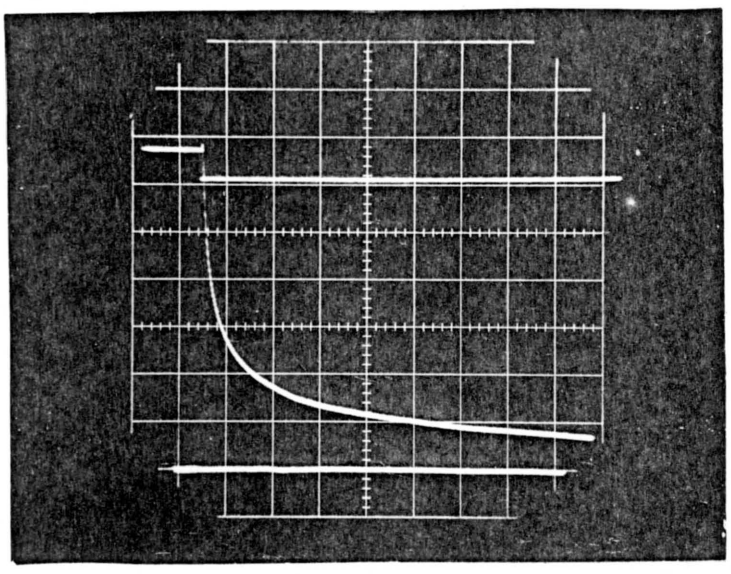


Fig. 5·4 DC Field effect trace(T=343K)

terminals was also used to minimise any stray capacitances due to the asymmetric geometric overlap of the gate and source-drain electrodes. Once the circuit was balanced, the source-drain switches were turned to position 2, which resulted in the field effect signal (Fig. 5.3, trace B).

In order to avoid any spurious effects due to non-linear charge distribution in the semiconductor, the source-drain voltage, V_{sd}, was always kept to less than 20% of the gate voltage.

Using the above procedure, field effect measurements in the frequency range 10 Hz to 1 kHz were made.

(2) Short Time Decay D.C. Field Effect

The circuit of Fig. 5.1 was used, except that the A.C. gate signal was replaced by a D.C. step voltage derived from a set of 90V dry cell batteries. After the application of the gate voltage ($\leq \pm$ 655V), the source-drain current decayed with time as shown in Fig. 5.4. In this configuration, the gate voltage was no longer used to drive the horizontal sweep of the C.R.O., but the internal C.R.O. trigger was used instead, and the field effect decay of the modulated signal with time (up to about 15 seconds) was measured.

In regimes (1) and (2) above, since both I_o, the source-drain current with $V_g = 0$, and ΔI, the change in the source-drain current due to application of V_g, could be measured, the ratio $\Delta I/I_o$ could be determined. This ratio was the same as $\Delta g/g_o$, the field effect modulation, where Δg was the change in sheet conductance, and g_o was the zero field conductance per square of the film.

(3) Long Time Decay D.C. Field Effect

The circuit of Fig. 5.2 was used for this purpose. Samples S_1 and S_2 were identical coplanar structures deposited simultaneously

on one substrate. They therefore had the same resistance (to ±10%). They were connected in the two arms of the wheatstone bridge circuit shown. A 10 turn potentiometer provided the other arms of the bridge circuit. A 616 digital Keithley electrometer was used as a null detector, and the electrometer output was monitored on a chart recorder.

The above circuit had the advantage that with the bridge balanced so that the voltmeter read zero (i.e. $\Delta V = 0$), any slight changes in the temperature of the ambient did not affect the balance because of the cancelling effects of S_1 and S_2. This meant that small conductance changes could be detected by measuring the out of balance voltage, ΔV, when the gate voltage was applied to the field effect sample S_1.

It can be shown that if the resistance of samples S_1 and S_2 with $V_g = 0$ are R_1 and R_2 respectively, then the fractional change in the resistance of S_1 when the gate voltage is applied is given by,

$$\frac{\Delta R}{R_1} = - \frac{(R_1 + R_2)^2}{R_1 R_2} \cdot \frac{\Delta V}{V_{sd}}$$

If $R_1 = R_2 = R_1$ then,

$$\frac{\Delta R}{R} = - \frac{4\Delta V}{V_{sd}} \qquad 5.1$$

It should be noted that even if R_2 and R_1 differ by 20%, the error introduced by taking $R_2 = R_1$ is only about 1%. Experimentally, R_1 and R_2 were within the above margin, and typically, they did not differ by more than 10%

The advantage of the bridge method is that since we are looking at the change in surface conductance by monitoring ΔV, much smaller fractional changes in the surface conductance of the specimen may be measured. In the present study, the lowest detectable value of ΔV was about 0.2 mV*, which corresponded to a fractional change in $\frac{\Delta R}{R_o}$ (and hence $\frac{\Delta g}{g_o}$) of about 5×10^{-4}. This compares to a value greater than 1×10^{-3} if the absolute value of source-drain current (i.e. $I_o + \Delta I$) is monitored on an ammeter. Furthermore, the ammeter method suffers from the shortcoming that, because of the slow decay, the rate of change of current with time is small, and therefore not easily detectable at longer times with this technique.

5.3 Results

In this section, the electrical and field effect properties of flash evaporated thin films of SeTAG of $Ch_{61}Y_{39}$ nominal bulk composition are presented.

5.3.1 Current-Voltage Characteristics

Fig. 5.5 shows the room temperature I-V characteristic of a $Ch_{61}\ Y_{39}$ thin film. With an electrode separation of 50 μm, the data show a linear, ohmic, variation of current with voltage from 2×10^{-3} V to 50 V, corresponding to applied electric fields in the range 0.4 V cm^{-1} to 10^4 V cm^{-1}. Reversing the polarity of the applied voltage did not affect the current.

---

*Neglecting the drift which was of the same order over about 1.5 hours

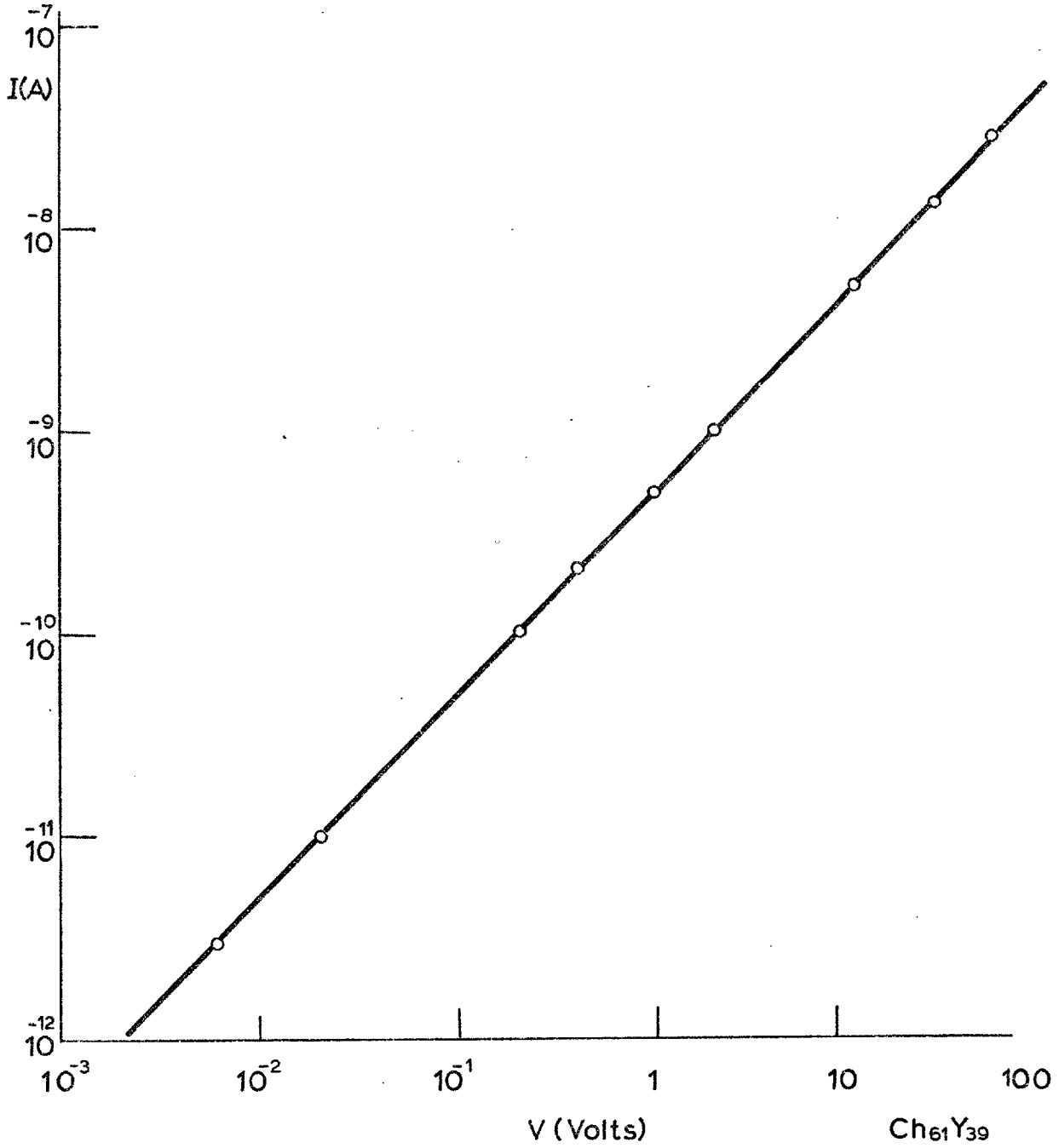


Fig.5·5 The current voltage characteristic in a $Ch_{61}Y_{39}$ thin film at room temperature (Electrode separation = 50 μm)

5.3.2 Resistance as a Function of Film Length

Although almost all the measurements were carried out on structures with a 50 μm film length, the variation of resistance with film length was measured in three coplanar structures with 25 μm, 50 μm, and 100 μm electrode separations. These were prepared during the course of the same evaporation, and the room temperature resistivity of the films was found to be independent of film length.

5.3.3 Resistivity as a Function of Film Thickness

Table 5.1 lists the variation of thin film resistivity with film thickness in the range 500Å to 1800Å. The results were recorded in air at room temperature. The relatively large scatter in resistivity values may be attributed to the following factors:

(1) Variation in room temperature.

(2) Errors in recording the film thickness due to the frequency drift of the quartz crystal.

(3) Slight compositional variation between the films.

With the above considerations in mind, no significant change in resistivity with film thickness is found, and an average room temperature (298 K) resistivity of about 3.8×10^5 ohm-cm compares to a bulk value of about 4.8×10^5 ohm-cm for a glass of the same nominal composition.

Ideally, for a true determination of thickness dependence of film resistivity, films of different thicknesses should be deposited during one evaporation, so that the above mentioned errors may be minimised. This has been done by Levy[11], and Marshall et al.[6] on STAG glass films. They both find no variation in resistivity with thickness.

Temperature (K)	Film Thickness (Å)	Resistivity (x 10^5 Ωcm)
298	520	10.4
298	620	2.9
298	700	9.0
299	1100	4.3
299	1150	3.6
299	1330	2.71
298	1350	2.4
298	1400	6.0
299	1450	3.1
300	1450	1.5
297	1500	4.4
295	1710	11.4
293	1770	6.4

Table 5.1. Room Temperature Resistivity as a Function of Film Thickness

5.3.4 Resistivity as a Function of Temperature

The temperature dependence of resistivity, ρ, was measured in detail from 228 K to 350 K for a 1400Å thick film, and from 272 K to 350 K for a 520Å film. Because of the limited temperature range employed in the latter, the plot of $\ln\rho$ vs. $1/T$ appeared as a straight line of activation energy, $E_{\sigma o} = 0.53$ eV. A plot of $\ln\rho$ vs. $1000/T$ for the 1400Å film is shown in Fig. 5.6. A slight curvature is observed in this plot, which is similar to that in the bulk material. The "average" slope of the curve in Fig. 5.6 is 0.51 eV (compared to 0.49 eV for bulk $Ch_{61}Y_{39}$). The difference in the "straight line" activation energies between the bulk and thin film specimens may be ascribed to compositional differences between the bulk and thin film samples.

Contrary to Levy's results[11], no change in the activation energies of the thin films was observed by thermal cycling between the above mentioned temperatures.

5.3.5 Measurement of Low Frequency Dielectric Constant

Capacitance at room temperature as a function of frequency was measured in thin films of SeTAG over the frequency range 500 Hz - 1 MHz. The 500 Hz capacitance of the films decreased by less than 10% compared to the 1 MHz value. The measurements* were made on films about 5000Å thick in a sandwich (cross-over electrodes) configuration. The common electrode area was typically 6 mm^2. A Wayne-Kerr Capacitance Bridge was used for these measurements.

---

* Carried out by Miss V. Heys, Electrical Engineering Department

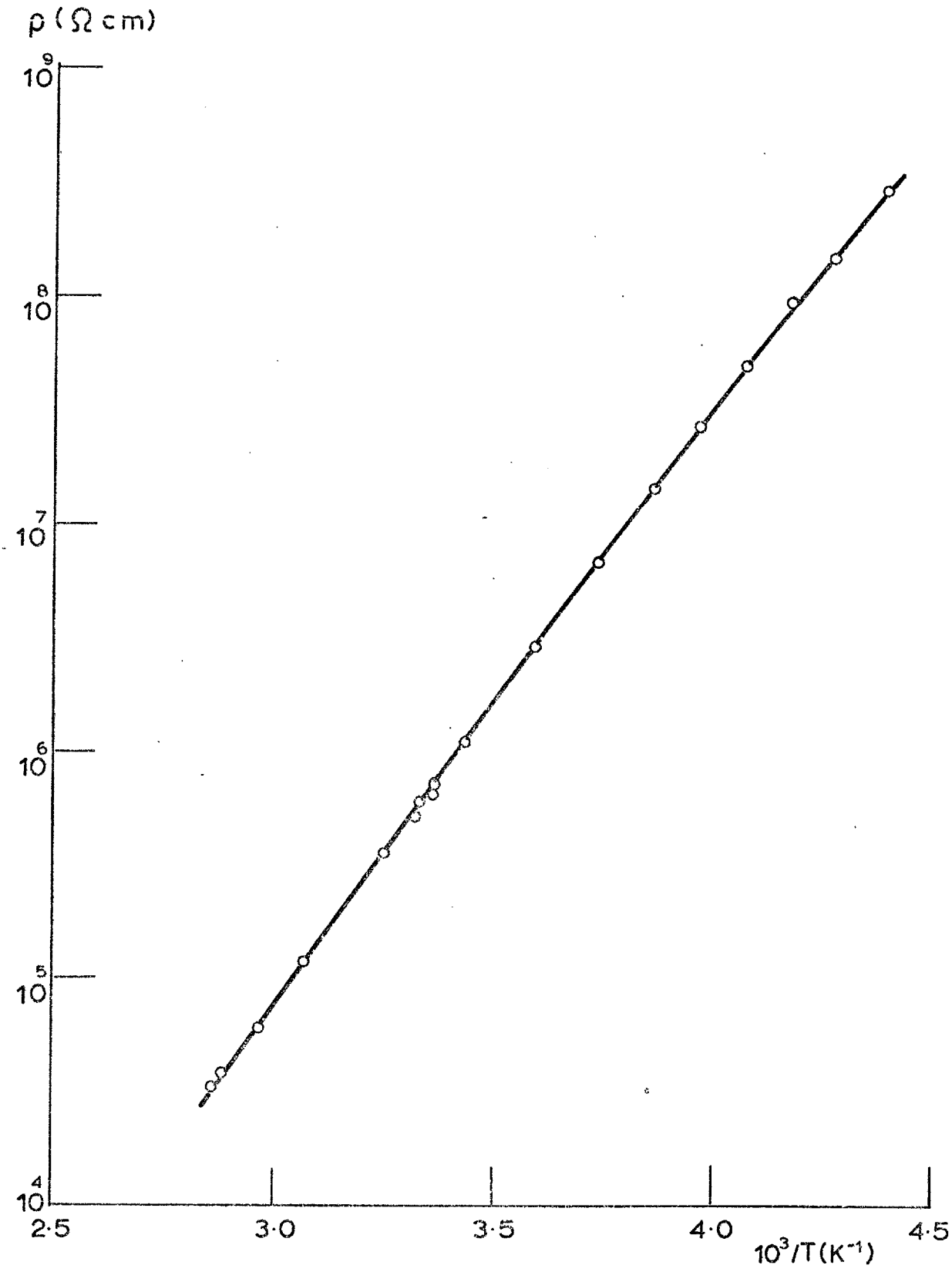


Fig.5·6 Resistivity vs reciprocal temperature in a $Ch_{61}Y_{39}$ SeTAG thin film (Film thickness = 1400 Å)

The low frequency dielectric constants of the films were found to be 8.8 ± 15%. The results were independent of the film thickness within the above experimental error, which was due to the measurements of the film thickness and area.

5.3.6 Field Effect Measurements

The typical field effect configuration used is shown in Fig. 4.13 (Chapter 4). In this type of structure, the gate electrode forms one plate of a parallel plate capacitor, while the semiconductor film acts as the other plate.

A space charge at the surface of a semiconductor may be produced by the application of a capacitative electric field between the gate and the source. A space charge may also occur owing to the presence of surface states.

The field effect structure has an equivalent capacitance circuit shown in Fig. 5.7, where C_{sc} is the space charge capacitance, C_{ss} is the capacitance due to the surface states, and C_g is the geometric capacitance of the device if the semiconductor were replaced by a metal. The total capacitance per unit area, C, is given by,

$$C = \frac{(C_{ss} + C_{sc})\, C_g}{C_{ss} + C_{sc} + C_g} \qquad 5.2$$

Since in the normal field effect configuration,

$$C_{ss} + C_{sc} \gg C_g ,$$

then

$$C \simeq C_g^{*} \qquad 5.3$$

---

*$C_g = \varepsilon_r \varepsilon_o / d$, where ε_r is the relative permittivity of the dielectric insulator, ε_o is the permittivity of free space (= 8.85×10^{-14} F cm^{-1}), and d is the thickness of the insulator. For mica, ε_r = 6.2 was used.

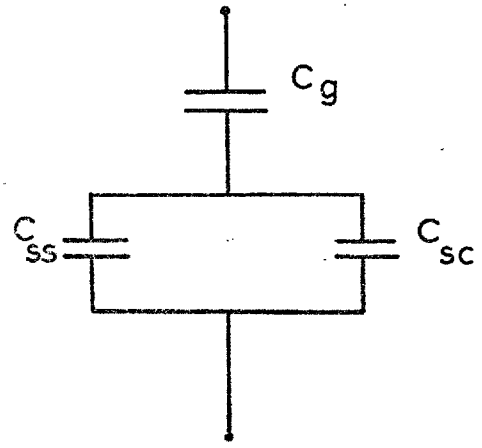


Fig.5·7 Equivalent capacitance circuit of the field effect structure.

Therefore, if a voltage V_g is applied to the gate, the induced charge per unit area, Q_g, at the semiconductor surface is given by,

$$Q_g = C_g V_g \tag{5.4}$$

The small signal field effect mobility, $\mu_{fe}(o)$, is then defined as,

$$\mu_{fe}(o) = \frac{d(\Delta g)}{dQ_g}\Bigg|_{Q_g = 0} \tag{5.5}$$

where Δg is the change in sheet conductance of the semiconductor film due to Q_g. If g_o is the original sheet conductance of the film, then $\Delta g/g_o$ is the fractional change in sheet conductance (i.e. the field effect modulation), and,

$$\begin{aligned} \mu_{fe}(o) &= g_o \cdot \frac{d(\Delta g/g_o)}{dQ_g}\Bigg|_{Q_g = 0} \\ &= \frac{\ell}{R_o w} \cdot \frac{d(\Delta g/g_o)}{dQ_g}\Bigg|_{Q_g = 0} \end{aligned} \tag{5.6}$$

where ℓ is the source-drain separation, w is the electrode width, and R_o is the bulk resistance of the film when $V_g = 0$.

Hence, the small signal field effect mobility may be obtained from the slope of $\frac{\Delta g}{g_o}$ vs. Q_g curve.

The large signal field effect mobility, on the other hand, is related to the total induced surface charge by,

$$\mu_{fe} = \frac{\ell}{R_o w} \cdot \frac{\Delta g/g_o}{\Delta Q_g} \tag{5.7}$$

As already mentioned, no standing field effect modulation was observed in SeTAG thin films. This is in agreement with the results of Egerton[3], and Green et al.[4] on STAG thin films. In both these glasses, the modulation was found to decay to zero with time.

Typical sets of data are presented in Sections 5.3.6.1 to 5.3.6.3 in terms of the dependence of $\Delta g/g_o$ and μ_{fe} on the induced surface charge (expressed in units of Q_g/e cm^{-2}, where $e = 1.6 \times 10^{-19}$ C), temperature, and time.

5.3.6.1 A.C. and Short Time Field Effect Modulations

Fig. 5.8 shows the room temperature (299 K) variation of the field effect modulation with Q_g/e at 4.8×10^{-3}s (210 Hz), 1.8×10^{-2}s (55 Hz), 2s and 10s after the application of the gate voltage to a 1330Å thin film (Film no. 40.79).

Similarly, Fig. 5.9 is the variation of $\Delta g/g_o$ with Q_g/e at 343 K in the same film.

The above data were obtained by recording the change in I_{sd} as a function of peak applied gate voltage (i.e.$\pm \hat{V}_g$).

The room temperature data of Fig. 5.8 illustrate the following points:

(1) No field effect minimum was observed. Hence $p\mu_p > n\mu_n$, where p and n are the hole and electron concentrations, and μ_p and μ_n the respective hole and electron mobilities.

(2) $\Delta g/g_o \propto Q_g$ in the enhancement mode.

(3) $\Delta g/g_o$ decreased with time.

The 210 Hz field effect modulation decreased from 0.39 at 299 K (Fig. 5.8) to 9.6×10^{-2} at 343 K (Fig. 5.9) for a surface charge of -3×10^{11} cm^{-2}.

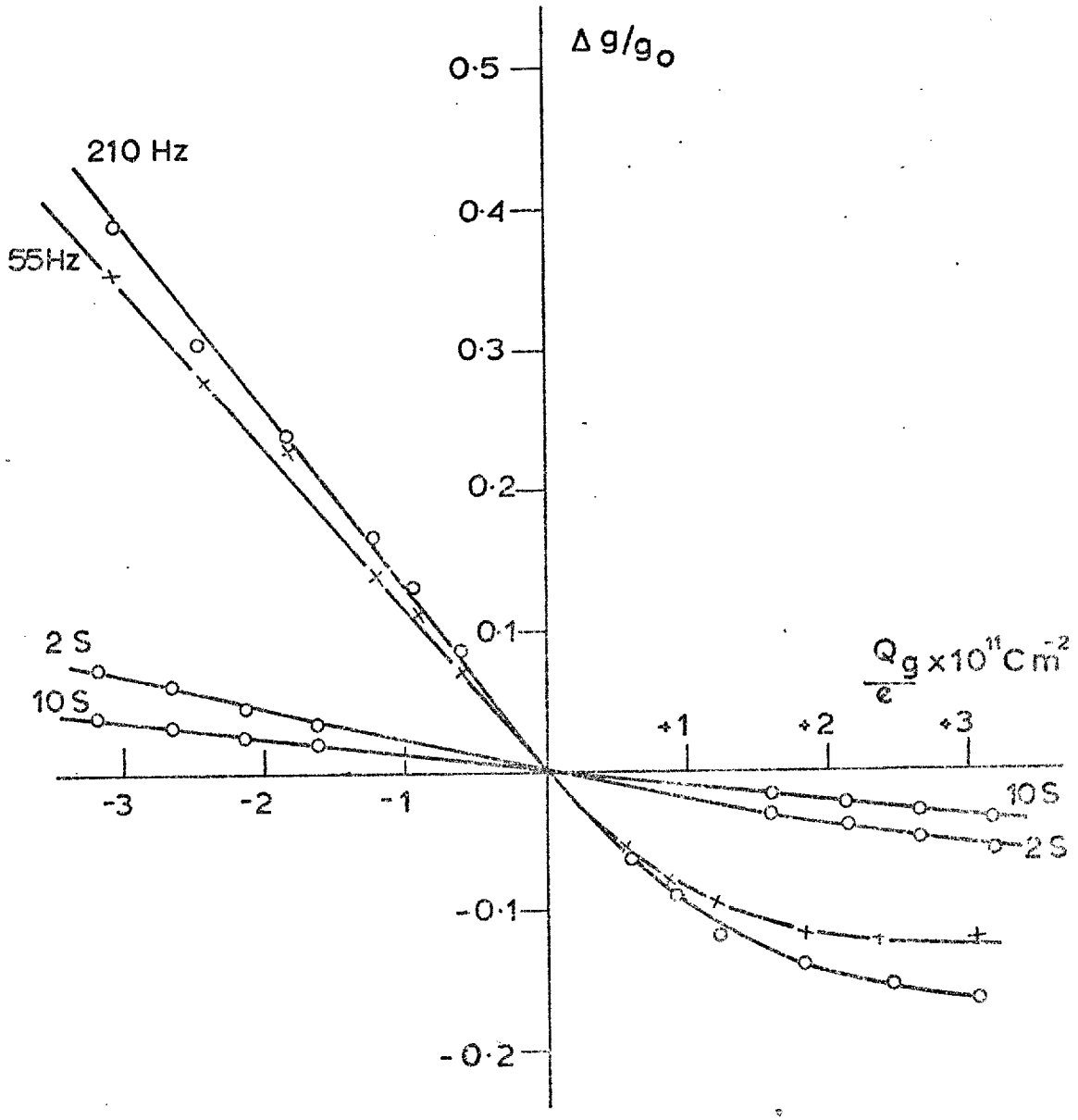


Fig.5·8 Room temperature(299K) field effect modulation as a function of time and charge in film 40·79 (Thickness 1330Å)

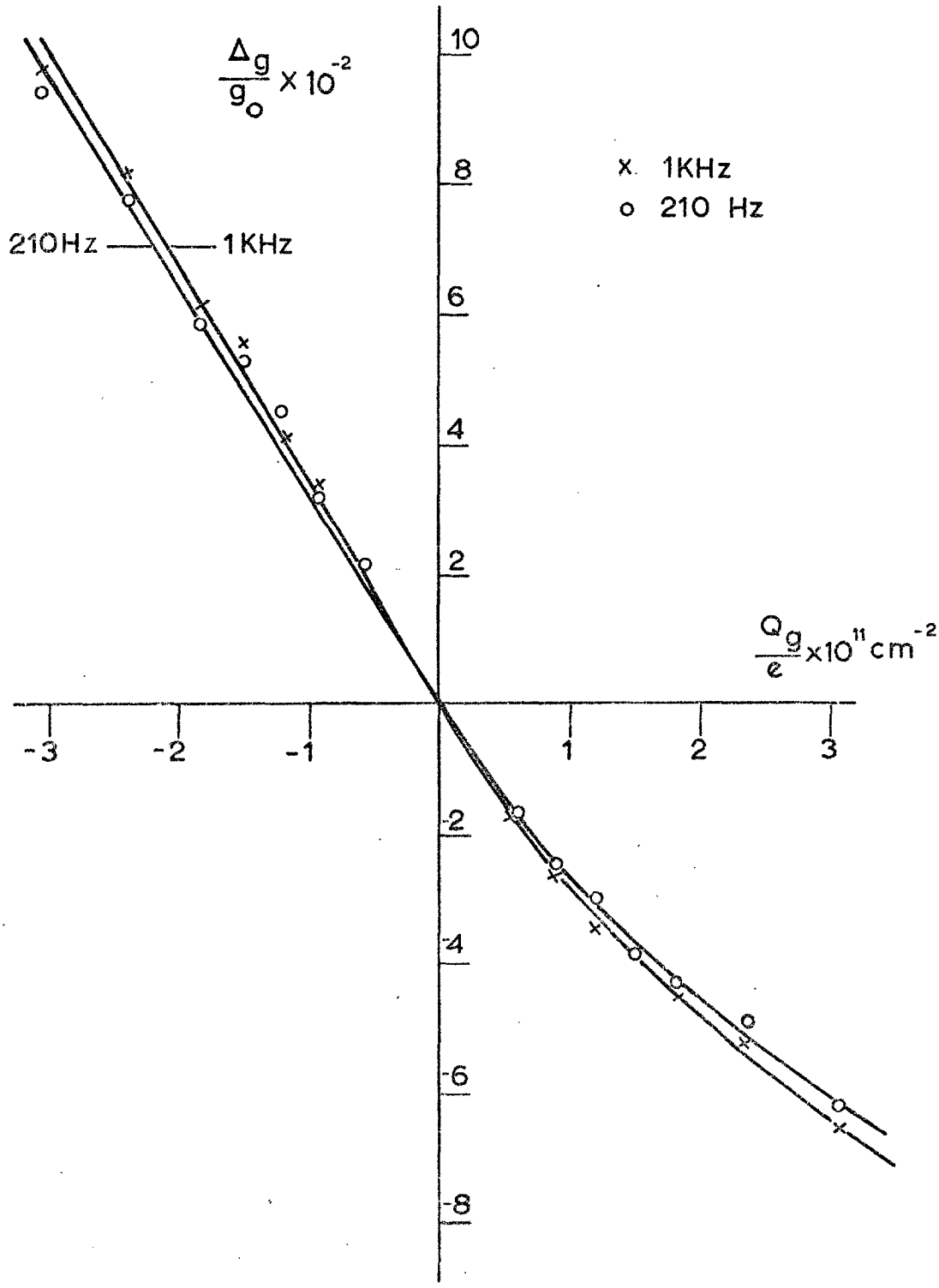


Fig. 5·9 210 Hz and 1 KHz field effect modulation as a function of charge in film 40·79 at 343 K.

The increase in $\Delta g/g_o$ with frequency from 210 Hz to 1 kHz was very small at 343 K. As time constants decrease with increasing temperature, the 210 Hz field effect represents the near maximum "saturation" value of $\Delta g/g_o$ at room temperature. The change in source-drain current, ΔI_{sd}, with frequency at a fixed applied gate voltage is shown in Fig. 5.10 for film 26.9. The near maximum value of ΔI_{sd} was reached at about 210 Hz. This is confirmed by Egerton's unpublished data on STAG glasses, which showed a 10% increase in $\Delta g/g_o$ in going from 200 Hz to 20 kHz using a pulsed technique.

As expected, there was a general increase in modulation with decreasing film thickness. However, there were errors in the observed modulations for the following reasons:

(1) Although the displacement currents were minimised, they were not always completely balanced out. The errors introduced because of this could be as high as 30% in the depletion mode. Since the magnitude of these errors varied from sample to sample, they were probably due to inhomogeneities and thickness variations of the mica insulator in the source-drain gap area. They were not sensitive to the amount of overlap between the gate and the source and drain electrodes.

(2) The thickness of the mica insulator, typically 50 μm, could only be measured to ±5 μm.

(3) Compositional variations between the films, and hence slightly varying film conductivities, also affected the data to some extent.

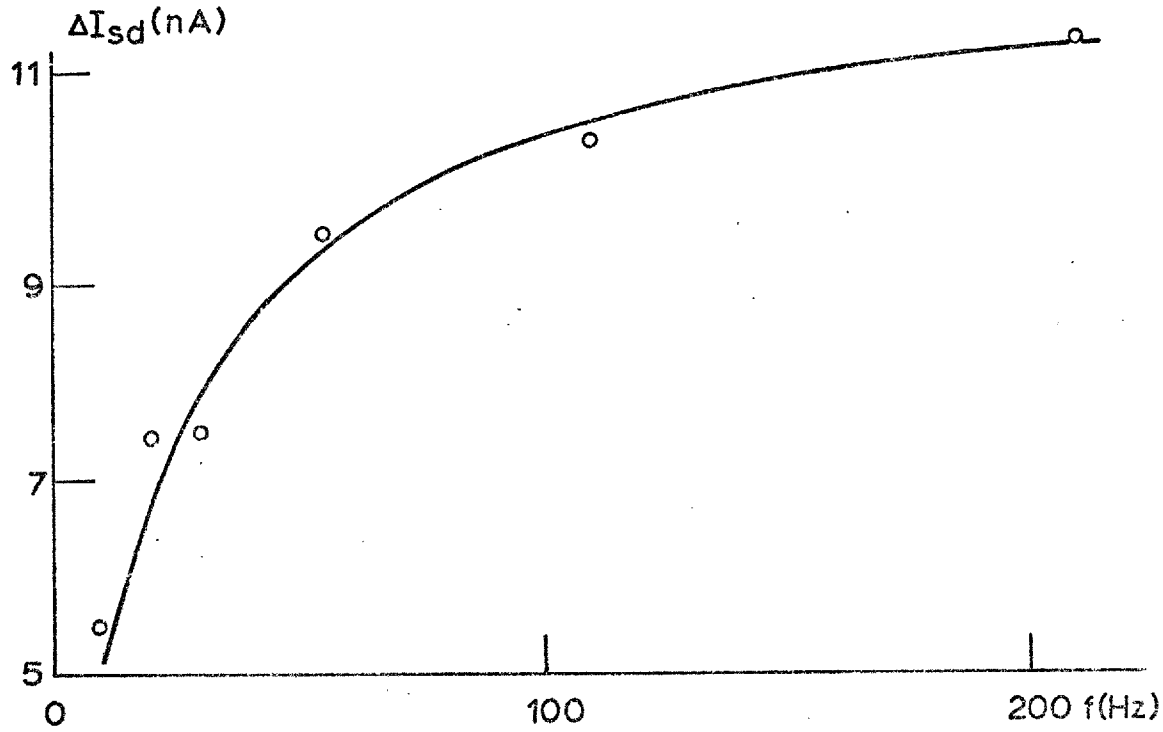


Fig. 5·10 Change in source-drain current at fixed voltage as a function of frequency.

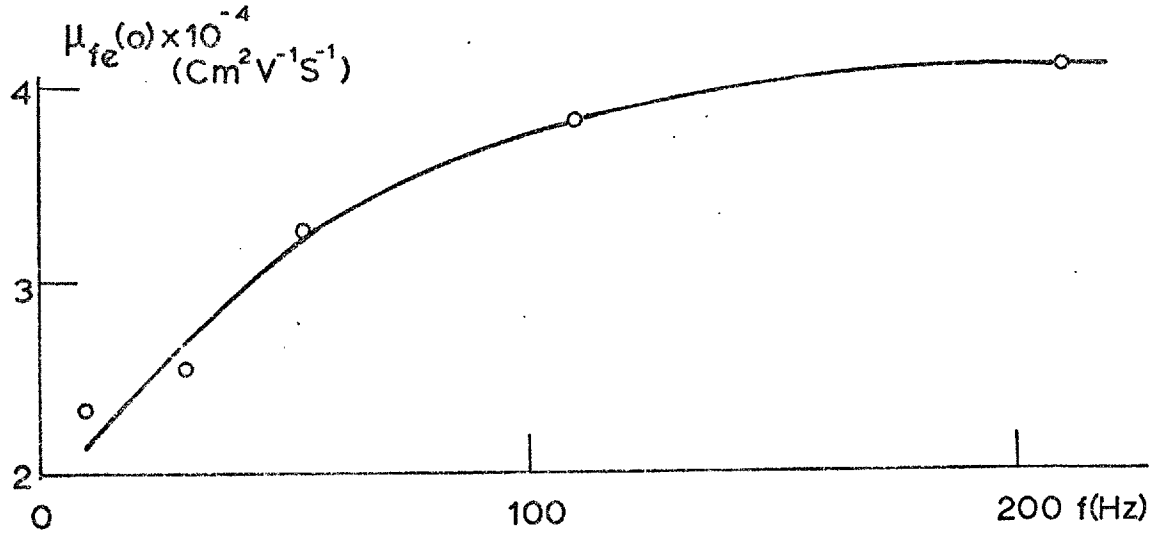


Fig. 5·11 Small signal field effect mobility as a function of frequency.

5.3.6.2 A.C. and Short Time Field Effect Mobilities

Fig. 5.11 shows the room temperature variation of small signal field effect mobility with frequency for film 26.9. It can be seen that a maximum value of about 4.1×10^{-4} cm^2 V^{-1} s^{-1} was reached at a frequency of about 200 Hz.

Figs. 5.12 and 5.13 have been drawn using the 299 K and 343 K data of Figs. 5.8 and 5.9. The former shows the change in μ_{fe} at different times as a function of induced surface charge, while the latter illustrates the time dependent decay in μ_{fe} towards zero irrespective of the sign of the charge on the surface.

5.3.6.3 Long Time D.C. Field Effect Data

The decay of $\Delta g/g_o$ with time and temperature is plotted in Fig. 5.14 for a 520Å film. The concentration of the excess surface charge was -3.7×10^{11} cm^{-2}. The data were obtained by using a step gate voltage of -655 V in the circuits of Fig. 5.3 (for short time measurements <15s) and Fig. 5.4 (for long time measurements >2s). Using the bridge technique the smallest out of balance voltage which could be measured was about 0.2 mV, which was of the order of the circuit noise. The decay in $\Delta g/g_o$ was faster at elevated temperatures and therefore easier to observe and more independent of drift. Since the rate of field effect current decay decreases with decreasing temperature, at low temperatures it is possible to mistake a slow decay for a standing, "steady state", modulation. As already mentioned, it is believed that some of the reported field effect data in the literature may suffer from this experimental artifact.

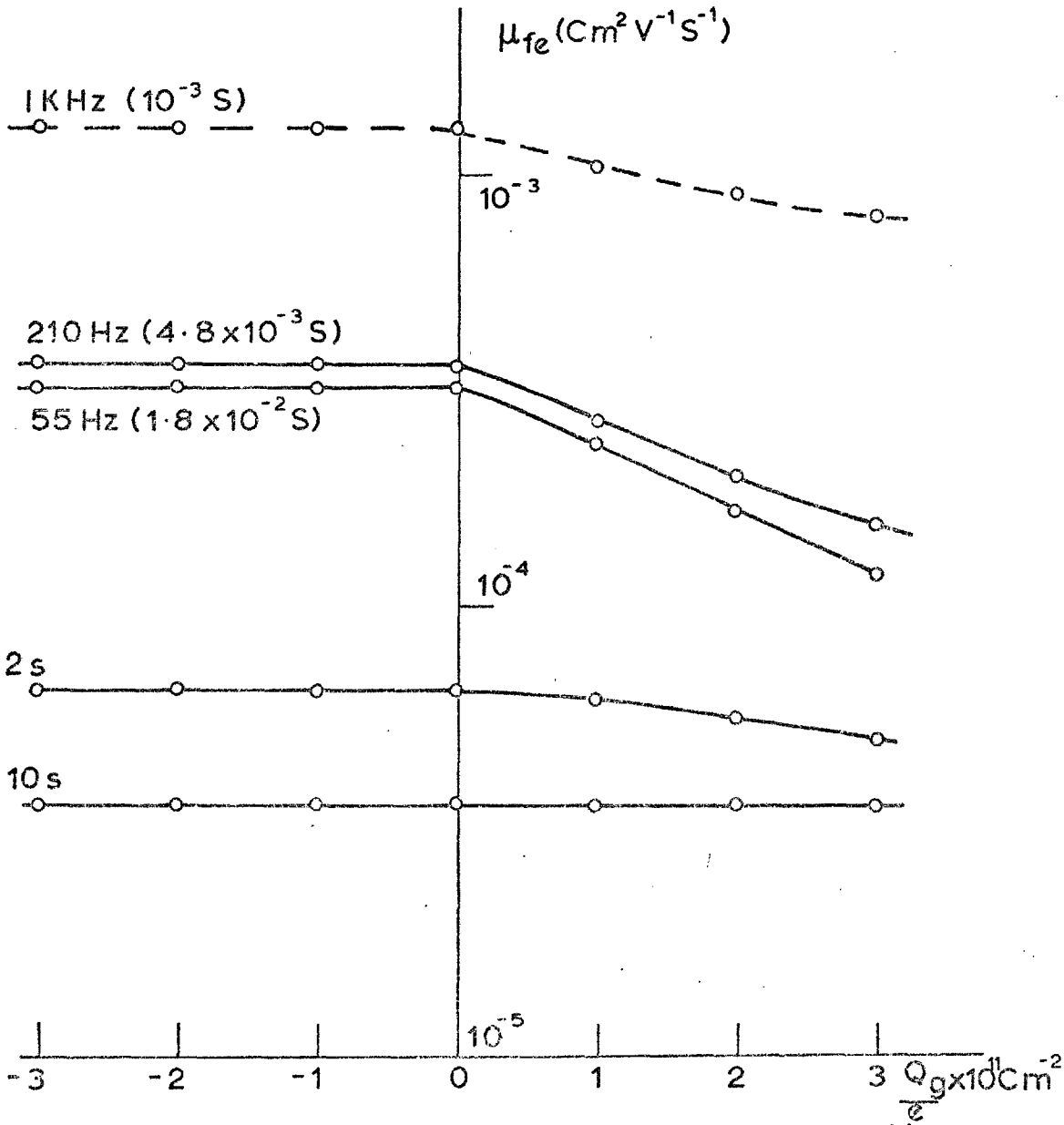


Fig. 5·12 Variation of large signal field effect mobility with induced surface charge at different times in film 40·79 (Solid lines: T = 299 K, broken line: T = 343 K)

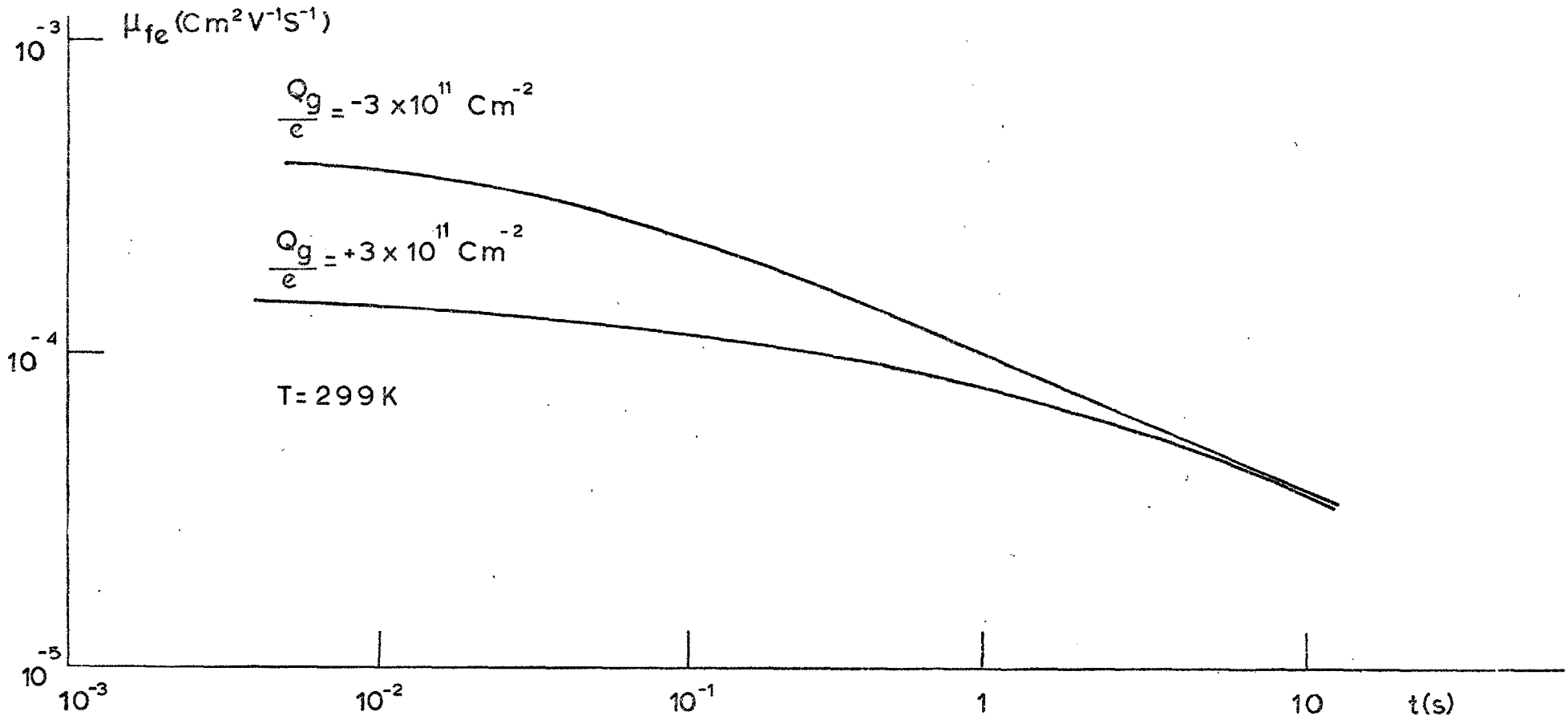


Fig. 5·13 Decay of field effect mobility as a function of induced surface charge in film 40·79.

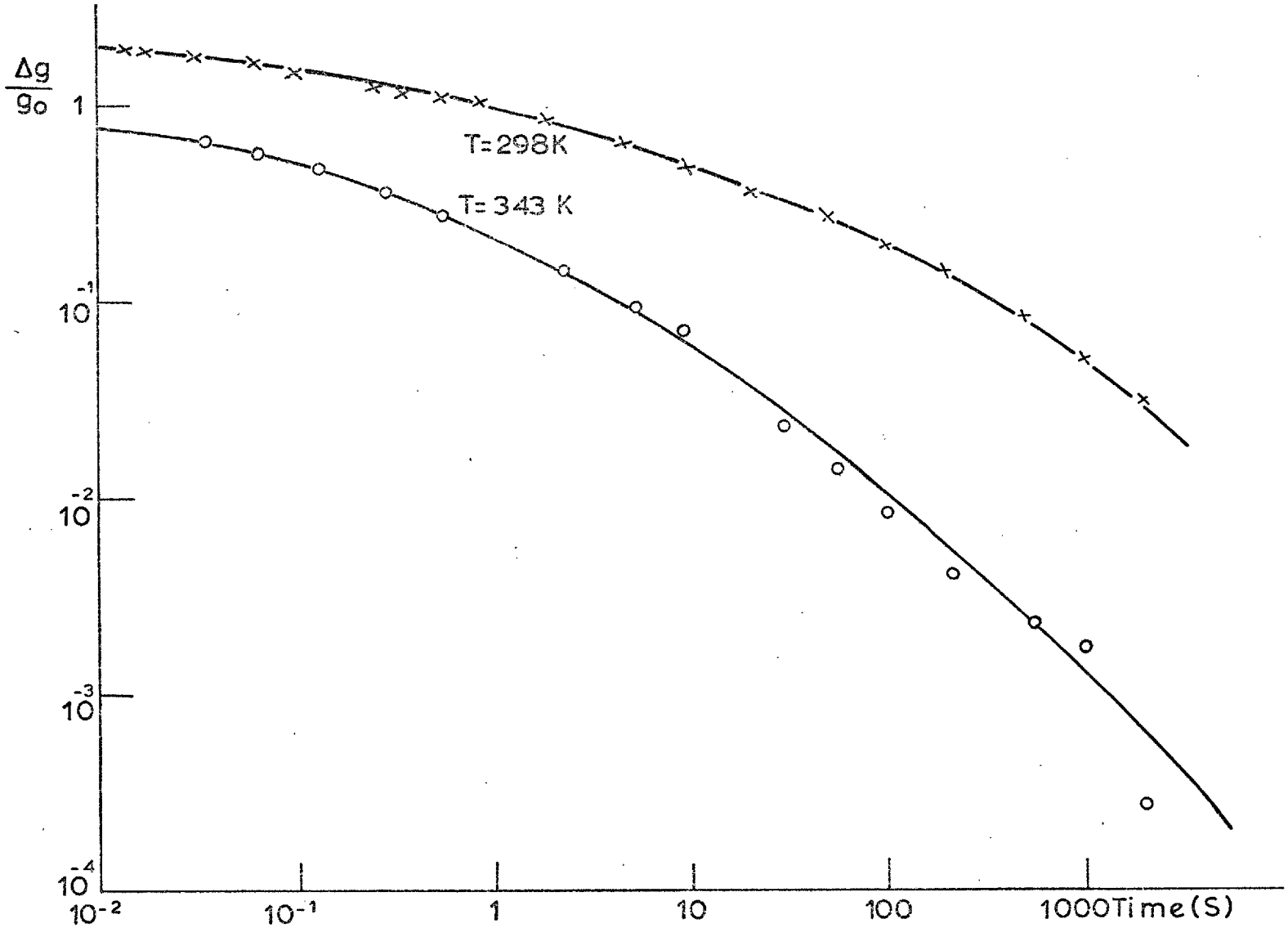


Fig. 5·14 Decay of field effect modulation with time at T=298K and 343K (Film thickness=520Å, $Q_{g/e}$=-3·7x10^{11} Cm^{-2})

The decay in $\Delta g/g_o$ is not attributed to slow states in the dielectric. It was possible to fabricate a few structures using sputtered quartz as the gate insulator : a similar decay in the fractional modulation was observed when a step voltage was applied to the gate. Furthermore, the field effect decay was also observed in STAG glass thin films when a field was applied to the free surface of a virgin film in vacuum[11].

Extrapolation of the data of Fig. 5.14 for times less than 10^{-2}s shows that $\Delta g/g_o$ reaches its effective maximum value at about 200 Hz in agreement with the earlier data of Figs. 5.10 and 5.11.

Fig. 5.15 shows the change in large signal field effect mobility with time for the data of Fig. 5.14. A decay towards zero for longer times is again illustrated (c.f. Fig. 5.13) to the lowest measurable μ_{fe} of about 3×10^{-7} cm^2 V^{-1} s^{-1}.

It should be noted that the R.C. time constant of the system was less than 10^{-4} seconds. The rise time of the current in the sample was not measured directly, but it was observed to be much less than 1 ms.

5.4 Analysis of Results

5.4.1 Resistivity Data

The linear I-V characteristics, and the linear dependence of film resistance on electrode separation both indicate "ohmic" contacts between the chromium electrodes and the semiconductor film.

The data of Table 5.1 show the room temperature resistivity to be independent of film thickness in the range 500 - 1800Å, and that any observed variation is random, and due to compositional and temperature effects. In other words, the bands

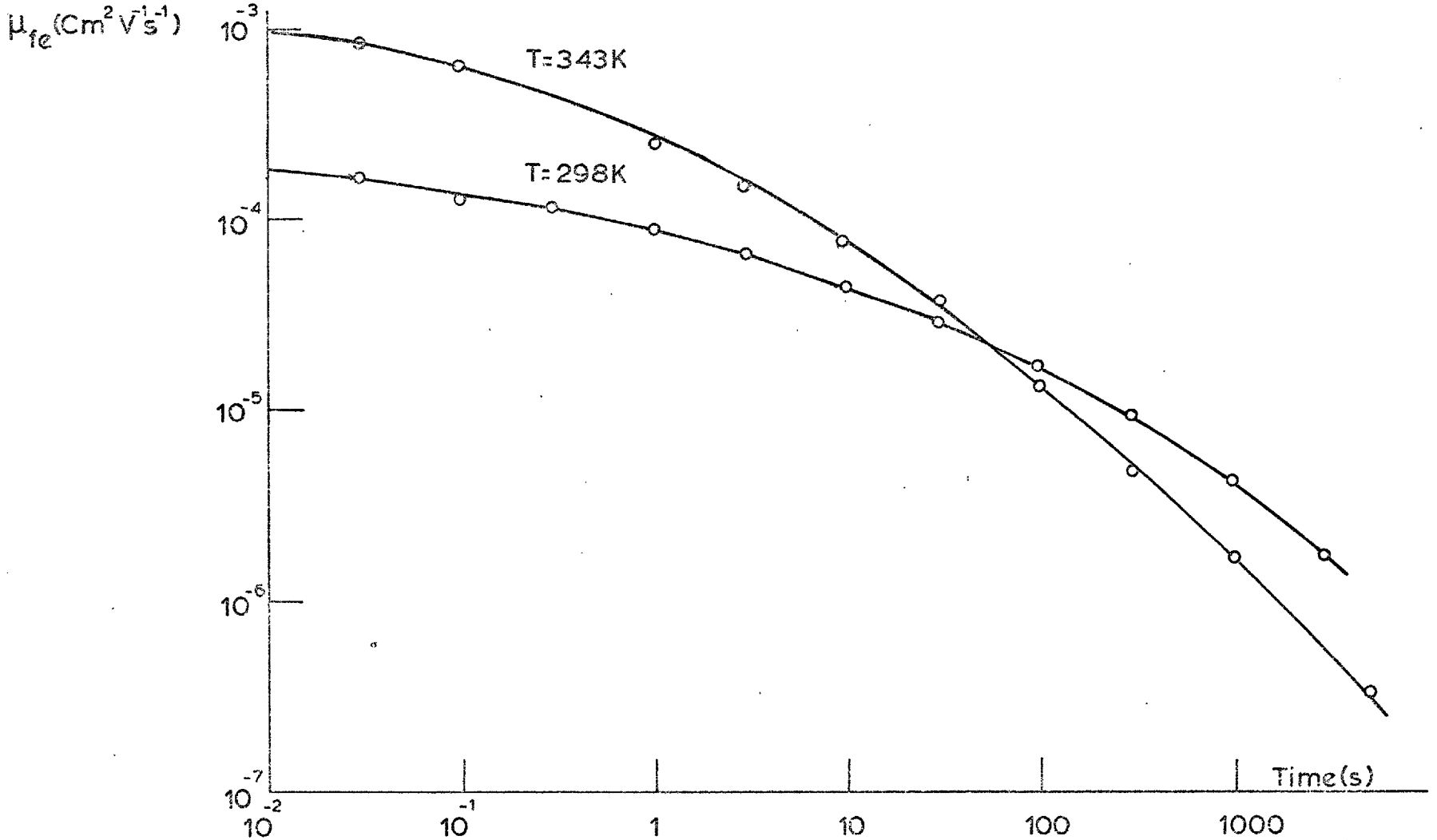


Fig. 5·15 The field effect mobility in film 30·9 as a function of time at T=298K and 343K $\left(\frac{Q_g}{e}=-3.7\times10^{11}\ cm^{-2}\right.$, film thickness= 520 Å$\left.\right)$

may be considered to be effectively flat at the surface, since no space charge effects can be observed.

The plot of logarithm of resistivity against the recirprocal of temperature does not result in a straight line, but instead some curvature is observed as in the bulk glass. This indicates that the bulk and thin film specimens behave in a similar manner, and that contrary to Mott et al.'s proposition[12], the curvature is intrinsic to the material and not sensitive to the method of specimen preparation. The thin films had average "straight line" activation energies of 0.51 - 0.53 eV compared to the bulk value of about 0.49 eV, which may be due to compositional changes in the thin film samples as compared to the bulk glass.

5.4.2 Field Effect Data

The A.C. field effect data are analysed in terms of the Barbe model using the CFO density of states distribution. A new model is also proposed to explain the decay in D.C. field effect modulation to zero.

5.4.2.1 A.C. Field Effect : The Barbe Model

Barbe used the CFO density of states model, and assumed that the donor and acceptor state densities were slowly varying functions of energy about the Fermi level, and that their sum was approximately constant over ±5 kT of E_F. The space charge calculations were further simplified by employing the zero degree Kelvin Fermi-Dirac function, which was a reasonable approximation for the case of constant density of states.

Poisson's equation is solved in the Barbe model by making the above assumptions. This leads to an expression for the Debye

screening length, L, given by,

$$L = (\varepsilon\varepsilon_o / e^2(N_A^F + N_D^F))^{\frac{1}{2}} \qquad 5.8$$

where ε is the low frequency dielectric constant of the semiconductor ($\varepsilon = 8.8$), and ε_o is the permittivity of free space ($\varepsilon_o = 8.8 \times 10^{-14}$ F cm^{-1}). N_A^F and N_D^F are the densities of acceptor and donor type localised states at the Fermi level respectively. The total density of states at E_F, $N(E_F)$, is,

$$N(E_F) = N_A^F + N_D^F$$

The charge on the field plate, Q_g, is equated to the total charge in the space charge region, Q_{sc}, and that in the surface states, Q_{ss}, i.e.,

$$Q_g = -Q_{sc} - Q_{ss}$$

where, by considering the electric field at the surface of the semiconductor, the above may be written as,

$$Q_g = \frac{\varepsilon\varepsilon_o kT}{e} \left(\frac{1}{L} + \frac{e^2(N_{As}^F + N_{Ds}^F)}{\varepsilon\varepsilon_o} \right) v_s \qquad 5.9$$

where v_s is the surface potential in kT units, and N_{As}^F and N_{Ds}^F are the number of donor and acceptor type surface states (per unit area per unit energy) at E_F.

The excess sheet conductance, Δg, is obtained by assuming Maxwell-Boltzmann statistics for mobile holes and electrons, i.e.

$$\Delta g = g(v_s) - g(o) = e(\mu_n \Delta n + \mu_p \Delta_p) \qquad 5.10$$

where, for electrons,

$$\left.\begin{aligned} \Delta n = n_b L \int_o^{v_s} \frac{e^v - 1}{v}\, dv = n_b L \sum_{m=1}^{\infty} \frac{v_s^m}{m.m!} = n_b L F_n \\ \text{and, for holes,} \\ \Delta p = p_b L \int_o^{v_s} \frac{e^{-v} - 1}{v}\, dv = p_b L \sum_{m=1}^{\infty} \frac{(-v_s)^m}{m.m!} = p_b L F_p \end{aligned}\right\} \qquad 5.11$$

Subscripts 'b' in the above refer to bulk values. From (5.10) and (5.11),

$$\Delta g = L(\sigma_{bn} F_n + \sigma_{bp} F_p)$$

The field effect mobility is defined as,

$$\mu_{fe} = \frac{d(\Delta g)}{dQ_g} = \frac{d(\Delta g)/dv_s}{dQ_g/dv_s} \qquad 5.12$$

For single carrier hole conduction, and neglecting surface states, equations 5.9 to 5.12 give,

$$\mu_{fe} = \frac{e^2 L^2 p_b \mu_p}{\varepsilon \varepsilon_o kT} \cdot \frac{dF_p}{dv_s} = \frac{eL^2 \sigma_b}{\varepsilon \varepsilon_o kT} \cdot \frac{dF_p}{dv_s} \qquad 5.13$$

where σ_b is the bulk conductivity.

For small signals, $\frac{dF_p}{dv_s} \simeq -1$, and therefore,

$$\mu_{fe}(o) = - \frac{eL^2 \sigma_b}{\varepsilon \varepsilon_o kT} \qquad 5.14$$

Also, the fractional change in sheet conductance relative to the zero field, flat band condition, g_o, is,

$$\frac{\Delta g}{g_o} = \frac{L\sigma_b F_p}{\sigma_b t} = \frac{LF_p}{t} \qquad 5.15$$

Experimentally, the slope of the A.C. field effect trace about $V_g = 0$ gives the small signal field effect mobility, i.e. (c.f. equation 5.6),

$$\mu_{fe}(o) = \frac{1}{V_{sd}} \cdot \frac{\ell}{w} \cdot \frac{\Delta I}{\Delta Q_g} \Big|_{Q_g = 0} \qquad 5.16$$

Equating 5.14 and 5.15, and putting $\sigma_b = \frac{I_o \ell}{V_{sd}\, \omega t}$, where I_o is the zero field current, one obtains,

$$L^2 = \frac{kT\varepsilon\varepsilon_o t}{e.I_o} \cdot \frac{\Delta I}{\Delta Q_g} \Big|_{Q_g = 0} \qquad 5.17$$

Also, from 5.8 and 5.17,

$$N(E_F) = \frac{I_o}{e.t.kT} \cdot \frac{\Delta Q_g}{\Delta I} \Big|_{Q_g = 0} \text{ cm}^{-3}\ \text{eV}^{-1} \qquad 5.18$$

if kT is in eV units.

Using equations 5.16-5.18, the values of $\mu_{fe}(o)$, L, and $N(E_F)$ for various films were calculated, and the results are shown in Table 5.2. It is emphasised that the above were obtained from the small signal A.C.field effect data. It can be seen that both $\mu_{fe}(o)$ and $N(E_F)$ increase with temperature, whereas the screening length shows a slight reduction.

Film No.	Thickness Å	T(K)	$\rho \times 10^5$ (Ωcm)	$\mu_{fe}(0) \times 10^{-4}$ ($cm^2 V^{-1} s^{-1}$)	L(Å)	$N(E_F) \times 10^{19}$ ($cm^{-3}\ eV^{-1}$)
26.9	1450	299	1.7	4.1	114	0.37
28.9	1450	299	3.1	3.8	150	0.21
30.9	520	298	10.4	1.94	146	0.22
30.9	520	343	0.69	10.2	127	0.30
40.79	1330	299	2.71	4.0	136	0.27
40.79	1330	343	0.20	14.0 (at 1 KHz)	79	0.87
46.9	1710	295	11.4	0.95	160	0.18
47.9	1500	297	4.4	4.2	170	0.17
48.9	1770	293	6.4	1.7	145	0.23
52.10	1100	299	4.3	1.6	106	0.43
52.10	1100	343	0.27	7.0	69	1.11

Table 5.2. 210 Hz Field Effect Mobility in SeTAG Thin Films, together with the Screening Length and the Density of States at E_F Computed from the Barbe Model by Neglecting Surface States.

5.4.3.2 D.C. Field Effect Modulation Decay

In conventional semiconductor theory, a very small field effect modulation may be ascribed to either most of the induced charge being trapped by the surface states, or to a very large bulk density of states at E_F. These possibilities will be examined in the light of the data obtained from the Barbe model. Consider the 343 K data of Fig. 5.14:

(a) Surface states

For induced charge trapped in surface states of density N_s^F,

$$N_s^F \cdot v_s = Q_g$$

and from equation 5.15 and Fig. 5.14 at 5000 seconds,

$$\frac{\Delta g}{g_o} = \frac{L}{t} F_p = 2.5 \times 10^{-4}$$

Take $t = 520\text{Å}$, and $L = 140\text{Å}$ (Table 5.2). Therefore,

$$F_p = 9.29 \times 10^{-4} \text{ kT units}$$

$$\simeq - v_s \text{ (small signal approximation)}$$

Hence

$$N_s^F \simeq \frac{3.7 \times 10^{11}}{9.29 \times 10^{-4}} = 4 \times 10^{14} \text{ cm}^{-2} (\text{kT})^{-1}$$

$$= 1.35 \times 10^{16} \text{ cm}^{-2} \text{ eV}^{-1}$$

Taking the molecular volume of SeTAG to be about 18 cm^3 (Table 2.2, Chapter 2), there are $\frac{6 \times 10^{23}}{18} = 3.3 \times 10^{22}$ atoms cm^{-3} in the solid, and 1.2×10^{15} atom cm^{-2} on the surface for a cubic lattice.

The Barbe model requires the total trapped charge to be within ±5 kT of E_F. Therefore, 4×10^{15} states cm^{-2} are required at the surface compared to about 10^{15} states cm^{-2} available if one surface state per atom is assumed. As such a large number of surface states is unreasonable, surface states cannot successfully account for the small modulations.

(b) Bulk states

From equations 5.16 and 5.18

$$N(E_F) \propto 1/\mu_{fe}$$

At 343 K and 210 Hz, $N(E_F) = 3 \times 10^{18}$ cm^{-3} eV^{-1}, and $\mu_{fe}(o) = 1 \times 10^{-3}$ cm^2 V^{-1} s^{-1}. After 5000 sec, the field effect mobility is about 3×10^{-7} cm^2 V^{-1} s^{-1}, which would, therefore, require 1×10^{22} states cm^{-3} eV^{-1}. Such a large density of states at E_F seems unreasonable, since this would correspond to a total density of 3×10^{21} cm^{-3} over ± 5 kT.

Since the above possibilities do not explain the decay in field effect conductivity to its zero field value, a model is proposed below, which considers a discrete distribution of charged centres in the semiconductor.

5.4.2.3 The Discrete Charge Model

Following Street and Mott[13], and Mott, Davis and Street[12], it is assumed that positively and negatively charged spin paired centres (D^+ and D^-) exist throughout the bulk of the semiconductor. These centres affect the energy distribution of the localised states in their close vicinity, but would cause only negligible perturbations in the extended states, since carriers

with extended wavefunctions will not be screened by any local fluctuations in charge density.

As a first approximation, the above centres may be considered to be imbedded in a dielectric. Qualitivately, the D.C. field effect decay may be explained as follows:

Initially, when the gate voltage is applied, there is excess accumulation of charge in the extended states. By Gauss' law, the applied field must terminate on charge : at zero time just after the application of the field, the field terminating charges are bulk distributed. Hence, most of the field variation occurs outside the regions of point charges, which causes a shift in the Fermi energy in the bulk, and hence a non-equilibrium distribution of carriers in the extended states. In this regime, the measured field effect mobility is expected to be trap limited.

With increasing time, there is continuous trapping and release of charge by states deep in the mobility gap. Under the influence of the field, however, this exchange is coupled with a general movement of the charge towards the field plate. Eventually, all the field terminating charge will be distributed near the semiconductor dielectric interface, and since the volume element in which the field varies around each charge is now limited to a narrow region near the interface, the amount of final modulation observed as a result of this will be shown to be small, and may even be zero.

Since the treatment of this problem for a totally random distribution of charged centres is prohibitive, the potential distribution around a charged centre may be considered using the Debye-Hückel (D-H) electrolyte model. This is derived for dilute solutions, in which the exponential term in the Boltzmann

distribution function is expanded and it is assumed that,

$$e^{-Q_i\psi/kT} \simeq 1 - \frac{Q_i\psi}{kT}$$

where $\frac{Q_i\psi}{kT} \ll 1$. Here, Q_i is the charge on an ion of type i, so that $Q_i\psi$ is the work required to bring the ion into a region of potential ψ. For a dilute solution, the interionic potential energy is small, and assumed to be much less than the average thermal energy (i.e. $Q_i\psi \ll kT$). In the case of the amorphous solid, it is assumed that a frozen Boltzmann distribution prevails, which is established near the molten state of the solid, where the D-H approximation remains valid. The D-H expression for the radial potential distribution, $\psi(r)$, about an ion of type i is,

$$\psi(r) = \frac{z_i e \cdot \exp(-b(r-a))}{4\pi\varepsilon\varepsilon_o r(1 + ba)} \qquad 5.19$$

where z_i is the sign and charge in units of e of ions of type i, b is the reciprocal Debye length (i.e. the screening length of the ionic atmosphere), a is the distance of nearest approach between ions, and the other symbols have their usual meanings. b is given by,

$$b = \frac{e^2(n_i|z_i|^2 + n_j|z_i|^2)}{\varepsilon\varepsilon_o\, kT_m} \qquad 5.20$$

where T_m is the melting temperature of the solid, and $n_i = n_j$, and $|z_i| = |z_j| = 1$. n is the concentration of the relevant ionic species.

It was found that a plot of $\psi(r)$ vs. r using the D-H approximation (for $r < a$, the coulomb potential was used) corresponded very well with the potential distribution computed by assuming that the positive and negative centres are located on lattice points in a cubic structure (see Green and Lee[15]). It was thus deemed permissible, to a first approximation, to consider the charged centres to be distributed uniformly in a cubic array in the semiconductor bulk.

5.4.2.3.1 Prediction of an upper limit for $\Delta g/g_o$ at long times

In any quantitative analysis, it would be useful to test the validity of the above theory by considering the maximum upper limit of the final predicted modulation as a result of a specified charge density on the gate plate. This may be done for the present model by considering the potential distribution due to a square array of charges in a plane $z = b$ from the field plate as shown in Fig. 5.16(a)*. The other defining parameters are also shown. If a is the lattice spacing in the square array, then a unit cell around a point charge may be defined (Fig. 5.16(b)), and the potentials at points in the triangle (0,0), ($^a/2$, 0), ($^a/2$, $^a/2$) due to all the point charges in the array in any z plane uniquely determine the potential distribution of the system in that plane.

Such a problem has been treated by Levine[16] for a square array of charged surface states at the semiconductor/dielectric interface in an MIS system. The only difference with the present case is that here the charge array is at a small distance from the

---

*The specific values of a and b shown in Fig. 5.16(a) refer to a case example, which is discussed later.

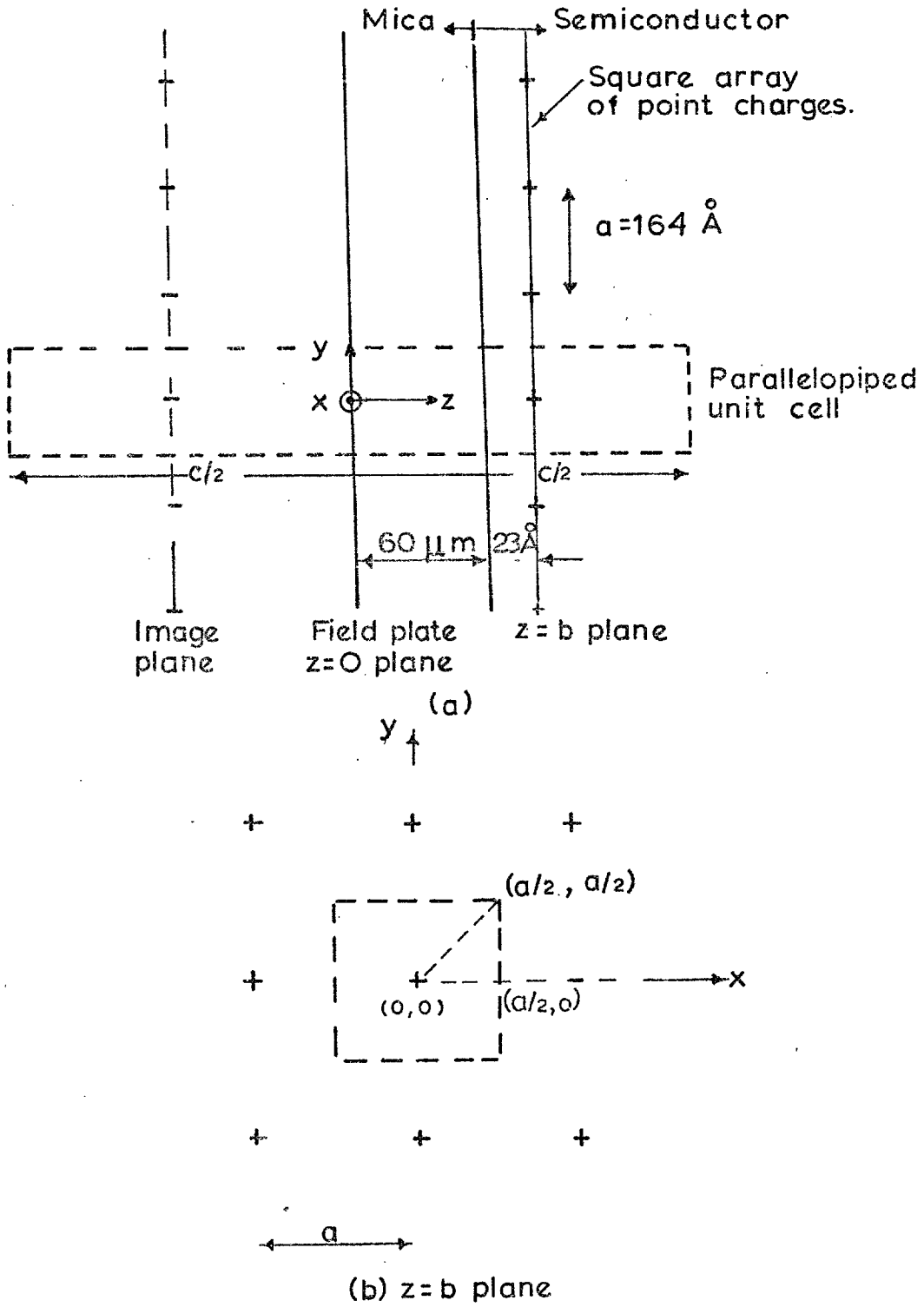


Fig. 5·16 (a) Model used to compute the potential distribution due to a plane of charges near the interface in an MIS system (b) Definition of a unit cell in a square array of charge.

interface into the semiconductor bulk. Levine derives an expression for the potential V(x,y,z), where (x,y,z) are the spatial cartesian coordinates shown in Fig. 5.16(a). By applying the method of images with Neumann boundary conditions* to the parallelopiped unit cell shown, Poisson's equation is solved, and V is expressed as the sum of a harmonic series in ℓ and m, where,

$$V = \sum_{\ell,m=-\infty}^{\infty} V_{\ell m}(x,y,z) \qquad 5.21$$

and ℓ, m define the various harmonic modes.

The zeroth harmonic, V_{oo}, in the above series is independent of x and y, and it represents the solution in the one-dimensional limit, i.e.,

$$V_{oo} = \frac{-|e|}{\varepsilon\varepsilon_o a^2}\left(\frac{|z+b| - |z-b|}{2}\right) \qquad 5.22$$

$$= \frac{-|e|b}{\varepsilon\varepsilon_o a^2} \qquad z \geq b$$

$$= \frac{-|e|z}{\varepsilon\varepsilon_o a^2} \qquad 0 \leq z \leq b$$

---

*For the negative charge, say, in the unit cell, these are,

$\partial V_-/\partial x = 0$ at $x = 0, a/2$

$\partial V_-/\partial y = 0$ at $y = 0, a/2$

$\partial V_-/\partial z = 0$ at $z = \pm c/2$ where $c >> b$

The other terms in the summation are expressed as,

$$V_{\ell m} = \frac{-|e|}{4\pi\varepsilon\varepsilon_o a} \cdot \frac{\cos(2\ell\pi x/a)\cos(2m\pi y/a)}{(\ell^2 + m^2)^{\frac{1}{2}}} \{\exp(-\frac{2\pi}{a}(\ell^2 + m^2)^{\frac{1}{2}}|z-b|) - \exp(-\frac{2\pi}{a}(\ell^2 + m^2)^{\frac{1}{2}}|z+b|)\} \quad 5.23$$

where ℓ and m are not both zero. For $|z+b| >> a$, the second exponential term in the above expression may be neglected. The potential, ϕ, is then defined as,

$$\phi(x,y,z) = \sum_{\ell,m=-\infty}^{\infty} V_{\ell m}(x,y,z) \quad 5.24$$

(ℓ and m not both zero)

The potential V_{oo} is not included in the above sum, i.e.,

$$\phi(x,y,z) = V(x,y,z) - V_{oo} \quad 5.25$$

From equations 5.23 and 5.24, ϕ is symmetrical about $z = b$, and is the sum of a convergent series (except at (o,o,b) where it goes to infinity).

In Fig. 5.17, ϕ (x,y) is mapped out in units of $e/4\pi\varepsilon\varepsilon_o a$ in three different z planes. With increasing x and y, the potential eventually changes sign over a region indicated approximately by the circular arcs shown. In any z plane, the potential goes through a maximum at (a/2, a/2), and a saddle point at (a/2, 0).

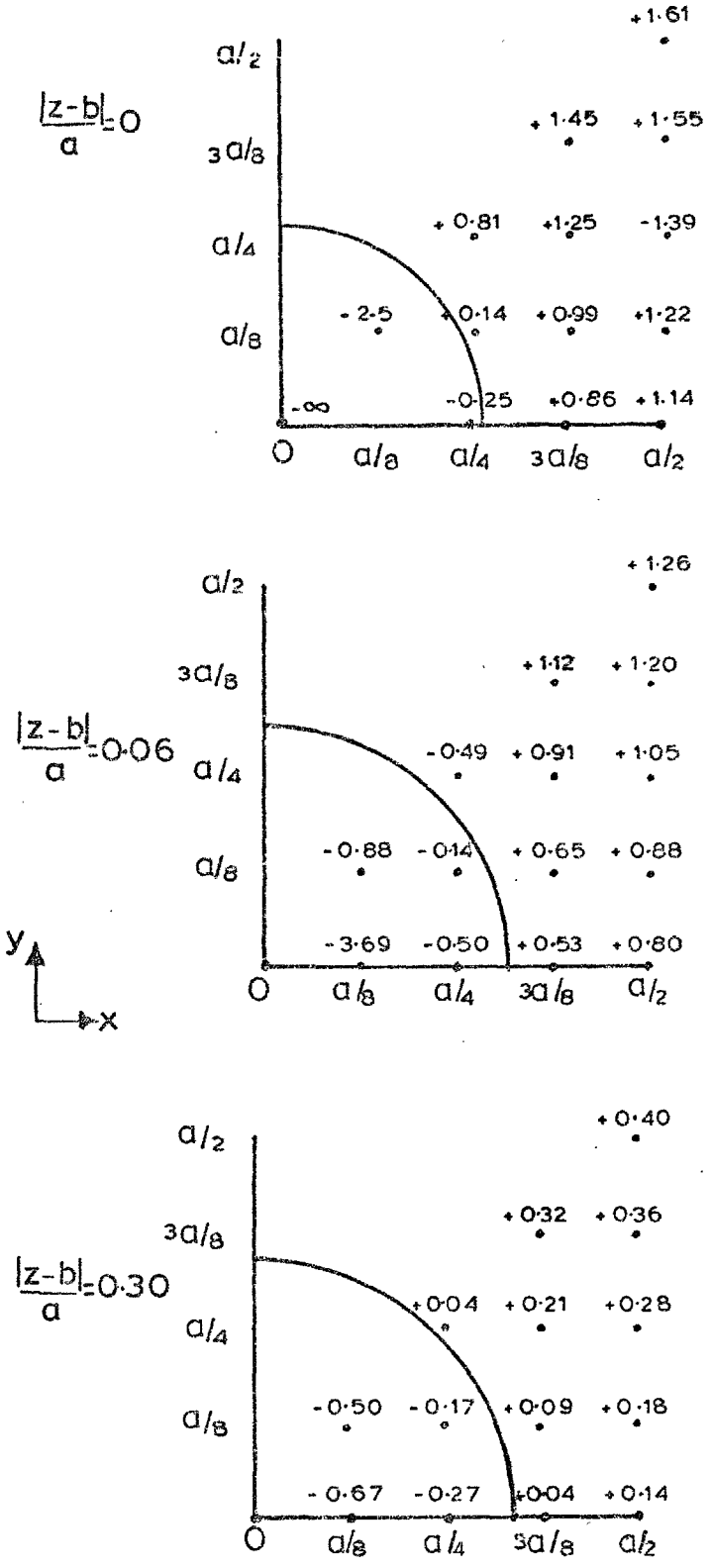


Fig. 5.17 $\phi(x,y)$ in units of $\frac{e}{4\pi\varepsilon_0 a}$ computed in various z-planes.

The case of film 30.9, whose conductivity modulation decay with time is shown in Fig. 5.14, is now considered. The experimental parameters relevant to this film were:

(1) $\frac{Q_g}{e} = -3.7 \times 10^{11}$ charges cm^{-2}

(2) Thickness of the dielectric = 60 μm

In a square array, 3.7×10^{11} charges cm^{-2} would correspond to a lattice length of 164Å. In other words, in Fig. 5.16(a), a = 164Å, if one considers the charge distribution to be uniform over the gate electrode, and the field terminating centres in the semiconductor to be in a plane parallel to the gate. It is also assumed that each centre carries a unit charge of equal and opposite sign to that on the gate electrode.

For a density of charged centres of 10^{19} cm^{-3} in the semiconductor bulk, arranged in a cubic lattice, the intercentre spacing is about 46Å. Hence, the average distance between the plane of charge near the semiconductor/dielectric interface and the interface is taken to be 23Å. Therefore,

$$b = 60\ \mu m + 23\text{Å}$$

as shown in Fig. 5.16(a).

Fig. 5.18 shows plots of $\phi(x,y,z)$ against $|z-b|$ for various values of (x,y), and using $\varepsilon = 8.8$ (i.e. neglecting the dielectric discontinuity at the interface). Both positive and negative values of ϕ are shown.

In Fig. 5.19, the effect of the V_{oo} term (equation 5.22) on the potential is shown (c.f. equation 5.25) by plotting ΔV against $|z-b|$, for the same (x,y) points as in the previous figure, where,

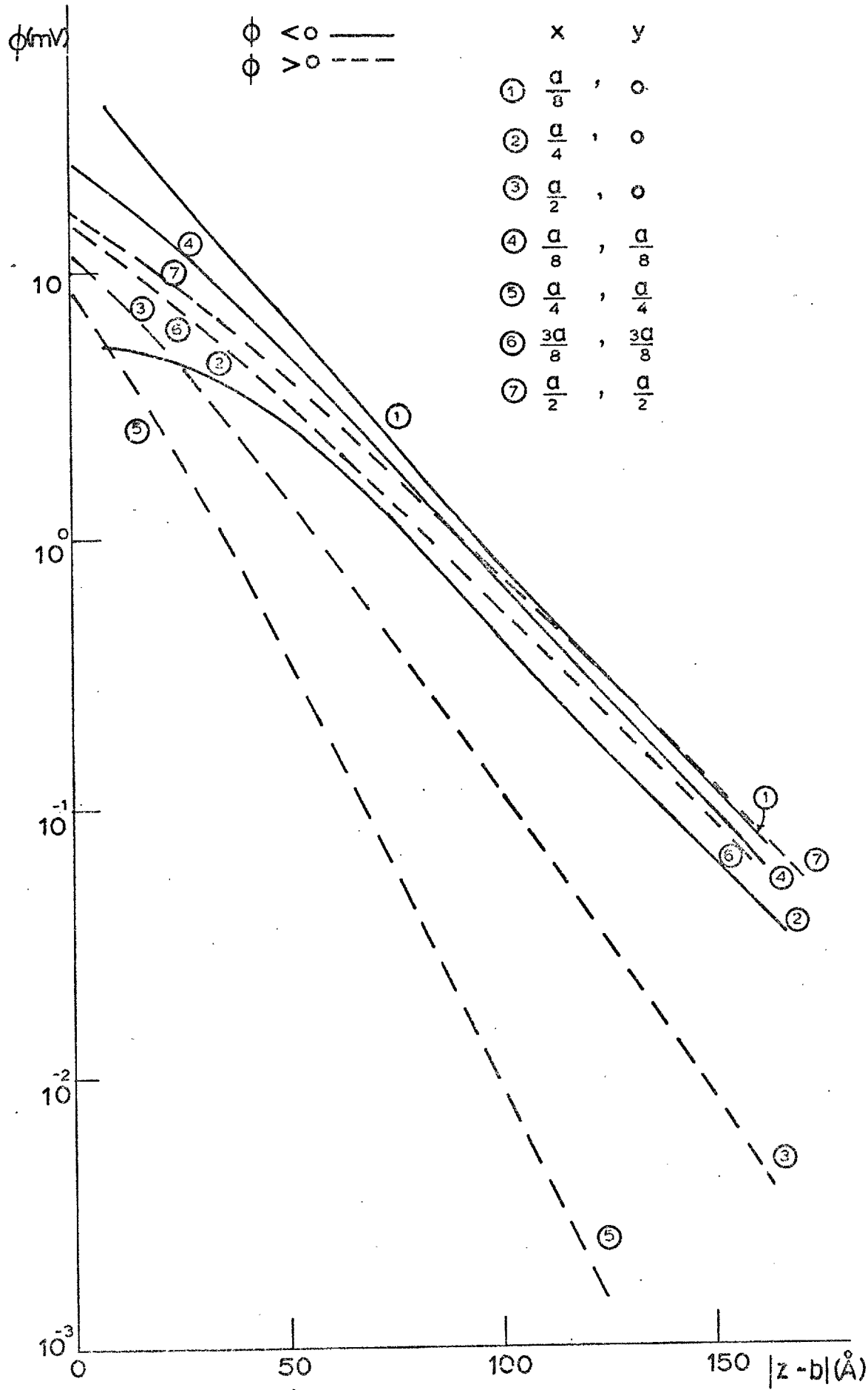


Fig. 5·18 $\phi(x,y,z)$ vs $|z-b|$ as a function of (x,y) using $\epsilon = 8{\cdot}8$ $a = 164$ Å

$$\Delta V = V(z) - V_{oo}(z = b) \qquad 5.26$$

with $V(z) = V_{oo}(z = b) + \phi(z)$, $z \geq b$

or $V(z) = V_{oo}(z) + \phi(z)$, $0 \leq z \leq b$

Examination of Figs. 5.17-5.19 illustrates that:

(1) There is an isolated region around x = 0, y = 0, which does not contribute to the conductivity in the xy plane at all (i.e. to the conductivity between the source and the drain electrodes).

(2) In between the isolated regions above, there are conducting channels which may contribute by varying degrees to the source-drain current, with the region around (a/2,a/2) offering the least amount of resistance, and that around (a/2, 0) being more resistive, but not totally insulating as in region (1) above.

(3) The potential variation is in three dimensions, and a carrier travelling in the x or the y direction will undergo continuous scattering because of this fluctuation. This makes an exact calculation of the conductivity modulation very difficult, since it involves a sum over all points in the triangle (0,0), (a/2, 0), (a/2, a/2) of Fig. 5.16(b) and for all z up to $|z-b| \sim a$. This has not been carried out in this work, although it can be seen from Fig. 5.17, that in any z-plane, most of the current would be carried along the direct path joining (a/2, a/2) and (a/2, 0). Instead, a straight forward space charge calculation was performed to estimate the absolute upper limit of the modulated conductivity assuming the potential at (a/2, a/2, z), where the maximum band bending occurs (curve 7, Fig. 5.19), to persist throughout the semiconductor: this is clearly highly artificial, but the results

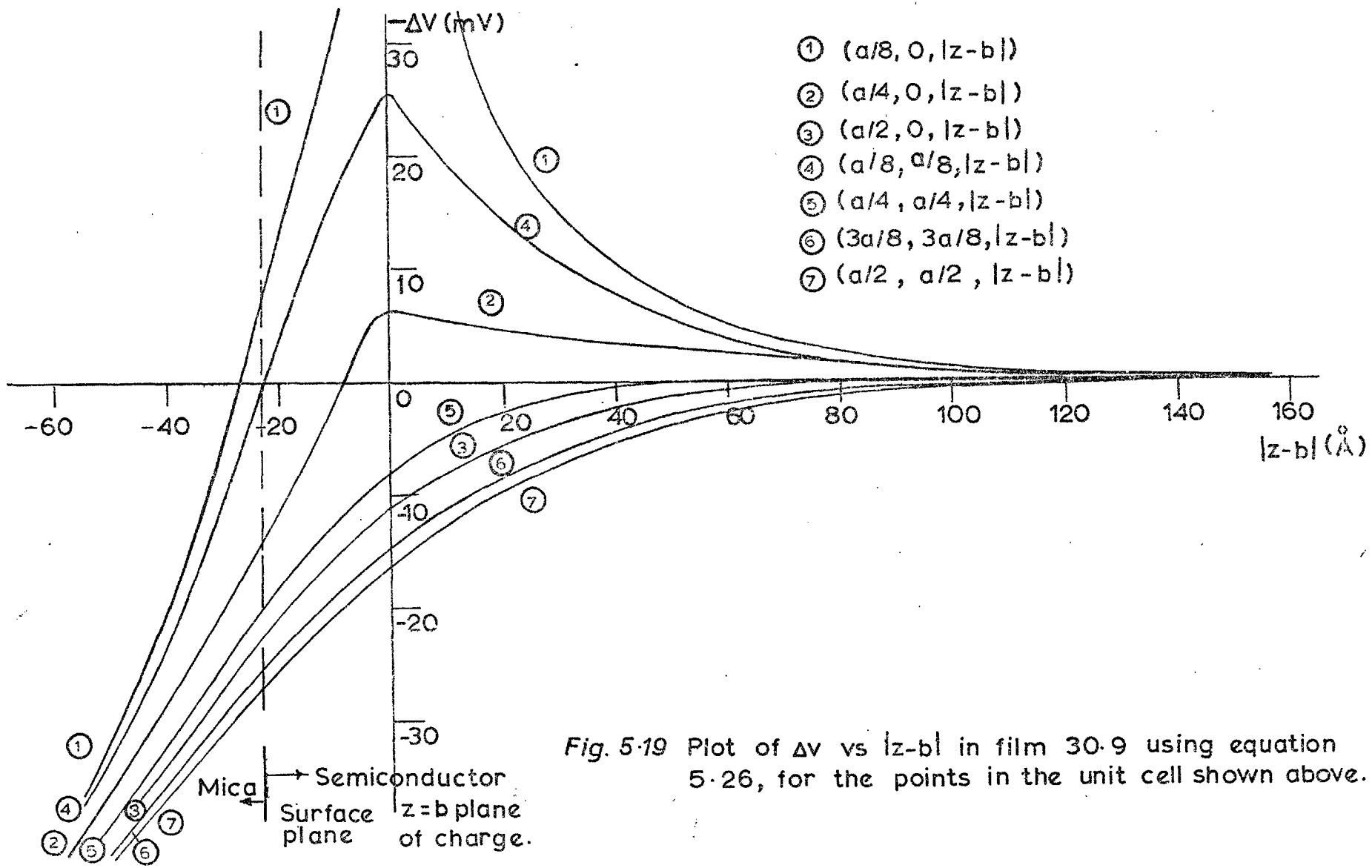


Fig. 5·19 Plot of Δv vs |z-b| in film 30·9 using equation 5·26, for the points in the unit cell shown above.

are interesting. Furthermore, all forms of scattering were neglected. This calculation was carried out in the following manner:

The shape of curve 7 in Fig. 5.19 may be approximated by an exponential, i.e.

$$\Delta V(z) = A \exp(- Z/L_D) \qquad 5.27$$

where A = 27 mV, $L_D = 43\text{Å}$, and Z is the distance from the semiconductor/dielectric interface into the semiconductor bulk. The use of the above approximation again slightly overestimates the modulated conductivity.

Hence the problem is to estimate the enhanced conductivity due to a space charge region given by equation 5.27 and shown in Fig. 5.20, where we define,

$$E(Z) = 0.027 \exp(-Z/L_D) + E_v \qquad 5.28$$

Let N_v be the effective density of states in the valence band, p the charge per unit volume in the semiconductor, P the charge per unit area in the semiconductor, and t the thickness of the semiconductor film as before. Then the excess charge per unit area, ΔP, due to the space charge region is,

$$\Delta P = P - P_b$$

where the subscript b refers to the flat band bulk value. Therefore,

$$\Delta P = N_v \int_o^t \exp - \left(\frac{E_F - E(Z)}{kT} \right) dZ - N_v \int_o^t \exp - \left(\frac{E_F - E_v}{kT} \right) dZ$$

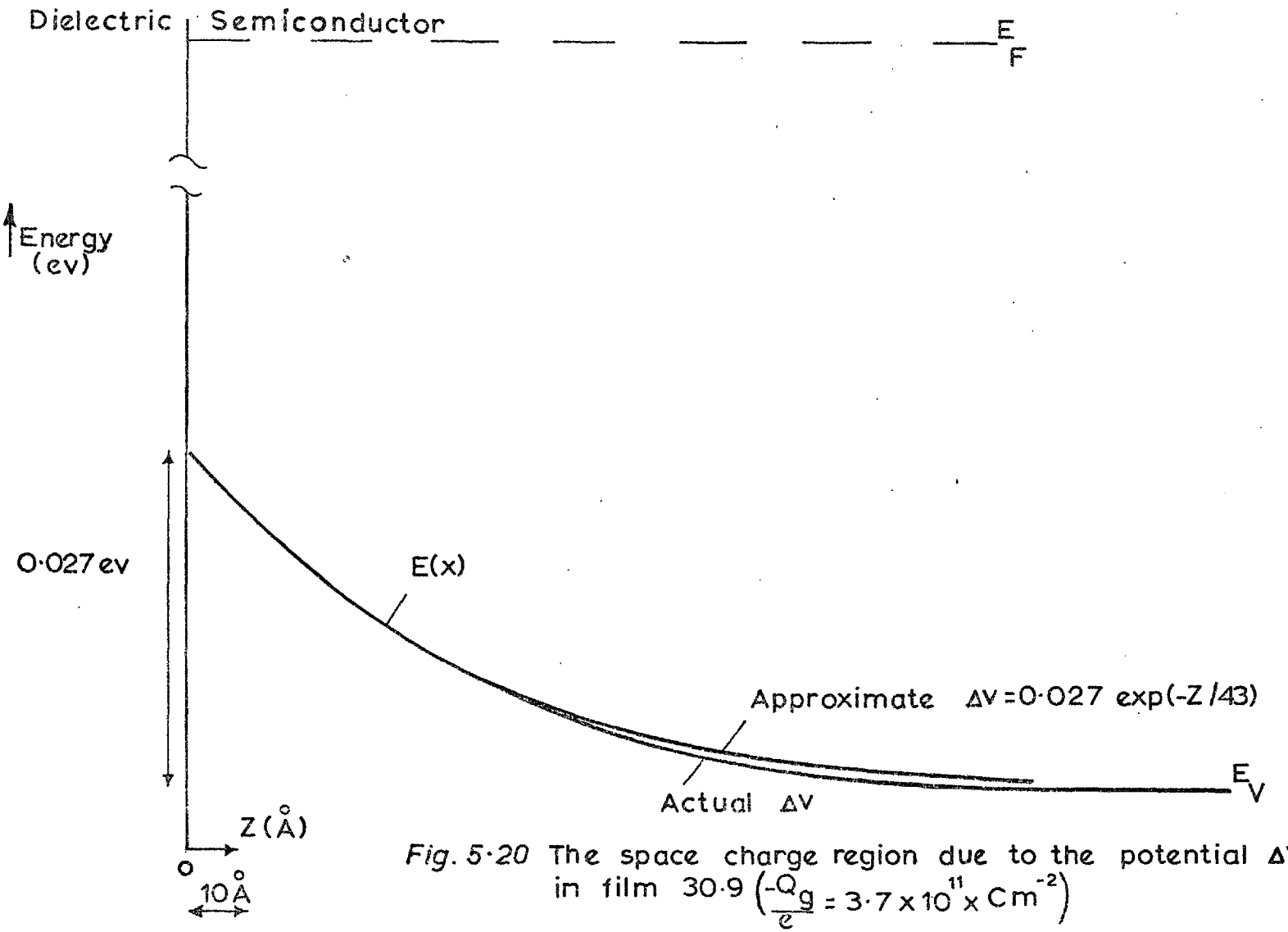


Fig. 5·20 The space charge region due to the potential $\Delta V(a/2, a/2, Z)$ in film 30·9 $\left(\frac{-Q_g}{e} = 3{\cdot}7 \times 10^{11} \times Cm^{-2}\right)$

Substituting from equation 5.28 for E(Z), and integrating the second term in the above,

$$\Delta P = p_b \{ \int_o^t \exp(\alpha e^{-Z/L_D}) \, dZ - t \}$$

where $\alpha = 0.027/kT$, and $p_b = N_v \exp -(\frac{E_F - E_v}{kT})$

Changing the variable of the integration to,

$$y = \alpha e^{-Z/L_D} ,$$

one obtains,

$$\Delta P = p_b \{ \int_{\alpha e^{-t/L_D}}^{\alpha} \frac{L_D}{y} e^y \, dy - t \}$$

Let $y = \alpha u$ in above,

$$\Delta P = p_b \{ L_D \int_{e^{-t/L_D}}^{1} \frac{e^{\alpha u}}{u} \, du - t \}$$

$$= p_b \{ L_D (\ln u + \alpha u + \frac{\alpha^2 u^2}{2.2!} + \ldots)_{e^{-t/L_D}}^{1} - t \}$$

$$= p_b \{ L_D (\alpha + \frac{\alpha^2}{2.2!} + \ldots - (-\frac{t}{L_D} + \alpha e^{-t/L_D} + \frac{\alpha^2 e^{-2t/L_D}}{2.2!} + \ldots)) - t \}$$

But, in the absence of any variation in the mobility,

$$\frac{\Delta g}{g_o} = \frac{\Delta P}{P_b} = \frac{\Delta P}{p_b t}$$

$$= \frac{L_D}{t}\{\alpha + \frac{\alpha^2}{2.2!} + \ldots - (\alpha e^{-t/L_D} + \frac{\alpha^2}{2.2!} e^{-2t/L_D} \ldots)\}$$

5.29

Taking the high temperature (T = 343 K) data of Fig. 5.14 for film 30.9, where t = 520Å, and substituting for L_D = 43Å, the above expression gives,

$$\frac{\Delta g}{g_o} \simeq 0.1$$

A similar calculation for the saddle point (x = a/2, y = 0) gives

$$\frac{\Delta g}{g_o} \simeq 5.8 \times 10^{-2}$$

It can be seen that the above value of $\frac{\Delta g}{g_o}$ is already about one order of magnitude smaller than that predicted by the Barbe model, where using equation 5.15, a value of $\frac{\Delta g}{g_o} \simeq 1.15$ is obtained for film 30.9 at 343 K.

It is apparent that the expected final modulation using the present model will be much smaller than the upper limit of 0.1 predicted above by using a simplistic approach. This is because of the large three-dimensional fluctuations in the potential distribution (and, therefore, in the space charge layer) as illustrated in Figs. 5.17-5.19, and hence the final modulation will be very much reduced from that predicted above.

Levine has also considered the effect of dielectric discontinuity. This only comes in as a scaling factor, whereby the value of ε is replaced by the dielectric mean of the gate insulator and the semiconductor for the space charge region in the semiconductor, and by the dielectric constant of the mica for the space charge region in the insulator. In our case, this means multiplying the above predicted $\Delta g/g_o$ by a scaling factor not greater than about 1.4.

A more detailed analysis of this treatment will not be carried out here, although the calculation of the expected conductivity modulation taking full account of the space charge fluctuation would be desirable.

5.4.2.3.2 A.C. Field Effect

Since the field effect measurements in the present study have been limited to room temperature and 343 K, it is not possible to determine uniquely the temperature dependence of the field effect mobility in SeTAG films. However, there is a good deal of evidence from Marshall and Owen's transient photoconductivity (briefly discussed in Section 3.8, Chapter 3) and field effect measurements in STAG films that the mobility is trap limited, although, as already pointed out in Section 5.1, the validity of some aspects of the data from the latter experiments may be in doubt.

Apart from the above evidence, examination of the field effect data at 210 Hz and 1 kHz in Figs. 5.8 and 5.9 shows $\Delta g/g_o$ to vary linearly with gate voltage in the accumulation region, which, as it will be shown below, also indicates a trap limited process. Therefore, this is assumed a priori in the following analysis.

The enhancement region is considered first ($V_g < 0$). It is proposed that immediately after the application of V_g, carrier conduction takes place in the extended states below E_v, with trapping in a set of traps of effective density N_t cm^{-3} at an energy E_t above the valence band mobility edge. If μ_d in the trap limited drift mobility, and the amount of charge trapped is much greater than that in the extended states, then,

$$\mu_{fe} = \mu_d = \mu_{ext} \cdot \frac{N_v}{N_t} \exp -\left(\frac{E_t - E_v}{kT}\right) \qquad 5.30$$

where μ_{ext} is the extended states mobility below E_v given by equation 3.23 in Section 3.7.1, Chapter 3. Also, by definition,

$$\mu_{fe} = \frac{\Delta g}{\Delta Q_g} = \frac{\Delta g/g_o}{\Delta Q_g} g_o \qquad 5.31$$

Therefore, from equations 5.30 and 5.31,

$$\frac{\Delta g}{g_o} = \frac{\Delta Q_g}{g_o} \cdot \mu_{ext} \cdot \frac{N_v}{N_t} \cdot \exp -(E_{tv}/kT) \qquad 5.32$$

where $E_{tv} = E_t - E_v$.

Since at constant temperature g_o is constant, then 5.32 shows $\Delta g/g_o$ to be directly proportional to ΔQ_g in agreement with the data of Figs. 5.8 and 5.9.

Also, for conduction in the extended states, the conductivity is given by*,

$$\sigma = C_{ext} \exp - \left(\frac{E_{FV,0}}{kT} \right) \qquad 5.33$$

where the preexponential constant, $C_{ext} = N_v \, e \, \mu_{ext} \exp(\gamma/k)$, $E_{FV,0} = (E_F - E_v)_{T=0}$, and $\gamma = 3.1 \times 10^{-4}$ eVK^{-1}.

Using the μ_{fe} data of Table 5.2 for films 30.9, 40.79 and 52.10, together with the conductivity data for each film, the estimated parameters listed in Table 5.3 below were obtained through equations 5.30 and 5.33. It can be seen that the set of traps controlling the field effect mobility in the enhancement mode are situated at 0.25-0.32 eV above the valence band mobility edge, and are of approximate density of 3×10^{19} cm^{-3}.

Film No.	μ_{fe}(299K) cm^{2}V^{-1}s^{-1}	μ_{fe}(343K) cm^{2}V^{-1}s^{-1}	E_{tv}(eV)	$\frac{N_v}{N_t} \mu_{ext}$ cm^{2}V^{-1}s^{-1}	C_{ext}(Ω^{-1}cm^{-1})	N_v(299K) cm^{-3}	N_t(cm^{-3})
30.9	1.9×10^{-4}	1.0×10^{-3}	0.32	51.3	921	9×10^{18}	3×10^{18}
40.79	4×10^{-4}	1.4×10^{-3}	0.25	6.7	2236	2.2×10^{19}	5.7×10^{19}
52.10	1.6×10^{-4}	7×10^{-4}	0.30	18.7	4526	4.4×10^{19}	4.1×10^{19}

Table 5.3. Trap Limited Drift Mobility Parameters Computed from A.C. Field Effect Data in the Enhancement Mode

*See equation 3.22, Section 3.7.1, Chapter 3.

When negative charge is put on the gate, positive charge is induced in the semiconductor below E_v. The above theory shows that these holes are trapped by a set of traps of energy E_{tv} above E_v, which we could associate with the D^- centres below E_F proposed by Mott, Davis and Street[12], Street and Mott[13]. When negative charge is induced in the semiconductor, however, the electrons cannot interact with the D^- centres which are hole traps, and if the same kind of trap limited process is present, then these traps can only be situated <u>above</u> E_F (i.e. D^+ centres). In this case, the field effect mobility in the depletion mode would predict the depth of the electron traps below the conduction band mobility edge. Because of the much lower mobility of the electrons compared to the holes in similar chalcogenide glasses, however, the absolute magnitude of $\Delta g/g_o$ will be smaller in the depletion regime as shown in Figs. 5.8 and 5.9. This model would also require $\Delta g/g_o$ to vary linearly with charge when the semiconductor is strongly depleted. It is not possible to say for certain whether this is what happens by the examination of the present data. Marshall and Owen's data on As_2Te_3 and STAG show $\Delta g/g_o$ to be independent of Q_g for strong depletion ($\frac{Q_g}{e} \gtrsim 1 \times 10^{12}$ cm^{-2}), whereas Mahan and Bube do not observe saturation in As_2Te_3 with $\frac{Q_g}{e} \gtrsim 1.5 \times 10^{12}$ cm^{-2}, and at comparable temperatures (T = 273 K). In fact, for temperatures above 320 K, it is found that inversion occurs in this material. They do not report a similar behaviour in As_2SeTe_2, and As_2Se_2Te, both of which are strongly p-type. Egerton's A.C. field effect data also shows a weak dependence of $\Delta g/g_o$ on Q_g at $\frac{Q_g}{e} = 2 \times 10^{12}$ cm^{-2}.

By taking the asympotic values of the 210 Hz and 1 KHz data of Figs. 5.8 and 5.9 respectively, the electron trap depth below the conduction band mobility edge is found to be about 0.34 eV (c.f. hole traps at 0.25 eV above E_v). A direct estimate of the density of D^+ centres is not possible, since the electron mobility and the effective density of states in the conduction band are not known. However, the theory requires the density of D^+ and D^- centres to be equal, and thus the density of the electron traps is expected to be about 6×10^{19} cm^{-3} as well.

5.5 Discussion and Conclusions

In this chapter, the electrical properties of SeTAG thin films prepared by flash evaporation from bulk ingots of $Ch_{61}Y_{39}$ nominal composition were reported.

Room temperature resistance measurements as a function of film length, and a linear I-V characteristic, both indicated ohmic contacts to be present between the Cr electrodes and the semiconductor film.

Variation of room temperature resistivity with film thickness showed no systematic functional relationship between these two parameters, and therefore, it was concluded that the bands were effectively flat at the surface. This conclusion was supported by the work of others on similar chalcogenide alloys.

Field effect measurments formed the most important part of the study of the electrical properties of thin films, which was carried out during the course of this work. The most significant observation has been the decay in field effect modulation with time towards zero. This is in direct contradiction to the two recently reported measurements by Marshall and Owen* on As_2Te_3 and STAG films,

---

*Henceforth referred to as MO in some instances.

and by Mahan and Bube* on As_2Te_3, As-Se-Te and Sb_2Te_3 films. Although the magnitude of the induced surface charge in the present study was kept to less than 4×10^{11} cm^{-2} in most cases, Egerton reported a very similar decay in STAG films for $\frac{Q_g}{e} \gtrsim \pm 2 \times 10^{12}$ cm^{-2}, which is comparable to the largest charge densities used by Marshall and Owen, where $\frac{Q_g}{e} \lesssim \pm 3 \times 10^{12}$ cm^{-2}.

As already pointed out in Section 5.1, however, the validity of Marshall and Owen's data may be in doubt, because of the film fabrication procedure and the experimental methods used. Also, all of their data were recorded at or below room temperature, where the observed decay in modulation is expected to be slower, and therefore more difficult to observe. However, there is almost no doubt about the validity of Mahan and Bube's data, where standing field effect modulations were recorded in the range 255 K < T < 345 K in the case of As_2SeTe_2 alloys. In the absence of any experimental artifacts giving rise to conflicting observations, the only difference between the films prepared in the present work and by Egerton on the one hand, and those prepared by MO and MB on the other, is that in the former cases they were flash evaporated, while the latter used R.F. sputtering. This point, and the expected dependence of the observed standing modulation on defect density will be returned to later in this section. First, the present data are discussed in the light of the Barbe model and the Discrete Charge Model.

The analysis of the 210 Hz field effect data was carried out in Section 5.4.2.1 using the Barbe model. However, even if a structureless, CFO type density of states pertinent to the model may be

---

*Henceforth referred to as MB in some instances.

assumed, the Barbe analysis results in pronounced curvature in the $\Delta g/g_o$ vs Q_g/e curves in both the enhancement and the depletion regimes because of the function F_p in equations 5.11 and 5.15. F_p has been plotted in Fig. 5.21, and any fitting procedure to the 210 Hz data involves only F_p and L/t, where the latter is only a scaling factor. This is effectively the method used by MB for their analysis of the field effect data, by assuming conduction to be controlled by the states at the Fermi level. Since the results on SeTAG show a linear variation of $\Delta g/g_o$ with Q_g/e in the enhancement mode, a Barbe type analysis does not seem to be applicable.

Turning instead to a trap limited field effect mobility mechanism, as proposed in the Discrete Charge model and by MO, the 210 Hz field effect was explained satisfactorily in terms of trapping of injected carriers by the D^- and D^+ centres in the accumulation and depletion regimes respectively. The various parameters for sample 40.79, which have been computed using this theory, are shown in Fig. 5.22*.

In Section 5.4.2.3.1, an estimate of the absolute upper limit for the conductivity modulation at long times was obtained by using Levine's analysis for the potential distribution arising from a square array of surface states at the semiconductor/insulator interface in an MIS system. $\Delta g/g_o$ was found to be about 0.1 under the conditions of maximum band bending, if all scattering present because of three dimensional fluctuations in the potential near the

---

*The data in this Figure compare to MO's findings of hole trapping centres of 10^{19} - 10^{20} cm^{-3} in density at 0.13 eV below E_F in STAG films.

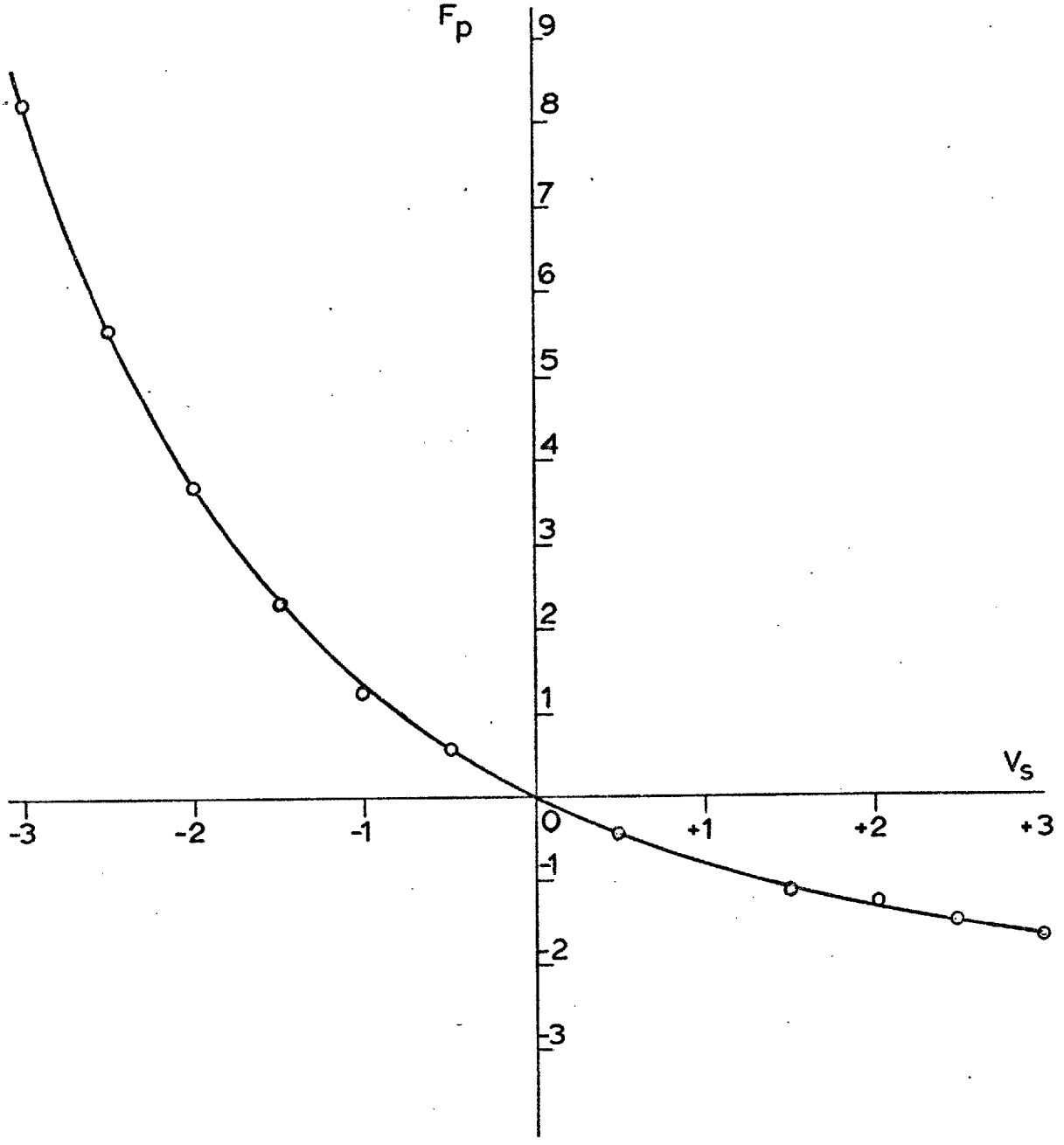


Fig. 5·21 Plot of $F_p = \sum_{m=1}^{\infty} \frac{(-V_s)^m}{m \cdot m!}$ against V_s

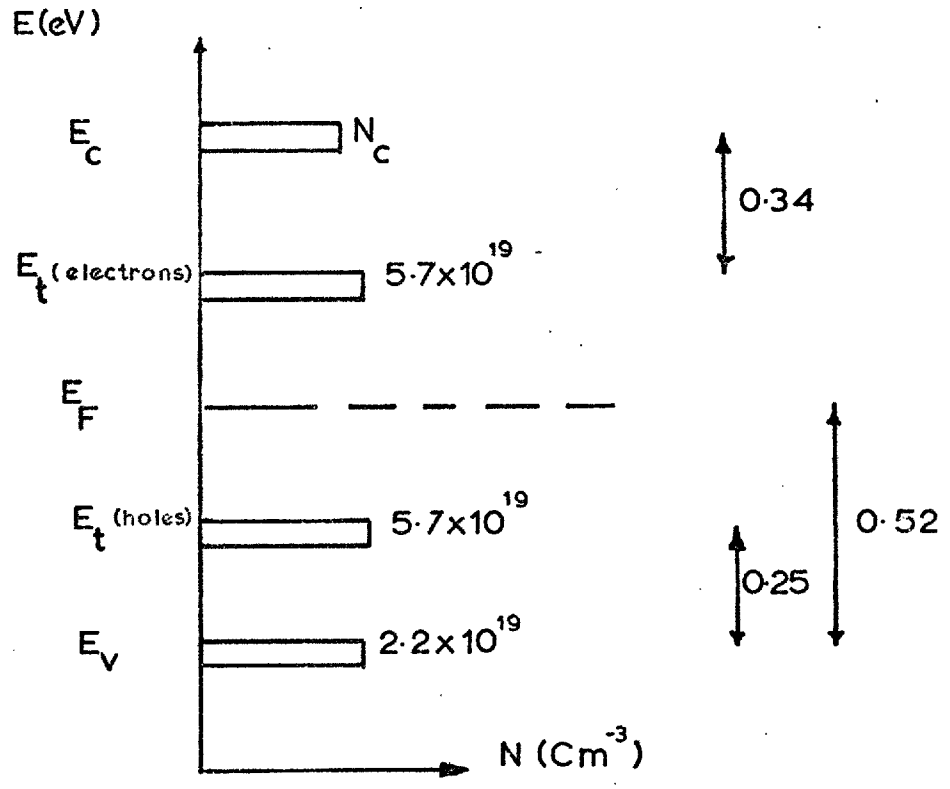


Fig. 5·22 Trap parameters computed for film 40·79 using the AC field effect data and the discrete charge model.

interface were neglected, and if the space charge due to the region in the material with maximum modulation were taken to persist throughout the semiconductor. Even under such optimum conditions, the predicted modulation was found to be about one-tenth of that calculated from the Barbe model. Because of the significance of scattering in a more precise computation of conductivity modulation, it is expected that the final $\Delta g/g_o$ will be much reduced from the value of 0.1 predicted above.

It is also interesting, thought not surprising, to note that the modulation calculated from the discrete charge model is highly sensitive to the defect density present in the solid. The lower the density of defects, N, the larger the average separation of the charged centres, taken to be $\frac{1}{2}N^{-1/3}$, from the dielectric interface, and hence the greater the degree of final modulation expected. In this vain, it is possible to understand why a steady state modulated conductivity may be observed in a material like As_2Te_3, but not in SeTAG, where because of more disorder, the defect density in the latter is expected to be larger. However, such a proposal does not clarify the apparent difference between the behaviour of sputtered and evaporated films, unless the various deposition parameters in each case (i.e. the deposition rate and the substrate temperature) are known. Marshall and Owen do not give any details of the sputtering conditions they used, but Mahan and Bube quote a rate of $67\mathring{A}\ min^{-1}$. This compares to an average rate of about $7\mathring{A}\ s^{-1}$ for flash evaporated SeTAG (although the higher R.M.S. peak values, when the grains are dropped into the hot boat, would be more relevant to the present discussion). Under the gross assumption of comparable substrate temperatures, one may expect a larger defect density in SeTAG owing to a higher deposition rate.

5.5.1 Suggestions for Future Work

In a recent paper, Mott and Street[17] have examined the discrepancies between the findings of MO and MB. They also conclude that the details of sample preparation may be important in understanding the various observed field effect properties in chalcogenide glass films. From the point of view of the data presented in this work, it would be useful to study the field effect in sputtered and evaporated films under the same experimental conditions.

Finally, this study has limited itself to the short time and long time processes at two different temperatures. More work as a function of temperature would be desirable. Also, the charge transfer mechanism in the intermediate time regime giving rise to the decay has not been considered quantitatively. A detailed analysis of this region should be carried out as well.

Chapter 5 - References

1. H. Fritsche, S.R. Ovshinsky, J. Non-Cryst. Solids, 2 (1970) 393

2. D.F. Barbe, J. Vac. Sci. Tech., 8 (1971) 102

3. R.F. Egerton, App. Phys. Lett., 19 (1971) 203

4. A.W. Levy, M. Green, W. Gee, J. Phys. C., 7 (1974) 352

5. P.A. Tick, J.H.P. Watson, J. Non-Cryst. Solids, 13 (1973-74) 229

6. J.M. Marshall, A.E. Owen, Phil. Mag., 33 (1976) 457

7.(a) T.C. Arnoldnssen, C.A. Menezes, Y. Nakagawa, R.H. Bube, Phys. Rev. B, 9 (1974) 3377

(b) R.H. Bube, J.E. Mahan, R.T.-S.Shiah, H.A. Vander Plas, App. Phys. Lett., 25 (1974) 419

8. J.E. Mahan, R.H. Bube, J. Non-Cryst. Solids, 24 (1974) 29

9.(a) M. Kastner, H. Fritsche, Mat. Res. Bull., 5 (1970) 631

(b) M. Green, W. Gee, A.W. Levy, P. Ming, J. Phys. D., 5 (1972) L55

10.(a) W.E. Spear, P.G. LeComber, J. Non-Cryst. Solids, 8-10 (1972) 727

(b) A. Madan, P.G. LeComber, W.E. Spear, J. Non-Cryst. Solids, 20 (1976) 239

11. A.W. Levy, Ph.D. Thesis, Council for National Academic Awards, 1972

12. N.F. Mott, E.A. Davis, R.A. Street, Phil. Mag., 32 (1975) 962

13. R.A. Street, N.F. Mott, Phys. Rev. Lett., 35 (1975) 1293

14. See, for instance, T.L. Hill, Introduction to Statistical Thermodynamics, Chapter 18, p.321, Addison Wesley Publishing Co., Massachusetts, 1960

15. M. Green, M.J. Lee, Solid State Surface Science, Vol. I, Chapter 3, p. 167, Dekker, New York, 1969

16. J.D. Levine, Surface Science, 10 (1968) 313

17. N.F. Mott, R.A. Street, Phil. Mag., 36 (1977) 33

18. M.H. Brodsky, M.A. Frisch, J.F. Ziegler, App. Phys. Lett., 30 (1977) 561

Chapter 6

Summary and Concluding Remarks

In this study, complex chalcogenide glass alloys in the series $Ch_x Y_{100-x}$, where Ch = $Se_{19.7} Te_{80.3}$, Y = $As_{74.4} Ge_{25.6}$, and x = 45%, 61% and 71% were prepared. The structure of the bulk ingots was investigated in Chapter 2 using scanning electron microscopy and X-ray powder diffraction. Electron probe microanalysis (EPMA) showed the bulk ingots to be homogeneous, and the nominal and actual composition of the ingots to be in agreement in the majority of cases. Softening temperature studies indicated that increasing chalcogen content led to a looser structure and a lower softening point.

Various thin film deposition techniques from the parent $Ch_{61}Y_{39}$ bulk glass were investigated in Chapter 4. For reasons of compositional inconsistency or poor electrical properties, the Knudsen cell and the D.C. sputtering methods were found to be unsatisfactory. Instead, flash evaporation was selected as the most reliable means of depositing SeTAG thin films. EPMA data indicated that these films were reasonably consistent in their compositions. Transmission electron microscopy showed the films to be amorphous, but it also indicated that they were very susceptible to damage and rapid crystallisation by the electron beam through heating.

The electrical transport properties of bulk $Ch_x Y_{100-x}$ SeTAG glasses were investigated in Chapter 3 by making D.C. conductivity and thermoelectric power measurements as functions of temperature and composition. The Seebeck coefficient data indicated that all the specimens were p-type. The temperature dependence of the optical gap in the $Ch_{61}Y_{39}$ glass was also measured, and it was found to be about 3.1×10^{-4} eVK^{-1}.

Slight curvatures were observed in all plots of conductivity and thermoelectric power against the reciprocal of temperature for the bulk specimens that were studied. The data could best be fitted to a model proposed by Nagels et al.[1] (NCD), in which p-type conduction was proposed to take place in parallel in the extended valence states and in the localised valence band tail in the mobility gap. The width of the localised valence band tail was found to increase with increasing compositional disorder in the chalcogen network (i.e. decreasing X in $Ch_X Y_{100-X}$) in agreement with NCD's observations in Si-As-Te glasses. However, in both SeTAG and Si-As-Te glasses, the effective density of states, N_V, in the valence band was about two orders of magnitude less than that in the localised valence band, N_B($N_B \sim 2 \times 10^{21}$ cm^{-3}). This was not considered possible, when the energy separation between the above two sets of levels was about 0.1 eV. It was concluded that although the band tail states may contribute to some extent to the total conduction process, the NCD model was not sufficiently refined to explain the conduction process in a totally satisfactory manner. It was proposed that the inclusion of the temperature dependence of the hopping mobility (neglected in the NCD analysis) and the shape of the density of states as proposed by Grant and Davis[2], together with a possible small deviation from linearity in the variation of $(E_F - E_V)$ with temperature, may lead to a more likely explanation of the observed bulk properties. In Chapter 3, the effect of heating in air of bulk SeTAG was also briefly investigated. Annealing was not observed, but instead it was found that a conducting 'skin' could be formed which enhanced the conductivity. Removal of the skin resulted in the restoration of the original electrical properties.

The field effect data on SeTAG thin films were presented in Chapter 5. The films were found to be p-type. A continuous decay of the field effect current with time was noted. The data were examined in two regimes in terms of a discrete charge model. The small observed modulations a long time after the application of the field were explained by the large potential fluctuations arising near the semiconductor-dielectric interface due to a thin charge built up in that region. The A.C., short time, field effect data above 200 Hz, on the other hand, were found to represent a trap limited drift mobility process, where, in the enhancement mode, the trapping centres, N_t, were roughly 0.25-0.32 eV above the valence band mobility edge, and of about 10^{19} cm^{-3} in density. The depletion data could also be explained in terms of a set of electron traps (i.e. D^+ centres in the paired dangling bond picture[3] above the Fermi level. The latter proposal was, however, tentative because of the limitations of the data in the depletion mode.

Finally, it should be noted that, assuming similar conduction mechanisms to be present in bulk and thin films of SeTAG, the deep hole trapping centres detected from the A.C. field effect measurements are not likely to be detectable in the bulk thermopower and conductivity measurements except at low temperatures not covered in this work.

References - Chapter 6

1. P. Nagels, R. Callaerts, M. Denayer in Amorphous and Liquid Semiconductors, Vol. II, p. 867, Taylor and Francis, 1974

2. A.J. Grant, E.A. Davis, Solid State Communications, 15 (1974) 563

3. (a) N.F. Mott, R.A. Street, E.A. Davis, Phil. Mag., 32 (1975) 961

(b) N.F. Mott, R.A. Street, Phil. Mag., 36 (1977) 33